



**HAL**  
open science

# Modelling of additive manufacturing processes : Case of polymer laser sintering

Lan Zhang

► **To cite this version:**

Lan Zhang. Modelling of additive manufacturing processes : Case of polymer laser sintering. Materials. INSA de Lyon, 2022. English. NNT : 2022ISAL0123 . tel-04147516

**HAL Id: tel-04147516**

**<https://theses.hal.science/tel-04147516>**

Submitted on 30 Jun 2023

**HAL** is a multi-disciplinary open access archive for the deposit and dissemination of scientific research documents, whether they are published or not. The documents may come from teaching and research institutions in France or abroad, or from public or private research centers.

L'archive ouverte pluridisciplinaire **HAL**, est destinée au dépôt et à la diffusion de documents scientifiques de niveau recherche, publiés ou non, émanant des établissements d'enseignement et de recherche français ou étrangers, des laboratoires publics ou privés.



# INSA

N°d'ordre NNT : 2022ISAL0123

## THESE de DOCTORAT DE L'INSA LYON, membre de l'Université de Lyon

Ecole Doctorale N° EDA162  
MEGA de Lyon

Spécialité/ discipline de doctorat :  
Mécanique des fluides

Soutenue publiquement le 14/12/2022, par :  
**Lan ZHANG**

---

# Modelling of additive manufacturing processes: case of polymer laser sintering

---

Devant le jury composé de :

RANDRIANALISOA, Jaona	Maître des Conférences HDR Université de Reims Champagne-Ardenne	Rapporteur
SCHMIDT, Fabrice	Professeur des Universités IMT Mines Albi	Rapporteur
BOYER, Séverine	Chargé de recherche CEMEF Mines de Paris	Examinatrice
HAMILA, Nahienne	Professeur des Universités Ecole nationale d'ingénieurs de Brest	Examineur
Boutaous, Mhamed	Maître de Conférences INSA-Lyon	Directeur de thèse
Xin, Shihe	Professeur des Universités INSA-Lyon	Co-directeur de thèse

## Département FEDORA – INSA Lyon - Ecoles Doctorales

SIGLE	ECOLE DOCTORALE	NOM ET COORDONNEES DU RESPONSABLE
<b>CHIMIE</b>	<b>CHIMIE DE LYON</b> <a href="https://www.edchimie-lyon.fr">https://www.edchimie-lyon.fr</a> Sec. : Renée EL MELHEM Bât. Blaise PASCAL, 3e étage secretariat@edchimie-lyon.fr	<b>M. Stéphane DANIELE</b> C2P2-CPE LYON-UMR 5265 Bâtiment F308, BP 2077 43 Boulevard du 11 novembre 1918 69616 Villeurbanne <a href="mailto:directeur@edchimie-lyon.fr">directeur@edchimie-lyon.fr</a>
<b>E.E.A.</b>	<b>ÉLECTRONIQUE, ÉLECTROTECHNIQUE, AUTOMATIQUE</b> <a href="https://edeea.universite-lyon.fr">https://edeea.universite-lyon.fr</a> Sec. : Stéphanie CAUVIN Bâtiment Direction INSA Lyon Tél : 04.72.43.71.70 secretariat.edeea@insa-lyon.fr	<b>M. Philippe DELACHARTRE</b> INSA LYON Laboratoire CREATIS Bâtiment Blaise Pascal, 7 avenue Jean Capelle 69621 Villeurbanne CEDEX Tél : 04.72.43.88.63 <a href="mailto:philippe.delachartre@insa-lyon.fr">philippe.delachartre@insa-lyon.fr</a>
<b>E2M2</b>	<b>ÉVOLUTION, ÉCOSYSTÈME, MICROBIOLOGIE, MODÉLISATION</b> <a href="http://e2m2.universite-lyon.fr">http://e2m2.universite-lyon.fr</a> Sec. : Bénédicte LANZA Bât. Atrium, UCB Lyon 1 Tél : 04.72.44.83.62 secretariat.e2m2@univ-lyon1.fr	<b>Mme Sandrine CHARLES</b> Université Claude Bernard Lyon 1 UFR Biosciences Bâtiment Mendel 43, boulevard du 11 Novembre 1918 69622 Villeurbanne CEDEX <a href="mailto:sandrine.charles@univ-lyon1.fr">sandrine.charles@univ-lyon1.fr</a>
<b>EDISS</b>	<b>INTERDISCIPLINAIRE SCIENCES-SANTÉ</b> <a href="http://ediss.universite-lyon.fr">http://ediss.universite-lyon.fr</a> Sec. : Bénédicte LANZA Bât. Atrium, UCB Lyon 1 Tél : 04.72.44.83.62 secretariat.ediss@univ-lyon1.fr	<b>Mme Sylvie RICARD-BLUM</b> Institut de Chimie et Biochimie Moléculaires et Supramoléculaires (ICBMS) - UMR 5246 CNRS - Université Lyon 1 Bâtiment Raulin - 2ème étage Nord 43 Boulevard du 11 novembre 1918 69622 Villeurbanne Cedex Tél : +33(0)4 72 44 82 32 <a href="mailto:sylvie.ricard-blum@univ-lyon1.fr">sylvie.ricard-blum@univ-lyon1.fr</a>
<b>INFOMATHS</b>	<b>INFORMATIQUE ET MATHÉMATIQUES</b> <a href="http://edinfomaths.universite-lyon.fr">http://edinfomaths.universite-lyon.fr</a> Sec. : Renée EL MELHEM Bât. Blaise PASCAL, 3e étage Tél : 04.72.43.80.46 infomaths@univ-lyon1.fr	<b>M. Hamamache KHEDDOUCI</b> Université Claude Bernard Lyon 1 Bât. Nautibus 43, Boulevard du 11 novembre 1918 69 622 Villeurbanne Cedex France Tél : 04.72.44.83.69 <a href="mailto:hamamache.kheddouci@univ-lyon1.fr">hamamache.kheddouci@univ-lyon1.fr</a>
<b>Matériaux</b>	<b>MATÉRIAUX DE LYON</b> <a href="http://ed34.universite-lyon.fr">http://ed34.universite-lyon.fr</a> Sec. : Yann DE ORDENANA Tél : 04.72.18.62.44 yann.de-ordenana@ec-lyon.fr	<b>M. Stéphane BENAYOUN</b> Ecole Centrale de Lyon Laboratoire LTDS 36 avenue Guy de Collongue 69134 Ecully CEDEX Tél : 04.72.18.64.37 <a href="mailto:stephane.benayoun@ec-lyon.fr">stephane.benayoun@ec-lyon.fr</a>
<b>MEGA</b>	<b>MÉCANIQUE, ÉNERGÉTIQUE, GÉNIE CIVIL, ACOUSTIQUE</b> <a href="http://edmega.universite-lyon.fr">http://edmega.universite-lyon.fr</a> Sec. : Stéphanie CAUVIN Tél : 04.72.43.71.70 Bâtiment Direction INSA Lyon mega@insa-lyon.fr	<b>M. Jocelyn BONJOUR</b> INSA Lyon Laboratoire CETHIL Bâtiment Sadi-Carnot 9, rue de la Physique 69621 Villeurbanne CEDEX <a href="mailto:jocelyn.bonjour@insa-lyon.fr">jocelyn.bonjour@insa-lyon.fr</a>
<b>ScSo</b>	<b>ScSo*</b> <a href="https://edsciencessociales.universite-lyon.fr">https://edsciencessociales.universite-lyon.fr</a> Sec. : Mélina FAVETON INSA : J.Y. TOUSSAINT Tél : 04.78.69.77.79 melina.faveton@univ-lyon2.fr	<b>M. Bruno MILLY</b> Université Lumière Lyon 2 86 Rue Pasteur 69365 Lyon CEDEX 07 <a href="mailto:bruno.milly@univ-lyon2.fr">bruno.milly@univ-lyon2.fr</a>

\*ScSo : Histoire, Géographie, Aménagement, Urbanisme, Archéologie, Science politique, Sociologie, Anthropologie

# Acknowledgement

First of all, I want to express my thanks to my family members, my Mum and Dad who dedicate half of their lives to educate me, support me and help me. Their dream is I staying with them, but they always support me to do anything that I want to do after they know what I want.

I would like to extend my sincerely gratitude to my supervisor Pro. M'hamed BOUTAOUS, and Pro. Shihe Xin. They give me the instructive advice and useful suggestions on my work and thesis, I will not finish my thesis if I do not have these suggestions. I am greatfulness to their patience that give me enough time to adapt the life in France, to understand the work and learn the relevant knowledge about this thesis. I am really grateful that they chose me to do this project. I am also grateful to Jacques Jay who help me to do the experiments of the temperature measurment.

Also my gratefulness to the China Scholarship Council who gives me the scholarship for me to achieve my doctoral degree.

Life is a long and short journey, I meet different people and things ever day, and I want to thank all of them who together make up my present, past, and future life.

# Summary

The present work focuses on one of Additive Manufacturing (AM) processes, Selective Laser Sintering (SLS) of polymer powders. It aims at improving, qualifying and validating the numerical tool developed on the one hand and on the other hand understanding and improving SLS processes. The numerical tool developed considers laser beam-polymer powder interaction, melting process, coalescence, air diffusion, porosity evolution, and crystallization. To qualify the numerical work performed and the results obtained, experiments are also conducted to measure surface temperature by an IR camera, sample dimension, and porosity distribution in the manufactured samples by X-ray computed tomography.

Important modeling work is realised on laser beam-polymer powder interaction: the Mie theory and the Monte-Carlo method are combined to take scattering into account and propose models for laser heat source. To qualify the proposed scattering models, they are used to perform numerical simulations of single-sweep/single-layer, multi-sweep/single-layer and multi-sweep/multi-layers SLS cases and the results obtained are compared with those provided by the experiments and the Beer-Lambert law. A scattering model distributes laser power in a larger but less deep zone compared with the Beer-Lambert law and numerical simulation using a scattering model predicts better the surface temperature and the thickness of the manufactured samples. Effects of the parameters such as anisotropy factor, porosity of the powder bed and particle size on the scattering model are analysed. Effects of the process parameters such as laser power, scanning speed, scanning space, scanning length, porosity, and preheating temperature are also studied.

Another important contribution of the present work concerns the prediction of the averaged porosity and the porosity distribution in the samples manufactured in multi-sweep/multi-layer cases. Comparison of the numerical results with the measurements of X-ray computed tomography shows a reasonable and encouraging agreement.

**Key words:** *selective laser sintering (SLS), numerical modeling, scattering model, temperature distribution and evolution, shrinkage, porosity.*

# Résumé

Le présent travail s'intéresse à l'un des procédés de Fabrication Additive, SLS (Selective Laser Sintering) des poudres de polymère. Il a pour objectif d'améliorer, qualifier et valider l'outil numérique développé d'une part et d'autre part de comprendre et améliorer les procédés SLS. L'outil numérique développé prend en compte l'interaction laser-poudres de polymère, le processus de fusion, la coalescence, la diffusion d'air, l'évolution de la porosité, et la cristallisation. Afin de qualifier les travaux numériques réalisés, les travaux expérimentaux sont également réalisés pour mesurer la température de surface à l'aide d'une caméra IR, les dimensions des échantillons et la distribution de la porosité dans les échantillons fabriqués à l'aide de la tomographie à rayon X.

L'important travail de modélisation a été réalisé sur l'interaction laser-poudres de polymère : la théorie de Mie et la méthode de Monte-Carlo sont associées pour modéliser la diffusion du laser et proposer des modèles de diffusion. Afin de qualifier les modèles de diffusion proposés, ils sont utilisés dans des simulations numériques et les résultats obtenus sont confrontés avec les mesures expérimentales et les résultats issus du modèle de Beer-Lambert. Le modèle de diffusion distribue la puissance d'un laser sur une zone plus grande et moins profonde par rapport au modèle de Beer-Lambert et son utilisation en simulation permet une meilleure prédiction sur la température de surface et l'épaisseur des échantillons fabriqués. Les effets des paramètres comme facteur d'anisotropie, porosité du lit et rayon moyen des particules sur les modèles de diffusion ont été étudiés. Les effets des paramètres de procédé comme puissance du laser, vitesse de scan, espacement des scans, longueur scannée, porosité du lit, et température du préchauffe sur les échantillons fabriqués sont aussi explorés.

Une autre contribution importante du travail concerne la prédiction de la porosité moyennée et la distribution de la porosité dans les échantillons fabriqués dans un procédé de multi-scans et multi-couches. La comparaison des résultats numériques avec les mesures de tomographie à rayon X montre un accord raisonnable et encourageant.

**Mots-clés:** *SLS (Selective Laser Sintering), modélisation numérique, modèle de diffusion, distribution et évolution de la température, retrait, porosité.*



# Contents

<b>Contents</b>	<b>i</b>
<b>List of Figures</b>	<b>v</b>
<b>List of Tables</b>	<b>xv</b>
<b>Introduction</b>	<b>1</b>
<b>1 General introduction of Additive Manufacturing (AM)</b>	<b>4</b>
1.1 Additive Manufacturing . . . . .	5
1.1.1 Applications of AM technology . . . . .	5
1.1.2 Categories of AM technologies . . . . .	7
1.1.3 Advantages and development of AM . . . . .	9
1.2 Overview of selective laser sintering process . . . . .	10
1.2.1 Introduction for SLS technology . . . . .	10
1.2.2 Laser types . . . . .	15
1.2.3 Properties of powder bed . . . . .	16
1.2.4 Polymer properties . . . . .	18
1.2.5 Quality of SLS objects . . . . .	25
1.2.6 Numerical method of the multiphysics coupling . . . . .	27
<b>2 Modeling and numerical methods in SLS process</b>	<b>30</b>
2.1 The Heat Transfer Model . . . . .	31
2.1.1 Governing equation . . . . .	31

2.1.2	Bondoury condition . . . . .	31
2.2	Laser-powders interaction model . . . . .	32
2.2.1	Flat-top type laser . . . . .	32
2.2.2	Gaussian laser: Beer Lambert model . . . . .	33
2.2.3	Gaussian laser: Scattering model . . . . .	35
2.3	Modeling of the thermo-physical properties . . . . .	40
2.3.1	Density and the specific heat . . . . .	40
2.3.2	Conductivity . . . . .	41
2.3.3	Emissivity . . . . .	42
2.4	Modeling of melting process . . . . .	43
2.4.1	Melting latent heat . . . . .	43
2.4.2	Viscosity of polymer . . . . .	44
2.4.3	Model of coalescence . . . . .	47
2.5	Modeling of crystallization . . . . .	52
2.6	SLS process modeling and numerical methods . . . . .	53
<b>3</b>	<b>Scattering in laser-polymer powder interaction</b>	<b>57</b>
3.1	Working configurations . . . . .	58
3.2	Models of laser-polymer powder interaction . . . . .	59
3.2.1	Beer-Lambert (unscattering) model . . . . .	59
3.2.2	Monte-Carlo scattering model . . . . .	61
3.3	Comparison between the BL law and the scattering model . . . . .	63
3.4	Parametric analysis of scattering effects . . . . .	65
3.4.1	Influence of anisotropy factor $g$ . . . . .	65
3.4.2	Influence of powder bed porosity and particle size . . . . .	67
3.5	Temperature distribution . . . . .	69
3.6	Dimension of the parts . . . . .	74
3.6.1	SLS process with PA6 . . . . .	74

3.6.2	SLS process with PA12 . . . . .	77
3.7	Summary . . . . .	78
<b>4</b>	<b>Single layer SLS processes</b>	<b>79</b>
4.1	Calibration of the IR camera . . . . .	81
4.2	Complementary results of single-sweep processes . . . . .	85
4.3	Multi-sweep and single-layer processes . . . . .	89
4.3.1	Influence of laser moving direction and laser power model . . . . .	89
4.3.2	Parametric analysis . . . . .	97
4.3.3	Comparison with experimental results . . . . .	101
4.4	Summary . . . . .	106
<b>5</b>	<b>Multi-layer SLS processes</b>	<b>107</b>
5.1	Thermal history in multi-layer processes . . . . .	108
5.1.1	Layer thickness of 100 $\mu m$ . . . . .	109
5.1.2	Layer thickness of 80 $\mu m$ . . . . .	111
5.2	Porosity of the manufactured parts . . . . .	113
5.2.1	Experimental results . . . . .	114
5.2.2	Porosity analysis using numerical simulations . . . . .	115
5.3	Summary . . . . .	131
	<b>Conclusions and perspectives</b>	<b>132</b>
	<b>References</b>	<b>135</b>
<b>A</b>	<b>Crystallization analysis</b>	<b>146</b>
A.1	DSC method and crystallinity . . . . .	146
A.2	Single-sweep and single-layer cases . . . . .	150
A.3	Multi-sweep : single-layer and multi-layer cases . . . . .	153
<b>B</b>	<b>Laser beam with <math>n_\sigma = 0.7071</math></b>	<b>154</b>

B.1	Single sweep case with laser beam of 15 W . . . . .	154
B.2	Multi-sweep case . . . . .	156
B.3	Multi-layer case . . . . .	158

# List of Figures

1	Additive Manufacturing for Automotive Part Production – 2019 - 2029 [4]. . . . .	1
2	Laser powder bed fusion of plastic powder in an SLS [5]. . . . .	2
1.1	Example of complex objects fabricated by the AM technique [8]. . . . .	6
1.2	3D printing for medical applications. . . . .	6
1.3	3D printing for art projects. . . . .	7
1.4	Summary of the AM processes employed for the main polymeric materials [16].	7
1.5	SLS machine for fabrication thermal plastic [18]. . . . .	11
1.6	Illustration of the SLS fabrication process. . . . .	12
1.7	(a) Scanning electron micrograph of sintered nickel spheres. (b) The mass transport pathways sintering process. . . . .	14
1.8	Image of powder melting from HSM: PP-A. . . . .	14
1.9	Schematic of $CO_2$ laser. . . . .	15
1.10	Absorptivity along the beam path for the powders. The insets show the powder and incident beam size at locations with low absorption (right) and high absorption (left) [48]. . . . .	17
1.11	A schematic drawing of one layer of the cross-section of 3D printed materials, shows the geometric model shows variations in porosity. $D$ is the track diameter; $L$ is the distance between the centres of neighbouring tracks; $H$ is the vertical distance between layers. [51] . . . . .	18
1.12	PA6 polymer particle size distribution. . . . .	19
1.13	Interconnection of different polymer properties to be organized for providing promising SLS materials [54]. . . . .	19
1.14	DSC profile of a semi-crystalline polymer the sintering windows [54]. . . . .	20
1.15	SEM images of the virgin and the used PA12 powders [58]. . . . .	20
1.16	DSC and . . . . .	21

1.17	Predicted the sinter radius based on Frenkel model [61]. . . . .	21
1.18	Schematic representation of the three types of nonisothermal crystallization of polymers [70]. . . . .	23
1.19	Microstructure for PA12 transformed after SLS process [60]. . . . .	23
1.20	DSC thermograms of PA6- $\alpha_1$ , PA6- $\alpha_2$ , and PA6- $\beta$ during the first heating [75].	24
1.21	The TGA curves of PA66 and PA66/Mclay nanocomposites [77]. . . . .	24
1.22	The crystalline structure characteristic of PA6 in SLS part: (a) Diffractograms d-spacing evolution of PA6 in the cooling process. (b) with different manufacturing laser power [75]. . . . .	25
1.23	(a) Height map of sample's surface.(b) Porosity tomography image [82]. . . .	26
1.24	Overview of the Discrete Element Method. At right, the variables associated with the collision mechanics are diagrammed [89]. . . . .	28
1.25	(a) View of initial and compacted specimens for mono-disperse and poly-disperse medium. (b) Time history of average possible contacts for one particle[91]. . . . .	28
2.1	Schematic of manufacturing dominates X, Y and Z direction. . . . .	32
2.2	Shaping of laser beam profile analysed by the CCD-camera. (a) Gaussian beam; (2) flat-top; (3) inverse Gaussian power distribution [94]. . . . .	33
2.3	Gaussian and flat top beams of the same optical power. . . . .	34
2.4	Comparison of the analytical and numerical relative intensity distribution in the beam center along the normal direction for five resolutions and three incident angles [100]. . . . .	35
2.5	Y-axis T-NPFD profile after scattering by 3.2-mm PA6 GF30 % plaque (line scan along X) compared with unscattered-beam profile (three sets of data are shown) [101]. . . . .	35
2.6	Phase function for $g$ , (a) $g = 0.06$ , (b) $g = 0.96$ [38]. . . . .	37
2.7	Relationship between anisotropy factor $g$ and reflection rate of medium [105]. .	37
2.8	Attenuation path of photon $k$ inside powder bed [105] [108]. . . . .	39
2.9	Schematic showing that the energy is absorbed by the powder bed and the base plate (red line). . . . .	42
2.10	liquid fraction versus temperature, linear and nonlinear models. . . . .	44
2.11	Shear viscosity data from capillary rheometry at 473K for PA-12 polymers, plotted as shear viscosity <i>vs</i> shear rate [121]. . . . .	45

2.12	Initial zero-shear viscosity-time profile for PA12 polymer [122]. . . . .	45
2.13	angle of clination–temperature. . . . .	46
2.14	Two-dimensional scheme of the sintering process in a polymeric powder bed [129].	48
2.15	Schematic of coalescence of two spherical particles [93]. . . . .	48
2.16	Flowchart of SLS simulation. . . . .	54
2.17	A example of one 2D section of a 3D control volume. . . . .	54
3.1	Schematic of the laser scanning path and the molten zone. Temperature at the surface of the molten zone and the geometry of the manufactured part (the molten zone) are important and should be measured and used to qualify and validate numerical predictions. . . . .	58
3.2	Ztereo Microscope . . . . .	59
3.3	Schematic behaviour of laser photons in a powder bed [43]. . . . .	61
3.4	The schematic of laser photons travel paths distribution in the powder bed. . .	62
3.5	Comparison of the absorbed power between the counting results of the photons' scattered map and the identified analytical model for the counting volumes in different vertical layers. . . . .	63
3.6	Photons' travel maps in the cases with and without scattering. . . . .	63
3.7	Transmitted power distribution in depth direction. Due to the absorption and scattering, the transmitted power is decayed from the surface to deeper positions.	64
3.8	Absorbed laser power distribution in the powder bed in the cases with and without scattering: absorbed laser power by certain horizontal layers with respect to the radial counting volumes. Without scattering, the laser power is absorbed in a deeper vertical and smaller horizontal zone while with scattering it is absorbed in a larger horizontal but smaller vertical zone. . . . .	64
3.9	Laser power transmission in the depth direction depends on the anisotropy factor $g$ . Due to the scattering increase ( $g$ decreasing) the power transmission is decreased and it is more attenuated. . . . .	65
3.10	Absorbed laser power versus $g$ in the powder bed: local distribution (left) and integrated laser power in the counting volumes (right). . . . .	66
3.11	Comparison of the absorbed laser power in the powder bed with different $g$ . . .	67
3.12	Attenuation coefficient ( $\beta$ ) with respect to powder bed density. . . . .	68
3.13	Influence of the initial porosity of the powder bed on temperature profile and melting latent heat. . . . .	68

3.14	Influence of the averaged radius of the polymer particles on attenuation coefficient. . . . .	69
3.15	Instantaneous surface temperature of the powder bed and illustration of the pixel area of the IR camera. . . . .	70
3.16	Time evolution of temperature in one camera pixel area: IR camera measurement and numerical results with and without scattering. . . . .	71
3.17	Numerical results of averaged temperature in one camera pixel area centered about the trajectory of the laser axis. . . . .	72
3.18	Instantaneous temperature fields in a vertical plane normal to the laser sweep in the scattering case. . . . .	72
3.19	Instantaneous temperature fields in a vertical plane normal to the laser sweep in the case without scattering. . . . .	73
3.20	Time evolution of point-wise surface temperature at several positions which are characterized by their distances to the trajectory of laser axis. . . . .	73
3.21	Instantaneous temperature profiles at several depth positions in the vertical plane normal to the laser trajectory at time = 0.0005 s. One can see that the horizontal influence zone in the scattering case is maximal and that in the case without scattering it is very small at this time (heat conduction will increase it slowly later on.). . . . .	74
3.22	Time evolution of relative contact length. Fig. 3.22 shows the contacted length change rate calculated by the Frenkel coalescence model, which is shown in Chapter-2, section of model of coalescence, the changing rate is major dependence on the viscosity of polymer that is expressed by the Eq. (2.60). . . . .	74
3.23	Dimension of the sample obtained in a single-sweep SLS using a power of 13 W. (a) Different values of minimum duration above $T = 474 K$ . (b) Different values of minimum temperature with a minimum duration of 0.05 s . . . . .	75
3.24	Photographs of the sample. . . . .	76
3.25	Dimensions of the samples under single-sweep conditions: comparison of numerical predictions with the measurements. . . . .	76
3.26	Dimensions of the samples: comparison between experimental and numerical results for different cases. . . . .	77
4.1	Schematic diagram of a multi-sweep SLS process [147]. The laser beam is scanning forward and backward and the heating overlap is controlled by the scanning space. . . . .	80
4.2	Scheme of the powder particles sintering [148]. . . . .	80
4.3	IR camera-TITANIUM 520. . . . .	81

4.4	Schematic of camera installation [151]. . . . .	82
4.5	Photos of SLS experimental set up. (a) The IR camera. (b) View of the manufacturing room (manufacturing). (c) View of the manufacturing room (after manufacturing). . . . .	82
4.6	Luminance of the sources. . . . .	83
4.7	Schematic of the experimental installation for testing the inclination angle. . .	84
4.8	IR images with different inclination angles. . . . .	84
4.9	Angle of inclination versus temperature . . . . .	85
4.10	$DL$ of a laser path measured by an IR camera. . . . .	86
4.11	Digital level and temperature evolution with time (Case 3). . . . .	86
4.12	Numerical and experimental results at the chosen positions in the single-sweep situation (Case 3). (a) Three positions chosen in experimental photo. (b) Four positions chosen in simulation points for comparison. . . . .	87
4.13	Numerical results at the chosen positions in the single-sweep situation (Case 3) : Time evolution of temperature. . . . .	87
4.14	Influence of the initial porosity of the powder bed on temperature evolution. .	88
4.15	Comparison of temperature time evolution between measurements and simulations. . . . .	89
4.16	Picture during a SLS manufacturing process. A multi-sweep process allows to melt polymer powder in the controlled areas in one single-layer and manufacture multiple pieces. This process can be repeated for multi-layers and allows to produce parts of bigger dimensions. . . . .	90
4.17	Sample picture showing its thickness. . . . .	91
4.18	Sample picture in $X - Y$ plane. . . . .	91
4.19	Scheme of laser moving directions. . . . .	91
4.20	Vertical scanning type: $DL$ distributions during the scanning. . . . .	92
4.21	Horizontal scanning type: $DL$ distributions during the scanning. . . . .	93
4.22	Surface temperature distribution during a multi-sweep SLS process (Case 1) using a scattering model: a scanning length of $0.05\ m$ is considered and the studied scanning is horizontal, but note that in the simulation laser power is only applied to a length of $1.2\ mm$ . . . . .	94
4.23	Temperature distribution in the $y - z$ plane at the mid-width during a multi-sweep SLS process (Case 1) using a scattering model: a scanning length of $0.05\ m$ is considered and the studied scanning is horizontal, but note that in the simulation laser power is only applied to a length of $1.2\ mm$ . . . . .	95

4.24	10 points in the central part of the computational domain are chosen for the comparison of temperature time traces. One point is chosen for each of the first 5 tracks and another 5 points are chosen between trac-3 and trac-4. . . .	95
4.25	Time evolution of temperature at various positions about the domain mid-width (Case 1) and numerical simulation is performed using a scattering model. (a) (b) At the tracks' centers. (c) At positions from position-1 to position-5. (d) At different depth positions under trac-3. Note that in (b) time delays between trac-3, trac-4 and trac-5 are removed by drawing $T_3(t)$ , $T_4(t - 0.0145)$ and $T_5(t - 0.029)$ . . . . .	96
4.26	Time evolution of temperature at various positions about the domain mid-width (Case 1) and numerical simulation is performed using BL model without scattering. (a) At the tracks' centers. (b) At positions from position-1 to position-5. (c) At different depth positions under trac-3. . . . .	97
4.27	Comparison of the results between the cases with and without scattering. Positions chosen are trac-1 and trac-4 on the bed surface and at a depth position of $200 \mu m$ . . . . .	98
4.28	Influence of scanning length: time evolution of temperature averaged over one IR pixel area centered on trac-4 (case-1). Scanning length specifies laser scanning frequency and therefore cooling time at a local position. . . . .	98
4.29	Influence of scanning space: time evolution of temperature averaged over one IR pixel area about the surface center. . . . .	99
4.30	Influence of laser power: time evolution of temperature averaged over one IR pixel area about the surface center. . . . .	99
4.31	Influence of scanning speed: time evolution of temperature averaged over one IR pixel area about the surface center . . . . .	100
4.32	Influence of initial porosity: time evolution of temperature averaged over one IR pixel area about the surface center. . . . .	101
4.33	Influence of preheating temperature: time evolution of temperature averaged over one IR pixel area about the surface center. . . . .	101
4.34	Digital level and conversion into temperature using various adjustment parameters (case 7 with energy density of $1.86 J/cm^2$ ). . . . .	102
4.35	Comparison between numerical and experimental results: time evolution of temperature about trac-4. Experimental results are obtained for both the horizontal and the vertical scannings. Numerical simulations are performed for scanning length varying from $0.05 m$ (experiment of horizontal scanning) to $0.01 m$ (experiment of vertical scanning). . . . .	102
4.36	Comparison between experimental and numerical results obtained for the horizontal scanning with the scanning length of $50 mm$ : time evolution of surface temperature. 8 cases are compared. . . . .	104

4.37	Comparison between experimental and numerical results obtained for the vertical scanning: time evolution of surface temperature. Three experimental curves are presented. . . . .	105
4.38	Thickness of the sintering samples for the cases 1-9: comparison of the experimental results with the numerical results yielded by both the scattering model and the BL model without scattering. . . . .	105
4.39	Shrinkage size for the test cases 1-9: numerical results using the scattering model. . . . .	106
5.1	Schematic of successive layers heated by multiple laser sweeps. . . . .	108
5.2	Schematic of the monitoring positions. The IR camera is measuring surface temperature of the powder bed. After adding the second layer, the monitoring point is switched from P1 to P2, the third layer switches it from P2 et P3, etc. One signal of an IR camera contains time evolution of surface temperature at several points. . . . .	109
5.3	Digital level measured by the IR camera. The peaks about $DL = 2500$ correspond to adding a new layer and it is at these moments that the monitoring point is switched from one to another. . . . .	109
5.4	Experimental and numerical results of surface temperature in a multi-layer process. . . . .	110
5.5	Comparison between the numerical and experimental results: time evolution of surface temperature. . . . .	111
5.6	Temperature evolution at the positions from P1 to P10 for 10 layer case. . . .	112
5.7	Time evolution of temperature on the top of each layer of $100 \mu m$ thick: time delays or waiting times between the curves are cancelled. . . . .	113
5.8	Thickness of the samples manufactured by multi-layer processes: comparison of the experimental results with the numerical results yielded by the scattering model, $E_a = 58 \text{ kJ/mol}$ with $465 \text{ K}$ preheating temperature. . . . .	113
5.9	Temperature evolution at the point P1 on the first layer: comparison between the layer thicknesses of $80 \mu m$ and $100 \mu m$ . . . . .	114
5.10	X-ray tomography machine used. . . . .	114
5.11	Grayscale image of a sample obtained by X-ray tomography for $E_\rho = 1.7 \text{ J/cm}^2$ . . . . .	115
5.12	Binarised image of the sample obtained with $E_\rho = 1.7 \text{ J/cm}^2$ : pores appear in white. . . . .	115
5.13	A 3D view of a sample. . . . .	116
5.14	Section images of X-ray tomography: PA6 samples sintered using different energy density. . . . .	116

5.15	Porosity distribution in the depth direction for $E_p = 1.7 J/cm^2$ : the experimental profile is obtained by averaging the results in both $x$ and $y$ directions. .	117
5.16	Porosity versus energy density. . . . .	117
5.17	Illustration of porosity evolution in the $y - z$ plane of the powder bed with the successively added layers. . . . .	118
5.18	Illustration of porosity distribution in the $z$ direction of the powder bed with the successively added layers. . . . .	119
5.19	Actual thickness of layers added during manufacturing, in the Case 3 ( $E_p = 1.7 J/cm^2$ ) with the $58 kJ/mol$ activation energy, the viscosity is $1000 Pa.s$ and the preheating temperature of $465 K$ . . . . .	120
5.20	Porosity distributions in the depth direction at the points defined in Fig. 4.24. .	120
5.21	The positions monitored in the first layer in order to understand the porosity evolution. P1 is on the layer surface, P2 at the depth position of $30 \mu m$ , P3 at the position of $50 \mu m$ , P4 at the position of $70 \mu m$ , P5 at the position of $100 \mu m$ , P6 at the position of $130 \mu m$ and P7 at the position of $150 \mu m$ . . .	121
5.22	Time evolution of temperature and porosity at the points P1-P7 in the first layer for Case 3 ( $E_p = 1.7 J/cm^2$ ) with the initial porosity of 0.3, the preheating temperature of $465 K$ and the thickness of $100 \mu m$ for the added layer. . . .	121
5.23	Time evolution of temperature and porosity at P1-P7 in a ten-layer process for case 3 ( $E_p = 1.7 J/cm^2$ ) with the initial porosity of 0.3, the preheating temperature of $465 K$ and the thickness of $100 \mu m$ for the added layer. . . .	122
5.24	Zoom on the first 8 seconds: time evolution of porosity and mass exchange at the points P1-P7 for Case 3 ( $E_p = 1.7 J/cm^2$ ) with the initial porosity of 0.3, the preheating temperature of $465 K$ and the thickness of $100 \mu m$ for the added layer. . . . .	122
5.25	Influence of laser power ( $13 W/14 W/15 W$ ) on the porosity distribution . . .	123
5.26	Porosity distribution obtained with . . . . .	124
5.27	Influence of the preheating temperature on the porosity with $E_p = 1.92 J/cm^2$ . 124	124
5.28	Porosity distribution obtained with an initial porosity of 0.56. . . . .	125
5.29	Influence of the initial porosity on shrinkage . . . . .	125
5.30	Viscosity and terminal relaxation time versus temperature obtained for two $E_a$ values and $\eta_0 = 580 Pa.s$ . . . . .	126
5.31	Time evolution of contact length for $E_a = 58 kJ/mol$ and $24 kJ/mol$ at temperature of $490 K$ and $540 K$ . . . . .	127
5.32	Influence of $\eta(T_0)$ on polymer viscosity and contact length with $E_a = 58 kJ/kg$ . 127	127
5.33	$E_p = 1.92 J/cm^2$ . . . . .	128

5.34	Dimension of the thickness and shrinkage for the cases listed in Table 5.2. . . . .	128
5.35	Porosity distribution versus energy density: comparison of measurements with numerical results. . . . .	129
5.36	Comparison of the averaged Porosity . . . . .	130
A.1	Influence of SLS processes on melting enthalpy and crystallinity versus energy density with different fabrication condition. . . . .	147
A.2	DSC curve of a sample manufactured in a single-sweep and single-layer process.	148
A.3	DSC curve of a sample manufactured in a multi-sweep and single-layer process.	148
A.4	DSC curve of a sample manufactured in a multi-sweep and multi-layer process	149
A.5	Crystallinity ((a) and (b)) and peak melting temperature ((c) and (d)) of the PA6 powders for the 1st and 2nd heating runs with respect to the iteration number (iteration 0 is the virgin powder) [154] . . . . .	149
A.6	Time evolution of relative crystallinity versus laser power (central of laser). . . . .	151
A.7	Time evolution of relative crystallisation rate at (a) several surface positions with different distance to the path of laser center, (b) the laser central with different depths to the surface (laser power of 13 W). . . . .	151
A.8	Molten zone [156]. . . . .	152
A.9	Time evolution of relative crystallisation rate at the five surface positions in multi-sweep and single-layer cases. . . . .	153
A.10	Time evolution of relative crystallisation rate in the 10-layer case. . . . .	153
B.1	Distribution of the absorbed power in the counting volumes for a laser beam radius defined at $1/e^2$ (13.5 %) of maximum. The results of the scattering model and the fitted analytical model are displayed for different vertical layers.	155
B.2	(a) (b) Instantaneous temperature profiles at several depth positions in the vertical plane normal to the laser trajectory at time = 0.0005 s. (c) (d) Numerical results of averaged temperature in one camera pixel area centered about the trajectory of the laser axis. . . . .	155
B.3	Time evolution of temperature in one camera pixel area: comparison of the cases with $n_\sigma = 0.7$ and $n_\sigma = 1$ . . . . .	156
B.4	Dimensions of the samples under single-sweep conditions: comparison of numerical predictions with the measurements. Change from $n_\sigma = 0.7071$ to $n_\sigma = 1$ has very weak effect on sample dimensions. . . . .	156
B.5	Time evolution of temperature at various positions in the domain mid-width plane (Case 1, $n_\sigma = 0.7071$ ). . . . .	157

B.6	Time evolution of temperature averaged over one camera pixel area. . . . .	157
B.7	Vertical profiles of porosity averaged in the $x - y$ plane obtained with $n_\sigma = 0.7071$ and the preheating temperature varying from 455 $K$ to 465 $K$ . . . . .	158

# List of Tables

2.1	Terminal relaxation time obtained from the Cole-Cole representation for different temperatures. . . . .	46
2.2	Terminal relaxation time obtained from the Carreau-Yasuda representation for different temperatures [124]. . . . .	47
3.1	Properties of PA6 powder bed. . . . .	60
3.2	Process parameters using PA6. . . . .	60
3.3	The fitting coefficients change with anistropy factor ( $g$ ). . . . .	65
3.4	Fitting coefficients versus initial porosity of the powder bed. . . . .	67
3.5	Fitting coefficients versus particle's radius. . . . .	69
3.6	PA12 Powder bed, SLS parameters and material properties used in model. . .	77
3.7	Process parameters for simulation. . . . .	77
4.1	Parameters used for testing how the inclination angles affect the experimental results. . . . .	85
4.2	Manufacturing parameters. . . . .	86
4.3	Summary of nine experimental cases. . . . .	90
5.1	Summary of the process parameters. . . . .	117
5.2	Summary of the polymer properties. . . . .	127
A.1	Thermal characteristics recorded during cycles 1, 3, and 6, for a maximum temperature reach to $240\text{ }^{\circ}\text{C}/280\text{ }^{\circ}\text{C}$ during the cycles [128]. . . . .	150
A.2	Process parameters for simulation. . . . .	151



# Introduction

## Research background

In recent decades, digital revolutions were undergoing in communications, imaging, architecture and engineering. Additive manufacturing (AM) can bring digital flexibility and efficiency in manufacturing products by using CAD software or the 3D scanning technique to direct the scanner to accurate geometric positions and melt materials layer by layer. The first patent about AM technology could go back to 1920 when Ralph Baker filed the US Grant US1533300A with the title 'Method of making decorative article' [1]. The first commercial usage of AM has been since the 1989s, due to a revolution in the 3D modern industry introduced in AM technology, the three-dimension model is suitable for designing and fabricating complex geometries objects [2]. In the 1990s [3], the 3D print technology is developed by MIT university which solidified thin layers of the ultraviolet light-sensitive liquid polymer by a laser, and the Extrude Hone company is built based on the binder jetting patents. In the early stage, AM has been used for theoretical studies or product development. The AM technology has been used in a wide range of industries and markets, including aerospace, automotive, construction, fashion, and healthcare. There still is a tremendous potent for promoting the AM technology, according to SmartTech Analysis's recent reports [4], as shown in Fig. 1, AM services production in the automotive segment will have an opportunity to reach overall 9 billions by 2029, and will have a revenue over 4 billions yearly from AM applications in tools and final parts production.

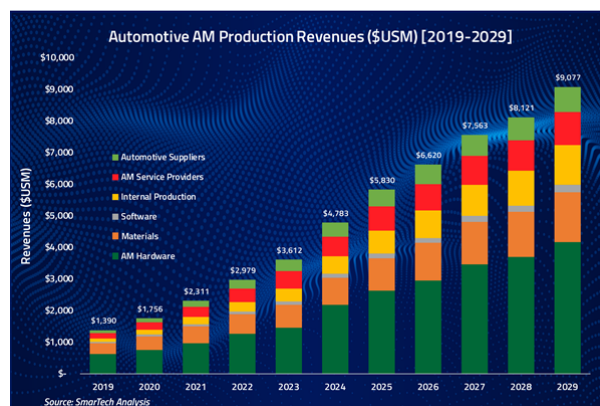


Figure 1: Additive Manufacturing for Automotive Part Production – 2019 - 2029 [4].

## Working methodology of the thesis

There are a variety of rapid prototyping techniques including the SLM (Selective Laser Melting), SLS (Selective Laser Sintering), EBM (Electron Beam Melting), SLA (Stereolithography) and so on. Selective laser sintering (SLS) is very popular in the field of polymer and metallic 3D printing to fabricate the plastic or metallic parts, the SLS technique uses a laser as a energy source to melt selectively powdered materials and fuse them together into a 3D printed part in a high productivity and low cost way. That allows the creation of very complex structures with freedom and without any support structures (Fig. 2). The development of the SLS process can be traced back to 1980s.



Figure 2: Laser powder bed fusion of plastic powder in an SLS [5].

The SLS technique will play a major role in the future industry fabricating domains. Lots of experiments are done for improving the final products' properties, they tested the material properties, studied the manufacturing circumstance and optimized the fabricating parameters. Experimental methods are an excellent way to research the SLS process, however, in most conditions, experimental methods are time consuming and of excessive cost, especially for the large workpieces. These aspects limit the widespread application of technology. Therefore, we want to use modeling method to study and monitor SLS processes of polymer powders. The SLS modeling method is based on multi-physical models involved in SLS processes and provides an effective and low cost way to study the SLS fabrication processes and improve the product's final quality. To promote wide usage of SLS processes in the industry manufacturing, the simulation tool developed must be validated under more and more complex conditions. Developing a validated numerical model to simulate the polymer material transformations and thermal histories of a SLS process is an important step in understanding and optimizing the SLS process.

As there need also experimental results to validate numerical modeling and most of the times there are no enough experimental results in the literature, we perform also some experiments to qualify our numerical tool.

## Outline of this thesis

The objective of this thesis is to develop a computational tool capable of accurately describing heat transfer in a SLS process. We will concentrate on laser photons-powder bed interaction and heat transfer in a powder bed, simulate the thermal history of a typical SLS process (time evolution of temperature) and predict the part's final properties (geometric dimension, polymer crystallinity and porosity).

**Chapter 1** concerns the general presentation of AM technique. We introduce first the development history of AM technique and the domains of its applications. We focus then on the SLS processes, laser characteristics, properties of the polymer powder bed (density and porosity (arrangement of polymer particles and size distribution)), polymer properties (sintering window, aging, crystallization), quality of the final parts (surface quality, micro-structure, and defects) and existing numerical methods for SLS modeling (Finite element method, finite volume method and discret element method).

**Chapter 2** introduces models and numerical methods necessary for modeling a SLS process. To better simulate the whole SLS process, lots of models have been built to describe the phenomena involved in. A detailed description of these models is given in Chapter 2. Heat transfer model under the assumption of an equivalent homogeneous medium is first introduced. Laser and its interaction with polymer powder bed are then discussed, Gaussian laser is the most common laser type used in the SLS process, its interaction with polymer powder bed is usually presented by the Beer-Lambert law and the modified Monte-Carlo method is detailed to take into account the scattering effect in the laser photon's interaction with the polymer particles. Modeling of thermo-physical properties (density, specific heat and thermal conductivity), melting (melting latent heat, coalescence and viscosity), and crystallization (enthalpy) is also presented. At the end of the chapter, models used to simulate a SLS process is summarized and numerical methods used to simulate SLS processes are briefly introduced.

**Chapter 3** is focused on the scattering phenomenon taking place during the laser photons transport in the polymer particles. The modified Monte-Carlo method allows to establish models with and without scattering. The influence of the scattering factor, the initial porosity of powder bed, the average size of polymer particles on the scattering are detailed. In order to qualify the scattering models obtained, a SLS process of single-sweep is simulated using models with and without scattering and surface temperature of the simulations are compared with the IR camera measurement. The dimensions of the final parts are important results and they are also used to qualify the scattering laser models.

**Chapter 4** is interested in single-layer SLS processes. Calibration of an IR camera is first detailed, complementary results of single-sweep processes are then presented and multi-sweep SLS processes are finally studied. In multi-sweep cases, influences of the laser transmission models with and without scattering and effects of other parameters such as laser power, laser moving speed, scanning space, scanning length, initial porosity of the powder bed and preheating temperature are analysed. Numerical and experimental results are compared in order to qualify the modeling methodology adopted.

**Chapter 5** introduces the X-ray computed tomography technique for measuring the porosity distribution in a sample manufactured by a multi-layer SLS process and presents the numerical simulations performed for predicting thermal history and porosity distribution. Parametric analysis is realised to understand how the process parameters and polymer viscosity affect the samples' porosity and comparison between the experimental and numerical results shows a reasonable agreement which is encouraging for the present modeling work.

Preliminary work realised on crystallisation which takes place at the end of a SLS process is presented in the appendix.

# Chapter 1

## General introduction of Additive Manufacturing (AM)

### Contents

---

<b>1.1 Additive Manufacturing</b>	<b>5</b>
1.1.1 Applications of AM technology	5
1.1.2 Categories of AM technologies	7
1.1.3 Advantages and development of AM	9
<b>1.2 Overview of selective laser sintering process</b>	<b>10</b>
1.2.1 Introduction for SLS technology	10
1.2.1.1 Manufacturing process	11
1.2.1.2 Laser-powder interaction process (scattering)	12
1.2.1.3 Sintering process	13
1.2.2 Laser types	15
1.2.3 Properties of powder bed	16
1.2.3.1 Preheating temperature of powder bed	16
1.2.3.2 Density of the powder bed	16
1.2.3.3 Particle size distribution	17
1.2.4 Polymer properties	18
1.2.4.1 Aging of polymer	20
1.2.4.2 Crystallization of polymer	22
1.2.4.3 TGA of PA6	24
1.2.4.4 XRD analysis of PA6	25
1.2.5 Quality of SLS objects	25
1.2.5.1 Defects of shape	25
1.2.5.2 Surface quality	26
1.2.5.3 Microstructure	27
1.2.6 Numerical method of the multiphysics coupling	27

---

## 1.1 Additive Manufacturing

The additive manufacture (AM) technique is a process to fabricate material layer by layer, the initial model is created by CAD software, which is a more freedom method to fabricate invisible and difficult reached complex geometry objects. Unlike traditional processing technology, AM technology produces parts by successive layers of materials that are added on top of each other. This process is good at processing dimension accuracy objects and reduces the additional cost when using this technique to fabricate complex objects.

### 1.1.1 Applications of AM technology

Nowadays, this rapid prototyping technology is widely used in industry domains: Areospace, automotive, dent, implant, drug deliver, jewel, sport and fasion design.

**Aerospace and automotive sectors:** Currently, AM technology is widely used in aerospace, aeronautics and automotive Fig. 1.1 sections. The aerospace industry needs thousands of complex produces with high functionality, high production efficiency and lightweight. AM technique is particularly suitable for fabricating these complex produces. AM leads to lower cost and simplified supply costs, reduces the product cycle time and changes the production methods. This technology has broad prospects for the manufacturing of spacecraft and automotive components. EOS company introduces a new simple 3D module to build the all-in-one base-plate which includes 248 components if use convention methods. The new design leads to a 50 % lower cost and shorter the working time because the number of welds and amount of potential rework is reduced. In astronautics, NASA tries to fabricate a turbopump exhaust port cover of the J-2X rocket engine using the SLM technique, which decreases 75 % fabrication cost after using the SLM technology [6]. SpaceX's SuperDraco's combustion chamber and engine are manufactured by mental laser sintering process, and the helmets of astronauts also were fabricated by 3D printing, which shorten the whole manufacture process and the cost [7]. In the aircraft area [8], AM can be used in large engine manufacturing companies, including GE, Rolls-Royce, and Pratt Whitney, for producing engine components, airframe parts, aircraft parts and systems, interior parts, secondary structures, and avionics parts. Boeing company uses AM technique to fabricate more than 7500 additive tools in 2018, and the number of additive tools increases to exceed 14000 in 2020.

**Medical sector:** In the medical areas, the human tissue are too complexity and obvious individual difference between patients, a lower cost and more reliable technology must be introduced. The advantages of AM technology perfectly fit for these requires. Today, the medical sector finds an increasing number of applications for bespoke custom-fitted implants and devices by using AM technology. A vast of materials are used to build medical projects by AM technology in the medical industry. Like plastic are used to fabricate thin tube in blood vessels, heart valve, and eyeglass frame, carbon fiber and metal are used for lost limb, bones, artificial joints and permanent implants so on. These materials all can be fabricated by AM technology. Current AM technology for medical care focuses on studying the fabrication of personalized bio-active permanent prosthesis implants, drug delivery, complex artificial life tissues and organs and pathological organ models to assist surgical treatment analysis [9] [10]. 3D printing is an advancements technique in implant printing [11] [12] [13], the printing of implants including the hip joint and elbow joint for replacing the human body. The implants' fabrication steps are as follows: the scanning process and imagining process are used to take

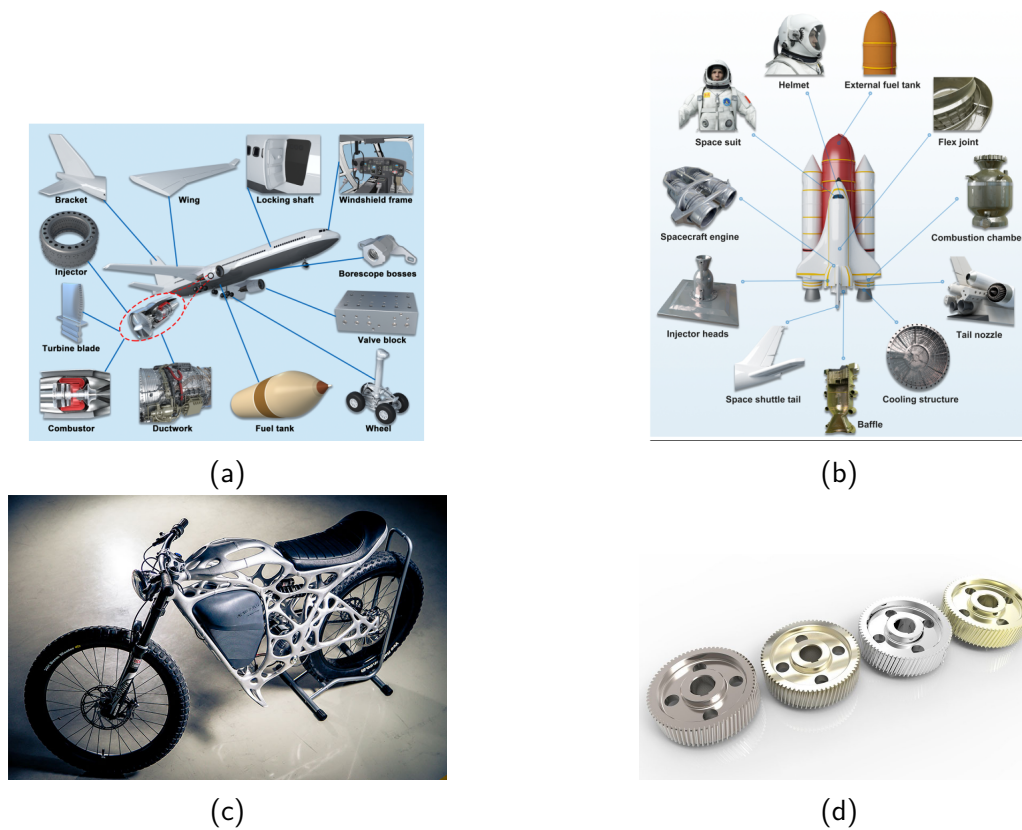


Figure 1.1: Example of complex objects fabricated by the AM technique [8].

the detailed image of organs' surfaces, bones and tissue, then software turns these images into complete models that could be fabricated by AM process. These complex, sterile and well match patient objects could be fabricated in a customization, quick, and effective way after introducing the AM technology (Fig. 1.2). AM technology can also be used to build hollow capsule shells with separate dual compartments in development the personalized "flexible-dose dispenser" drug delivery systems [14].



Figure 1.2: 3D printing for medical applications.

**Fashion sector:** Traditional decoration manufacturing process must go through carving, casting, polishing and various process, which is a complex and time-consuming effort. However, AM technique provides a great personalized free design way to make complex articles that the time-consuming process is avoided. The CAD software facilitates the personality design to promote the fabricate process, these techniques are especially fit for the art and jewel industry, because design and creativity are the two key features for jewelry art [15]. Fashion designers adopt AM techniques to fabricate fashion garments and show the 3D-printed garment at the 2010 Amsterdam Fashion Week. Besides garments (Fig. 1.3). AM is also widely used by jewelry designers and companies. Unlike 3D printed garments limited to polymers, jewelry could

be fabricated using wider materials including metals, ceramics, polymers, and other precious metals. And the selective laser melting (SLS) and electron beam melting are common methods to be chosen.

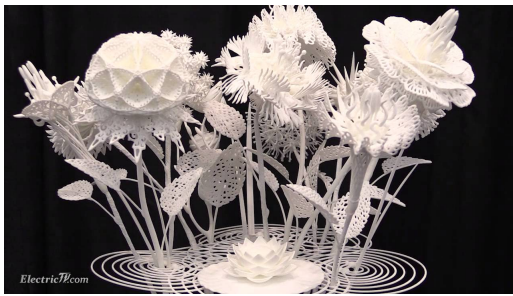


Figure 1.3: 3D printing for art projects.

### 1.1.2 Categories of AM technologies

AM processes for polymers						
CATEGORY	powder bed fusion	vat photopolymerisation	material extrusion	material jetting	binder jetting	sheet lamination
DENOMINATIONS	SLS - Selective Laser Sintering SHS - Selective Heat Sintering MJF - Multi Jet Fusion	SLA - Stereolithography DLP - Digital Light Processing DLS - Digital Light Synthesis	FDM - Fused Deposition Modeling FFF - Fused Filament Fabrication	PolyJet MJM - Multi-Jet Modeling	3DP - 3D Printing	LOM - Laminated Object Manufacture SFP - Solid Foil Polymerisation
STATE	powder	liquid	solid	liquid	powder	solid
MATERIALS	polyamides, PEEK, polypropylene (PP), polycarbonate (PC), polystyrene (PS), thermoplastic elastomers (TPE)	epoxy or acrylic photopolymers	polylactic acid (PLA), ABS, PC	acrylic photopolymers	polycaprolactone (PCL), polyvinyl alcohol (PVA), PLA	PMMA, PVC
PRINCIPLE	selective fusion and solidification	light reactive photopolymer curing	extrusion of melted material and solidification	jetting of melted material and solidification / UV curing	consolidation through binder	lamination through thermal or chemical bonding

  AM technologies considered in the Review

Figure 1.4: Summary of the AM processes employed for the main polymeric materials [16].

AM technology is also called "3D printing", allowing to creation objects with precious shapes by using a 3D object scanner and CAD software. Based on the physical state of the material, AM processes can be further grouped into three types [16]. The first type of AM is sintering whereby the material is heated without fully melting to create objects, including the selective laser sintering (SLS) process that is always used in manufacturing thermoplastic. The second type of AM is using an electron laser to fully melt the materials being liquid, used for metal material. The third type of AM technology is stereolithography/photopolymerization,

whereby an ultraviolet laser is fired into a vat of photopolymer resin to create torque-resistant ceramic parts that can endure extreme temperatures. AM prototype classifier depends on the material state and machine technology used [16]. Fig. 1.4 lists the common commercial name of the AM technologies and the common commercial materials used in each type of the prototypes.

**SLS (Selective laser sintering)** - Selective laser sintering (SLS) is developed since 1900s, which is a variable technique for fabricating solid thermoplastic polymer, like low fusion temperature polymer PA6, PA12 polyamides, amorphous polymers, more technique polymers such as PEEK (polyetheretherketone) or PEKK (Polyetherketoneketone) [17]. A high power laser is the energy source, the moving track controlled by the computer for sintering the polymer particles layer by layer, binding these particles together to create complex parts. For sintering the powders together, the laser needs to heat the powders until the temperature above the melting points of metal and softening point of polymers. In some cases, the sacrificial materials, also called as binder materials are added for promoting the sintering processes for some high melting points and large size particles materials (commonly of a metal material) [18] [19].

**SLM (Selective laser melting)** - SLM technique [20] belongs to laser consolidation technology, start in 1995 in Germany, which is almost identical to SLS, the main difference with SLS is that all particles have been totally melted under the laser power, also known as direct metal laser melting (DMLM). This way is more suitable for single metallic materials, like steel, Ti and Al alloys. This way is better suitable to produce full density parts, for example, it is demonstrated that the density of Ti6Al4V could arrive 99.98 % by controlling the processing parameters. SLM processes need higher energy to melt all the materials, however, inappropriate parameters will cause surface roughness and micro-structural defects to increase, will increase the rate of the internal pores and will increase the risk of distortion and delamination of samples. In order to get a satisfactory surface quality of the sample, the median grains size should be in the range of 30 - 60  $\mu m$ . In SLM, laser power, scanning speed, hatch spacing, laser intense and layer thickness are the common process adjustment parameters to optimize the process.

**EBM (Electron beam melting)** - EBM technology belongs to the powder bed fusion family, which can be used either with metals or polymers. EBM is a precious process using electron beam to fuse the metal materials layer by layer, while the scanning sweeps is discontinuous. The high-velocity electrons concentrated into a narrow beam that directly work toward the powders, allowing a faster scanning speed and a higher molten pool than SLM. In EBM, the laser scans the materials point by point, this manufacturing methods increase the fabricating speed because this method separates the fabricating powders into several fabricating places simultaneously, but the wider electron beam diameter reduces the accuracy of productions at the powder level.

**SLA (stereolithography)** - Stereolithography [21] is an early used manufacturing technology since 1984, which uses UV laser as the heat resource to fabricate photo-polymer resin. The photocurable resin polymerizes into a 2D patterned layer under the UV laser. After a layer is cured, the new uncured resin is deposited on the platform. The curing reaction requires the manufacturing materials must highly absorption photoinitiators and UV. The depth of the polymerization and the quality of the final product are decided by the energy absorption rate, the laser scan speed and laser power. The possible cytotoxicity of residual photoinitiator, high cost of the system and limitation of materials choose to suppress the development of this technology widely used in industry.

**Polyjet printing** - Polyjet 3D Printing [22] [23] is a fast and flexible technology fabricating objects used in UV curable powder materials, belongs to solid freedom fabricated AM technique that developed at the end of 1990s, that builds samples by jetting thousands of photopolymer droplets onto a build platform and solidifying when exposed to UV light. It's one of the fastest and most accurate AM technologies for resins. In this system, the head prints selective liquid binder onto thin layers of powders based on object profiles that have been generated by CAD. The selective Inkjet deposition of UV curable is a method by liquidizing compositions and forcing the material immediate solidification by exposure to flood UV radiation, then removing the supporting materials. PolyJ usually uses at least two materials in the building process, the binder and powder materials selection are key factors in the successful fabrication process. The advantage of this process is that it does not require much monitoring and additional manual intervention for mixing materials. PolyJ also has many defects like flowability, wettability, and lower reinforcement of the particles.

**FDM (Fused deposition model)** - Fused deposition model (FDM) [24] is an extrusion deposition process that belongs to rapidly growth prototyping technologies. The key of the FDM system includes material feed mechanism, liquefier in which the polymer melted, print head, gantry, building surface and building environment. FDM starts with CAD system, the material is melted and softened inside the liquefier when the temperature is above its melting temperature, then the liquid material is extruded from the nozzle head, fabricating objects layer by layer. FDM is especially suitable for low-cost, molten thermoplastic materials, such as ABS, PLA, flexible PLA, and PP. Recently, much researches are focused on adding short fibers in plastic for reinforcement filament by using FDM methods. These short fibers in filament show great improvement for modulus and strength, and reduce tape swelling at the printing heat time [25].

**LOM (Laminated Object Manufacturing)** - In Laminated Object Manufacturing (LOM) [26] [27], adhesive raw materials are deposited on the platform by using a heated roller. Each layer is cut to the required shape by a computer controlled laser, then a new layer is added on the topper previous one. This procedure is repeated until the process finishes. LOM materials are non-toxic, easily handled and easily disposed of materials, including fabrics, synthetic materials, plastics, composites, and sheet metals. This kind of rapid prototyping technology has been commercialized since 1991. The disadvantages of this technology include wasting materials, difficulty in controlling the laser beam penetration into the previous layers and higher energy consumption.

**FEAM (Fiber encapsulation additive manufacture)** - Fiber encapsulation additive manufacture process (FEAM) [28] is an innovative additive manufacture process, which allows to integrate fibers and metal conductors into the thermoplastic polymer enabling enhancing the functionality of the matrix. This way is used in constructing electromechanical devices such as voice coil actuators, solenoid valves and live sensors. Also, FEAM process still has many challenges to overcome. Such as finding the ways to control encapsulation of fiber by matrix material, control of cutting the fiber in arbitrary locations, and finding a way to create inter-layer and inter-layer junctions between metal fibers with adequate conductivity.

### 1.1.3 Advantages and development of AM

AM provides a simple way to quickly fabricate complex shape products, this technique allows for achieving customized personal requirements, and can take advantage to fabricate unique ob-

jects where the original parts are no longer produced, especially used in medical and aerospace sections. The advantages of AM technology include [29]: First, AM does not require special extra molds, it just needs the digital model to fabricate products, and the unused material can be recycled for later use at the end of the process. Second, AM technology omits another complex post-tooling process that saves fabrication time compared to traditional fabrication processing. Third, parts of the previously required assembly from multiple pieces can also be fabricated as a single object which to improve the strength and durability of products. AM technology has upsurged quickly in recent decades and many companies rethink the transformation of traditional manufacturing techniques to new techniques. Some of the challenges are still discussed by researchers, end consumers, and manufacturers. If the change is successful, the manufacturer will be closer to the customers, and the cost and the capital deployment will be reduced. Before achieving these goals, it is important to simplify the design processes for AM models and eliminate the gap between academia and industry settings and the companies need to plan new supply chains and scheduling systems.

## 1.2 Overview of selective laser sintering process

The development of plastic manufacture technology - Selective laser sintering (SLS) is a promotion of material science, it is a very new and promoting technique belonging to AM. The SLS technology uses an easy way to fabricate the plastic, and the products' can have good mechanical properties. The widespread application of SLS technology in industry has a significant positive impact on industrial development. However, this technology has not been widely used in the whole industry due to the technical shortcomings. The maximum operating temperature of powder bed and chamber of common commercial SLS machines are always around 200 °C. The choice of SLS commercial materials is either limited by its SLS working windows or melting points because purchasing the high-temperature SLS machines cost over 1 million euros. The high cost and restriction of the materials limit this technique to become the majority of technology in the industry [30]. The following parts will study the details of this technology, including the laser characteristics, plastic properties, polymer thermal properties, manufacturing environments, and the qualities evaluated factors of final products.

### 1.2.1 Introduction for SLS technology

The selective laser sintering (SLS) technology is a part of laser powder bed fusion technology. SLS technology uses a laser as a power source, automatically aims at points in space defined by CAD 3D model, sinters the materials and binds the materials together to form a new solid structure. The SLS is one of the most advanced and reliable technology in the field of additive manufacture. The SLS technology was initially developed in the 1980s by Beaman and Deckard [31]. The SLS market enlarge quickly in recent years due to its ability to produce good mechanical properties and high-level details objects at a low cost. The SLS technique is extensively demanded in aerospace, aeronautics, and healthcare industries because these are demands for sophisticated, personality and complex objects. Advanced SLS materials, machinery, and software are developed for a wide range of AM industries in recent years. Since 2015, the SLS based equipment is developed quickly. In 2018, the SLS sintering market arrives at USD 339.5 millions and is project to reach USD-950 millions in 2023.

### 1.2.1.1 Manufacturing process

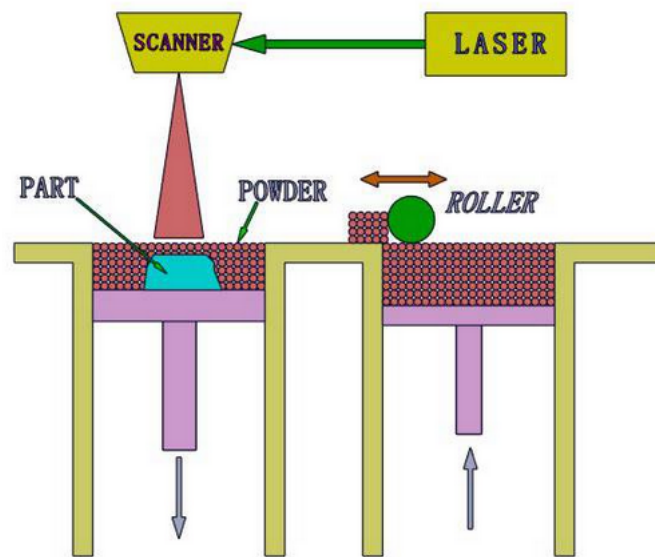


Figure 1.5: SLS machine for fabrication thermal plastic [18].

The principal elements in SLS machine are shown in Fig. 1.5, including [18] [32]:

(1) Energy source: The laser source has a critical function of fusion powder particles,  $CO_2$  laser is chosen for heating polymers because its high absorption rate.

(2) Scanning motion device: This system controls the movements of the heat source over the powder bed and precisely the laser density uniform distribution in determined areas according to the CAD design.

(3) Powder feeder and roller: Feeder is a mechanism for adding new powders on plats, roller is used for smoothing and compressing the powders on the upper layer. Both of them are important for controlling the initial density of the powder bed.

(4) Elevator: This machine is necessary to lower the powders after each layer has been scanned by the heat source in order to allow the feeder to add another layer, which decided the thickness of the new layer.

(5) Enclosed chamber: The enclosed chamber is existed for fulfillment specific ambient requirements. The requirements include the fabrication temperature, preheating temperature, moisture of the fabricating condition, and other special environments. Fulfillment these requirements will prevent the polymer aging, decrease the material thermal stress, and promote polymer crystallization, which is the key to improve the quality of the produces.

The SLS fabrication processes are including (Fig. 1.6) [33] [34]: First, the SLS process starts by repeated depositing uniform powders into the part of the platform until a set depth powder layer is deposited over the platform. All the spare materials inside the machine and the chamber are heated just below the melting temperature and kept at this temperature until the laser arrives. Second, when the parts of powder layers are scanned by the  $CO_2$  laser, the laser melts the materials at a predefined area in the powder bed, the fused polymer powders connect and coalesce together, meanwhile the air between the grains escapes through the open pores and the air diffuses in solid after the pores closing. After a while, the separated

powders connect together to be a whole when the solidification process is end. Third, when the fusion and coalescence are completed, the platform moves downward and a new thin layer of powders is deposited over the old layers, then the laser scanning and coalescence process are repeated. The total processes are repeated until the whole parts are finished. The key variables in the SLS process include the laser power, polymer particles diameter, porosity/density of the powder layers, laser beam diameter, powder bed preheating temperature, laser moving speed, scanning space and the thickness of the powder layers and so on.

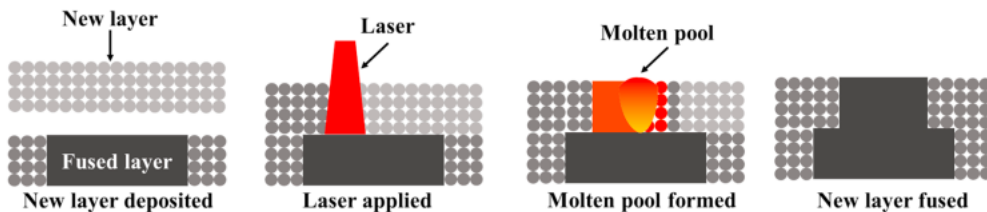


Figure 1.6: Illustration of the SLS fabrication process.

The SLS process is characterized by three main processes: (1) powder spreading. (2) laser energy absorption and heat transfer in the powder bed. (3) polymer sintering and cooling process. In the stage of SLS, the multiple phase transition are involved in each of these processes and accompanied by both thermal energy absorption and release. During each process, the material properties change drastically as a result of temperature fluctuation. Classical numerical methods such as finite elements method (FEM) and finite volume methods (FVM) are used for simulating the powder mass as a homogeneous porous medium, the governing equations are derived from the conservation of energy applied to an arbitrary control volume. Particle-based methods separate the mediums into solid and void parts. The discrete element method (DEM) is used to simulate the heat convection between the connection particles. The DEM method is easily consider the conduction effective effect by unevenly distribution of particle shape, size and stacking methods. However, the computational costs made this way use far less common.

For the following part, we will detail introduce the involved processes, including how the laser photons interaction with polymer particles, the sintering process, the melting process, and the crystallization process, also the materials' physical properties change caused by the heating cycle are also be discussed in the following. And the numerical methods are also described in detail as follows.

### 1.2.1.2 Laser-powder interaction process (scattering)

During the SLS process, the manufacturing part consists of thousands of particles, and the paths of laser transfer traces in the particles are changed because the photons hit on the polymers, and the reflection rate change between the different mediums. Therefore, the value of the absorption coefficient is affected by the reflection and the updated transmission traces are affected by the scattering phenomena need to be considered. In previous researches, the modified Monte Carlo method(MC) model had been widely used in simulating heat laser transmission in laminated mediums, like tissue or neural tissue. Joseph M. Stujenske.et al [35] used MC method to simulate the high-intensity light transmission and the heat propagation in vivo brain tissues, they discussed how the wavelength of the light and fiber size effect the light and heat propagation. Furthermore, they used a thermistor probe measuring the temperature

variation with the different distance between the tips of the thermistor and fibre in vivo brain tissue under continuous light. The comparison results of temperature distribution in vivo tissues between simulations and measurements prove the reliability of the MC model used in simulating the laser scattering phenomenon. The MC methods are not just restricted to simulate the laser transmission in tissues, this method can also be promoted usage to simulate the light photons travel by Ray-tracing method, including the scattering and reflection among particles layers according to E. Nisipeanu's research [36], which showed the ability of the Monte Carlo method to offer the correct solution to radiative transfer problems in a dispersion of particle. Jianhua Zhou [37] had proved that the modified Monte-Carlo method is good at simulating the laser radiative travelling in the bimodal random packing structures that were composed of particles with different sizes. Their model also could be used to predict the particles' emissivity evolution during the SLS process. Mariana Ilie et. al [38] introduced scattering phenomenon in laser-powder interaction model, they used Monte-Carlo algorithm and the Mie-theory to study the laser beam scattering phenomenon in the semi-transparent polymers in absence of absorption. Their results prove that the scattering phenomenon affected the laser travel traces, and the Monte-Carlo methods can be chosen to mold the laser-polymer powder interaction phenomenon. How the diameters of the particles and the wavelength of laser affect the attenuation of the laser in the powders were analysed in their research. Liu Xin et.al [39] used a modified Monte Carlo ray-tracing method combination with the Discrete Element Method (DEM) to predict the physical change behavior of discrete particles during the SLS process, made a comparison between modified Monte-Carlo method with scattering phenomenon and Beer-Lambert un-scattering methods, and discussion in detail how the scattering phenomenon influence the laser travel paths.

### 1.2.1.3 Sintering process

**Sintering:** Sintering is an important process in the additive manufacture, widely existing in polymers, metals, ceramics, and other materials. Sintering is a process for compacting partly melt materials to form a whole solid production under heat or pressure. The materials transmission take place at the grain boundaries between the contacting particles, while the mass transmission will lead to grains coarsening. The classic sintering models are established for amorphous materials with Frenkel and Mackenzie-Schuttleworth model [40]. Fig. 1.7a shows the sintering bonds formed between the spherical particles, the grain build connection with all the grains around him, making them form a stronger body. The mass transport pathways are illustrated in Fig. 1.7b. During the sintering process, smaller particles are easier to finish sintering, because the smaller particles have more melting parts, which promote the material diffusion, and less mass is required to build a relatively bond between the small particles.

**Coalescence:** Coalescence is the process by which two or more droplets, bubbles or particles merge during contact to form a single daughter droplet, bubble or particle. It is widely existed in sintering process, which is a basic principle for merging particles together for forming a new project. In the coalescence process, the merged particles can be fully molten, half molten or not molten at all. Fig. 1.8 shows a series of the coalescence images take from the video footage during heating the PP polymer that was observed by the hot-stage microscopy(HSM) [41]. HSM technology is used for observing temperature-dependent structure transformation in polymers, especially the melting behaviors in powder. These figures clearly show the initial coalescence at the onset of melting takes place at a temperature below the peak melting temperature(168 °C). The particles are independent at the beginning of melting, then, the particles expand and the edge of the particles change the phase forming

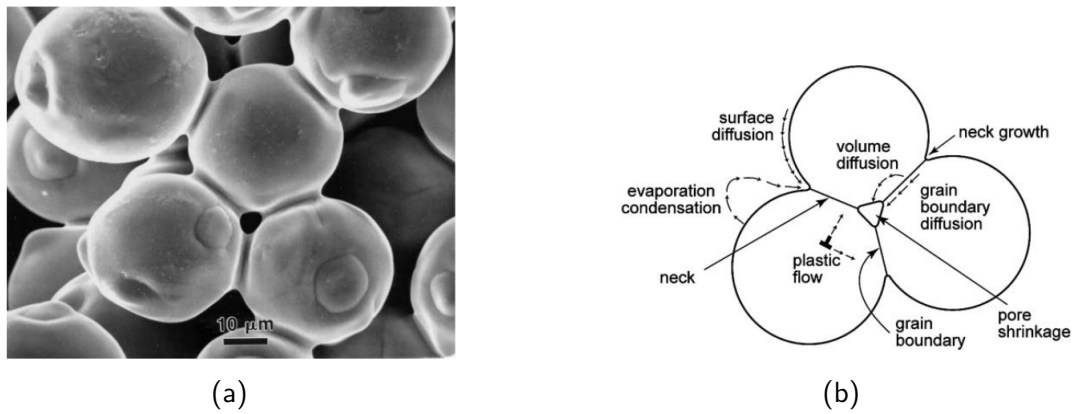


Figure 1.7: (a) Scanning electron micrograph of sintered nickel spheres. (b) The mass transport pathways sintering process.

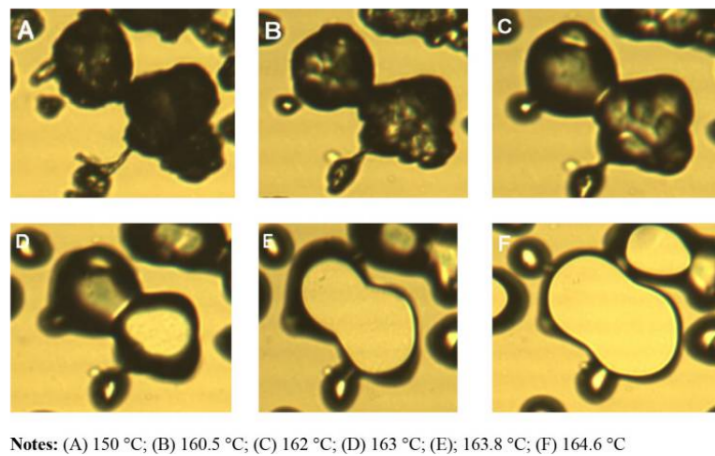


Figure 1.8: Image of powder melting from HSM: PP-A.

more contact points with the temperature increasing, the melting initiates from the center of contact points and the neck grows radially as the powder particles coalesce. Observing these images, the structural order is observed in the solid, semi-crystalline particles, but gradually eliminate with melting continue. The material becomes transparent to polarised light when the material resides in its amorphous melt-state.

**Binding mechanism:** In the SLS system, binding mechanism technology can be divided into three main categories, the solid-state process, the liquid-solid process, and the full melting process [42]. The solid-state binding process occurs while the material's temperature is below the material melting points. The adjacent powder grains bond together by forming the necks at the boundary of the powders, and the material is transferred by atoms diffusion when the temperature generated by the laser beam is sufficiently high to supply the kinetic energy. The diffusion types include volume diffusion, surface diffusion, and boundary diffusion. For completing the diffusion process, powders need to be kept at a certain temperature for a long time. Solid-state sintering is a long process, and preheating is an important stage because it affects the molecular diffusion rate. The liquid-solid assisted sintering process is widely used in 3D fabrication technology, especially for polymers and mix-materials, like ceramic materials incorporation of small size polymer. While the heat supplied to the powder bed is not enough to fully melt all particles and only enough to melt the grain's border or just the small particles, the melting parts form the necks to connection particles. Also, the liquid-solid assisted sintering process involves a thermal activated chemical reaction, the

chemical thermal between particles promotes the molecules bonding together. For decreasing the porosity, adding reaction chemical composition and providing high-temperature treatment are necessary. Nowadays, many methods are studied for promoting the liquid-solid process widely used in commercial, the study points focus on decreasing the cost and the time for post-process processing. The third type of binding mechanism is the full melting sintering technique. The full melting sintering technique fast the binding and densification process, avoids the length post-processing step and nearly gets the full density object, which is always used in metallic and ceramic materials, and a part of polymer material. The full melting technique uses the laser beam heating the powders above the melting temperature, total melting of all materials to liquid in one step. The presence of the full liquid accelerates the sintering process because the diffusion that takes place between the molten materials is more rapid in the liquid phase than in the solid phase.

## 1.2.2 Laser types

The common types of high power lasers used in commercial additive manufacture machines are  $CO_2$  laser, Nd:YAG fibre laser, Yb-fiber laser and excimer laser [19] [43]. These lasers can be specified with power stability, laser wavelength, spectral bandwidth, pulse energy, pulse duration, and repetition rate. These parameters are related to the light-material interaction process and the manufacture efficiency. These lasers always consist of a pumping energy source, a gain medium, a amplifier which amplifies the light beam supplied by a pump source and an optical resonator, shown in Fig. 1.9. The detailed specifications of each laser are shown in follows:

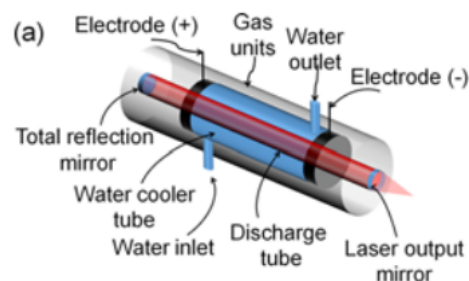


Figure 1.9: Schematic of  $CO_2$  laser.

### (1) $CO_2$ laser

The  $CO_2$  laser is the earliest gas laser development science 1964. The infrared output wavelength of  $CO_2$  laser is from  $9.0 \mu m$  to  $11.0 \mu m$ , the most widely used wavelength in AM is  $10.6 \mu m$ . The long wavelength is more suitable for laser energy absorbing by plastic material (absorption rate usually higher than 90 %) and organic materials such as wood, acrylic, and rubber.  $CO_2$  laser provides high output power ( $0.1 - 20 kW$ ), high efficiency and the overall optics maintenance periods could arrive to 2000 hours, these characteristics could make  $CO_2$  laser widely used in cutting, drilling, welding and other material processing.

### (2) Nd:YAG laser/Nd:YAG fibre laser:

The Nd:YAG laser with a short wavelength of  $1.06 \mu m$  is better absorbed by metallic materials (Fe, Sn, Ti, Pb) and ceramics (CuO, SiC, TiC, WC), the peak power could arrive to

20 kW, but the low electrical-optical power conversion efficiency and low beam quality limit its in industry areas [44]. The development of Nd:YAG fiber laser (Yb-laser) is based on the Nd:YAG laser in which the active gain medium is a rare-earth doped optical fiber. Yb-laser with high power generation because the quantum efficiency could arrive around 94 %, this advantage makes Yb-laser becoming to the most promising laser source in industry.

### (3) Excimer gas laser:

The excimer laser uses 'excimers' as the gain medium to generate UV pulses, the wavelength range from 157 nm to 351 nm, especially for factoring materials with high absorptive UV light, like polymerization. Stereolithography (SLA) is one of the earliest developed AM methods, which uses ultraviolet (UV) laser onto photosensitive polymer resin.

## 1.2.3 Properties of powder bed

### 1.2.3.1 Preheating temperature of powder bed

For getting high quality objects, the materials need to be preheated before the laser arrives. If the preheating temperature is too low, the corners and edges of the sintering layers will be distorted and warped. Conversely, if the preheating temperature of the powder bed is too high, removal of the around parts will be more difficult because the higher temperature will cause the supporting powders around the part to become hard, reducing the degree of recyclability and resulting in a poor definition and accuracy. The preheating temperature for semi-crystalline polymer is typical just below melting temperature ( $T_m$ ), it is equal to or just below the glass transition temperature ( $T_g$ ) for amorphous polymers [45]. In the SLS process, preheating minimizes the amount of energy required by laser consolidation and the thermal gradient between the sintered and non sintered, also minimizing the thermal expansion of the powders. The right preheating temperature helps to improve the properties of the material and the dimension accuracy and reduce the risk of distortion and the shrinkage that occurs during the cooling and crystallization process.

### 1.2.3.2 Density of the powder bed

The particles packing condition affects the material properties, especially the flow properties of the material. The material particles should have a good flowing ability and a good fluidization rate in order to allow homogeneous deposition and the packing density of powder layers. The particle shape, particle size distribution, inter-particle force, moisture and temperature are the important factors that affect the particles' flow properties [46]. Many factors are used to test the static and dynamic powder state conditions, like the bed expansion ratio, ring shear cell, and angle of repose methods used to measure the particles' fluidization performance. Nowadays, in order to research the packing density, a serious packing prediction model had been developed by researchers, and many techniques had been done for evaluating and arsing the flowability of the powders, especially for the complex nature of powders or for the mix powders. Haeri et.al [47] used the DEM method to model the rod-shaped particles spreading behavior in a realistic AM situation and investigated how the particle shape and operating conditions affect the powder bed's packing quality, their deposition model was also used to characterize the surface roughness and solid volume fraction of the powder bed.

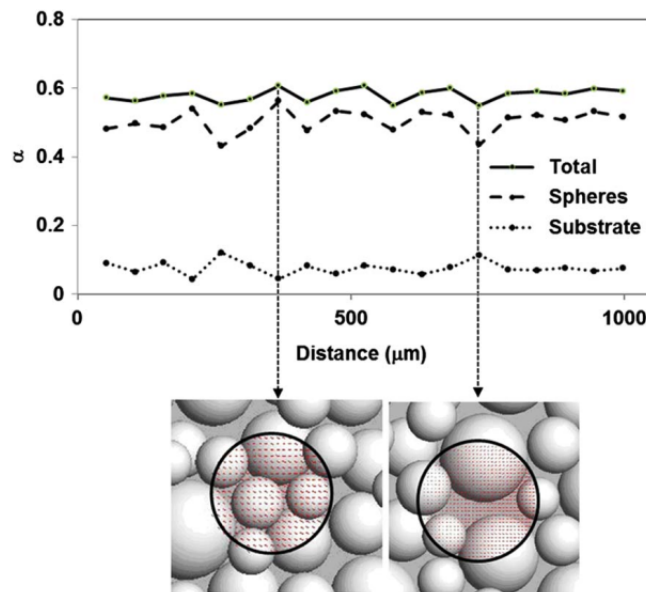


Figure 1.10: Absorptivity along the beam path for the powders. The insets show the powder and incident beam size at locations with low absorption (right) and high absorption (left) [48].

In the SLS process, the density of the powder bed directly affects the thermal transmission, the typical polymer powder bed's density falls into the range of 20 % to 60 % . Usually, the regular spherical particles powder bed density is more desirable (uniform and tight), because irregular particles' shape inhibits tight packing and results in a low packing density [49] [50]. In actual conditions, the density of the powder is not uniform because the particles' size and shape are irregular distribution, the parts with high density and lower density are mixed. Fig. 1.10 shows the absorption rate with different types of particle sizes arrangements for stainless steel. In the left insert, higher laser absorption is induced by the higher density (around 80 %) of the powder bed where the space on the periphery of larger spheres surrounds by small spheres. For the right insert, the powders show a loose arrangement, which leads to fewer reflection rates and a lower absorption rate. Most simulation methods are based on simplifying the powder bed as a homogeneous media with fixed density. Fig. 1.11 is the simple geometrical model of 3D printed material which assume a roller passes the deposited layer [51], where the average porosity of powder bed is between 20 % to 50 % .

### 1.2.3.3 Particle size distribution

The deposition of new powder layers on the previous layer or the built initial powder area is the first step for SLS. The layer's thickness is usually around 100  $\mu m$  to 200  $\mu m$ , and the particle size limit reducing the layer thickness [52]. Nylon is the most common polymer used in SLS technology. Fig. 1.12 shows the near-spherical PA6 powders' size distribution, the original PA6 powders have a relatively uniform sphere shape, the particle size ranges around 30 - 90  $\mu m$  and with a median size  $D_v(50)$  of 58.9  $\mu m$  and obeys Gaussian distribution. However, the average particle size of PA6 decreased from 58.9  $\mu m$  to 52  $\mu m$  after thermal aging behaviors. The reason is that the particles' surface fragmenting and cracking occur if the polymer particles are exposed to high temperature and high-pressure situations for the long period, which due to the heating effect coupled with long-term recycling will cause the material repeated expansion and shrinkage. The particles fragmenting and cracking change the polymer surface morphology from smoothing to rough and irregular, enlarge the particles'

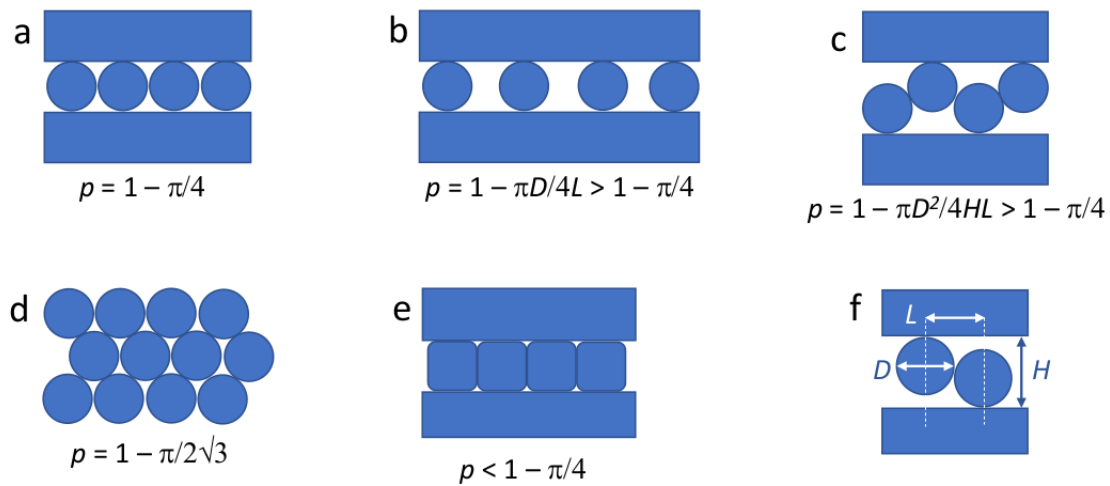


Figure 1.11: A schematic drawing of one layer of the cross-section of 3D printed materials, shows the geometric model shows variations in porosity.  $D$  is the track diameter;  $L$  is the distance between the centres of neighbouring tracks;  $H$  is the vertical distance between layers. [51]

size range distribution, and decrease the median size of powders [53].

## 1.2.4 Polymer properties

The SLS technology is one of the most promising plastics production technique in the future industry. However, only a narrow variety of polymers is used in this process. There list five fundamental factors in selecting right polymers used for SLS manufacture: (1) Shape and surface of single particles, which link to the power density and the free flowing spread behavior. (2) The powder size distribution is a important factor, and the favorable particles' size are between  $20 \mu m$  and  $100 \mu m$  for commercial machines. (3) Polymer's optical properties that link to the energy absorption rate, its need to be good at absorbing  $CO_2$  laser (wavelength is equal to  $10.6 \mu m$ ). (4) The surface tension and viscosity of the polymer decide the coalescence process. It requires a very low initial viscosity at a temperature lower than glass transition temperature, and a high viscosity when the temperature is higher than the glass transition points. (5) The polymer needs to have great thermal properties, it must have a metastable thermodynamic region, called "sintering windows". The interconnection of polymer properties is shown in Fig. 1.13, including [54]

Fig. 1.14 depicts a DSC curve for semi-crystalline polymer materials, the sintering windows depends on the DSC curve. During the whole SLS process, a property maintenance temperature needs to be considered, the crystallinity should be controlled at a low level because too quick crystallization rates promote the sample shrinkage, the distortion of the heating part prevents the stable adding of new powders it during the spreading stage. The SLS process maintenance temperature  $T_0$  needs to be set in a range of the SLS sintering windows, which between the crystallization start temperature  $T_c$  and the melting start temperature  $T_m$ . If  $T_0$  is too close to the crystallization start point, the deformation aggravates after removing the surrounding powders, and if  $T_0$  is too close to the melting temperature, the resolution will decrease because the surrounding particles stick on the edge of laser tracks. The polymer used in the SLS process is divided into two types, semi-crystalline thermoplastic and amorphous ther-

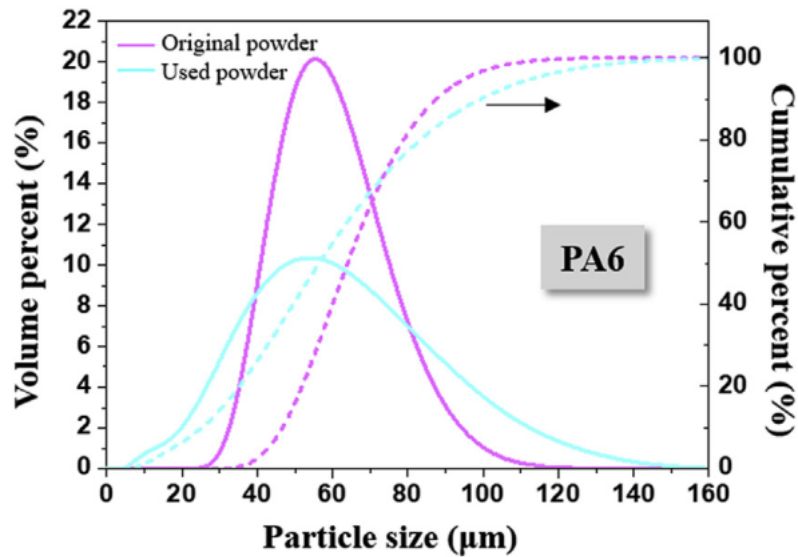


Figure 1.12: PA6 polymer particle size distribution.

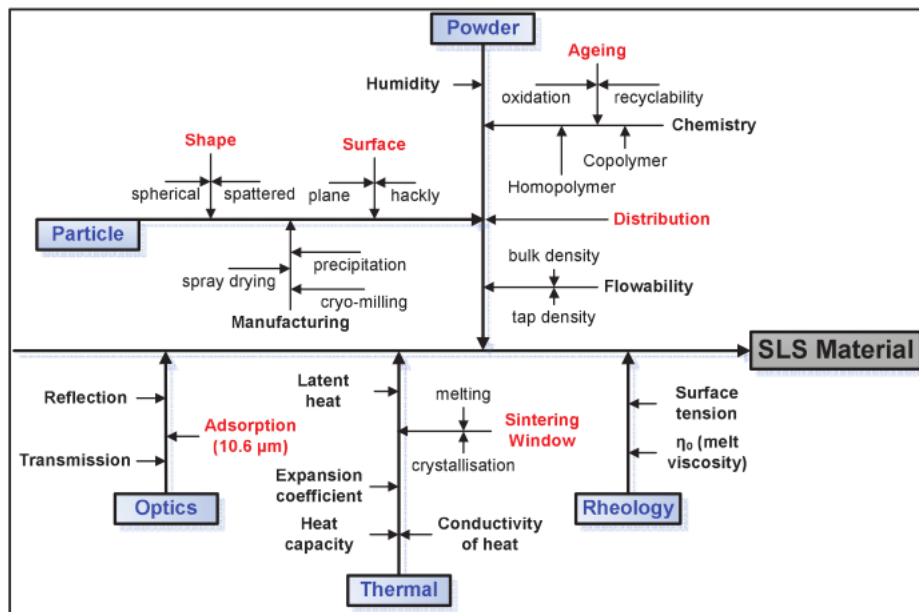


Figure 1.13: Interconnection of different polymer properties to be organized for providing promising SLS materials [54].

moplastic. The commonly used SLS polymers include: Polyamide(PA) series polymer which includes PA12, PA11, and PA6, and other types of polymers which include polyetheretherketone(PEEK), thermoplastic rubber(TPE), thermoplastic polyurethanes(TPU), Polyether Block Amide(PEBA), polypropylene(PP) and polyethylene(HDPE, LLDPE) [20] [55]. Because of the excellent performance in intrinsic and extrinsic performance of these polymers, they all are the good material chosen as common commercial SLS materials, which are widely used in 3D printing industry.

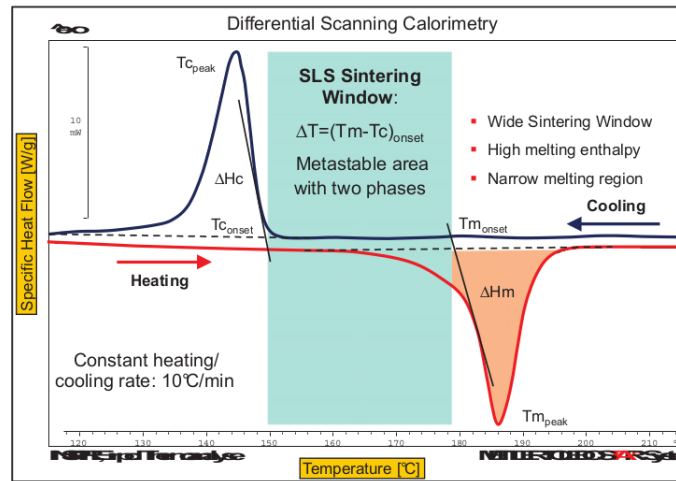


Figure 1.14: DSC profile of a semi-crystalline polymer the sintering windows [54].

### 1.2.4.1 Aging of polymer

Aging is a physical phenomenon involving molecular-level relaxation that manifests the macroscopic physical properties. The aging process widely exists in polymer heating treatments, affects the polymer manufacture, storage, and physical properties [56]. The long-term aging phenomenon was widely researched in commercial polymer materials. As shown in Fig. 1.15, the new PA12 powders have a good spherical morphology, whereas the reclaimed aged powders have irregular shapes with cracks on the surface. After manufacturing polymers with SLS, we observe an obvious difference between the surface morphology of new powders and extremely aged powders. The new powders exhibit a smooth and flat surface without unmolten particles, however, for the aging powders, the surface exists many un-sintering particles [57].

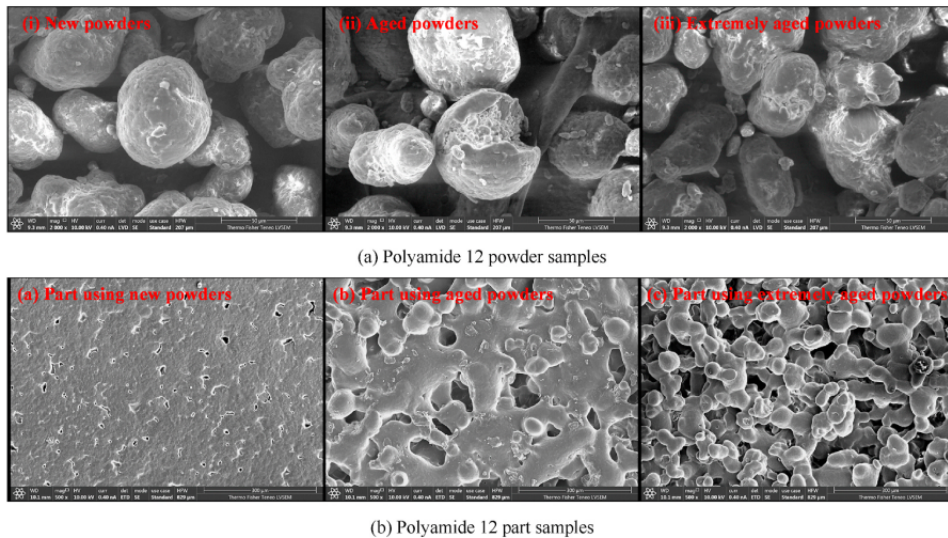


Figure 1.15: SEM images of the virgin and the used PA12 powders [58].

Polymer aging is separated to physical aging and chemical reaction occurring. Physical aging occurs when the polymer is in a non-equilibrium state, it is caused by molecular relaxation that is biased in the direction required to drive the material closer to equilibrium, including thermal aging and photochemical aging two types. Thermal aging is caused by elevated temperature and photochemical aging occurs by the weather change, the usual weather change

trials include solar ultraviolet (UV) radiation, water, pollution, and temperature change [59]. Aging changes the polymer morphology and macroscopic physical properties on the molecular level, like semi-crystallization polymers aging by the photo-oxidation will cause a chain scission and secondary crystallization, which decrease the ductility and increase material density and Young's modulus. During the SLS process, the thermal aging is important and affects the quality of samples. H. Zarringhalam [60] did a series of experiments measuring the properties of virgin Nylon powders and used Nylon powders for testing the producibility and final product's mechanical properties. Fig. 1.16a shows the DSC results for virgin PA2200 and the reused PA2200 powders, the crystallinity with refresh powders slightly decreased by around 1 %, and the melting temperature slightly increased by 1 °C. Fig. 1.16b is the GPC results with virgin PA12 powders and the reused powders. The average molecular weight for virgin powders is 70000  $g/mol$  and the used powder is 170000  $g/mol$ .

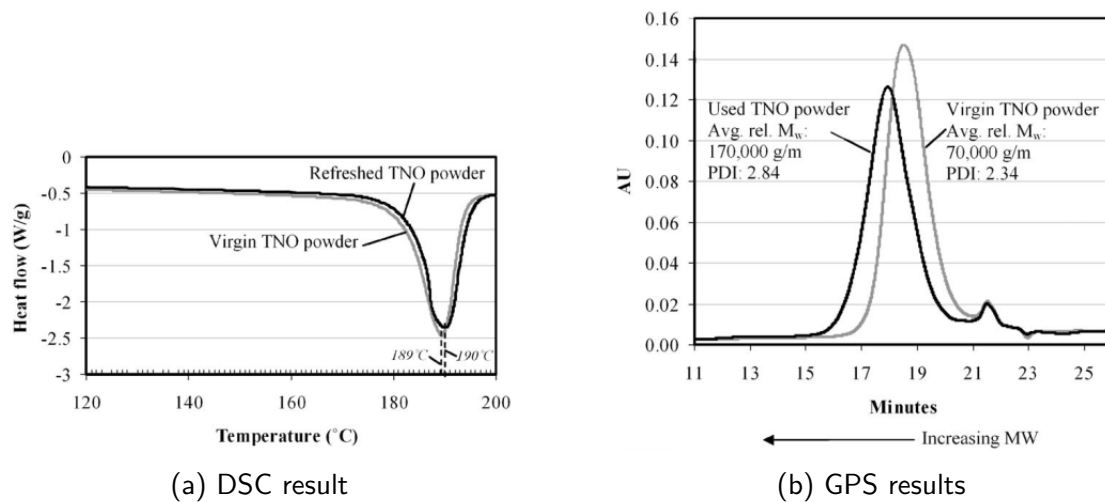


Figure 1.16: DSC and

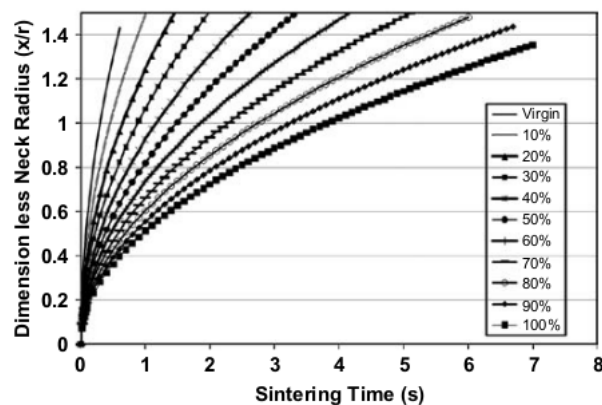


Figure 1.17: Predicted the sinter radius based on Frenkel model [61].

Fig. 1.17 shows the sintering process variation with different proportions of virgin and used mixed PA polymer. The viscosity for used polymers is higher than virgin powders because of the solid-state post condensation phenomenon. Usually, the powders, especially around the samples used in the SLS process, are mixed with recycled and virgin particles, the higher viscosity for recycled particles with low flowability will slow down coalescence [61].

The chemistry aging of polymer is a complex process, and many studies have been focused on physical aging in semi-crystallization polymers. The thermal degradation usually induced by the chemistry aging of polymers changes the molecular structure, crystal structure,

and chemical structure (molecular weight) of polymer, which influence the properties of materials. In the SLS process, using the degraded semi-crystallization polymer manufacturing products will decrease the samples' surface quality and the sintering rate. For example, the aging principle for PA6 can be explained through the structure of polyamide. Polar amide groups (-NHCO-) through the electron share between atoms attract to together, the individual polymer chain fold back over on itself, other polymer chains similarly are attracted to each other, this structure results in extra strength and stiffness. However, after the polyamides absorbed water molecules, the water polar molecules interfere with this charged area and form a weak connection to the C=O and H-N bonds [62]. These interfering molecules reduce the polar attractions between the chains and increase chain mobility. The absorbed water will increase the chain mobility and drop the glass transition. This means that PA6 is easier to age if it is stored in a moisture condition.

#### 1.2.4.2 Crystallization of polymer

Crystallization of polymer is controlled by nucleation and crystal growth. The crystallization rate can be increased by adding nucleating agents and decreasing the crystallization temperature. The crystallization of semi-crystalline polymers includes non-isothermal and isothermal crystallizations.

In ideal condition, where the parameters like temperature, pressure, etc, the Avrami equation is used for analysing the crystallinity elapsed with time under isothermal conditions, the general Avrami equation is [63] [64] :

$$1 - X(t) = \exp(-Kt^n) \quad (1.1)$$

where  $X(t)$  is the crystallinity,  $K$  is constant and decides the crystallization rate that is temperature dependent,  $n$ , the Avrami index, contains the information on nucleation and crystal growth, which is affected by the phase transformation, crystallization rate, annealing and different mechanisms involved during the manufacture process.

However, in real condition, the thermal conditions always change continuously. A series of model are proposed for describing these conditions, including Ozawa model [65], Ziabicki model [66], Nakamura [67] [68] model and Dietz model, which all are based on Avrami model for analysing the non-isothermal conditions. The modified Hoffman-Lauritzen model [69] is used to simulated the isothermal crystal growth rate for non-isothermal crystallization for nucleated and non-nucleated polymers.

Usually, there are three types of non-isothermal crystallization processes that are presented in Fig. 1.18, which are melt-crystallization, cold-crystallization and recrystallization [70].

Melt-crystallization is defined as heating the material to the molten state where the temperature is higher than melting temperature and then cooling the material with different cooling rates. For the major part of polymers, the crystalline forms highly depend on the cooling rate. At the low cooling rate, melt-crystallization occurs at a temperature far above the glass transition temperature, decrease in crystallinity seems to be proportional to the logarithm of the previous cooling rate. At a higher cooling rate, crystallinity decreases exponentially with increasing previous cooling rates.

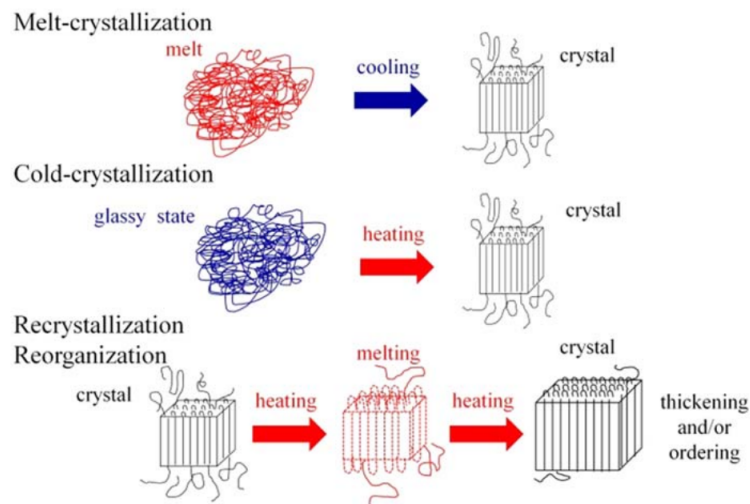


Figure 1.18: Schematic representation of the three types of nonisothermal crystallization of polymers [70].

Cold-crystallization is defined as an exothermic crystallization process taking place upon heating from a glassy, amorphous phase, crystallization happens at lower temperature than cooling from melt. The enthalpy of cold-crystallization is zero at extremely high heating rate ( $50000\text{ K/s}$ ), because crystal growth process is totally suppressed since there is not enough time for crystal growth starting from a small number of heterogeneous or homogeneous nuclei. This behavior exists in polymers that get new formation and transformation of crystals. This process occurs involuntarily when the temperature of crystalline or semi-crystalline materials reaches to a certain value or polymers are deformed by external mechanical forces. It is related to the mobility of the particles and highly influenced by the heating and cooling rate.

Recrystallization is a procedure that dissolves the polymer compound in a solvent with increased temperature, and the pure material is insoluble at a low temperature. This process leads the polymer crystal structure from a metastable form to a stable form during heating, which is an effective way of obtaining a pure material [70].

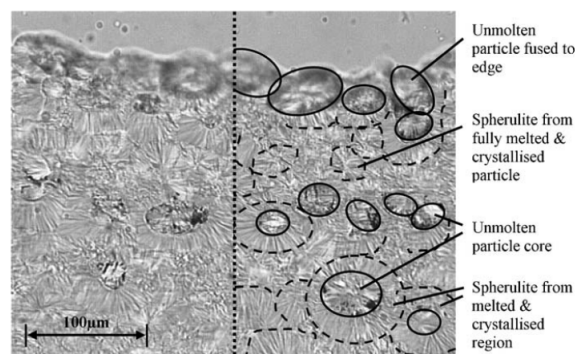


Figure 1.19: Microstructure for PA12 transformed after SLS process [60].

Nylon/PA6 usually has two stable crystal structures  $\gamma$  and  $\alpha$ . The  $\gamma$  form is a hexagonal or pseudohexagonal type crystal and  $\alpha$  form always is a monoclinic crystal. The  $\gamma$  form is always more ductile and thermo-dynamically stable and has a higher melt temperature than  $\alpha$  form [71] [72] [73] [74]. If polymer exists  $\alpha$  form structure [60], the PA6 usually involves melt-crystallization and recrystallization process in SLS manufacturing process. Polymer is not fully molten during the sintering process, the particles coalesce together driven by the viscosity.

Fig. 1.19 shows a crystal morphology of the cross-section of the sintering parts with the annotations on the right-hand side. It is seen in the heterogeneous states of particles after the SLS process. The particles have fused at the top edge of the parts, and the bottom part composed of particle cores and surrounded by spherulites can be described as partially molten particles when particles do not receive enough heat to fully melt.

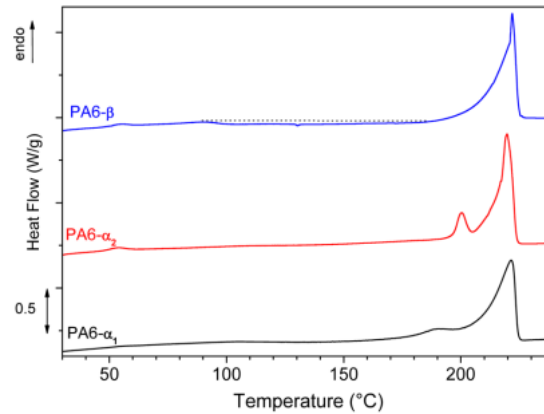


Figure 1.20: DSC thermograms of PA6- $\alpha_1$ , PA6- $\alpha_2$ , and PA6- $\beta$  during the first heating [75].

The fusion latent heat is different between different types of crystal forms. Fig. 1.20 shows thermograms of PA6- $\alpha_1$ , PA6- $\alpha_2$  and PA6- $\beta$ . In  $\alpha_1$  and  $\alpha_2$  phases, a smaller melting endotherm caused by the secondary crystal is shown between the main melting endotherm. However, at the  $\beta$  phase, there is only one melting peak [75] [76].

### 1.2.4.3 TGA of PA6

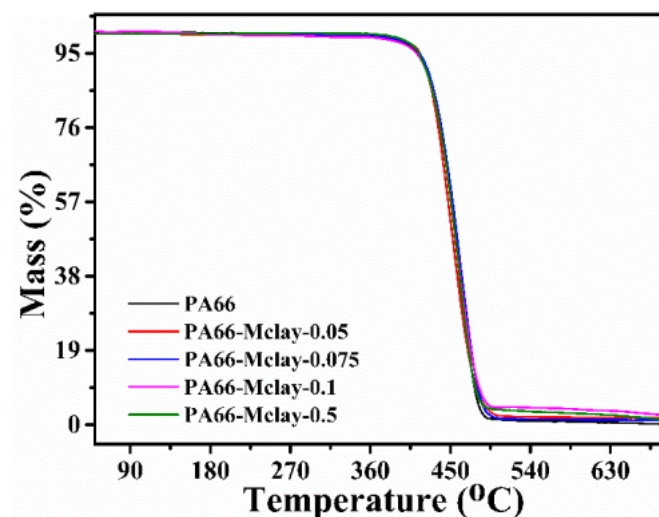


Figure 1.21: The TGA curves of PA66 and PA66/Mclay nanocomposites [77].

The thermal stability of PA66 is obtained by the TGA technique, shown in Fig. 1.21. PA66 rapid decomposition when the temperature is above 370 °C. This result suggests to us that the maximum temperature at the SLS process should not be higher than the decomposition temperature. Therefore, the laser intensity, laser speed and scanning space need to be controlled.

### 1.2.4.4 XRD analysis of PA6

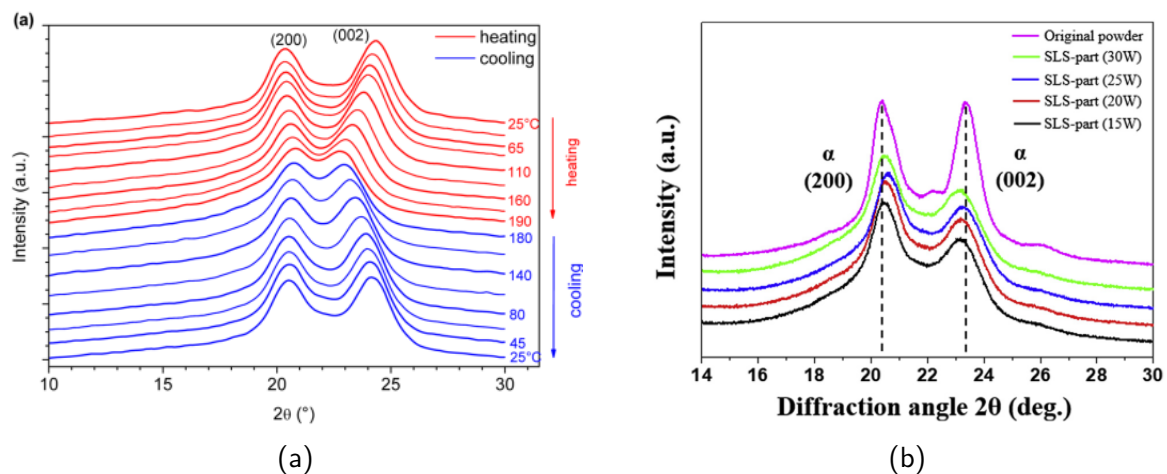


Figure 1.22: The crystalline structure characteristic of PA6 in SLS part: (a) Diffractograms d-spacing evolution of PA6 in the cooling process. (b) with different manufacturing laser power [75].

Fig.1.22a shows the evolution of the XRD curves which represent the crystalline structure of PA6 (initial from  $\alpha_1$ ) heating from room temperature ( $25^\circ\text{C}$ ) to  $190^\circ\text{C}$  and cooling from  $190^\circ\text{C}$  to room temperature. With the heating temperature increasing, the structures of PA6 are slowly changing [75]. The crystalline structure change influence by the fabricating laser power is shown in Fig. 1.22b. The two peaks of XRD curves correspond to the diffraction of (200) and (002) plans. The (200) plane contains chains only linked by van der Waals force whereas the other planes contain chains referring to the hydrogen-bonded sheets. The two diffraction peaks have similar intensities to the original powder. However, after the SLS process, both the two peaks are depressed, and the hydrogen-bonded (002) plane is more sensitive to the laser energy change to van der Waals force during this temperature range [53].

## 1.2.5 Quality of SLS objects

### 1.2.5.1 Defects of shape

The polymer is sensitive to thermal gradient because of the in-homogeneous crystallization, and the thermal gradient is the main source for inducing the products' defects. The defects include shrinkage, surface deformation and surface defect. Shrinkage is a common defect that exists in SLS manufacturing products caused by air escaping. Shrinkage includes sintering shrinkage and thermal shrinkage, while sintering shrinkage is due to densification process, and thermal shrinkage is due to the thermal cycle. The main surface deformations are warping and distortion: warping means a surface bent out of its natural shape and distortion means any types of change in the appearance of the surface, this causes the geometric inaccuracy of projects, and thus reducing the mechanical properties of sample. Thermal stress, laser power, scanning length, scanning specification, deposition starting points, powers preheating temperature, circumstance temperature, dimension of the plats, and the number of layers all are the contributing parameters for distorting and warping. Thermal stress is caused by the thermal gradient that exists between the scanning zone and the accumulated zone, this is an important reason for distorting the samples. Increasing the length of the plat and the number

of layers will increase the deformation [78]. The fractures, cracks, holes, inadequate fusion bonds between layers and particles, balling, and porosity are common defects in the powder bed additive process. These defects lead to weak mechanical properties. Choosing appropriate manufacturing parameters, room conditions, maintenance temperature can eliminate these defects. In summary, shrinkage, surface deformation, cracks, and porosity limit the repeatability and precision of manufacturing the objects, prevent the technology from spreading, and decrease the accuracy of samples. Understanding and eliminating these defects must take an enormous improve considerably this technology [79].

### 1.2.5.2 Surface quality

Surface roughness and morphology are the most important criterion for measuring the quality of SLS objects because the defects on the function surface can fail the product. Understanding the characteristic of surface topography is a highlight to improve surface quality. We introduce  $S_a$  describing the surface roughness, it represents the values of the arithmetical mean height of the surface, and is calculated by the following equation:

$$S_a = \frac{1}{A} \iint_A |z(x, y)| dx dy \quad (1.2)$$

The rough surfaces caused by layered manufacturing and adherence of incomplete molten particles depend on various process parameters. There exist many works analysing the roughness of the powders and their production. Bacchewar et al. [80] used the ANOVA (analysis of variance) method to analyse how the parameters like laser power, beam speed, build orientation, layer thickness, and hatching spacing influence the average surface roughness in SLS process. Anish Sachdeva et al [81]. fabricated the PA12 by SLS process and analyzed the connection between surface roughness and the process parameters (laser power, preheating temperature, hatch space, and hatch length) by experimental methods. Their experimental results showed optimal manufacturing parameters for PA12 polymer, the optimal parameters are the laser power between 28 - 32 W, the hatching space equal to 0.2 mm, and bed preheating temperature at 449 K. These parameters would lead to the lowest surface roughness of PA12. Zicheng Zhu et al. [82] studied the connection between real surface and the process parameters, porosity, and predict the product' mechanical properties. They revealed that reducing the porosity of the object could smooth the object's surface. The results mean that suitable process parameters (sinter speed, laser power, and ink grey level) would lead to improving the product's mechanical properties through adjustment of porosity.

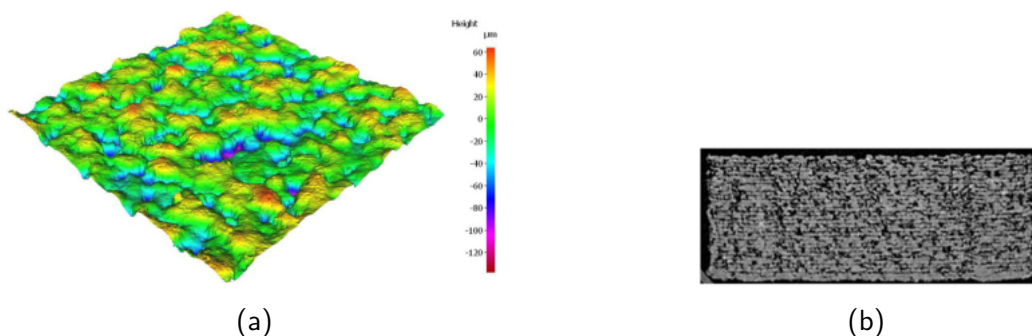


Figure 1.23: (a) Height map of sample's surface.(b) Porosity tomography image [82].

### 1.2.5.3 Microstructure

Anisotropy, heterogeneity, and porosity all highly affect the microstructure of the fabricated parts. The anisotropy is affected by the laser scan direction and layer orientation. Scanning direction influences the mechanical properties of the sample. The highest compressive strength and densification are got when the layer orientation relative to Z-axis is equal to  $90^\circ$ , while the weakest compressive strength is got when the orientation is equal to  $0^\circ$  according to Mihaela's experiments [83]. The heterogeneity of the manufactured part is affected by the powder spreading condition, scan strategy, environment temperature and laser density. These parameters influence the thermal distribution in the powders, appropriate parameters promote the sample's melt density and lead to a better microstructural homogeneity [84] [79]. Porosity is a common defect widely existing in SLS process and lead to poor mechanical properties. Many reasons and parameters influence the porosity of the fusion zone. These parameters are, but not limited to the laser specification, scan direction, laser density, balling, powder stacking density, powder morphology, surrounding temperature, surrounding gas flow condition and so on [85].

## 1.2.6 Numerical method of the multiphysics coupling

SLS technology is a process that uses a laser source to melt the powders quickly, then the fused particles are connected for forming a new product. A critical element widely used in the additive manufacturing processes for designing and fabricating products is development of an accurate and efficient model to reflect a series of complex thermal histories and physical phenomena in this process. Lots of numerical methods are undertaken by researchers.

### (1) Finite element method (FEM)

In the SLS process, heat conduction takes place in a heterogeneous system made of solid particles and voids. The powder bed can be considered as an equivalent homogeneous medium and simulation can be done by using the finite element method (FEM) the grain level. The FEM is a good way to model the sintering process and thermal behavior under different parameters, and many commercial software were developed based on the FEM method. Omar Lopez-Botello et al. [86] combined two-dimensional Cellular Automata (CA) and Finite Element (FE) (CA - FE) together for considering the powders melting and crystalline transformation, and tracking the interaction between several melt pools. In this model, the FE is used for considering higher temperature problems, and CA is used for considering the grain growth problems. Finally, the CA - FE model is also used for predicting melt pool cooling and solidification rates, size of the molten pool and the type of micro-structure growth in the SLM process.

Dai, K., Shaw et al. [87] used FEM to build a numerical model simulating thermal conduction and mechanical behavior of metal and ceramic powders. F.R. Liu et al. [88] also used a micro 3D FEM for building a multi-layer particles cubic stacking model to describe the thermal evaluation of the porous bed in SLS process. There are many kinds of research focused on using FEM methods to simulate the whole SLS process, it is a useful method to help us to understand thermal evolution in the powders, microstructural formation, and densification process of semicrystalline phenomenons in AM manufacture. However it is difficult to take into account volume shrinkage and deposition of a new layer, this method too much relies on empirical values which are hard to predict and measure during the sintering process, and it is

not possible to capture the physical phenomenon of interacting grains.

## (2) Discrete Element Method (DEM)

The discrete Element Method (DEM) is a numerical method used to solve all involved physics equations at the grain level during AM technology. This method is useful for simulating phenomena with discontinuous connections and linking all the physical phenomena with interacting separate particles. And in optimizing the SLS process, the DEM method gives a more natural and accurate numerical result [39].

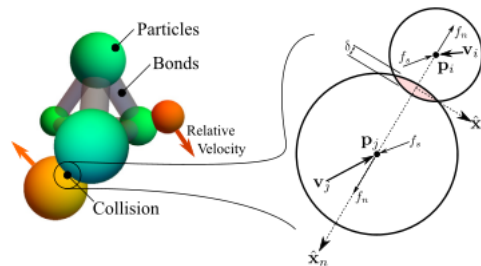


Figure 1.24: Overview of the Discrete Element Method. At right, the variables associated with the collision mechanics are diagrammed [89].

John C. Steuben et al. [89] [90] used the DEM method simulating the thermal transfer in the particles, making a detailed discussion on the broader inter-particles bonds formation in the contact and collision situation. A schematic overview of interacting spherical particles is shown in Fig. 1.24. The contraction models are built according to normal and shear forces between the particles.

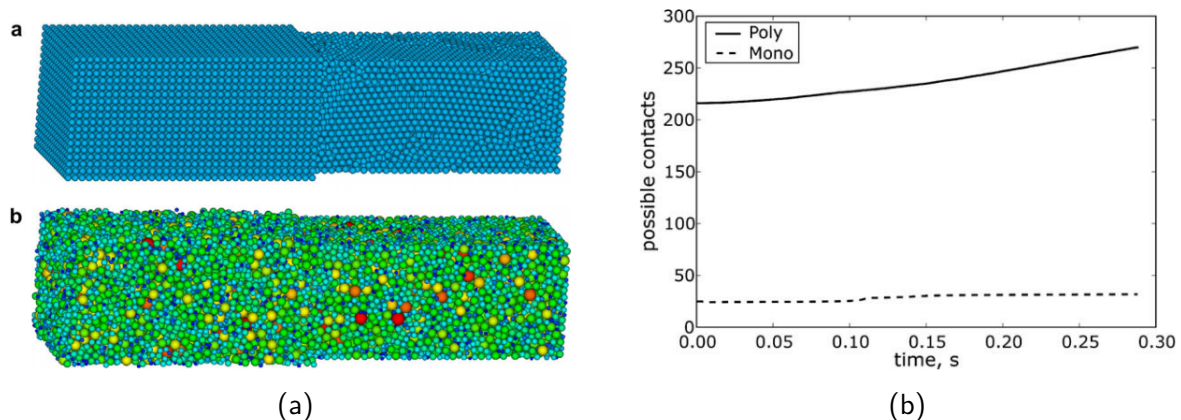


Figure 1.25: (a) View of initial and compacted specimens for mono-disperse and poly-disperse medium. (b) Time history of average possible contacts for one particle[91].

Rimantas et al. [91] used DEM methodology to express the constitutive behaviors of the SLS process and presented the temporal evolution of microscopic behavior for poly-dispersed material with the normal size distribution. Their results are shown in Fig. 1.25, indicate that particles dispersion formation influences the contact possibility, further influencing the heat flux transmission behaviors. The uneven distribution of heat transfer rates is caused by dispersion of the particle size, these phenomena just can be simulated by the DEM method, which is the biggest advantage of this method. However, its computation cost makes its method's extension to the real part scale difficult.

### (3) Finite volume methods (FVM)

In the scope a homogeneous medium, the finite volume method (FVM) also could be used for modeling all the involved physical phenomena in the SLS process, and it is easier to consider the volume shrinkage and deposited layers, but these still exists problems to get the accuracy value of sintering the parameters. Pengpeng Yuan et al. [92] based on CFD software developed the FVM and successfully simulated the thermal behavior and molten pool dynamics during the SLM of  $TiC/AlSi_{10}Mg$  nanocomposites. Aoulaiche Mokrane et al.[93] assumed the powder bed as a homogeneous medium and the FVM model was used to simulate the involved multi-physical behaviors, which include thermo-physical properties, laser power distribution, coalescence process, fusion, gas diffusion, shrinkage and crystallization. The governing equations are discretized in time using a second-order semi-implicit Crank–Nicolson scheme and using third-order Runge-Kutta methods discretized time-dependent models in time.

# Chapter 2

## Modeling and numerical methods in SLS process

### Contents

---

<b>2.1</b>	<b>The Heat Transfer Model</b>	<b>31</b>
2.1.1	Governing equation	31
2.1.2	Boundary condition	31
<b>2.2</b>	<b>Laser-powders interaction model</b>	<b>32</b>
2.2.1	Flat-top type laser	32
2.2.2	Gaussian laser: Beer Lambert model	33
2.2.3	Gaussian laser: Scattering model	35
2.2.3.1	Introduction	35
2.2.3.2	The scattering methods	36
2.2.3.3	Laser energy	40
<b>2.3</b>	<b>Modeling of the thermo-physical properties</b>	<b>40</b>
2.3.1	Density and the specific heat	40
2.3.2	Conductivity	41
2.3.3	Emissivity	42
<b>2.4</b>	<b>Modeling of melting process</b>	<b>43</b>
2.4.1	Melting latent heat	43
2.4.2	Viscosity of polymer	44
2.4.3	Model of coalescence	47
<b>2.5</b>	<b>Modeling of crystallization</b>	<b>52</b>
<b>2.6</b>	<b>SLS process modeling and numerical methods</b>	<b>53</b>

---

The SLS technology has been studied for many years, and there are still many aspects that need to be studied: many projects focus on laser sources and new types of materials, trying to find an effective and reliable method to fabricate the polymers. The level of laser melting technology is still far from mature enough to be applied in various industrial fields. It is important to develop a mathematical model for promoting technology wide usage in industrial.

## 2.1 The Heat Transfer Model

### 2.1.1 Governing equation

In a SLS process, heating power is brought by moving laser beam and contributes to increasing temperature and melting polymer. During the cooling phase, there will be crystallization and the corresponding enthalpy. In the powders there are laser-particles interaction resulting in a source term, heat conduction, melting resulting in coalescence and densification, and crystallization. Due to melting, coalescence, densification and crystallization, thermo-physical properties of the powder bed change in time. If we consider the powder bed as an equivalent homogeneous medium, heat equation governing a SLS process can be defined as:

$$\rho C_p \frac{\partial T}{\partial t} = \nabla(\lambda \nabla T) + Q + S_f + S_c \quad (2.1)$$

where  $T$  is the temperature of the powder bed,  $\rho$  is the density of the powder bed,  $C_p$  its specific heat,  $\lambda$  its thermal conductivity,  $Q$  the heat source brought by laser beam through laser-particles interaction,  $S_f$  the melting latent heat, and  $S_c$  is the crystallization enthalpy. In a SLS process,  $Q$  is brought first and results in  $T$  variation, then  $S_f$  becomes significant because of melting. After various laser scanning and layer adding, the parts are cooled down and  $S_c$  becomes important due to crystallization. This means that  $Q$ ,  $S_c$  and  $S_f$  are almost never non-zero at the same time.

### 2.1.2 Bondoury condition

Simulation the whole SLS process is a time cost process, we chose a smaller part in the X and Y directions inside the products to simulate the thermal distribution and material physical evolution in the whole Z direction, shown in Fig.2.1. The energy transfer through the surrounding environment of the whole powders is achieved through two boundary conditions. The top surface of the powder bed is in contact with air, there is therefore heat exchange by convection and radiation during the SLS process:

$$-k \frac{\partial T}{\partial n} = -h_{tot}(T - T_{ext}) \quad (2.2)$$

$$h_{tot} = h + \varepsilon \sigma (T^2 + T_{ext}^2)(T + T_{ext}) \quad (2.3)$$

where  $h$  is heat transfer coefficient of natural convection, assumed to be equal to 15,  $\varepsilon$ , the surface emissivity, is equal to 0.8,  $\sigma$  is the Stefan-Boltzman constant,  $T_{ext}$  is the ambient temperature and  $n$  is the surface normal direction [93]. On the bottom and lateral surfaces, there is no heat exchange and the adiabatic condition is given as follows:

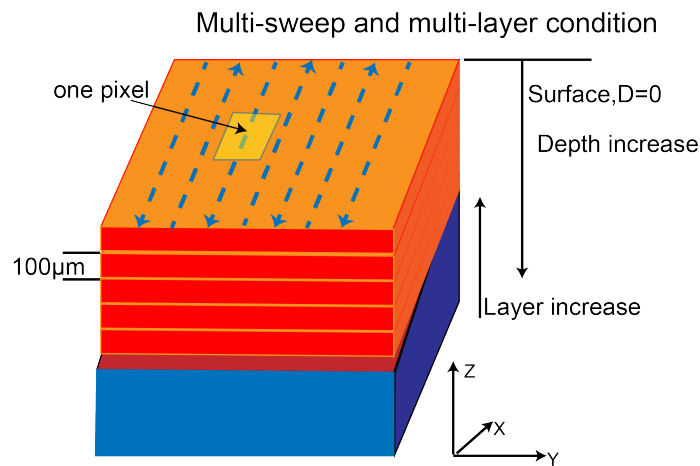


Figure 2.1: Schematic of manufacturing dominates X, Y and Z direction.

$$-k \frac{\partial T}{\partial n} = 0 \quad (2.4)$$

## 2.2 Laser-powders interaction model

Usually, two types of laser source launching models are considered, they are uniform flat-field beam profile and Gaussian beam profile [94]. The propagation and analysis equations can be applied to describe all these types. Fig. 2.3 shows Gaussian, Flat-top and inverse Gaussian three profiles of laser beams, and the effective diameters are detected by the CCD camera. The launching laser beam types directly affect the thermal distribution, maximum temperature, heating zone, and mechanical properties of the products. Usually, the Gaussian laser beam concentrates more energy on the laser beam center than its periphery, leads to deeper molten zone at the center of the track. The energy distribution of the flat-top types of the laser beam is more uniform, and presents a regular molten zone: the particle connection bonds are more homogenized than Gaussian types. The inverse Gaussian laser always leads to a smaller width of the free-of-powder consolidation zone, which is one of the reasons for the irregularity of the single track.

### 2.2.1 Flat-top type laser

The shape of heat flux transfer in the powder bed is cylindrical if the laser source is the flat-top type. This model assumes that the laser radiation is constant at all points delimited by the surface of the laser spot. The heat flux decay in the  $Z$  direction can be defined as follows:

$$Q_2 = \frac{P}{\pi R^2} (e^{-\beta z}) \quad (2.5)$$

where  $P$  is the power of the laser and  $R$  is the radius of laser beam, and  $\beta$  is the average attenuation coefficient. The flat-top laser type also can be applied to predict the temperature field during laser sintering of metal powders and polymers. The flat-top beam is not as cost-efficiency as the Gaussian beam, because the flat-top laser is not naturally preserved as the beam propagates, it must need an additional beam shaping assembly to convert the laser

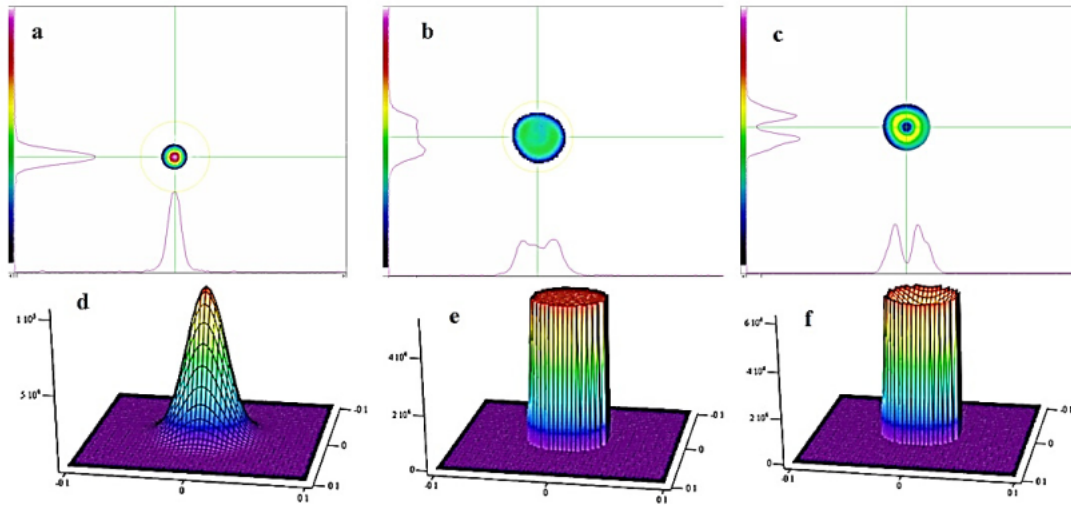


Figure 2.2: Shaping of laser beam profile analysed by the CCD-camera. (a) Gaussian beam; (2) flat-top; (3) inverse Gaussian power distribution [94].

into the flat top. The advantage is the flat-top type laser overcomes the disadvantages of Gaussian laser that lead to an energy waste caused by the laser "wings", and the flat-top beams often result in more accurate and predictable results, easier to get cleaner cuts, and sharper edges [95].

## 2.2.2 Gaussian laser: Beer Lambert model

The interaction between the laser and the polymer particles is the most important part of the simulation of the thermal distribution in the powder bed. The interaction process is affected by the wavelength of the radiation laser, the energy intensity, the type and shape of the laser beam, the chemical composition of the material, and the stacking of materials. The common laser interaction model is the Beer-Lambert distribution model, which just considered the scattering and absorption and neglects the scattering part. Zhenguang Jiang et al [96] used the Beer-Lambert law to simulate the energy distribution in the Invar alloy during laser oscillating welding. L. Dong et al [97] used this method to simulate the laser beam transmission in the polycarbonate powders and prove the reliability of this method after comparing their simulation results with Williams's experiment results [98].

Gaussian type laser is the most common laser type for the fusion of the materials in the SLS process. The laser intensity decreases radially as a near Gaussian function. If the no-scattering is considered, the laser attenuation along the depth direction follows Beer's law, and the laser distribution at the radius direction follows the Gaussian relationship [99] [44]. The Beer lambert law is one of the useful tools for directly evaluating the laser absorption in laser powder bed additive manufacture. The volumetric power of heat generated by the laser beam is the following:

$$Q = \beta_2(1 - R_e)Ie^{-\beta_2 z} \quad (2.6)$$

$$I = \frac{2P}{\pi w^2} e^{-\frac{2r^2}{w^2}} \quad (2.7)$$

$$w = \frac{R_l}{C} \quad (2.8)$$

$$C = \sqrt{\frac{\ln R_e}{-2}} \quad (2.9)$$

where  $P$  is the power of laser,  $r$  is the radial distance to the laser center, and  $R_l$  is the radius of the laser beam,  $\beta_2$  is the average attenuation coefficient,  $C$  is the coefficient of the distribution,  $R_e$  is the surface reflectivity of the polymer powder bed, which is equal to 4 % for  $CO_2$  laser in PA polymer. Moreover, the reflectivity is related to material properties, temperature and the wavelength of the laser.

Fig. 2.3 shows the optical power distribution map with Gaussian and flat-top laser beams. The peak of the Gaussian laser is almost twice as large as that of the flat top with the same laser intensity.

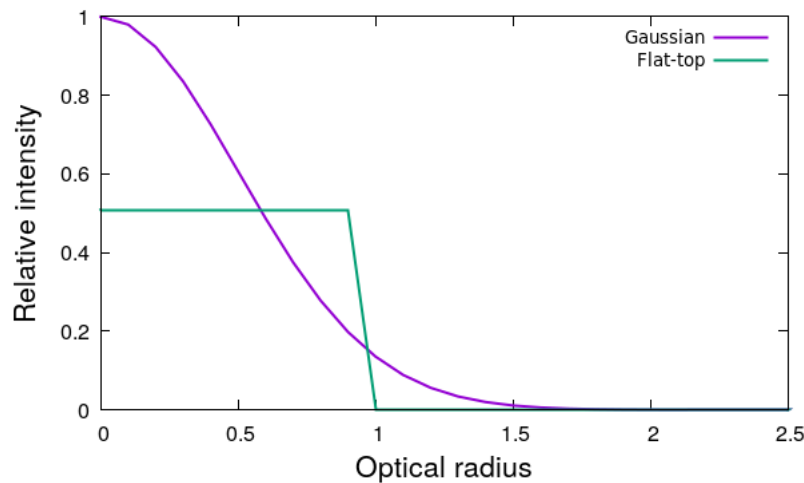


Figure 2.3: Gaussian and flat top beams of the same optical power.

The laser input incident angle is also an important factor that influences heat transfer, the incident angle affects the heat efficiency, and further influences the product's quality. Faud et al [100] compared the relative intensity distribution in PA plat surface with three different incident angles ( $\theta_\mu$ ) of  $0^\circ$ ,  $45^\circ$  and  $78^\circ$ . The incident angle rearranges the laser photons distribution in the powder bed. The results of laser beam relative intensity distribution in the beam center along the normal direction for five resolutions and three incident angles are shown in Fig. 2.4. The volumetric of power generated by the laser beam is following,

$$I(x, y, \beta) = \frac{P}{\sigma\sqrt{2\pi}} e^{-\left(\frac{x^*-x_0}{2w}\right)^2} e^{-\sigma y^*} \quad (2.10)$$

$$x^* = x - \sqrt{y^{*2} - y^2} \quad (2.11)$$

$$y^* = \frac{y}{\cos\theta_\mu} \quad (2.12)$$

where  $x_0$  is the center of the beam and the value of the beam diameter is  $w$ , the correction factor, the refraction angle  $\sigma$ , is introduced to modify the Beer-Lambert laws. In SLS process, the incident angle ( $\sigma$ ) is 0.

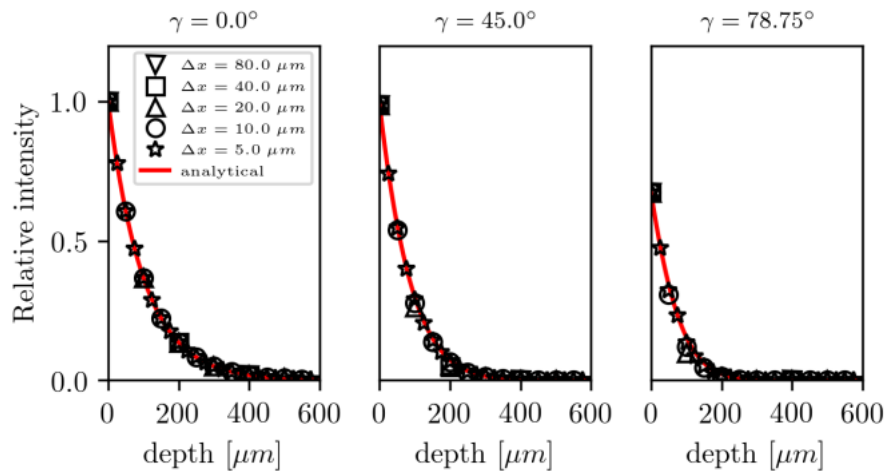


Figure 2.4: Comparison of the analytical and numerical relative intensity distribution in the beam center along the normal direction for five resolutions and three incident angles [100].

## 2.2.3 Gaussian laser: Scattering model

### 2.2.3.1 Introduction

The real polymeric materials contain a large variety of heterogeneities, the laser transmission in this zone is strongly influenced by reflectance, transmittance, and absorptance. The laser photons traveling in the polymer powder bed are similar to the electromagnetic wave traveling through a medium, the attenuation is all caused by the extinction phenomenon, in which absorption and scattering phenomena can equally coexist or prevail over each other. G. Zak et al. [101] use pinhole techniques to measure the laser-transparent part in laser transmission welding. Fig. 2.5 shows the T-NPFD profile along the Y direction, the experiments illustrate the beam scattering enlarges the laser "wing" and decreases the central laser. The scattering phenomenon widely exists in laser transmission in particles, the scattering changes laser travel paths, and rearranges the enlarged distribution, Therefore, for better simulating the heat distribution in the powder bed, the heat flux equation needs to be modified and the scattering phenomenon must be considered.

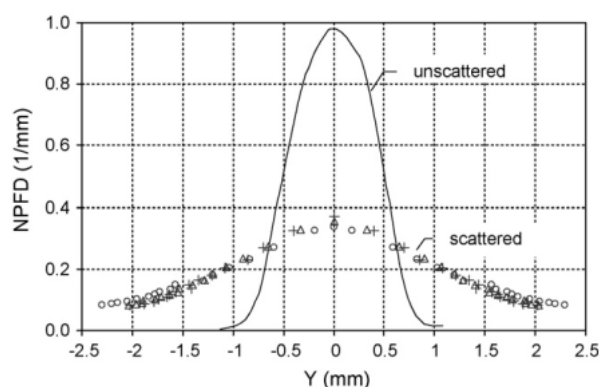


Figure 2.5: Y-axis T-NPFD profile after scattering by 3.2-mm PA6 GF30 % plaque (line scan along X) compared with unscattered-beam profile (three sets of data are shown) [101].

The analytical solution of using Maxwell's equation and Mie theory to solve the electromagnetic plane wave from spherical and homogenous particles are given by Mie G [102]

since 1908. Because of the similarity of the laser photons and the electromagnetic waves, the Mie scattered theory combined with the Monte Carlo method can be used to simulate the laser scattering phenomena in semi-transparent polymers. When the laser interacts with the powder bed, the photons will be reflected, absorbed, or scattered by the particles. If one photon is not absorbed or reflected outside by the polymer particles, it will go back and forth between grains: the scattering phenomenon changes the photons' travel directions. The Mie theory determines the photon's hitting directions in the detecting area. Most of the times, a photon should undergo several scattering steps before being absorbed. The modified Monte-Carlo ray-tracing method can retrace the paths of photon's transported within the powder bed. The analytical solution of photons scattering in homogeneous particles provides information on how the polymer particles scatter the laser and how the scattering parameters efficiently influence the particle scattering. The absorbed part of the photon's energy is calculated following the Beer-Lambert absorption principle, the attenuation rate depends on the absorption attenuation coefficient and the absorption lengths. The scattered part follows the Mie scattering theory, and the reflected part follows the Fresnel principle [103] [38] [104].

### 2.2.3.2 The scattering methods

#### Photons initialization

The initial laser energy is equally divided into millions of photons. For better mapping of the laser beams and the spatial distribution of photons in the powder bed, at least 1,000,000 photons are required. The power carried by a photon is set to  $I_0 = P/N$ , where  $P$  is the power laser,  $N$  is the number of photons, we choose  $N = 2,000,000$  in the simulation. The photons considered come from laser source and arrive at the powder surface. The laser photons' initial positions is defined by the laser radius and the beam angles, the laser intensity distribution in radial direction obeys the Gaussian distribution. The photons being located on the powder surface move all in the  $z$  direction (incident angle of  $0^\circ$ ), where the initial propagation directions are  $\vec{u}_0 = (0, 0, 1)$  and their initial positions are defined as follows:

$$\begin{aligned}x_0 &= r \cos(\phi) \\y_0 &= r \sin(\phi) \\z_0 &= 0\end{aligned}$$

where  $r = n_\sigma R_l \xi_1$  is the radial position with  $R_l$  the radius of the laser beam, and  $\phi = 2\pi\xi_2 \in [0, 2\pi]$  is the azimuthal position,  $\xi_1$  is pseudo-random numbers satisfying the Gaussian distribution and  $\xi_2$  is the random numbers uniform distributions in the range of  $[0, 1]$ ,  $n_\sigma$  is the present the standard deviation in the range of  $[0.5, 1]$ , and it is equal to 1 in our simulation.

#### Photons scattering

In the modified Monte Carlo method, a three dimension travel path of a photon travel in the powder bed is determined by multiple times scattering. The deflection angle ( $\theta$ ) for photon's scattering in powder bed is characterized by Henyey-Greenstein functions:

$$\cos(\theta) = \frac{1}{2g} \left\{ 1 + g^2 - \left[ \frac{1 - g^2}{1 - g + 2g\xi_1} \right]^2 \right\} \quad (2.13)$$

where  $g$  is the anisotropy factor, its value is between -1 to 1, and  $\xi_1$  is a pseudo random number. As shown in Fig. 2.6, when  $g$  is equal to 1, it indicates that photons are undergoing

forward-directed scattering,  $g$  equal to 0 indicates isotropic scattering and  $g$  equal to -1 indicates back-directed scattering. Normally,  $g$  is between 0.6 to 0.98 in the SLS process and depends on the reflection rate. The relationship between the reflection rate and the value of  $g$  is shown in Fig. 2.7. For manufacturing PA polymers, the reflection is always equal to 4 %, hence, the value of  $g$  is equal to 0.93.



Figure 2.6: Phase function for  $g$ , (a)  $g = 0.06$ , (b)  $g = 0.96$  [38].

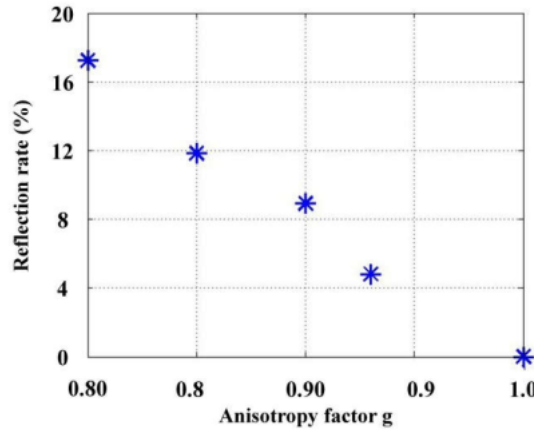


Figure 2.7: Relationship between anisotropy factor  $g$  and reflection rate of medium [105].

In the case of scattering, the photons' travel distances in the powder bed can be longer than the particles' diameter. These photons are scattered several times through the particles. Laser energy is repeatedly absorbed by polymer particles and the absorption rate of polymer powders is different from that of solid polymers. The photons' scattering directions and travel angles are independent parameters that can be calculated by Mie-theory. Denoting the longitudinal and azimuthal angles of a photon's moving direction by respectively  $\theta \in [0, \pi]$  and  $\phi \in [0, 2\pi]$  in the spherical coordinates, the initial moving direction is  $(\phi, \theta) = (0, 0)$  and the photon's new moving direction can be calculated for an unpolarized radiation by:

$$\phi = 2\pi\xi_2 \quad (2.14)$$

where  $\xi_2$  is a pseudo random number with a uniform distribution between  $[0, 1]$ . If the deflection angle  $\theta$  and the azimuthal angle  $\phi$  decided, the photons' new moving directions  $(\mu'_x, \mu'_y, \mu'_z)$  are calculated according to the given direction  $(\mu_x, \mu_y, \mu_z)$  and angles  $(\phi, \theta)$  :

$$\mu'_x = \frac{\sin(\theta)}{\sqrt{1 - \mu_z^2}} (\mu_x \mu_z \cos \phi - \mu_y \sin \phi) + \mu_x \cos \theta \quad (2.15)$$

$$\mu'_y = \frac{\sin(\theta)}{\sqrt{1 - \mu_z^2}} (\mu_y \mu_z \cos \phi - \mu_x \sin \phi) + \mu_x \cos \theta \quad (2.16)$$

$$\mu'_z = -\sin \theta \cos \phi \sqrt{1 - \mu_z^2} + \mu_z \cos \theta \quad (2.17)$$

If the photon's propagation is almost colinear with the z-axis, when  $|\mu_z| > 0.99999$ , to avoid the blow-up, the following Snell's equation should be used:

$$\mu'_x = \sin(\theta) \cos(\varphi) \quad (2.18)$$

$$\mu'_y = \sin(\theta) \sin(\varphi) \quad (2.19)$$

$$\mu'_z = |\mu_z| \sin(\varphi) \quad (2.20)$$

where  $\mu'_z$  returns 1 if  $\mu_z$  is positive, and returns -1 if  $\mu_z$  is negative. The photon's propagation in powder bed is defined by  $l = \frac{-\ln(\xi_3)}{\alpha_a}$  where  $\xi_3$  is a random variable uniformly distributed between 0 and 1 and  $\alpha_a$  is the absorption coefficient. However, as the photon's distribution is influenced by the powder bed density, the photon's propagation is modified as follow:

$$l = \frac{-\ln(\xi_3)}{\alpha_a} (a \ln(A) + b) \quad (2.21)$$

where  $l$  represents the photon's travel distance between scattering/ absorption,  $A$  is the relative density of the powder bed and  $a$  and  $b$  are constants equal to -0.46 and 1 respectively. This is equivalent to:

$$\alpha_{all} = \alpha_a + \alpha_s \quad (2.22)$$

where  $\alpha_{all}$ ,  $\alpha_a$  and  $\alpha_s$  represent the total attenuation, the absorption and the scattering coefficients respectively.  $\xi$  is random variable uniformly distributed between 0 and 1.

The photon's position is determined by the three spatial coordinates and the two angles for the travel direction. Once the photon's travel distance is determined, its new position is updated accordingly:

$$x' = x + \mu_x \cdot l \quad (2.23)$$

$$y' = y + \mu_y \cdot l \quad (2.24)$$

$$z' = z + \mu_z \cdot l \quad (2.25)$$

## Photons' absorption

Except for laser photons reflection, scattering, and transmission, most parts of the photons are absorbed by the polymer(Fig. 2.8). Most kinds of polymers show a high absorptance for  $CO_2$  laser which with wavelength equal  $10.6 \mu m$ , the absorption rate is usually between 0.73 to 0.94 [106]. The absorbed parts are calculated following the Beer-Lambert absorptance laws that can be simple written as follows,

$$I(d) = \int_a I_{\lambda_0} e^{-\alpha_\lambda d} d\lambda \quad (2.26)$$

where the  $\alpha_\lambda$  is the monochromatic attenuation coefficient,  $\lambda$  is the wavelength of the laser,  $I(d)$  is the radiation energy intensity connected with the physical length of absorption, given as  $d$ ,  $I_{\lambda_0}$  is the initial radiation energy intensity. The absorption rate is decided by the absorption coefficient and the absorption length. The absorption coefficient depends on the polymer's physical properties and the packing structure of the powder bed.

In the polymer laser sintering process, we always use  $CO_2$  laser as the heat source is a unique wavelength,  $\alpha$  is the attenuation coefficient for this laser absorbed in this type polymer, is equal to 17000, the Beer-Lambert attenuation equation can also be written as [107]:

$$I(d) = I_0 e^{-\alpha d} \quad (2.27)$$

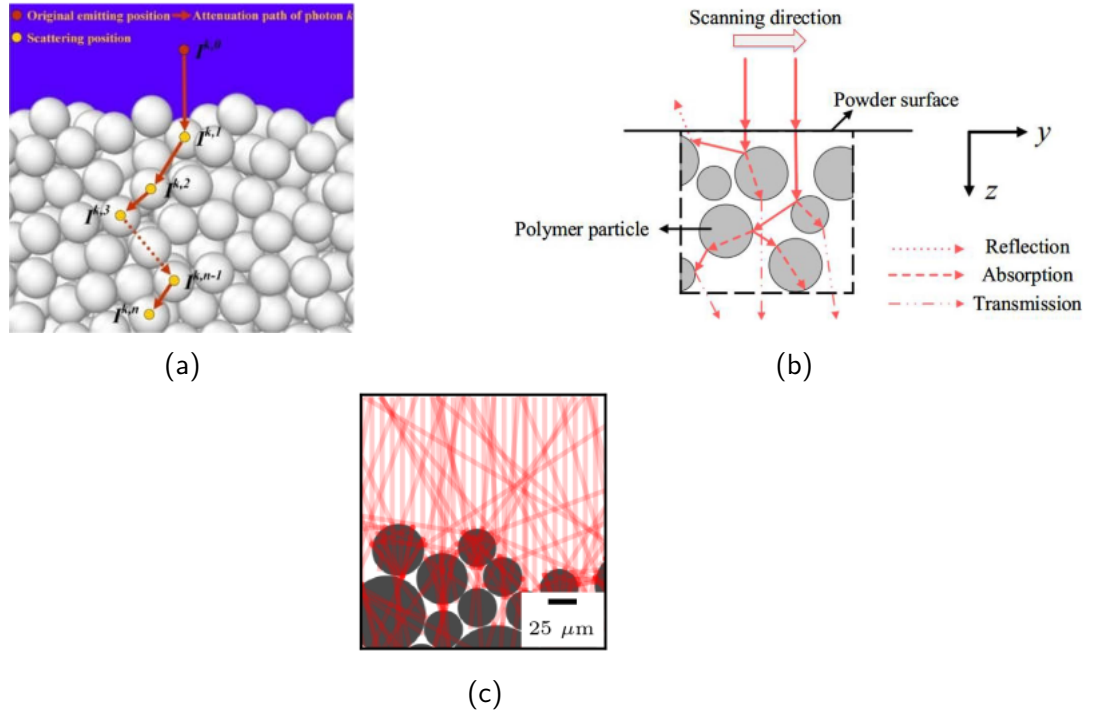


Figure 2.8: Attenuation path of photon  $k$  inside powder bed [105] [108].

where  $I_0$  is the laser energy carried by each photon,  $d$  is the absorption length.

In our SLS simulations, we assume the powder bed is a homogeneous medium with combined with polymer particles and air holes, the laser is only absorbed by the polymers and totally transform in the air. The photons' scattering travel length ( $L$ ) between two scatterings are expressed as follows:

$$L^2 = (x_i - x_{i+1})^2 + (y_i - y_{i+1})^2 + (z_i - z_{i+1})^2 \quad (2.28)$$

where  $(x_i, y_i, z_i)$  and  $(x_{i+1}, y_{i+1}, z_{i+1})$  are the positions of photons at  $i$  times scattering and  $(i + 1)$  times scattering. The values of  $L$  is the photons' scattering travel length, which is different from the absorption length used in Eq. 2.27, because the laser photon is just absorbed by the polymer but not absorbed by air. The real absorption( $d$ ) lengths consider both the size of particles and the powder bed's density( $D$ ). If the scattering travel length ( $L$ ) is shorter than the powders' diameter( $2 * r_1$ ), the laser photon must come out from the particles if the laser photon enters the particles until it has been totally absorbed by the polymer. Therefore, the absorption length( $d$ ) is equal to the powder's diameter. If the scattering travel length is longer than the powder's diameter, the absorbed length is equal to the particles diameter plus the free part, which is calculated by the powder bed's density( $D$ ) and the random number( $\xi_4$ ). The real absorption length ( $d$ ) can be calculated by the following:

$$I(i, j) = I(i, j - 1) * e^{-\alpha d} \quad (2.29)$$

$$d = 2 * r_1 + \xi_4(L - 2 * r_1) * D \quad \text{if } L > 2 * r_1 \quad (2.30)$$

$$d = 2 * r_1 \quad \text{if } L \leq 2 * r_1 \quad (2.31)$$

### Photons reflection

When photons are reaching the surface or the bottom of the powder bed, the possibil-

ity that a photon is reflected or transmitted is computed by the Fresnel's reflection coefficient:

$$R(\theta) = \frac{1}{2} \left[ \frac{\sin(\theta_i - \theta_t)^2}{\sin(\theta_i + \theta_t)^2} + \frac{\tan(\theta_i - \theta_t)^2}{\tan(\theta_i + \theta_t)^2} \right] \quad (2.32)$$

$$\theta_i = \cos^{-1} \mu_z \quad (2.33)$$

where  $\theta_i$  represents the angle of incidence on the boundary, and  $\theta_t$  is the transmission angle which can be calculated by Snell's law:

$$n_i \sin(\theta_i) = n_t \sin(\theta_t) \quad (2.34)$$

with  $n_i$  and  $n_t$  representing respectively the incident and transient refraction coefficients.

A random number  $\xi$  uniformly distributed in range of  $[0, 1]$ , is used to decide whether the photon is reflected outside the powder bed or transmitted in it.

If  $\xi \leq R(\theta_i)$ , then the photon is internally reflected, the photons stay on the boundary, the position and direction of the photons are updated accordingly reversing the  $z$  component, the new direction is:  $(\mu'_x, \mu'_y, \mu'_z) = (\mu_x, \mu_y, -\mu_z)$ . Otherwise, if  $\xi > (R(\theta_i))$ , the photon leave the powder bed. And when the photon leave from the bottom boundary, the photon is recorded as transmitted radiation. When the photon leave from the top boundary, these photons are called back-scattered radiation.

### 2.2.3.3 Laser energy

After considering the scattering phenomenon, the photons' transport paths in the powder bed are rearranged, we obtain a renewed absorbed photons' final distribution map which represents the energy distribution brought by the laser beam into the powder bed. Data fitting is then performed using the power distribution map, a similar but more complex expression to the Beer-Lambert law is chosen:

$$Q = \beta_1(1 - R_e)P \left( \frac{n}{\pi b^2} e^{-\frac{r^2}{b^2}} + \frac{c + az}{\pi b^2} e^{-\frac{az}{b^2}} \right) e^{-\beta_1 z} \quad (2.35)$$

where  $Q$ , the heating power of the laser beam, depends on the radial and vertical positions  $(r, z)$ ,  $P$  is the power of the laser beam,  $\beta_1$  is the total attenuation coefficient in the vertical direction of the powder bed,  $n$ ,  $a$ ,  $b$ , and  $c$  are the coefficients relative to the radial distribution of the heating power, these correction coefficients depend on powder density, powder size, and laser reflection rate. Note here that the term depending on  $a$  and  $c$  is resulted from scattering because without scattering photons' transport paths are only in  $z$  direction and that, as is suggested and can be seen later on, with  $z$  increasing the laser heating power is more concentrated around the laser axis.

## 2.3 Modeling of the thermo-physical properties

### 2.3.1 Density and the specific heat

The density( $\rho$ ) and the specific heat ( $C_p$ ) of the homogenized powder bed change with the material's phase change, which are calculated by using the parallel model,

$$\rho = (1 - \varphi)[(1 - f_l)\rho_{ps} + f_l\rho_{pl}] + \varphi\rho_{gas} \quad (2.36)$$

$$C_p = [(1 - \varphi)[(1 - f_l)\rho_{ps}(C_p)_{ps} + f_l\rho_{pl}(C_p)_{pl}] + \varphi\rho_{gas}(C_p)_{gas}]/\rho \quad (2.37)$$

where  $\varphi$  is the gas fraction or the porosity,  $f_l$  is the liquid fraction, 'ps', 'pl', 'gas' are solid phase, liquid phase and gas phase respectively.

### 2.3.2 Conductivity

Heat transport in complex porous materials is an essential requirement for modeling the SLS process. Models used for the low porosity material ( $\varphi < 10\%$ ), the medium density material with porosity between 15 % and 85 % and the material with high porosity higher than 90 % [109] are different.

#### (1) high porous material

If the porosity higher than 10 %, the effective thermal conductivity is calculated by Maxwell model and expressed as [110]:

$$\gamma = \frac{\lambda_p - \lambda_{gas}}{\lambda_p + (d - 1)\lambda_{gas}} \quad (2.38)$$

$$\lambda = \lambda_{gas} \frac{1 + 2\gamma\varphi}{1 - \gamma\varphi} \quad (2.39)$$

where  $d$  is the geometric factor to calibrate the model ( $d = 3$  or  $4.5$ ),  $\lambda_{gas}$  is the thermal conductivity of gas,  $\lambda_p$  is the conductivity of semi-crystalline polymer, without melting,  $\lambda_p$  is the same as solid polymer conductivity ( $\lambda_{ps}$ ).

#### (2) medium porous material

The modified Maxwell's model proposed by Chiew and Glandt [111] is used to calculate the thermal conductivity in the medium dense material:

$$\lambda = \lambda_{gas} \frac{1 + (d - 1)\gamma\varphi + (k_2 - 3\gamma^2)\varphi^2}{1 - \gamma\varphi} \quad (2.40)$$

A linear relation between  $k_2$  and  $\gamma$  is proposed according to Chiew and Glandt's report conductivity equation is corrected as follows after taking the best value of  $k_2$ :

$$\lambda = \lambda_{gas} \frac{1 + 2\gamma\varphi + (2\gamma^3 - 0.1\gamma)\varphi^2 + \varphi^3 0.05 \exp(4.5\gamma)}{1 - \gamma\varphi} \quad (2.41)$$

#### (3) lower porous material

The final effective conductivity of the powder bed can be calculated from Hailton and Crosser's model [112], the grain's shape, arrangement, composition and the porosity of the powder will influence the conductivity of two-component mixtures [113] [114].

$$\lambda = \lambda_p \frac{1 + (d - 1)\gamma(1 - \varphi)}{1 - \gamma(1 - \varphi)} \quad (2.42)$$

$$\gamma = \frac{\lambda_p - \lambda_{gas}}{\lambda_p + (d - 1)\lambda_{gas}} \quad (2.43)$$

With melting, the thermal conductivity of the polymer is calculated as follows [115]:

$$\lambda_p = (1 - f_l)\lambda_{ps} + f_l\lambda_{pl} \quad (2.44)$$

where  $\lambda_p$  is the polymer thermal conductivity,  $\lambda_{ps}$  is the solid polymer thermal conductivity, and  $\lambda_{pl}$  is the liquid polymer thermal conductivity, and  $f_l$  is the liquid fraction. The proportion of the liquid and gas phase highly influence the density, specific heat and conductivity of the polymer powder.

### 2.3.3 Emissivity

The material surface can exchange energy in the form of radiation, the effectiveness in emitting energy as thermal radiation is called emissivity, a ratio varying from 0 to 1. The amount of energy emitted by the surface depends on the material's temperature and surface properties. The thermal emissivity of the powder bed  $\varepsilon_{bed}$  is decided by the materials and the powder bed's base plate, shown in Fig. 2.9, the emissivity is expressed as follows [116]:

$$\varepsilon_{bed} = F_{pc}\varepsilon_{pc} + (1 - F_{pc})\varepsilon_{bp} \quad (2.45)$$

where  $F_{pc}$  is the area fraction of the powder coverage region of the base plate,  $\varepsilon_{pc}$  is the emissivity of powder, and  $\varepsilon_{bp}$  is the emissivity of the base plate.  $F_{pc}$  is in the range of 0 - 1. If the initial thickness of the powder layer is thicker enough and the particles fill all the plate, the powder bed can be seen as a complete powder packing box and  $F_{pc}$  is equal to 1. This condition is fulfilled by the initial layer in the SLS process. The thickness of a new layer is around 100  $\mu m$  and does not fully cover the polymer particles of the former layer,  $F_{pc}$  is taken to be equal to 0.933.

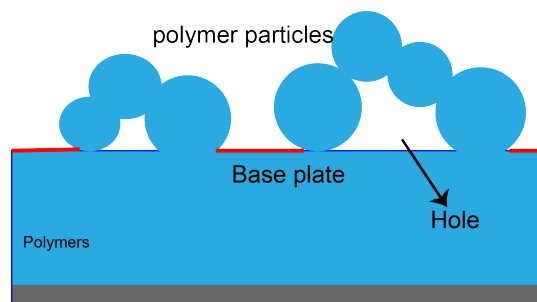


Figure 2.9: Schematic showing that the energy is absorbed by the powder bed and the base plate (red line).

The emissivity of powder ( $\varepsilon_{pc}$ ) is calculated following the Sih and Barlow's law [117]. The emission of the powder combines the emitting polymer particles with the emitting holes among these particles.

$$\varepsilon_{pc} = A_h\varepsilon_h + (1 - A_h)\varepsilon_s \quad (2.46)$$

where  $A_h$  is the area fraction of the surface which is calculated by the porosity of the powder bed, and  $\varepsilon_h$  is the emissivity of the holes. The holes can be seen as black and  $\varepsilon_h$  is equal to 1 for the holes.

$$A_h = \frac{0.908\varphi_{pc}^2}{1.908\varphi_{pc}^2 - 2\varphi_{pc} + 1} \quad (2.47)$$

$$\varepsilon_h = \frac{\varepsilon_s [2 + 3.082 (\frac{1-\varphi_{pc}}{\varphi_{pc}})^2]}{\varepsilon_s [2 + 3.082 (\frac{1-\varphi_{pc}}{\varphi_{pc}})^2] + 1} \quad (2.48)$$

where  $\varphi_{pc}$  is the traction porosity of the powder coverage region that can be calculated by:

$$\varphi_{pc} = 1 - \frac{1 - \varphi}{F_{pc}} \quad (2.49)$$

where  $\varphi$  is the fractional packing porosity of the whole powder bed. With laser heating the polymer part, the surface porosity decrease because of the polymer molten and hole collapse, the emissivity of powder bed decreases slowly and tends to the polymer emissivity.

## 2.4 Modeling of melting process

### 2.4.1 Melting latent heat

A melting process is accompanied by the absorption of latent heat. In terms of heat balance, the melting can be represented by the heat sink  $S_f$  in Eq.(2.1).  $S_f$  can be calculated by Voller's theory [118]:

$$S_f = -(1 - \varphi) \delta h \frac{\partial f_l}{\partial t} \quad (2.50)$$

where  $\varphi$  is the porosity of the powder bed,  $f_l$  is the liquid volume fraction which varies from 0 to 1 and  $\delta h$  is the latent heat absorbed by the melting polymer. The melting phase change is accompanied with latent heat evolution, the latent heat absorbed by the melting polymer is calculated as follows :

$$\delta h = \rho L f_l + \rho_{pl} \int_{T_l}^T (C_p)_{pl} d\theta - \rho_{ps} \int_{T_s}^T (C_p)_{ps} d\theta \quad (2.51)$$

$$f_l + f_s = 1 \quad (2.52)$$

where  $L$  is the latent heat of polymer,  $f_l$  and  $f_s$  are respectively the volume fractions of liquid and solid,  $\rho_{pl}$  and  $\rho_{ps}$  are respectively the densities of liquid polymer and solid polymer,  $T_s$  and  $T_l$  are the melting start temperature and end temperature, and  $(C_p)_{pl}$  and  $(C_p)_{ps}$  are respectively the specific heat of liquid polymer and solid polymer [119]. Note that  $f_l$  is a function of the temperature and that it is first supposed to be linear in the present work:

$$f_l(T) = (T - T_s)/(T_l - T_s) \quad (2.53)$$

with  $T_s = 471K$  and  $T_l = 487K$ . This linear function, simple and easy to use, has a drawback with discontinuous first derivative.

In order to obtain a continuous function, the liquid fraction can be expressed as a third-order polynomial:

$$f_l(T) = aT^3 + bT^2 + cT + d \quad (2.54)$$

when  $a$ ,  $b$ ,  $c$  and  $d$  are the constants to be determined. Using  $f_l(T_s) = f_l'(T_s) = f_l'(T_l) = 0$  and  $f_l(T_l) = 1$ , the constants are identified as  $a = -4.8e-4$ ,  $b = 0.7$ ,  $c = -336$  and  $d = 53612.8$ . Fig. 2.10 shows the difference between the two models.

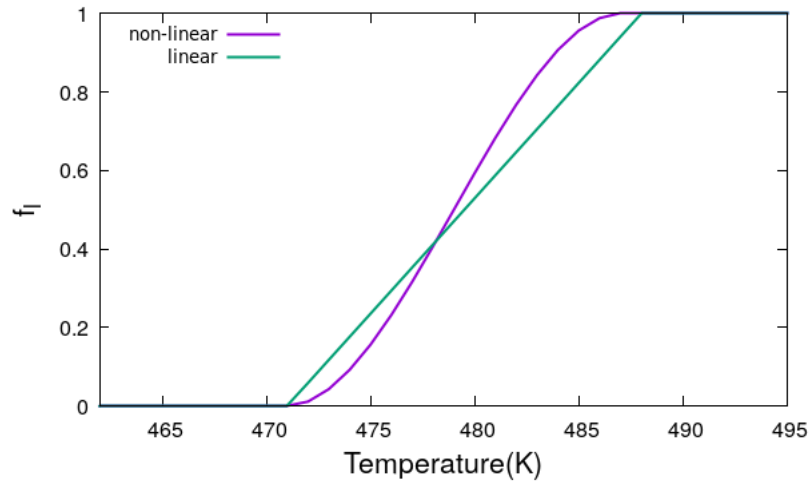


Figure 2.10: liquid fraction versus temperature, linear and nonlinear models.

## 2.4.2 Viscosity of polymer

Studying the laser sintering process involves heating cycle and change of temperature-dependent properties. In the SLS process, the physical properties include viscosity, surface tension, heat capacity, and thermal conductivity. Among these parameters, the rheology and viscosity are two important parameters of the fabricating process using polymeric material because the dynamics of particles sintering is the viscous flow. The heating cycles induce the polymer chains to entangle together arising from poly-condensation effects, leading to an increase in molecular weight and the polymer viscosity.

For most commercial plastics, the values of zero-shear viscosity ( $\eta_0$ ) depends on the critical molar mass, the value of zero shear viscosity ( $\eta_0$ ) is decided by the polymer molecular weight, and can be expressed as [120]:

$$\eta_0 = C(M_w)^n \quad (2.55)$$

where  $M_w$ , the molecular weight, is sensitive to the melting cycle, and  $C$  is a constant equal to 0.18 for PA6. Theoretical values of index  $n$  for commercial polymers is usually in the range of 3.4 - 3.6, and the  $n$  is equal to 1 if the  $M_w$  is less than polymer critical molecular weight

The value of zero shear viscosity changes dramatically during the SLS process. Barry Haworth et al. [61] tested the molecular weight of virgin and used PA6 polymer particles. The molecular weight ( $M_w$ ) of virgin polymer particle is 18900 *g/mol*, and the molecular weight of the "used" polymer particle increased to 58050 *g/mol* which is much higher than virgin powder. The zero-shear viscosity for the recycled particles increase to 5090 *Pa.s*, which is more than ten times higher than that of virgin polymer particles (309 *Pa.s*). Fig. 2.11 shows the viscosity with four types of PA12 material in the low shear rate range. The variation in viscosity and the molecular weight between used and new polymers are caused by the solid-state post condensation phenomenon. The polymer molecular weight increase caused by the post-condensation phenomenon is confirmed by GPC experiments, the virgin, used and mixed polymer powders show a large difference in molecular weight on GPC curve [121] [61]. These observations indicate that the flow behavior of PA12 is much influenced by the polymer usage status. In reality, the lower relative molecular weight favors the sintering process, but the higher molecular weight with more polymer entangling together promotes the enhancement of mechanical properties.

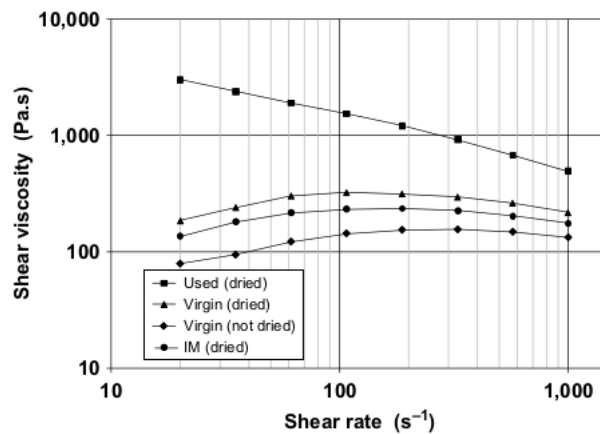


Figure 2.11: Shear viscosity data from capillary rheometry at  $473K$  for PA-12 polymers, plotted as shear viscosity  $vs$  shear rate [121].

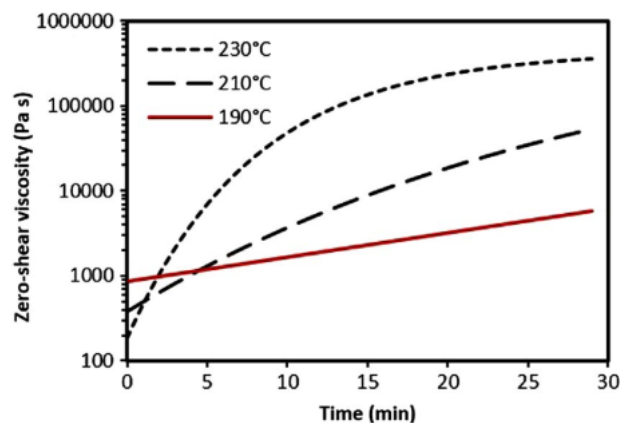


Figure 2.12: Initial zero-shear viscosity-time profile for PA12 polymer [122].

It is difficult to get accurate viscosity values because the SLS polymer powder bed mixes the used and virgin polymers. The aging rate for the used polymer is difficult to control because the number of heating cycles, the maximum temperature, and the preheating temperature influence the polymer's initial zero-shear viscosity. Sasan Dadbakhsh's paper [122] showed the connection between isothermal temperatures and the powders' aging rate. As shown in Fig. 2.12, the virgin powders are kept at various isothermal temperature ( $190\text{ }^{\circ}\text{C}$ ,  $210\text{ }^{\circ}\text{C}$  and  $230\text{ }^{\circ}\text{C}$ ) with different periods. Higher temperature and longer time induce higher polymer aging degree, and the initial zero-viscosity of the polymer, because the post condensation phenomenon makes more "cross-linking" of the polymer. For studying the flow behavior, there are several viscosity models developed for modeling the shear viscosity of the polymer. Including the Cole-Cole model which is used for simulating the constant viscosity region at low shear rates and the Carreau and Cross WLF models, which account for the tendency towards Newtonian behavior (non-linear strain rate dependence) and temperature sensitivity [123].

### (1) Cole-Cole model

The nonlinear rheological behavior is that the viscosity  $\eta$  of a polymer melt in steady shear crosses over from the shear rate-independent plateau to the shear thinning regime, K.S.

Cole and R.H. Cole express the behavior as follows [124] [125] [126].

$$\eta(J_e) = \frac{\eta_0}{(1 + J_e \tau_{relax})^h} \quad (2.56)$$

where  $\eta_0$  is the viscosity in the limit of the zero shear rate,  $\tau_{relax}$  is the relaxation time,  $J_e$  is the shear rate and  $h$  is the shear thinning exponent. The viscosity and the relaxation time decrease with temperature increasing. Tab. 2.1 summarises the relaxation time of PA12 at different temperature calculated by the Cole-Cole viscosity model from temperature ranging from 170 °C to 230 °C.

Table 2.1: Terminal relaxation time obtained from the Cole-Cole representation for different temperatures.

Temperature(°C)	170	180	190	200	210	220	230
$\tau_0$	4	1.9	1.3	0.7	0.5	0.2	0.1

## (2) Carreau-Yasuda model

According to Carreau and Yasuda [124], the viscosity as a function of frequency changes with temperatures (Fig. 2.13).

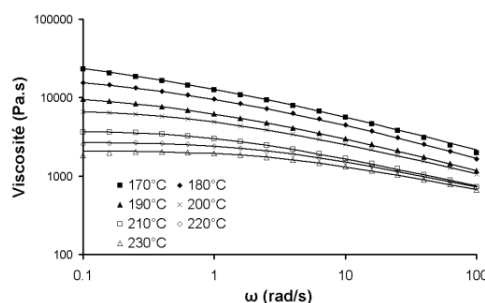


Figure 2.13: angle of clination–temperature.

The terminal relaxation time can be calculated as follows:

$$\tau_{relax} = \eta J_e^0 \quad (2.57)$$

where  $\tau_{relax}$  is the longest relaxation time in the relaxation time distribution,  $\eta$  is the shear viscosity [Pa.s] and  $J_e^0$  is the steady state shear compliance,

$$J_e^0 = \frac{1.798 M_e}{\rho R T} \quad (2.58)$$

$$\rho(T) = 1308.8 - 1.2(T - 273) \quad (2.59)$$

where  $M_e$ , the average molecular weight between entanglements, is equal 1980 g/mol for PA6 according to experimental data on mono-disperse system,  $\rho$  is the polymer density at temperature  $T[K]$ , and  $R$  is the constant of perfect gas [127]. The shear viscosity ( $\eta$ ) can be calculated as follows:

$$\eta(T) = \eta_0 \exp\left(\frac{E_a}{R} \left(\frac{1}{T} - \frac{1}{T_0}\right)\right) \quad (2.60)$$

where  $\eta_0$  is the initial viscosity at the temperature equal to  $T_0$  [128] and  $E_a$  is the activation energy, depending on the polymer's properties. The post condensation of solid polymer

particles induces the aging phenomenon and decreases the activation energy. The activation energy for the PA6 varies from 24.1  $kJ/mol$  to 105  $kJ/mol$ .

Tab. 2.2 shows the viscosity and relaxation time calculated by the Carreau-Yasuda model. Compared with Tab. 2.1 calculated by the Cole-Cole model, the relaxation time is in the same order of magnitude.

Table 2.2: Terminal relaxation time obtained from the Carreau-Yasuda representation for different temperatures [124].

Temperature( $^{\circ}C$ )	170	180	190	200	210	220	230
$\eta_0(Pa.s)$	50000	22313	12276	7269	3805	2726	2093
$\tau$	5.4	1.9	1.9	1.3	1.0	0.5	0.4

The surface tension of the PA6 is calculated by the following equation:

$$\Gamma = -0.0556 \times T + 40 \quad (2.61)$$

where  $T$  is the temperature ( $^{\circ}C$ ) and  $\Gamma$  is the surface tension ( $mN/m$ ).

### 2.4.3 Model of coalescence

Sintering results in melting, particles coalescence and air bubble escaping which form a process of compaction caused by heating or pressure and can happen in metals, ceramics, plastics and other materials. Above the melting temperature, the air diffuses through the particles' boundaries, while the particles coalesce together as a solid object [129]. The procedure of particles coalescence and the molten part densification is shown in Fig. 2.14.

A sintering process can be separated into three stages: the first stage of sintering is the connection necks forming between the particles. Polymeric particles are heated above the melting or glass transition temperature, they melt and adjacent particles are connected. This process is usually finished at the heating period, before the temperature decreases below the initial melting temperature. During this period, the polymer particles' interfacial energy is reduced more than 50 % because of the neck growing, other factors like pressure, density, particles size distribution and area of the free surface all influence this stage. The classical analytical models is based on the Newtonian flow assumption, where the work done by surface tension is opposed to the energy dissipated by viscous flow, and the effects of gravity and sintering shear rate are neglected [129]. At the second stage, the particles form stable periphery grain boundaries, and smaller grains are eliminated to form large grains with large pores. At this stage, the densification occurs with grains enlargement and fusion. When the porosity fall to smaller than 6 %, the sintering process is in the third stage. At the third stage, the material continues transporting for filing the pores, forcing the air inside the bubbles to diffuse in the polymers. This stage is really slow compared to the previous two stages [130].

The coalescence is the collective name for the first and second stages. The coalescence is a process that the two or more particles merge to form one large particle under partial molten situation, the schematic of coalescence process is shown in Fig. 2.15. The coalescence control factors include the polymer particle size, morphology of the particles, shear rate, volume fraction, viscosity ratio and the type of block co-polymer. Higher shear rate and lower viscosity promote the coalescence rate because they improve the flow ability of molten

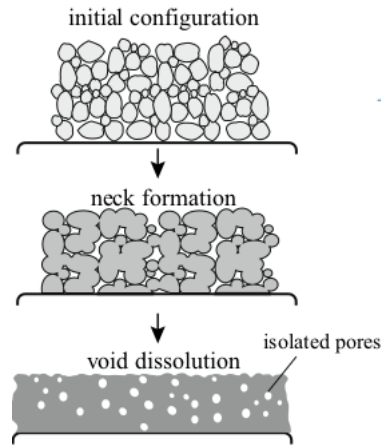


Figure 2.14: Two-dimensional scheme of the sintering process in a polymeric powder bed [129].

material, high mobility of polymer reduces the particles connection resistance. In addition, adding small copolymer is a good method for promoting the coalescence rate [131]. Different sintering stages can be represented by different the sintering models. We briefly review the classical viscous sintering models, including Frenkel's model [132], Cluster model [133] [134], and Mackenzie–Shuttleworth's model [135], which are used respectively in the first, second, and third stages. The general ideas are the following. First, the number of necks formed for each particle of mono-dispersed spheres varies from 3 to 8, the average number is equal to 5. Second, the sintering only happens on polymer effective surface. Third, the boundary for choosing a different model is not clear. If  $\rho_r > 0.96$ , we think the coalescence process is totally finished, all the pores are closed and the air inside can only escape by the diffusion in the powder bed.

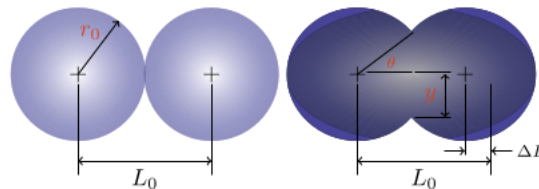


Figure 2.15: Schematic of coalescence of two spherical particles [93].

### Modified Frenkel's model

There are several models describing the viscous sintering of polymer particles. Frenkel [132] proposed an equation to describe how the surface tension and viscosity influence the coalescence of two particles at the initial stage of the sintering, this model is suitable for spherical particles [136] [52]. It is based on the energy balance between the work of surface tension and the viscosity dissipation, the shape of two merging particles is shown in Fig. 2.15. The initial distance between the particles is  $L_0$ , they have only one contact points and the distance between the particles decreases with the sintering .

The modified Frenkel's model describes the Newtonian sintering process (the first sintering process). During this process, the coalescence rate is affected by the material's surface tension and particle size [137]. The growth rate of connection neck length is calculated by the following equation:

$$r(t) = r_0 \left( \frac{4}{(1 + \cos(\theta(t)))^2 (2 - \cos(\theta(t)))} \right)^{\frac{1}{3}} \quad (2.62)$$

where  $r(t)$  is the particle radius and  $\theta(t)$  is the sintering angle. The total particles' surface change with sintering angle is the following

$$S = 4\pi r^2(1 + \cos \theta) = \frac{8\pi r_0^2 2^{\frac{1}{3}}}{(1 + \cos \theta)^{\frac{1}{3}}(2 - \cos \theta)^{\frac{2}{3}}} \quad (2.63)$$

The work done by surface tension,  $W_s$ , depends on the rate of surface reduction. It is calculated as follows:

$$W_s = -\Gamma \frac{dS}{dt} \quad (2.64)$$

where  $\Gamma$  is the coefficient of surface tension and  $S$  is the surface of the sintering particles. For considering the particle radius change with times, the rate of surface reduction is corrected as follows:

$$W_s = \Gamma \frac{8\pi a_0^2 2^{\frac{1}{3}} \cos \theta \sin \theta}{(1 + \cos \theta)^{\frac{4}{3}}(2 - \cos \theta)^{\frac{5}{3}}} \theta' \quad (2.65)$$

The dissipated energy during the sintering process is equal to the work of viscous force  $W_v$ , which is defined as:

$$W_v = 32\pi r_0^3 \eta \frac{1 - \cos(\theta)}{(1 + \cos \theta)(2 - \cos \theta)^2} (\theta')^2 \quad (2.66)$$

According Frankel's theory, the surface energy ( $W_s$ ) reduction is equal to the viscosity dissipation ( $W_v$ ) rate during in surface deformation process. The  $\theta'$  is always positive, by equating the work of surface tension to the viscous dissipation, the transform equation can be expressed as follows:

$$\theta' = \frac{d\theta}{dt} = \frac{\Gamma}{r_0} \frac{2^{-\frac{5}{3}} \cos \theta \sin \theta (2 - \cos \theta)^{1/3}}{\eta (1 - \cos \theta)(1 + \cos \theta)^{1/3}} \quad (2.67)$$

$$\sin(\theta) = x/r \quad (2.68)$$

The  $x$  is the neck radius,  $\Gamma$  and  $\eta$  are surface tension and viscosity of the polymer respectively. When the laser melts the polymer grains, the melted neighboring particles will form a neck between them, driven by surface tension, these particles merge into one particle gradually. For a smaller angles with  $\theta$  approach to 0,  $\sin(\theta) = \theta$ , and  $\cos(\theta) = 1 - \theta^2/2$ , and  $\theta(0)$  is 0 at the initial condition.

Based on the Frenkel's and Eshelby's model which use viscosity to describe the coalescence angles evolution in a sintering process, the following non-linear differential equation is obtained for viscoelastic fluids according to the balance of energy dissipation:

$$8(\wedge \tau_1 k_1 \frac{\partial \theta}{\partial t})^2 + (2 \wedge \tau_1 k_1 + \frac{\eta r_0 k_1^2}{\Gamma k_2}) \frac{\partial \theta}{\partial t} - 1 = 0 \quad (2.69)$$

$$k_1 = \frac{\sin \theta}{(1 + \cos \theta)(2 - \cos \theta)} \quad (2.70)$$

$$k_2 = \frac{2^{-\frac{5}{3}} \cos \theta \sin \theta}{(1 + \cos \theta)^{\frac{4}{3}}(2 - \cos \theta)^{\frac{5}{3}}} \quad (2.71)$$

where  $\theta$  is the angle between two particles,  $\Gamma$  is surface tension,  $\eta$  is viscosity of the polymer and  $r_0$  is the radius of the grains. The initial condition of  $\theta$  is an asymptotic approximation for 0,  $\Lambda$  is the Maxwell model constant that can be equal to -1, 1, or 0, and the value of  $\Lambda$  corresponds to the upper, lower and co-rotational derivatives, respectively. Then,  $(\theta^2)'$  is obtained by the following equation known as Bellehumeur's Law:

$$\frac{d(\theta^2)}{dt} = \frac{-\Lambda \tau_1 - 2\frac{\eta r_0}{\Gamma} + [(3\Lambda \tau_1)^2 + 4\Lambda \tau_1 \frac{\eta r_0}{\Gamma} + 4(\frac{\eta r_0}{\Gamma})^2]^{\frac{1}{2}}}{2(\Lambda \tau_1)^2} \quad (2.72)$$

During this stage, the porosity evolution connects to the coalescence angle  $\theta$ , which was calculated by Scherer et al. [138]. They also proposed a simplified assumption that connected the neck growing based on Frenkel's viscous model:

$$\left(\frac{x}{2r}\right)^2 = \frac{3W_s t}{8\eta_t r} \quad (2.73)$$

where  $x$  and  $r$  are respectively the neck radius and the radius of the particles,  $\eta_t$  is the viscosity at the time  $t$ , and  $W_s$  is surface energy.

The distance between the centers of the spheres can be related to the neck growth  $x$  for better describing the evolution about the shape of the neck:

$$\left(\frac{x}{2r}\right)^2 = \frac{\Delta L}{L_0} \quad (2.74)$$

where  $L(t)$  is the distance between the centers of spheres,  $L_0 = 2r$ , and  $\Delta L = L_0 - L(t)$  that can be seen as the linear shrinkage after the sintering. This approximation is only valid for the beginning of the sintering.

Scherer [138] makes a connection between the melting part's densification and the sintering process using the modified Frenkel's model. Under the condition that the number of pores per unit solid volume is one pore per unit cell, the number of pores ( $n$ ) is calculated by  $n = (L_0^3 \rho_0 / \rho)^{-1}$ . The powder bed's density evolution can be simplified by the shrinkage length with Scherer's model:

$$\frac{\Delta L}{L_0} = 1 - \left(\frac{\rho_0}{\rho}\right)^{\frac{1}{3}} \quad (2.75)$$

with  $\rho = 1 - \varphi$ ,  $\rho_0 = 1 - \varphi_0$  and  $\sin(\theta) = x/r$ , the equation 2.75 can be described as follows:

$$\varphi(t) = 1 - \frac{1 - \varphi_0}{\left[1 - \left(\frac{\sin \theta(t)}{2}\right)^2\right]^3} \quad (2.76)$$

$\varphi_0$  and  $\varphi(t)$  are the initial porosity and the porosity at time  $t$  of the powder bed. This equation is derived for a linear arrangement of particles, the volume shrinkage can be calculated by Eq. (2.76). As each particle usually has 3 to 8 neighbors, it develops an average of 5 sintering necks in the process.

By now, how the neck forming process in the first sintering stage affects the porosity evolution is presented. This model uses a simple method to analyze the coalescence change rate, and particle radius change driven by the viscosity of polymer spheres. This model describes the isotropic sintering of mono-dispersed spherical particles and suitable for the first and second stages of the sintering ( $\rho < 0.96$ ).

## MS model

Mackenzie and Shuttleworth developed an elegant model [139] [135] for simulating the shrinkage of spherical bubbles in a viscous matrix, which is used in higher relative density situations ( $\rho > 0.96$ ). At this stage, the adjacent particles touch each other, and the closed pores are full of the air trapped in the melted region, the escaping rate for this trapped air is very slow. Therefore, densification evolution in this sintering stage is slow, the densification rate is described by Mackenzie–Shuttleworth (MS) sintering model. In this model, the surface tension and the viscosity of the melted parts are two major factors:

$$\frac{d\varphi}{dt} = \frac{-3\Gamma}{2r_0\eta}\varphi \quad (2.77)$$

where the  $r_0$  is the initial radius of the pores,  $\Gamma$  is surface tension and  $\eta$  is viscosity of the polymer respectively. Actually, we approximated the pore radius,  $r(t)$ , by the constant  $r_0$ , while the pore number remains fixed. This approximation slightly underestimates the actual sintering kinetics in the latest stages.

## The clusters model

The coalescence speed is different for polymer particles, the smaller particles may be sintered rapidly and clustered preferentially in the open spaces left by larger particles. The larger ones may be delayed towards the end of the process. The MS and Frenkel's models can not accurately describe the sintering process of pressed compaction of irregular-shaped polymer particles. Therefore, the Cluster model is introduced to analyse the sintering kinetics and assessing the pores size evolution during the SLS process [133] [134] [140]. The sintering rate depends on the volume fraction of particles ( $f_r$ ), and the densification kinetics controlled by temperature is expressed as follows:

$$\rho(t) = \frac{\sum_r [\rho_F(r, t)\xi_r\theta_F(t_{0.8} - t) + \rho_{MS}(r, t)\theta_F(t - t_{0.8})]f_r}{\sum_r [\xi_r\theta_{MS}(t_{0.8} - t) + (r, t)\theta_{MS}(t - t_{0.8})]f_r}$$

This equation shows the density for each cluster that has different particle size changes with time  $t$ . In the initial stage of the sintering, under the condition of  $\rho(r, t) 0.8$ ,  $\rho(r, t)$  is calculated following the Frenkel model, while  $\rho(r, t) = \rho_F(r, t)$ ,  $\theta_F$  is equal to 1 and  $\theta_{MS}$  is equal to 1. In the final sintering stage, under the condition of  $\rho(r, t) 0.8$ , the  $\rho(r, t)$  is calculated following the Mackenzie and Shuttleworth model, while  $\rho(r, t) = \rho_{ML}(r, t)$ ,  $\theta_{MS}$  is equal to 1 and the  $\theta_F$  is equal to 1. For each cluster,  $\xi_r$  is a normalized overall average of the number of necks forming ability of each particle size  $r$ , the empirical expression is  $\xi_r = 1/r^c$  and the coefficient  $c$  is depending on the particle size distribution, which is usually equal to 1 in fabricating polymer materials. Eq. (2.4.3) can be explicitly written as follows ( $\xi_r = 1$  corresponds to a narrow particle size distribution):

$$\rho(t) = \sum_r \left\{ \frac{\rho_0}{\rho_g \left[ 1 - \frac{3W_s t}{8\eta t r} \right]^3} \theta(t_{0.8} - t) + \theta(t - t_{0.8}) \left[ 1 - \left( 1 - \frac{\rho_0}{\rho} \right) \exp(-3W_s t 2r_0 \eta t r) \right] \right\} f_r \quad (2.78)$$

where  $f_r$  is the volume fraction with the radius  $r$  and  $r_0$  is the particles' radius in the initial MS process.

## 2.5 Modeling of crystallization

Non-isothermal crystallization takes place under cooling condition due to the thermal exchange between the environment and polymer. The crystallization process is a combination of nucleation with growth. During a crystallization process, the crystallization heat  $S_c$  can be calculated by the following equation [119]:

$$S_C = \rho_{ps} \frac{\partial \alpha}{\partial t} \delta H_c \quad (2.79)$$

where  $\delta H_c$  represents the crystallization enthalpy and  $\alpha$  represents the crystallization rate.

The non-isothermal crystallization rate is computed according to Nakamura's expression, the crystallization kinetics theories are described by the evolution of crystallization rate ( $\alpha$ ) as a function of temperature ( $T$ ):

$$\frac{\partial \alpha}{\partial t} = nK(T)(1 - \varphi) \left[ \ln\left(\frac{1}{1 - \varphi}\right) \right]^{\frac{n-1}{n}} \quad (2.80)$$

where  $n$ , the Avrami index, depends on the geometry of crystalline and  $K(T)$ , the non-isothermal nucleation rate, is obtained by Hoffman-Loritzen's theory:

$$K(T) = \ln(2)^{\frac{1}{n}} K_0 \exp\left(\frac{-U}{R(T - T_{|\infty})}\right) \exp\left(\frac{-K_G(T + T_0)}{2T^2 \Delta T}\right) \quad (2.81)$$

where  $K_0$  is a temperature-independent constant,  $U$  is the activation energy of the crystallization transformation which takes the universal value of  $6270 \text{ J/mol}$ ,  $T_G$  is the glass transition temperature,

$$T_{|\infty} = T_G - 30K$$

corresponds the end temperature of crystallization,  $K_G$  is a constant related to the nucleation characteristics and  $R$  is the ideal gas constant ( $R = 8.314 \text{ J/mol/K}$ ).

Crystallization occurs only in the liquid part of the polymer. The physical properties of the crystallizing liquid part like density, heat capacity, and thermal conductivity are calculated, according to the proportions of relative volume fraction [141] [142], as follows:

$$\rho_{pc} = \alpha \rho_{ps} + (1 - \alpha) \rho_{pl} \quad (2.82)$$

$$(C_p)_{pc} = [\alpha \rho_{ps} (C_p)_{ps} + (1 - \alpha) \rho_{pl} (C_p)_{pl}] / \rho_{pc} \quad (2.83)$$

$$\lambda_{pc} = \alpha \lambda_{ps} + (\alpha - 1) \lambda_{pl} \quad (2.84)$$

where  $pc$  signifies the crystallizing liquid part while  $ps$  and  $pl$  indicate solid and liquid phases in the crystallizing liquid part. Note that, to recover the global thermo-physical properties of the polymer bed during a crystallization process,  $\rho_{pc}$ ,  $(C_p)_{pc}$  and  $\lambda_{pc}$  must be used instead of  $\rho_{pl}$ ,  $(C_p)_{pl}$  and  $\lambda_{pl}$  while  $f_l$  should be frozen.

If the material is prepared to incorporate two types of polymers or with the two-stage crystallization, the isothermal crystallization kinetics follows the two-stage crystallization model by using the modified Hillier model [143] [144]. The primary crystallization is expressed as:

$$\alpha_1(t) = 1 - \exp(-K_1 t^{n_1}) \quad (2.85)$$

The secondary crystallization process is expressed as:

$$\alpha_2 = \int_0^t \alpha_1(\theta) \times \frac{d}{dt}(\alpha_2(t - \theta))d\theta \quad (2.86)$$

The total crystallization rate at time  $t$  is expressed as:

$$\alpha(t) = w_1\alpha_1(t) + w_2\alpha_2(t) \quad (2.87)$$

$$\alpha(t) = w_1[1 - \exp(K_1 t^{n_1})] + w_2 K_2 n_2 \int_0^t [1 - \exp(K_1 \theta^{n_1})] (t - \theta)^{n_2 - 1} \exp[-K_2 (t - \theta)^{n_2}] d\theta$$

where  $\alpha_1(t)$  and  $\alpha_2(t)$  are the rates of the primary and second crystallizations at time  $t$  expressed by Avrami model.  $w_1 + w_2 = 1$  indicates that the crystallization rate at the infinite time is unity.

## 2.6 SLS process modeling and numerical methods

The previous sections introduced the mathematical equations (heat equation and boundary conditions), laser shapes, laser-polymer powder interaction, and modeling of multi-physical phenomena involved in a SLS process. In the present modeling work, we choose the Gaussian-type as the laser initial shape, a scattering model for laser-polymer powder interaction by using the modified Monte-Carlo method and Mie theories, parallel models for bed's density and specific heat, Maxwell model and Hailton and Crosser's model for thermal conductivity according to the medium density, Voller's approach for the melting process, Frenkel's model and Mackenzie and Shuttleworth's model for the coalescence process and Nakamura's model for the crystallization process.

Flowchart of the SLS modeling is shown in Fig. 2.16. The heat source from the laser beam is either the BL model or the scattering model provided by the modified Monte-Carlo method and Mie theories. The melting latent heat when the laser heats the powder is calculated by liquid volume fraction. After melting the polymer particles, the fluidity of liquid materials promotes particles merging (coalescence). After the heating phase by laser the part is cooled down and with temperature decreasing the crystallization process takes place.

To simulate the transient phenomena during a SLS process, appropriate time and spatial discrete schemes are necessary. A fixed Cartesian grid is used for all the quantities and it is formed by control volumes (Fig. 2.17, for example). The transient heat equation is discretized in space by using the finite volume methods (FVM), energy balance is assured by the heat fluxes on the surfaces of a control volume and finally surface heat fluxes are discretized by a second-order central-difference scheme.

We integrate Eq. (2.1) in space over a control volume  $\Omega_{cv}$  with  $Q_f = -\rho_l L \frac{\partial f_l}{\partial t}$  and  $Q_c = \rho_{sc} h_c \frac{\partial \alpha_c}{\partial t}$  and have:

$$\int_{\Omega_{cv}} \rho(T) C_p(T) \frac{\partial T}{\partial t} d\Omega = \int_{\Omega_{cv}} \nabla \cdot (\lambda \nabla T) d\Omega + \int_{\Omega_{cv}} Q d\Omega - \int_{\Omega_{cv}} \rho_l L \frac{\partial f_l}{\partial t} d\Omega + \int_{\Omega_{cv}} \rho_{sc} h_c \frac{\partial \alpha_c}{\partial t} d\Omega \quad (2.88)$$

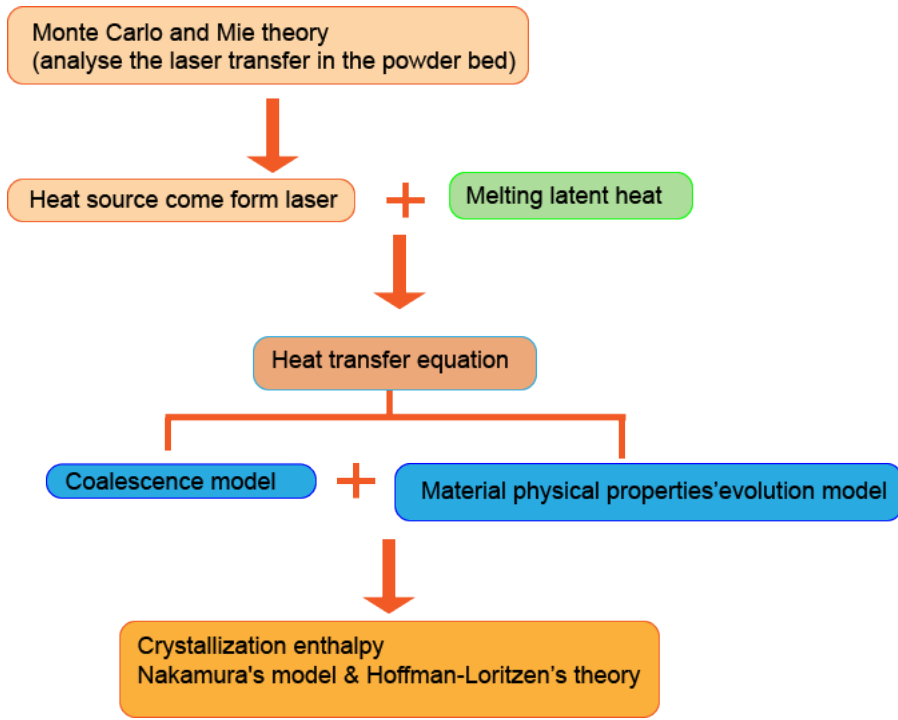


Figure 2.16: Flowchart of SLS simulation.

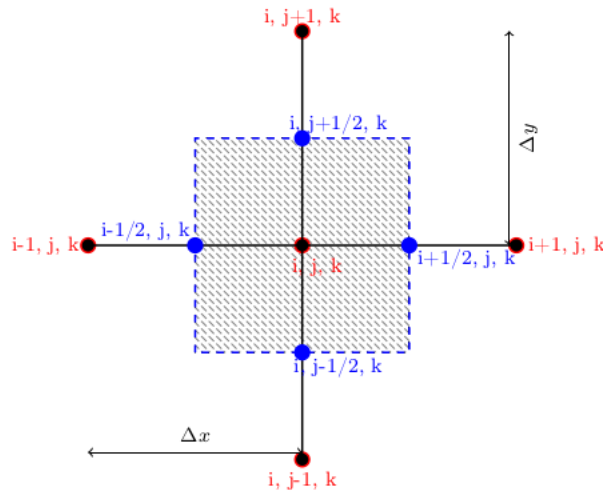


Figure 2.17: A example of one 2D section of a 3D control volume.

Given the volume,  $\Delta x \Delta y \Delta z$ , and the index,  $(i, j, k)$ , of  $\Omega_{cv}$ , the Gauss theorem leads to:

$$\begin{aligned}
 \rho_{i,j,k} (C_p)_{i,j,k} \frac{\partial T}{\partial t} \Big|_{i,j,k} \Delta x \Delta y \Delta z &= (\lambda \frac{\partial T}{\partial x})_{i-1/2,j,k}^{i+1/2,j,k} \Delta y \Delta z + (\lambda \frac{\partial T}{\partial y})_{i,j-1/2,k}^{i,j+1/2,k} \Delta x \Delta z \\
 &+ (\lambda \frac{\partial T}{\partial z})_{i,j,k-1/2}^{i,j,k+1/2} \Delta x \Delta y + \hat{Q}_{i,j,k} (e^{-\beta_2 z_{k-1/2}} - e^{-\beta_2 z_{k+1/2}}) \Delta x \Delta y \\
 &- \rho_l L \frac{\partial f_l}{\partial t} \Big|_{i,j,k} \Delta x \Delta y \Delta z + (\rho_{sc})_{i,j,k} h_c \frac{\partial \alpha_c}{\partial t} \Big|_{i,j,k} \Delta x \Delta y \Delta z
 \end{aligned} \quad (2.89)$$

with  $Q = \beta_2 \hat{Q} e^{-\beta_2 z}$ .

We continue the temporal integration over the interval  $[t_n, t_{n+1}]$  and have

$$\begin{aligned} \int_{t_n}^{t_{n+1}} \rho_{i,j,k} (C_p)_{i,j,k} \frac{\partial T}{\partial t} \Big|_{i,j,k} dt &= \int_{t_n}^{t_{n+1}} (\lambda \frac{\partial T}{\partial x})_{i-1/2,j,k}^{i+1/2,j,k} \frac{1}{\Delta x} dt + \int_{t_n}^{t_{n+1}} (\lambda \frac{\partial T}{\partial y})_{i,j-1/2,k}^{i,j+1/2,k} \frac{1}{\Delta y} dt \\ &+ \int_{t_n}^{t_{n+1}} (\lambda \frac{\partial T}{\partial z})_{i,j,k-1/2}^{i,j,k+1/2} \frac{1}{\Delta z} dt + \int_{t_n}^{t_{n+1}} \hat{Q}_{i,j,k} (e^{-\beta_2 z_{k-1/2}} - e^{-\beta_2 z_{k+1/2}}) \frac{1}{\Delta z} dt \\ &- \int_{t_n}^{t_{n+1}} \rho_l L \frac{\partial f_l}{\partial t} \Big|_{i,j,k} dt + \int_{t_n}^{t_{n+1}} (\rho_{sc})_{i,j,k} h_c \frac{\partial \alpha_c}{\partial t} \Big|_{i,j,k} dt \end{aligned} \quad (2.90)$$

Applying rectangular rule for integration, we obtain the following equation:

$$\begin{aligned} \rho_{i,j,k}^{n+1/2} (C_p)_{i,j,k}^{n+1/2} \frac{T_{i,j,k}^{n+1} - T_{i,j,k}^n}{\Delta t} \Delta t &= \left[ (\lambda \frac{\partial T}{\partial x})_{i-1/2,j,k}^{i+1/2,j,k} \right]^{n+1/2} \frac{\Delta t}{\Delta x} + \left[ (\lambda \frac{\partial T}{\partial y})_{i,j-1/2,k}^{i,j+1/2,k} \right]^{n+1/2} \frac{\Delta t}{\Delta y} \\ &+ \left[ (\lambda \frac{\partial T}{\partial z})_{i,j,k-1/2}^{i,j,k+1/2} \right]^{n+1/2} \frac{\Delta t}{\Delta z} + \hat{Q}_{i,j,k}^{n+1/2} (e^{-\beta_2 z_{k-1/2}} - e^{-\beta_2 z_{k+1/2}}) \frac{\Delta t}{\Delta z} \\ &- \rho_l L \frac{(f_l)_{i,j,k}^{n+1} - (f_l)_{i,j,k}^n}{\Delta t} \Delta t + (\rho_{sc})_{i,j,k}^{n+1/2} h_c \frac{(\alpha_c)_{i,j,k}^{n+1} - (\alpha_c)_{i,j,k}^n}{\Delta t} \Delta t \end{aligned} \quad (2.91)$$

which, with  $A = \rho C_p$ ,  $\delta T = T^{n+1} - T^n$  and  $(T^{n+1/2} = (T^{n+1} + T^n)/2 = \delta T/2 + T^n)$ , can be written as:

$$\begin{aligned} \delta T_{i,j,k} &= \frac{\Delta t}{2A_{i,j,k}^{n+1/2} \Delta x} (\lambda^{n+1/2} \frac{\partial \delta T}{\partial x})_{i-1/2,j,k}^{i+1/2,j,k} + \frac{\Delta t}{2A_{i,j,k}^{n+1/2} \Delta y} (\lambda^{n+1/2} \frac{\partial \delta T}{\partial y})_{i,j-1/2,k}^{i,j+1/2,k} \\ &+ \frac{\Delta t}{2A_{i,j,k}^{n+1/2} \Delta z} (\lambda^{n+1/2} \frac{\partial \delta T}{\partial z})_{i,j,k-1/2}^{i,j,k+1/2} - \frac{\Delta t}{A_{i,j,k}^{n+1/2} \Delta x} (\lambda^{n+1/2} \frac{\partial T^n}{\partial x})_{i-1/2,j,k}^{i+1/2,j,k} \\ &- \frac{\Delta t}{A_{i,j,k}^{n+1/2} \Delta y} (\lambda^{n+1/2} \frac{\partial T^n}{\partial y})_{i,j-1/2,k}^{i,j+1/2,k} - \frac{\Delta t}{A_{i,j,k}^{n+1/2} \Delta z} (\lambda^{n+1/2} \frac{\partial T^n}{\partial z})_{i,j,k-1/2}^{i,j,k+1/2} \\ &+ \frac{\Delta t}{A_{i,j,k}^{n+1/2} \Delta z} \hat{Q}_{i,j,k}^{n+1/2} (e^{-\beta_2 z_{k-1/2}} - e^{-\beta_2 z_{k+1/2}}) \\ &- \frac{\rho_l L}{A_{i,j,k}^{n+1/2}} (f_l)_{i,j,k}^{n+1} - (f_l)_{i,j,k}^n + \frac{(\rho_{sc})_{i,j,k}^{n+1/2} h_c}{A_{i,j,k}^{n+1/2}} ((\alpha_c)_{i,j,k}^{n+1} - (\alpha_c)_{i,j,k}^n) \end{aligned} \quad (2.92)$$

with  $\delta T$  as unknown.

Alternative Direction Implicit (ADI) is used to decompose the above 3D problem into three groups of 1D problems as follows:

$$\begin{aligned} \left( 1 - \frac{\Delta t}{2A_{i,j,k}^{n+1/2} \Delta x} (\lambda^{n+1/2} \frac{\partial}{\partial x})_{i-1/2,j,k}^{i+1/2,j,k} \right) \left( 1 - \frac{\Delta t}{2A_{i,j,k}^{n+1/2} \Delta y} (\lambda^{n+1/2} \frac{\partial}{\partial y})_{i,j-1/2,k}^{i,j+1/2,k} \right) \\ \left( 1 - \frac{\Delta t}{2A_{i,j,k}^{n+1/2} \Delta z} (\lambda^{n+1/2} \frac{\partial}{\partial z})_{i,j,k-1/2}^{i,j,k+1/2} \right) \delta T = S_{\delta T} \end{aligned} \quad (2.93)$$

where

$$\begin{aligned} S_{\delta T} &= -\frac{\Delta t}{A_{i,j,k}^{n+1/2} \Delta x} (\lambda^{n+1/2} \frac{\partial T^n}{\partial x})_{i-1/2,j,k}^{i+1/2,j,k} - \frac{\Delta t}{A_{i,j,k}^{n+1/2} \Delta y} (\lambda^{n+1/2} \frac{\partial T^n}{\partial y})_{i,j-1/2,k}^{i,j+1/2,k} \\ &- \frac{\Delta t}{A_{i,j,k}^{n+1/2} \Delta z} (\lambda^{n+1/2} \frac{\partial T^n}{\partial z})_{i,j,k-1/2}^{i,j,k+1/2} + \frac{\Delta t}{A_{i,j,k}^{n+1/2} \Delta z} \hat{Q}_{i,j,k}^{n+1/2} (e^{-\beta_2 z_{k-1/2}} - e^{-\beta_2 z_{k+1/2}}) \\ &- \frac{\rho_l L}{A_{i,j,k}^{n+1/2}} (f_l)_{i,j,k}^{n+1} - (f_l)_{i,j,k}^n + \frac{(\rho_{sc})_{i,j,k}^{n+1/2} h_c}{A_{i,j,k}^{n+1/2}} ((\alpha_c)_{i,j,k}^{n+1} - (\alpha_c)_{i,j,k}^n) \end{aligned}$$

Due to the fact that  $\delta T \sim \mathcal{O}(\cdot \perp)$ , the ADI treatment preserves the second-order accuracy of the semi-implicit scheme.

Temperature gradient appeared in Eq. (2.93) and the corresponding boundary conditions can be discretized by a second-order central scheme, for example  $(\frac{\partial T^n}{\partial z})_{i,j,k-1/2} = \frac{T^n_{i,j,k} - T^n_{i,j,k-1}}{\Delta z}$  and  $(\frac{\partial T^n}{\partial x})_{i+1/2,j,k} = \frac{T^n_{i+1,j,k} - T^n_{i,j,k}}{\Delta x}$ . The central-differencing scheme results in tri-diagonal matrices in one spatial direction. Thomas Algorithm is used to solve the tri-diagonal systems: to solve discretized Eq. (2.93) it is applied first in  $x$  direction, then in  $y$  direction and finally in  $z$  direction. This allows to obtain  $\delta T$  and  $T^{n+1} = T^n + \delta T$ .

Due to the fact that Eq. (2.93) is nonlinear,  $f^{n+1/2}$ , for any field  $f$  representing  $\rho$ ,  $C_p$ ,  $\lambda$ , and  $\rho_{sc}$ ,  $f_l^{n+1}$  and  $(\alpha_c)^{n+1}$  depend on the solution to be found ( $\delta T$  or  $T^{n+1}$ ). In practice, we can either use iterative methods or take advantage of extrapolation method to extrapolate temperature to  $t_{n+1/2}$  ( $\tilde{T}^{n+1/2} = (3T^n - T^{n-1})/2$ ) and  $t_{n+1}$  ( $\tilde{T}^{n+1} = 2T^n - T^{n-1}$ ). Extrapolated temperature is used to estimate  $f^{n+1/2}$ ,  $(f_l)^{n+1}$  and  $(\alpha_c)^{n+1}$ . Note that using extrapolation method Eq. (2.93) is solved only once per time-step while using iterative methods Eq. (2.93) is solved per time-step several times to reach the convergence condition. Obviously the first choice enhances computational efficiency and the second one stresses the stability of the time scheme.

As far as is concerned the liquid volume fraction,  $f_l$  is related to temperature either by a linear or by a nonlinear function. As the melting latent heat term containing  $f_l$  increases diagonal dominance,  $(f_l)^{n+1}$  can be integrated into the matrix instead of staying at the rhs especially when iterative methods are used to solve the problem. We can also write  $(f_l)^{n+1} = (f_l)^n + \delta f_l$ . Using Taylor series,  $\delta f_l$  is related to  $\delta T$  and integrated into the matrix diagonal.

The shrinkage is calculated according to the mass conservation. At each time step  $n + 1$ , the actual volume occupied in each finite volume is updated based on the the ratio of the local densities. The filling rate ( $\Omega$ ) in each calculated volume is calculated as follows:

$$\Omega^{n+1} = \frac{\rho^n}{\rho^{n+1}} \Omega^n \quad (2.94)$$

If  $\Omega^{n+1} < 1$ , it is adjusted to 1 by bringing polymer from the upper neighbouring finite volume. Therefore, this approach considers only the downward movement of polymer bed.

Crystallization process occurs later in the SLS processes.  $(\alpha_c)^{n+1}$  is treated iteratively and left at the rhs.

The last model of the multiphysical phenomena that needs to be solved is the coalescence model which can be cast into a classical ODE. A higher order time scheme is necessary to simulate the coalescence kinetics: a 3rd-order Runge-Kutta scheme was used in the past and is kept in the present work.

# Chapter 3

## Scattering in laser-polymer powder interaction

### Contents

---

<b>3.1</b>	<b>Working configurations . . . . .</b>	<b>58</b>
<b>3.2</b>	<b>Models of laser-polymer powder interaction . . . . .</b>	<b>59</b>
3.2.1	Beer-Lambert (unscattering) model . . . . .	59
3.2.2	Monte-Carlo scattering model . . . . .	61
<b>3.3</b>	<b>Comparison between the BL law and the scattering model .</b>	<b>63</b>
<b>3.4</b>	<b>Parametric analysis of scattering effects . . . . .</b>	<b>65</b>
3.4.1	Influence of anisotropy factor $g$ . . . . .	65
3.4.2	Influence of powder bed porosity and particle size . . . . .	67
<b>3.5</b>	<b>Temperature distribution . . . . .</b>	<b>69</b>
<b>3.6</b>	<b>Dimension of the parts . . . . .</b>	<b>74</b>
3.6.1	SLS process with PA6 . . . . .	74
3.6.2	SLS process with PA12 . . . . .	77
<b>3.7</b>	<b>Summary . . . . .</b>	<b>78</b>

---

In this chapter, thermal transmission of laser power in a bed of polymer particles is investigated through numerical simulations. In the literature Beer-Lambert model which does not consider scattering is used most of the times to represent the thermal transmission of laser power in a powder bed. In terms of polymer particles, scattering can be an important phenomenon because most of polymers are semi-transparent with respect to the lasers used in SLS. Therefore, scattering needs to be considered in the laser-powder interaction model.

To simulate the scattering phenomenon, the modified Monte-Carlo method and Mie-scattering theory which have been detailed in the last chapter are used. The numerical results obtained concern the spatial distribution of the laser power absorbed by the powder bed for the cases with and without scattering. Comparison between the results obtained with and without scattering will be performed to illustrate the effects of scattering. As there is no experimental result on the spatial distribution of the absorbed laser power, the numerical results obtained can not be validated directly neither with nor without scattering, which is not satisfying. To qualify and even validate them, the idea consists in using spatial distribution of the absorbed laser power, simulating an experimentally studied SLS process and comparing the corresponding experimental and numerical results. Unfortunately experimental results of polymer SLS are rare in the literature. We have to rely on both the rare results in the literature and our own experimental results on single-layer and single-sweep SLS processes.

This chapter is organized as follows, we first analyse how the scattering influences the laser transmission in the powder bed, compare the results obtained with the MC scattering modeling and Beer-Lambert modeling without scattering, analyse the effects of the scattering and how the laser power and laser moving speed influence thermal behavior and molten pool dimension, and make a comparison between experiments and simulations to assess the numerical approach.

### 3.1 Working configurations

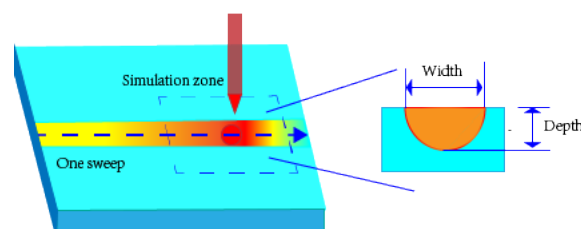


Figure 3.1: Schematic of the laser scanning path and the molten zone. Temperature at the surface of the molten zone and the geometry of the manufactured part (the molten zone) are important and should be measured and used to qualify and validate numerical predictions.

In a SLS process, the molten polymers bond together to form a new part, and the bonding degree depends on the thermo-physical properties of the polymer and the process conditions. As is illustrated by Fig. 3.1, the geometry of the manufactured part depends on

the properties of the polymer powder bed and the process parameters. A comparison of the numerical results of the part geometry with the measurements allows to qualify and validate the modeling approach. Among the rare experimental studies, the work on PA12 performed by Riedlbauer *et al* [145] was chosen for this purpose in the previous study [93] and is also used in the present work. We choose the simplest process configurations with single-laser-path for a single layer.

As there need experimental results, we also set up an experimental bench: the ProMaker P1000 machine is used to carry out single-laser-path SLS experiments with a laser moving speed of  $3.5 \text{ m/s}$  and a laser power in the range from  $13 \text{ W}$  to  $15 \text{ W}$ , the preheating temperature is  $471 \pm 7 \text{ K}$ , commercial PA6 powder (Sinterline-6) is used, and the particles' size distribution is between  $10 \text{ }\mu\text{m}$  to  $120 \text{ }\mu\text{m}$  (the averaged size is about  $60 \text{ }\mu\text{m}$ ). During the experiments, time evolution of the temperature at the powder surface is measured by an IR camera (Cedip-TITANIUM Series). The samples fabricated with single-laser-path for a single layer are inspected under Ztereo Microscope (Zeiss Stemi SV6, see Fig. 3.2) and pictured by a camera. The dimensions of the samples are measured by the Vernier calipers.



Figure 3.2: Ztereo Microscope

The thermal physical characteristics of polymer (PA6) are summarized in Tab. 3.1. The process conditions, characteristics of powder bed and the laser parameters are shown in Tab. 3.2.

As far as is concerned the work on PA12 performed by Riedlbauer *et al* [145], the inputs used will be provided in the corresponding section because PA6 will be used to show the effects of scattering.

## 3.2 Models of laser-polymer powder interaction

### 3.2.1 Beer-Lambert (unscattering) model

The laser source, the driving force for fusion of the polymer material in SLS process, follows in the cases without scattering a Gaussian relationship which is exponentially decayed in the depth direction, and is described by the Beer-Lambert (BL) law [99]. In terms of the transmitted power, the Beer-Lambert law of a laser beam is the following:

$$q = \beta_2(1 - R_e)Ie^{-\beta_2 z} \quad (3.1)$$

Table 3.1: Properties of PA6 powder bed.

Characteristics	Values
Initial melting temperature [K]	471
Final melting temperature [K]	487
Enthalpy of fusion [J/kg]	115000
Density of the gas [kg/m <sup>3</sup> ]	0.739
Density of solid polymer [kg/m <sup>3</sup> ]	700
Density of liquid polymer [kg/m <sup>3</sup> ]	1020 - 1.2 × T (°C)
Heat capacity of the air [J/kg]	1049
Heat capacity of the solid polymer [J/kg]	812 + 5.3 × T (°C)
Heat capacity of liquid polymer [J/kg]	2650
Heat conductive of air [W/m K]	0.033
Heat conductive of solid polymer [W/m K]	0.28
Heat conductive of liquid polymer [W/m K]	0.24

Table 3.2: Process parameters using PA6.

Characteristics	Values
Relative density of the powder bed	0.7
Porosity rate of the powder bed	0.3
Averaged radius of the grains [μm]	30
Anisotropy factor, <i>g</i>	0.93
Absorption coefficient	0.96
Attenuation coefficient in BL methods( $\beta_2$ )	7500
Total attenuation coefficient of polymer particles ( $\beta$ )	17000
Diameter of the laser beam [μm]	450
Laser power [W]	15,14,13
Laser moving speed [m/s]	3.5
Thickness of the initial powder layer [μm]	60
Preheating temperature [K]	465
Ambient temperature [K]	465

$$I = \frac{nP}{\pi w^2} e^{-\frac{2r^2}{w^2}} \quad (3.2)$$

where  $q$  (W/m<sup>2</sup>) is the transmitted laser power,  $\beta_2$  is the attenuation coefficient used in the BL law, equal to 7500 m<sup>-1</sup>,  $R_e$  is the reflection coefficient of the polymer powder bed, equal to 4 % normally,  $n$  is a factor equal to 2,  $P$  is the power of laser,  $r$  is the radial distance from the laser axis, and  $w = r_{laser}/1.5$ , and  $r_{laser}$  is the radius of laser beam. Note that the absorbed power appearing in the heat equation,  $Q$ , takes the form of  $-\frac{dq}{dz}$ .

Peyre et al. [146] simulated the thermal evolution in time and predicted the fusion depths by using FEM (finite element methods). They used Beer-Lambert law for heat deposit with a suitable PA6 attenuation coefficient (7500 m<sup>-1</sup>) determined by experiment, simulated the thermal profile and predicted the fusion depths for several SLS processing conditions. The corresponding numerical results were compared with the experimental results. In their simulations, they assumed that only 40 % of laser power is absorbed by the polymer powders and that nearly 60 % of laser light is reflected or diffused in the powder bed. However, the efficiency of CO<sub>2</sub> laser absorbed by PA and PEEK powders are higher than 95 % [99]. This could be why the comparison of the thermal profiles was not very successful. At the same time the discrepancy raises also concern that Beer-Lambert's law is not sufficient to reflect

the laser transmission in the powder beds.

### 3.2.2 Monte-Carlo scattering model

The modified Monte-Carlo ray-tracing method is used to retrace the paths of photons transport within the powder bed formed by polymer particles. The light photons inside the powders go through scattering, absorbing and reflection, as shown in Fig. 3.3. The absorption part is calculated following the Beer-Lambert absorption principle, the attenuation rate is decided by the attenuation coefficient and the absorption lengths. The scattering part follows the Mie scattering theory, and the reflection part follows the Fresnel principle [38], [103], [104].

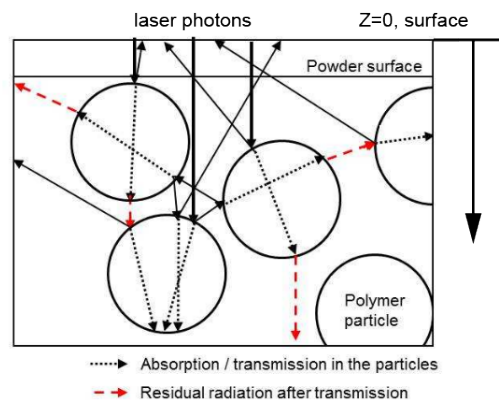


Figure 3.3: Schematic behaviour of laser photons in a powder bed [43].

Laumer et al. [108] measured the reflectance, transmittance, and absorptance of a  $CO_2$  laser radiation in PA solid foils and powders of the same thickness. The values of reflectance, transmittance, and absorptance obtained are equal to 0.05, 0.2, and 0.75 respectively in a PA12 foil of thickness  $200 \mu m$ . Concerning a PA12 powder bed of the same thickness, the laser reflectance is equal to 0.06, similar to a PA12 foil, the transmittance decreased considerably to 0.01, and the absorptance increased to 0.93 that is 1.24 times higher than in a PA12 foil. As the laser absorptance rate reflects the attenuation coefficient, it means that the attenuation rate of the particles is around 1.24 times bigger than in the solid polymer. The attenuation coefficient in PA12 bulk is  $13000 m^{-1}$  according to the experiment of Osmanic et al. [100], the attenuation coefficient of polymer particles,  $\beta$ , influenced by scattering and multi-reflections in a polymer powder bed is estimated to be equal to  $17000 m^{-1}$ . The attenuation coefficient belongs to polymers particles and it is not the attenuation coefficient of the powder bed. The attenuation coefficient of the powder bed will be obtained according to the modified Monte-Carlo method and the Mie theory. In the simulation, we assume the powder bed consists of polymer particles and the empty gas space, the laser is only absorbed by the polymer but not by air.

According to the modified Monte-Carlo method and the Mie theory introduced in Chapter 2, a photon of the laser beam travels, according to the travel direction and scattering theory, to a position and its energy is partly absorbed there. It repeats the travels until its energy is completely absorbed and its final position is saved and displayed. To study the laser power distribution in the polymer powder bed, we consider a laser's diameter of  $450 \mu m$ , a porosity of the powder bed of 0.3, a reflection coefficient of 0.04, and an averaged diameter of the powder of  $60 \mu m$ . It corresponds to the experimental working configuration we set up using PA6 powder. With scattering, the map of photons' final positions is displayed in Fig. 3.4

and it indicates the region in which the laser beam is absorbed. Quantitative results can be obtained by calculating the absorbed power in the powder bed.

In order to show quantitative results, the powder bed is divided into horizontal layers limited by  $z$  and  $z + \Delta z$  in the vertical direction and into rings limited by  $r$  and  $r + \Delta r$  in the radial direction. The absorbed power is calculated for each counting volume limited by  $[z : z + \Delta z]$  and  $[r : r + \Delta r]$ . Note that a counting volume is equal to  $\int_z^{z+\Delta z} \int_0^{2\pi} \int_r^{r+\Delta r} \tilde{r} d\tilde{r} d\theta d\tilde{z} = \pi[(r + \Delta r)^2 - r^2]\Delta z = \pi(2r + \Delta r)\Delta r\Delta z$  and increases linearly with  $r$ . In the case of the input laser power,  $P$ , equal to 15 W, the reflection rate equal to 4 %, and the initial powder bed porosity of 30 %, a counting volume is characterized by  $\Delta z = 10 \mu m$  and  $\Delta r = 22.5 \mu m$ . Fig. 3.5 displays with symbols the power absorbed by each counting volume in certain vertical layers. One can see that near the bed surface the maximum absorbed power occurs in the 6th counting volume and that with  $z$  increasing the maximum absorbed power moves to the 3rd counting volume. This suggests that two Gaussian distributions should be used for the data fitting of the absorbed laser power and that one of the two Gaussian distributions should depend on  $z$ . Inspired by the BL law, the following power distribution is proposed for data fitting:

$$Q = (1 - R_e) \left( \frac{nP}{\pi b^2} e^{-\frac{r^2}{b^2}} + \frac{(az + c)P}{\pi b^2} e^{-\frac{9r^2}{b^2}} \right) e^{-\beta_1 z} \beta_1 \quad (3.3)$$

where  $R_e$  is the reflection coefficient,  $P$  is the laser power,  $\beta_1$  ( $m^{-1}$ ) is the attenuation coefficient in the vertical direction of the powder bed,  $n$ ,  $a$  ( $m^{-1}$ ),  $b$  ( $m$ ), and  $c$  are the coefficients. The values of these parameters are obtained from a data fitting process. Eq. (3.3) is therefore the scattering model proposed for the absorbed power of the laser beam in the scattering case.

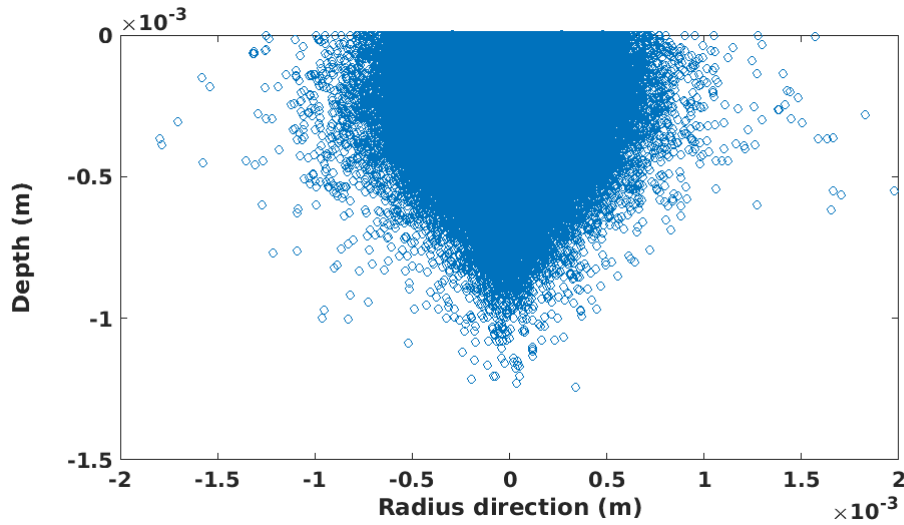


Figure 3.4: The schematic of laser photons travel paths distribution in the powder bed.

Eq. (3.3) is first integrated in a counting volume limited by  $z$  and  $z + \Delta z$  in the vertical direction and  $r$  and  $r + \Delta r$  in the radial direction. This gives rise to the absorbed power,  $(1 - R_e)P \{ n[e^{-r^2/b^2} - e^{-(r+\Delta r)^2/b^2}](e^{-\beta_1 z} - e^{-\beta_1(z+\Delta z)}) + [a(e^{-\beta_1 z} - e^{-\beta_1(z+\Delta z)})/\beta_1 + a(z e^{-\beta_1 z} - (z + \Delta z) e^{-\beta_1(z+\Delta z)}) + c(e^{-\beta_1 z} - e^{-\beta_1(z+\Delta z)})][e^{-9r^2/b^2} - e^{-9(r+\Delta r)^2/b^2}]/9 \}$ , corresponding to the symbols in Fig. 3.5. The least square fitting is then used to identify the parameters  $\beta_1$ ,  $a$ ,  $b$ ,  $c$  and  $n$  and allows to obtain  $\beta_1 = 11580 m^{-1}$ ,  $a = 9000 m^{-1}$ ,  $b = 2.5e - 4 m$ ,  $c = 1.068$  and  $n = 0.76$ . The absorbed power provided by the identified model is shown in curves in Fig. 3.5. The comparison between photons' statistical absorbed power and its identified analytical model displays only a small difference and indicates that the fitting equation, Eq. (3.3), could well represent the absorbed laser power in the powder bed in the cases with scattering.

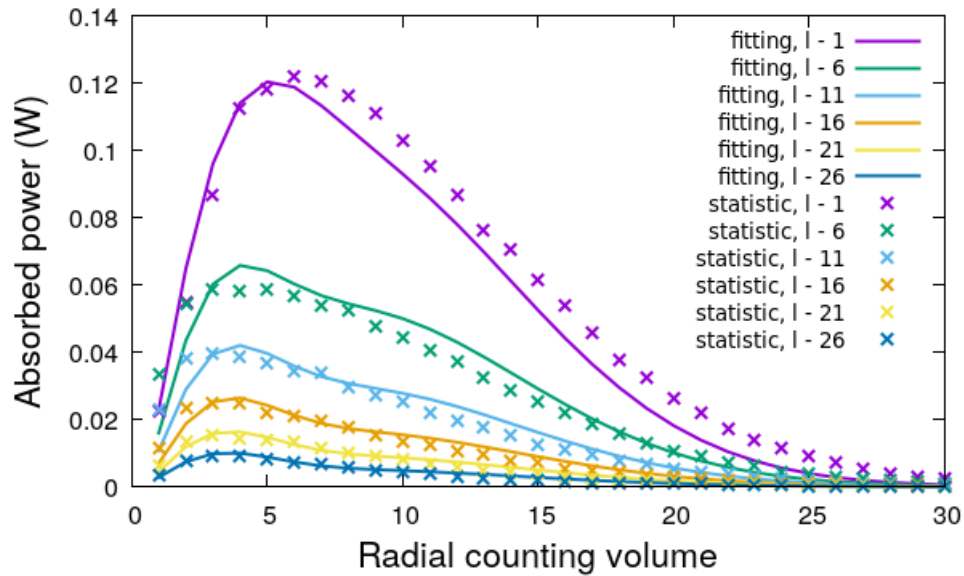


Figure 3.5: Comparison of the absorbed power between the counting results of the photons' scattered map and the identified analytical model for the counting volumes in different vertical layers.

### 3.3 Comparison between the BL law and the scattering model

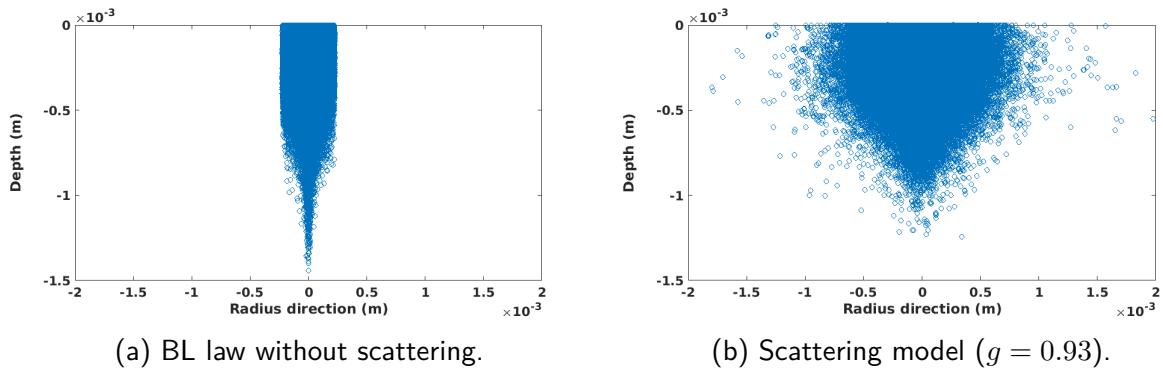


Figure 3.6: Photons' travel maps in the cases with and without scattering.

Fig. 3.6 presents the photons' propagation traces (final positions) in the powder bed. Fig. 3.6a shows the photons' map in the case without scattering: the anisotropy factor  $g$  is equal to 1, all the photons propagate forward and the reflection rate is equal to 0. Fig. 3.6b shows the photons' map in the scattering situation where the anisotropy factor  $g$  is equal to 0.93.

In the situation without scattering, the longest photon's travel distance in depth is about  $0.0015\text{ m}$  and the photons are concentrated inside the laser beam. While considering the scattering, the photons are spread out of the laser beam in the powder bed and the diameter of the influenced area is about three times the laser beam diameter. The travel distance in the depth direction is shorter in the case with scattering. These two figures reveal that scattering influences the laser photons' distribution in the powder bed in the following way: it enlarges the photons' influence area in the radial (horizontal) direction and decreases the influence

depth. This means that the energy of the laser beam is distributed in a much larger radial (horizontal) area and in a smaller vertical area than in the case of Beer-Lambert's law. This conclusion was already drawn in the work by X. Liu [39].

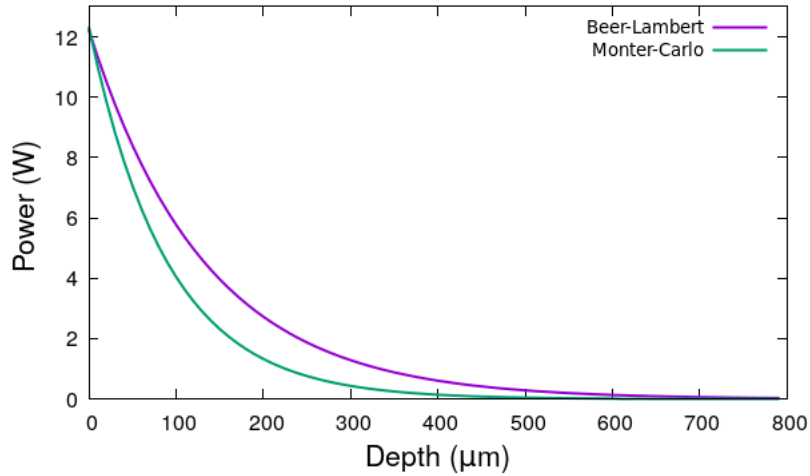


Figure 3.7: Transmitted power distribution in depth direction. Due to the absorption and scattering, the transmitted power is decayed from the surface to deeper positions.

To illustrate the effects of the scattering, the transmitted power in the depth direction is shown in Fig. 3.7: it is decayed from the surface to deeper positions. The attenuation coefficient is equal to  $9100 \text{ m}^{-1}$  in Beer-Lambert's law according to the simulation result shown in Fig. 3.6a. However, the attenuation coefficient increases to  $11580 \text{ m}^{-1}$  after considering scattering, the power decay rate is larger in the scattering case. The influential depth is around  $600 \mu\text{m}$  (60 layers) in the case of Beer-Lambert law, it is reduced to  $400 \mu\text{m}$  (40 layers) in the scattering case. The scattering forces the photons' travel directions to be deviated from forward, enlarges the photons' radial travel area, promotes the multiple backward and forward travels in a fixed thickness, increases the photons' absorption in the same thickness and hence decreases the influential thickness in the depth direction.

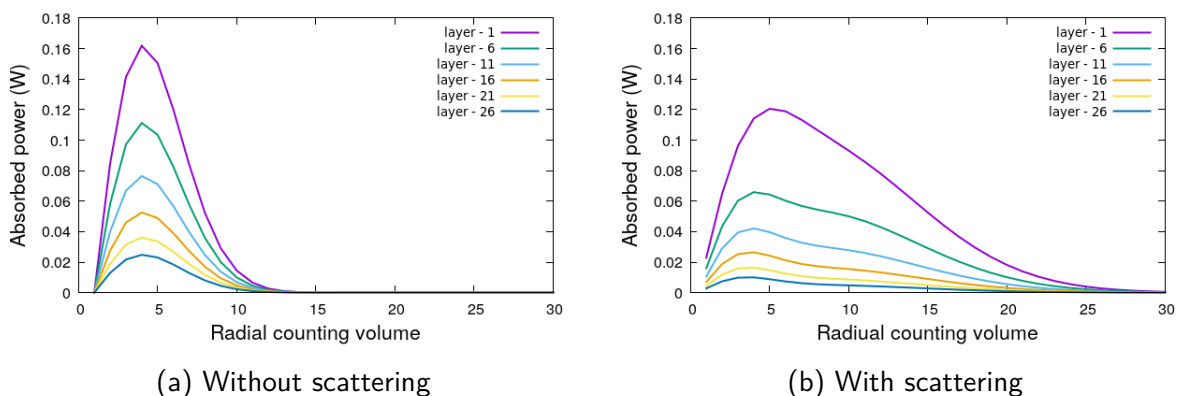


Figure 3.8: Absorbed laser power distribution in the powder bed in the cases with and without scattering: absorbed laser power by certain horizontal layers with respect to the radial counting volumes. Without scattering, the laser power is absorbed in a deeper vertical and smaller horizontal zone while with scattering it is absorbed in a larger horizontal but smaller vertical zone.

In order to make a detailed comparison and highlight the scattering phenomenon, the absorbed power in certain horizontal layers is shown as a function of the radial counting

volumes. The 2D absorbed laser intensity distribution with depths and optical radius are computed by the theoretical volumetric model based on Beer-Lambert law and modified Monte-Carlo method are shown in Fig. 3.8. It can be seen that the power absorption takes place in the ten first counting volumes in the case of Beer-Lambert's law while it occurs at least in the twenty first volumes in the scattering case. The maximum power absorption happens in the fourth counting volume for all the layers in the case without scattering while it shifts from the sixth counting volume near the bed surface to the third counting volume in the deep layers. Furthermore, for the same layer the maximum power absorption in the case of Beer-Lambert's law is more important than in the scattering case, for example in the first layer it is equal to  $0.16 W$  in the case of Beer-Lambert law against  $0.12 W$  in the scattering case. In terms of total absorption per layer, the case without scattering absorbs  $0.84 W$  in the first layer while the scattering case absorbs  $1.65 W$  (almost 2 times larger) because the photons' radial influential area is 1.5 times larger than laser beam radius.

## 3.4 Parametric analysis of scattering effects

### 3.4.1 Influence of anisotropy factor $g$

Table 3.3: The fitting coefficients change with anisotropy factor ( $g$ ).

anistropy factor ( $g$ )	0.9	0.8	0.6
n	0.76	0.735	0.76
a	9000	2835	-2573
b	2.5e-4	2.55e-4	2.57e-4
c	1.068	1.215	1.168
$\beta$	11580	12900	14870

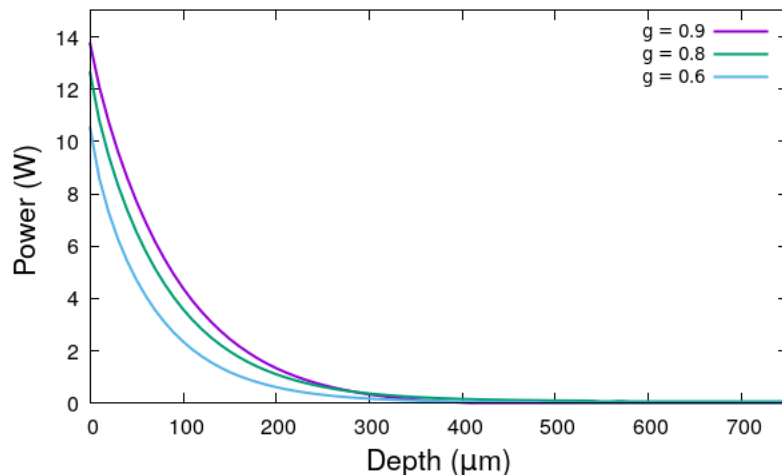


Figure 3.9: Laser power transmission in the depth direction depends on the anisotropy factor  $g$ . Due to the scattering increase ( $g$  decreasing) the power transmission is decreased and it is more attenuated.

In order to analyze how the scattering rates influence laser photons distribution in the powder bed in a scattering case, three values of anisotropy factor  $g$  are chosen, they are equal respectively to 0.93, 0.8, and 0.6. In Monte-Carlo methods,  $g$  is an important factor related to

the scattering and reflection rate. It influences laser attenuation rate, laser influential depth, and reflection rate. When  $g$  is equal to 1, it means that all photons travel in forward direction and that the reflection rate is equal to zero. With the value of  $g$  decreasing, the photons' travel directions turn to isotropic and the scattering tends to be isotropic ( $g = 0$ ), therefore more photons are reflected outside the powder bed and the laser's efficiency is decreased. Fig. 3.9 presents the laser's power transmission in the depth direction. The attenuation rate of power transmission increases with the scattering rate increasing ( $g$  decreasing), the attenuation coefficients are equal to 11580, 12900 and 14870 respectively for  $g$  equal to 0.93, 0.8 and 0.6, because with decreasing  $g$  more photons are deviated from forward direction to radial and backward directions.

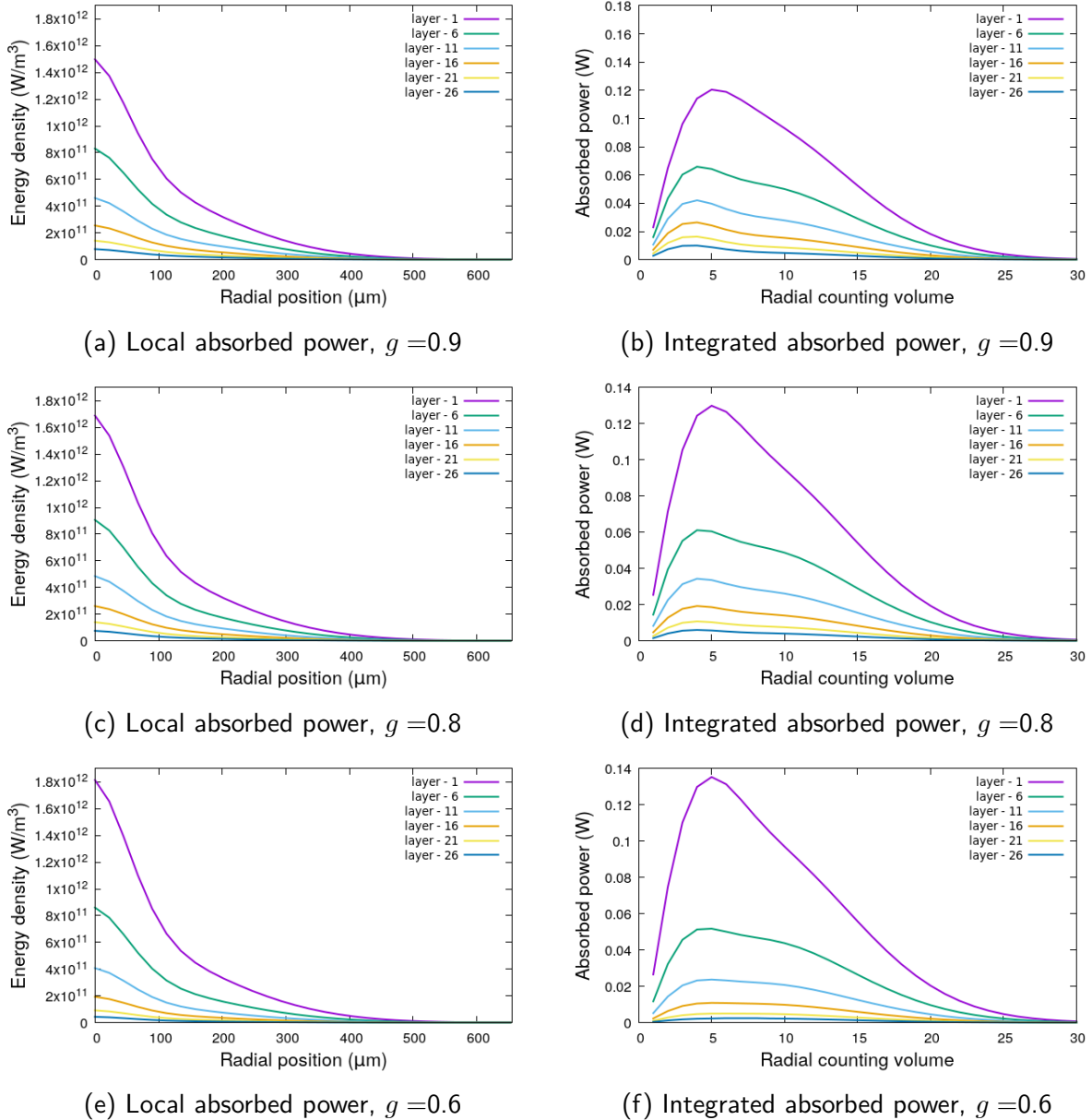


Figure 3.10: Absorbed laser power versus  $g$  in the powder bed: local distribution (left) and integrated laser power in the counting volumes (right).

Fig. 3.10a, Fig. 3.10c and Fig. 3.10e show for three values of  $g$  investigated the distributions of the absorbed laser power in the powder bed: one distinguishes local and integrated distributions. The results on the left are local distributions of the curves obtained by data fitting while on the right are displayed the integrated laser power absorbed in the

counting volumes. Fig. 3.10b, Fig. 3.10d and Fig. 3.10f indicate that laser power absorption is similar for the three anisotropy factors. As the attenuation coefficient is bigger for smaller  $g$ , more laser power is absorbed by the top layers of the powder bed for smaller  $g$ . The maximum power absorption takes place in the sixth counting volume at the bed surface while for the 21st layer the maximum absorption occurs in the 3rd counting number, this means that the fitting factors in the radial direction are similar, the fitting coefficients are shown in Fig. 3.3.

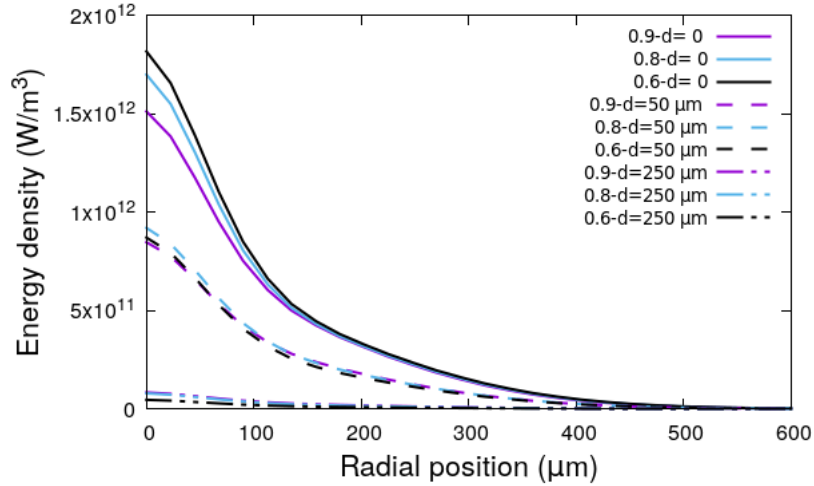


Figure 3.11: Comparison of the absorbed laser power in the powder bed with different  $g$ .

In Fig. 3.11, we chose three depth positions to summarise the absorbed power distribution and make a comparison for different anisotropy factors. Under strong scattering condition with small  $g$  ( $g = 0.6$ ), higher power absorption is concentrated on the surface of the powder bed. With the depth increasing, the absorbed laser power with small  $g$  is decreased faster: at the depth position of  $250 \mu m$ , the absorbed laser power with  $g = 0.6$  is the smallest because the attenuation rate is the largest with  $g = 0.6$  (see Fig. 3.9). However, in the radial direction, the influence of the anisotropy factors is not clear as the radius of the influenced zone is about  $500 \mu m$  under the three scattering conditions. It means that the propagation of the scattered photons in the radial direction is not sensitive to the anisotropy factor  $g$  and that the scattering rate influences mainly the vertical size of the influenced area.

### 3.4.2 Influence of powder bed porosity and particle size

Table 3.4: Fitting coefficients versus initial porosity of the powder bed.

initial porosity	0.2	0.3	0.45	0.53	0.65
$\beta$	12000	11580	9918	9300	8072
$n$	0.773	0.76	0.78	0.77	0.775
$b$	$2.5e-4$	$2.5e-4$	$2.54e-4$	$2.5e-4$	$2.57e-4$
$a$	7518	9000	6930	7750	5495
$c$	1.195	1.068	1.116	1.05	1.094

As is observed above, scattering plays an important role in laser transport in the powder bed, changes the laser photons' travel direction and causes laser photons' re-absorption by one particle. Because we assume that the absorption was only affected by the polymer part and that air does not absorb the laser energy at all, the powder bed's density is the main

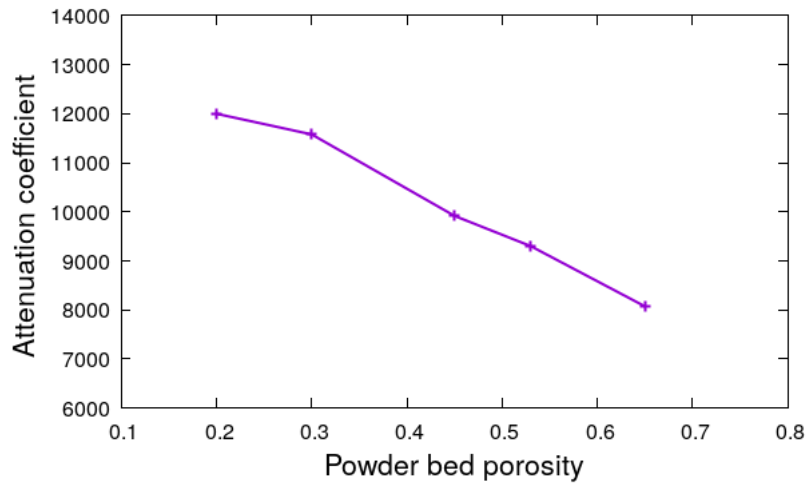


Figure 3.12: Attenuation coefficient ( $\beta$ ) with respect to powder bed density.

factor that effects the laser attenuation process. The attenuation coefficient in each polymer solid particle is kept to be equal to 17000 in our simulations. The influence of powder bed density on the attenuation coefficient is shown in Fig. 3.12. The average radius of particles is set to  $30 \mu\text{m}$ . The attenuation coefficients of the powder beds are equal to 12000, 11580, 9918, 9300 and 8072 respectively for the bed porosity of 0.2, 0.3, 0.45, 0.53 and 0.65.  $\beta$  and other fitting coefficients are listed in Tab. 3.4. The laser attenuation rates are decreasing with decreasing powder bed porosity because high bed density (low bed porosity) increases the chance of laser scattering through the polymer particles, which promotes more energy absorption in a powder layer of the same thickness powder. Similar fitting coefficients shown in Tab. 3.4 indicate that the laser photons distribution in the radial direction is less influenced by the initial porosity.

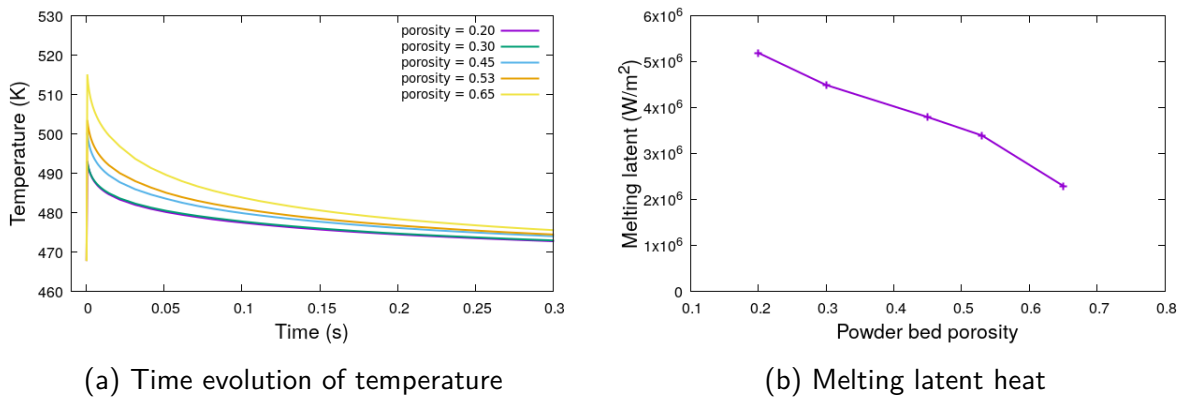


Figure 3.13: Influence of the initial porosity of the powder bed on temperature profile and melting latent heat.

The main effect of the initial porosity is the attenuation coefficient,  $\beta$ :  $\beta$  decreases with increasing initial porosity. It means that more energy is absorbed by the surface layers for small initial porosity. More absorbed energy in the surface layers would induce logically higher surface temperature. However, the numerical simulations performed indicate an opposite result (Details of the numerical simulations and the monitoring point can be found in the next section.). Time evolution of surface temperature is displayed in Fig. 3.13a with respect to initial porosity: the highest maximum temperature is observed for the initial porosity of 0.65. In fact this result is due to the melting latent heat which is the heat sink in the governing

equation. The equivalent density and specific heat of the powder bed decrease with increasing initial porosity, the melting latent heat is thus increasing with decreasing initial porosity of the powder bed as is shown in Fig. 3.13b. With decreasing initial porosity, although the absorbed energy near the bed's surface increases, increase in melting latent heat prevent the surface temperature from reaching higher maximum temperature.

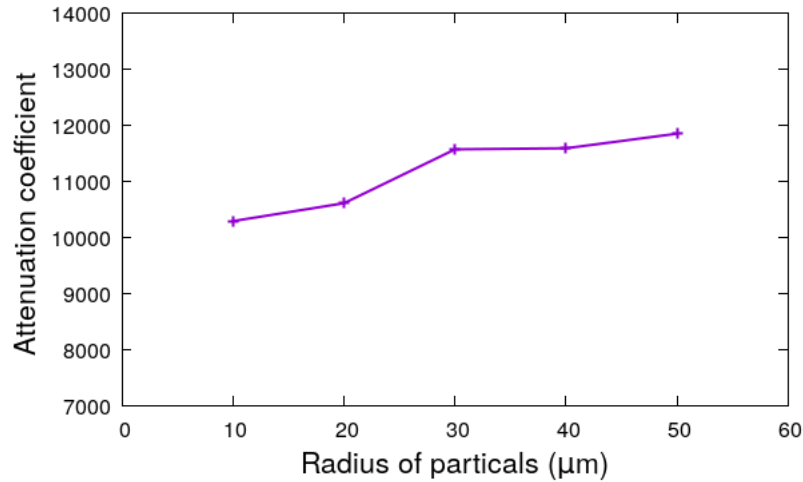


Figure 3.14: Influence of the averaged radius of the polymer particles on attenuation coefficient.

The size of polymer particles in the powder bed usually follows the Gaussian distribution. In our simulations, we fix the initial porosity to 0.3 and use the averaged size of polymer particles regardless of the difference between the particles. But, the average size of polymer particles still affects the laser photons' distribution. As shown in Fig. 3.14, the values of attenuation coefficients are varying from 10050 to 11580 for an averaged radius between 10  $\mu\text{m}$  and 50  $\mu\text{m}$ . The laser attenuation coefficient increases with increasing the polymer particle size. Tab. 3.5 presents the attenuation coefficient and other fitting coefficients obtained:  $\beta$ ,  $n$  and  $b$  change slowly with the particles' radius while  $a$  and  $c$  change very much.

Table 3.5: Fitting coefficients versus particle's radius.

particles' radius [ $\mu\text{m}$ ]	10	20	30	40	50
$\beta$	10300	10620	11580	11600	11860
$n$	0.64	0.63	0.76	0.6525	0.668
$b$	2.5e-4	2.7e-4	2.54e-4	2.5e-4	2.47e-4
$a$	22300	14710	9000	21731	21762
$c$	-0.19	0.6	1.068	-0.18	-0.5085

### 3.5 Temperature distribution

As stated previously no experimental result is available for validating the results obtained for the cases with scattering. To qualify the scattering models obtained, the idea is to use the absorbed laser power in numerical simulations of the SLS processes and compare the numerical simulations with the available experimental results such as temperature at the bed surface and dimensions of the parts. In this section we perform numerical simulations of PA6 SLS processes

and compare the numerical and experimental results of the temperature on the bed surface and also the temperature fields obtained with BL and scattering models.

The computational domain of the numerical simulations is set to be a volume of  $1 \times 1 \times 0.6 \text{ mm}^3$ , it is discretized with a regular mesh of  $50 \times 50 \times 60$  cells. The time step used is equal to  $5 \mu\text{s}$  during the laser scanning process and  $100 \mu\text{s}$  after the laser scanning. We simulated the heating and cooling processes of the SLS process: the simulation starts when the laser interacts with the powder bed through the heating process and finishes when the temperature of the manufacturing area decreases to the initial temperature.

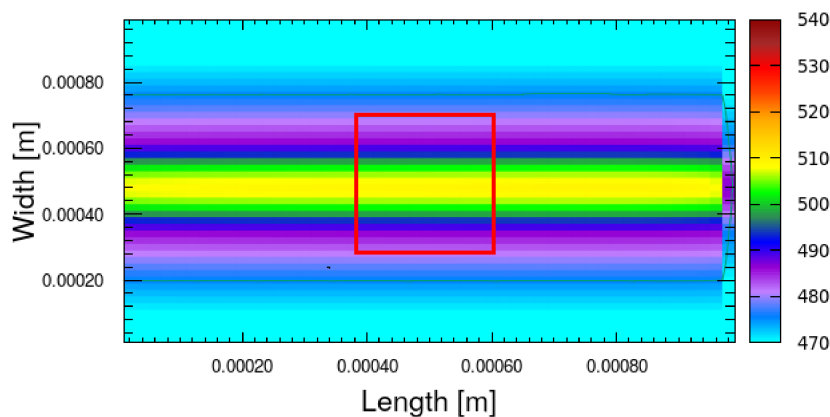


Figure 3.15: Instantaneous surface temperature of the powder bed and illustration of the pixel area of the IR camera.

We set the following SLS parameters for both the simulations and the experiments: laser radius of  $225 \mu\text{m}$ , laser energy of  $15 \text{ W}$ , scanning speed of  $3.5 \text{ m/s}$  and initial porosity of 0.3. Let's recall that the anisotropy factor used in the modified Monte-Carlo method is equal to 0.93 in the scattering case. In the experiments, we introduce the IR camera thermal technique to measure the surface temperature of the powder bed and obtain time evolution of surface temperature for each measured pixel. (Details on the camera calibration can be found in Chapter 4.) We then compare the measured time evolution with that provided by numerical simulations. The size of one pixel of the IR camera is equal to  $460 \mu\text{m} \times 460 \mu\text{m}$ , it is larger than the laser's diameter on the one hand and on the other hand much larger than that of the numerical simulation ( $20 \mu\text{m} \times 20 \mu\text{m}$ ). The IR camera reflects therefore an averaged temperature in the pixel and it is difficult to capture with accuracy the temperature at any position that is not on the trajectory of the laser axis in single-sweep situations. In our simulations, the important variation in temperature at a position on the trajectory of the laser axis and on the edge of the laser can be observed, but to be able to compare with the IR measurement, we have to average the numerical results in the same measured zone as one pixel of the IR camera. Fig. 3.15 displays an instantaneous surface temperature of the powder bed and illustrates one pixel of the IR camera.

We choose the trajectory of the laser axis as the center line to average temperature in one camera pixel area ( $460 \mu\text{m} \times 460 \mu\text{m}$ ). In order to show the quality of the scattering model, numerical simulation is also performed for the BL model without scattering. Fig. 3.16 presents the comparison of the experimental and numerical results: time evolution of surface temperature in one camera pixel area. From the curves one observes first a very short phase of very fast increase in temperature which is followed by a long phase of temperature de-

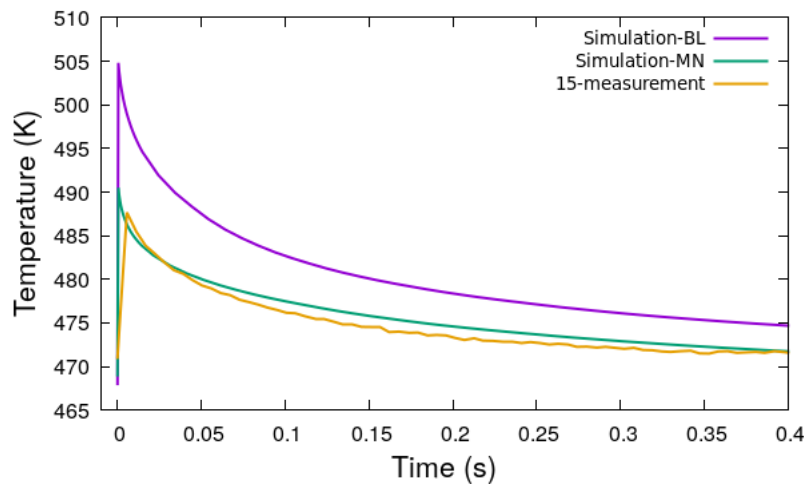


Figure 3.16: Time evolution of temperature in one camera pixel area: IR camera measurement and numerical results with and without scattering.

crease. The short phase of very fast increase in temperature corresponds to the laser scanning phase and the longer one to the cooling phase. The comparison shows that at any time the Beer-Lambert model (without scattering) predicted the highest surface temperature which is higher than the prediction using the scattering model provided by the modified Monte Carlo method, furthermore the results using the scattering model are in better agreement with the experimental measurement. The comparison exercise seems to indicate that the scattering model provided by the modified Monte-Carlo method reflects better the real temperature and its time evolution, which means the importance of the scattering and the need to consider it in the laser-powder bed interaction and the numerical simulation of the SLS process.

Note nevertheless that there is still discrepancy between the prediction using the scattering model and the measurement. It may be due to the experimental limitations: longer shutter time and uncertain emissivity of the sample surface. The shutter time of the IR camera which is equal to  $0.0056\text{ s}$  is too long to capture the rapid change in temperature in a SLS process, especially during the heating phase. This can also be understood by the small time steps we used in numerical simulations:  $5\ \mu\text{s}$  during the scanning phase and  $100\ \mu\text{s}$  after scanning. Also, the emissivity of the powder bed surface is not constant: it is affected by the phase change of polymer particles and the surface condition and known with an error of 5%. The discrepancy may also come from the numerical simulation, our simulation is based on the assumption that the powder bed is a homogeneous medium, however, the real powder bed is more complicated.

The time evolution of temperature at different depth positions is shown in Fig. 3.17. On the bed surface the peak temperature is observed at the end of the scanning phase while going further in depth of the powder bed it is more and more delayed. As is seen from the absorbed laser power, in the case without scattering higher surface temperature and larger influence zone in the depth direction are observed. Peak surface temperature in the case without scattering is  $17\text{ K}$  higher than that in the scattering case. At the depth position of  $200\ \mu\text{m}$  temperature obtained without scattering is about  $3\text{ K}$  higher than that in the scattering case. The main reason is that without scattering the photons can travel only forward and that in the scattering case they can travel horizontally and even backward.

Figs. 3.18 and Fig. 3.19 illustrate the powder bed's 2D temperature distribution map

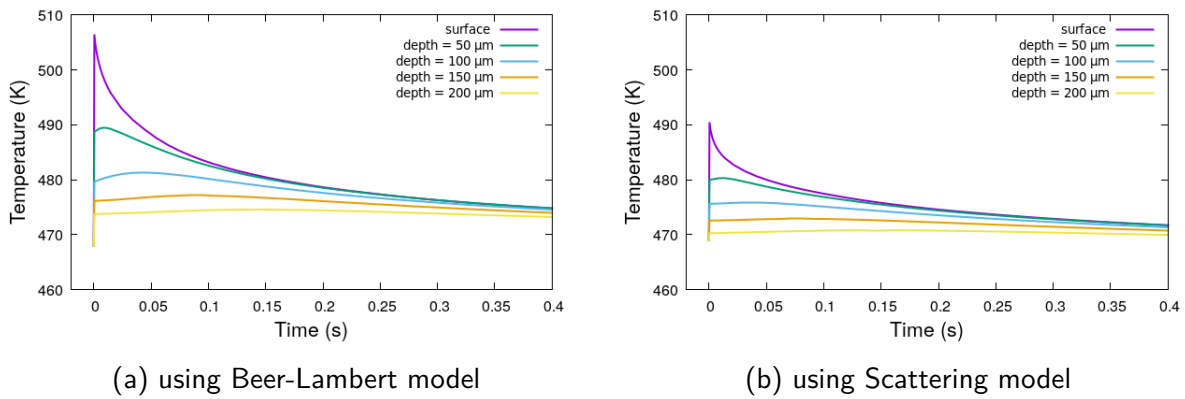


Figure 3.17: Numerical results of averaged temperature in one camera pixel area centered about the trajectory of the laser axis.

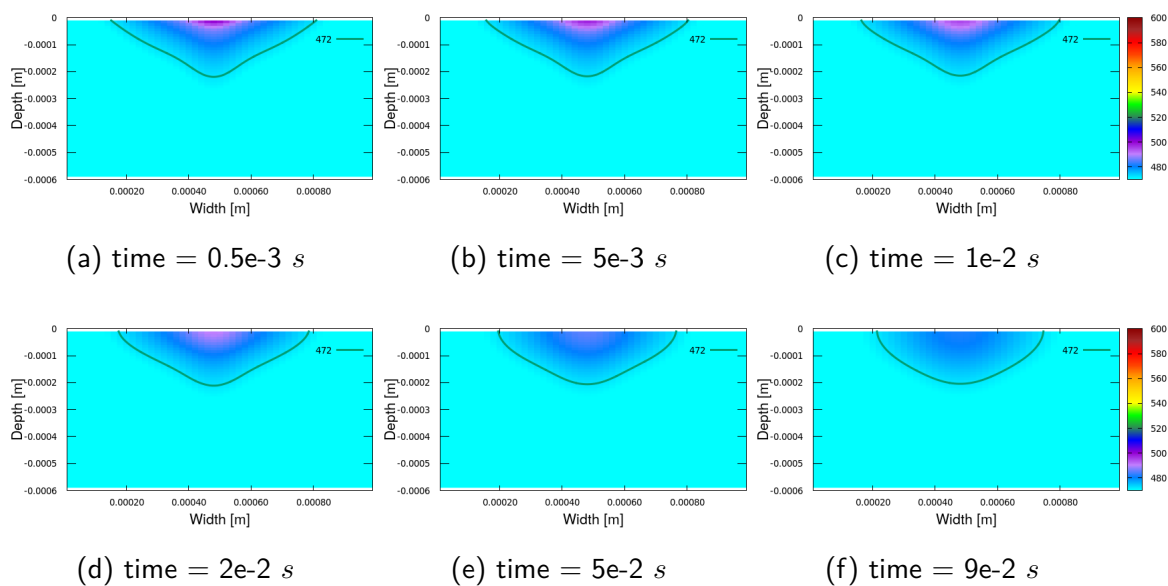


Figure 3.18: Instantaneous temperature fields in a vertical plane normal to the laser sweep in the scattering case.

at different times simulated respectively for the cases with scattering and without scattering. One can easily observe, in the scattering case, a larger horizontal influence area near the bed surface, a smaller vertical influence zone and a lower surface temperature. While in the case without scattering the vertical influence zone is larger, the horizontal influence area is smaller and the surface temperature is higher. In the scattering case, the horizontal influence area reaches the maximum size at the end of heating phase (at  $t = 5e-3$  s for example) due to the distribution of the absorbed laser power induced by scattering. In the case without scattering, the horizontal influence zone is only limited to the laser diameter at the end of heating phase and it continues during the cooling phase to increase slowly due to heat conduction. If the SLS process is sufficiently long, heat conduction can overcome the shortcoming of the absorbed laser power distribution and yield a large horizontal influence zone. Fig. 3.19 indicates that at  $t = 9e-2$  s the horizontal influence zone is slightly larger.

Fig. 3.20 shows the time evolution of point-wise surface temperature at several points with different distances to the trajectory of laser center. With single-sweep, maximum temperature is always located on the trajectory of laser center, away from the trajectory

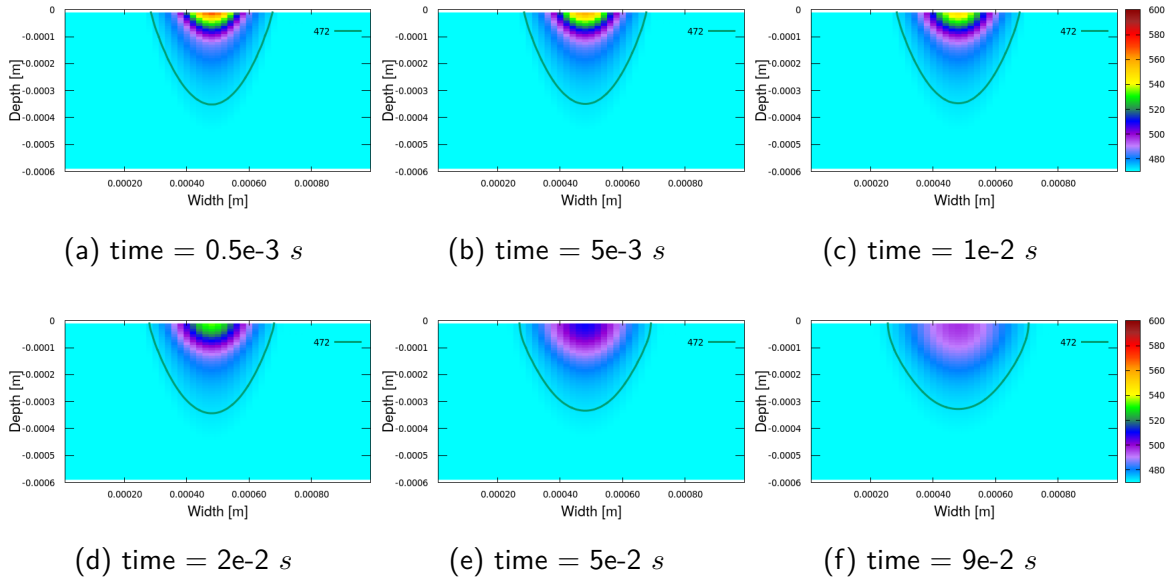


Figure 3.19: Instantaneous temperature fields in a vertical plane normal to the laser sweep in the case without scattering.

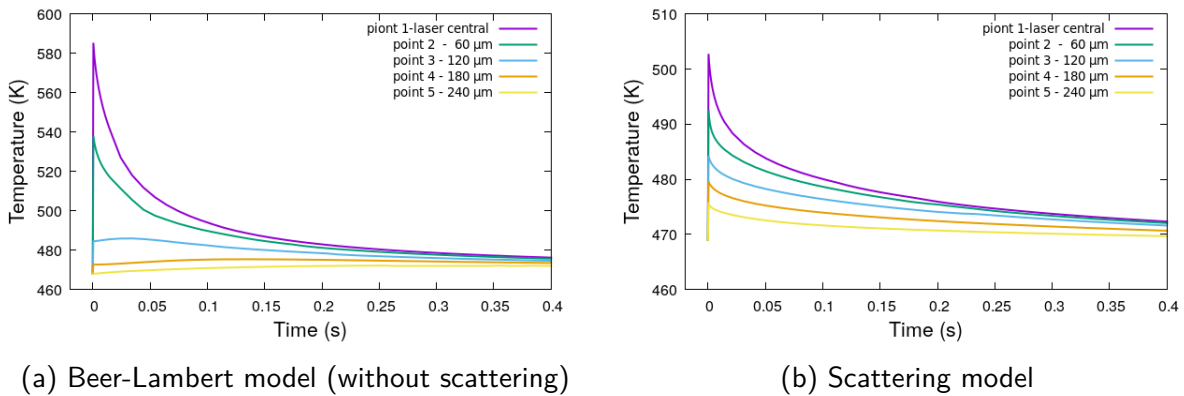


Figure 3.20: Time evolution of point-wise surface temperature at several positions which are characterized by their distances to the trajectory of laser axis.

temperature decreases rapidly. Given the fact that these points cover an area which is slightly larger than the area of one camera pixel, maximum point-wise temperature is higher than the maximum temperature averaged over the area of one camera pixel: in the scattering case the maximum temperature is equal to  $503\text{ K}$  to be compared with  $490\text{ K}$  of averaged temperature (Fig. 3.17b); in the case without scattering the maximum is equal to  $585\text{ K}$  to be compared with  $506\text{ K}$  (Fig. 3.17a). In the scattering case, maximum temperature at a distance of  $240\text{ }\mu\text{m}$  to the trajectory of laser axis is higher than  $474\text{ K}$ , it means that at this position melting is taking place and that polymer particles can form a good connection bond. It would be possible that the melting pool extends to this position. But in the case without scattering maximum temperature at the same position exceeds never  $472\text{ K}$ , melting does not take place at the moment and, as stated before, heat conduction may extend the melting pool to this position.

$K$  at the same vertical position. This means that the vertical size of influence area is smaller in the scattering case.

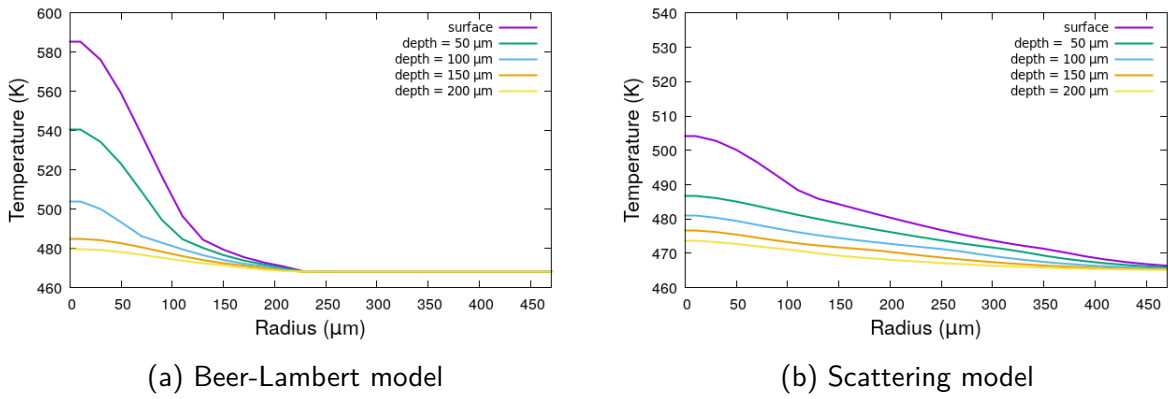


Figure 3.21: Instantaneous temperature profiles at several depth positions in the vertical plane normal to the laser trajectory at time = 0.0005 s. One can see that the horizontal influence zone in the scattering case is maximal and that in the case without scattering it is very small at this time (heat conduction will increase it slowly later on.).

In summary, the scattering enlarges the horizontal influence area and decreases the vertical influence area. This is why lower maximum temperature is obtained in the scattering case although more power is absorbed by the top layers. The scattering prevents the overheating near the laser center and this is good for improving the sample quality.

In the next section, dimensions of the final parts will be investigated to qualify the scattering model.

## 3.6 Dimension of the parts

### 3.6.1 SLS process with PA6

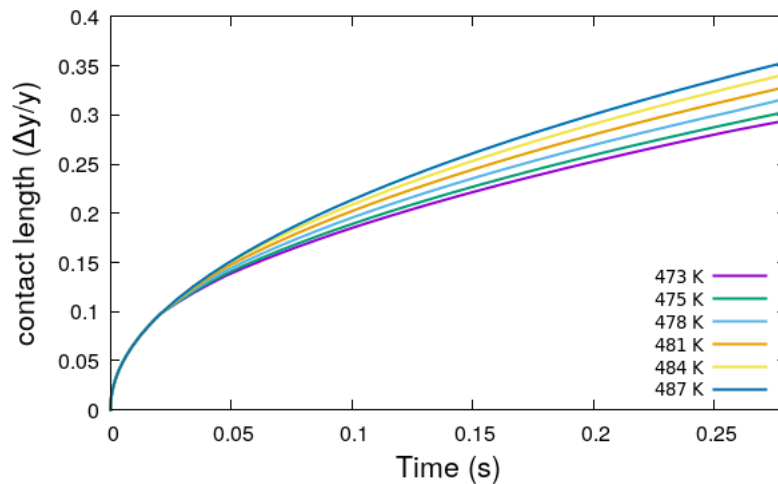


Figure 3.22: Time evolution of relative contact length. Fig. 3.22 shows the contacted length change rate calculated by the Frenkel coalescence model, which is shown in Chapter-2, section of model of coalescence, the changing rate is major dependence on the viscosity of polymer that is expressed by the Eq. (2.60).

With the laser melting the powders, the molten polymer particles sinter together to form a new object, predicting the dimensions of the new object is an important part in a modeling study. As there is no exist external mechanical force working on the powders during the SLS process, the melting degree directly depends on temperature and period during which polymer remains in the molten state. A SLS process which is a transient process is in general long and very complex. For single-sweep SLS processes although it includes a heating phase from the preheating temperature to the highest temperature and a cooling phase from the maximum temperature back to the preheating temperature, it is very short compared with the coalescence process. In fact, coalescence of molten particles is still ongoing when single-sweep SLS processes are finished. Fig. 3.22 shows the contacted length change rate calculated by the Frenkel coalescence model, which is presented in the model section of Chapter 2. The changing rate depends mainly on the viscosity of polymer expressed by Eq. (2.60). As shown in Fig. 3.22, the percentage of contact length just reaches 35 % after 0.3 s and if we want to finish the whole coalescence process, another 0.5 s is at least needed. As single-sweep SLS processes are not long enough, coalescence does not finish in most of the times. The question is to know if good connections are established between these polymer particles so that they remain connected together. Good connection just means that firm bonds are formed between particles. This raises a real concern which is how to decide the dimension limit: what are the right minimum temperature and the corresponding minimum duration necessary for a firm bond ?

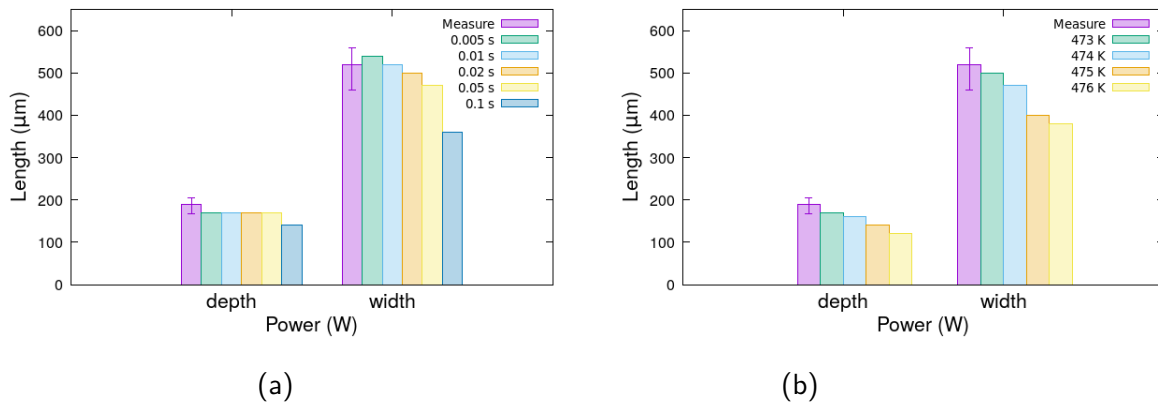


Figure 3.23: Dimension of the sample obtained in a single-sweep SLS using a power of 13 W. (a) Different values of minimum duration above  $T = 474 K$ . (b) Different values of minimum temperature with a minimum duration of 0.05 s

Numerical simulation is performed for a laser power of 13 W. Several values of minimum duration are tested for the minimum temperature equal to 474 K in order to determine the product's dimensions. The minimum duration requested varies from 0.005 s to 0.1 s and the results obtained are shown in Fig. 3.23a. One observes that using the minimum temperature of 474 K the product's dimensions decreases with increasing minimum duration: the decrease in depth is weak while the decrease in width is more important. The experimental results seem to indicate the optimal minimum duration of 0.02 s. When keeping the minimum duration equal to 0.05 s, several values of minimum temperature, ranging from 473 K to 476 K, are tested and the corresponding product's dimensions are displayed in Fig. 3.23b: we observe again the decrease in product's dimensions with increasing minimum temperature and a more important decrease in width than that in depth. These tests indicate that the optimal minimum temperature is equal to 473 K. Combing the comparison results with the coalescence-time curves (Fig. 3.22), we assume that the contact length percentage equal to 13 % is the connection limit, where the limited melting temperature and the minimum dura-

tion are equal to  $474\text{ K}$  and  $0.05\text{ s}$ , respectively. If the particles' contact length rate is higher than this limit (13 %), there are firm bonds and these particles are well connected as a whole object because one particle has at least three connection points.

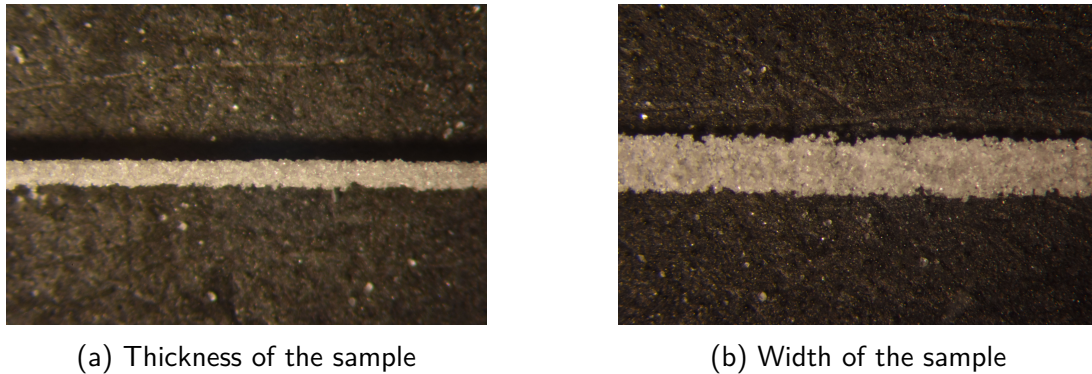


Figure 3.24: Photographs of the sample.

Fig. 3.24 shows the photographs of the experimental sample obtained by single-sweep SLS: we can clearly see that the particles' edges are connected by bond necks. This confirms that the coalescence between these particles is not finished in experiment. These photographs prove the reason for setting the contact length rate to 13 % as the limit. It is based on this limit that we predict the depth and width of the samples obtained under single-sweep conditions and make a comparison with the measurements.

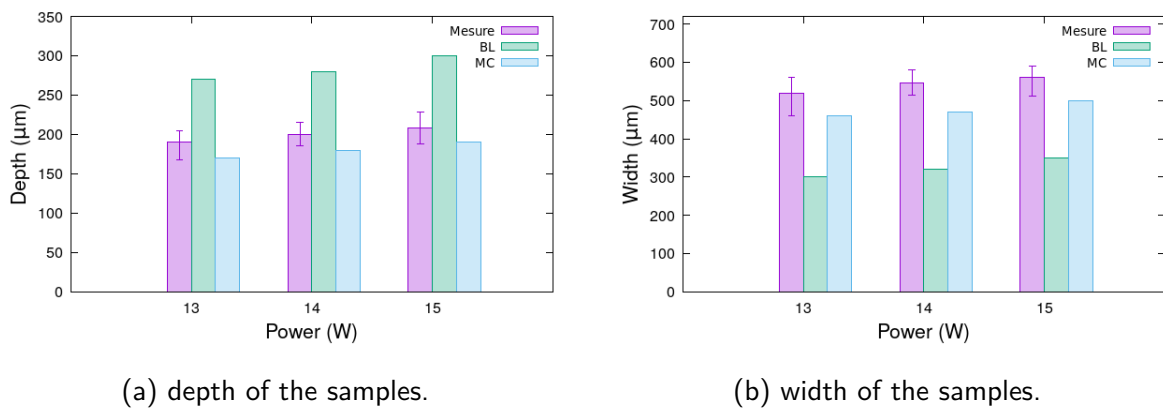


Figure 3.25: Dimensions of the samples under single-sweep conditions: comparison of numerical predictions with the measurements.

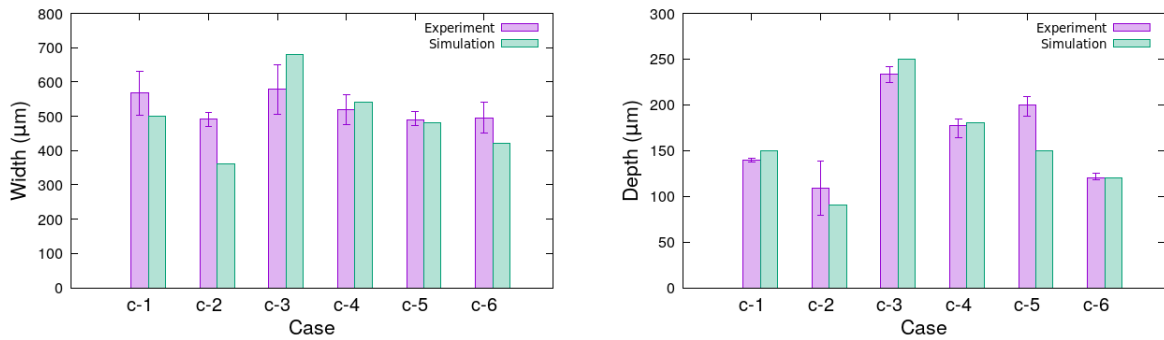
Fig. 3.25a and Fig. 3.25b show the dimensions of the samples obtained for several laser powers: numerical results are compared with experimental data. In order to show the influence of scattering, numerical simulations using Beer-Lambert model are also performed for the cases without scattering. Concerning the sample width and depth, the experimental and numerical results are in agreement in the scattering case while in the case without scattering discrepancy is more important. The results using Beer-Lambert model are much smaller in terms of the sample width and much higher in terms of the sample depth. This confirms that the absorbed laser power is evenly distributed in space in the case without scattering: the laser power is absorbed in a smaller horizontal but larger vertical zone. In the radial direction although heat conduction enlarges the melting zone in the case without scattering it is not enough.

In the scattering case, with the laser power increase from 13  $W$  to 15  $W$ , the sample depth increases from 170  $\mu m$  to 190  $\mu m$ , and the sample width increases from 460  $\mu m$  to 500  $\mu m$ . In the Beer-Lambert case without scattering, the molten pool's thickness increases from 270  $\mu m$  to 300  $\mu m$ , and the width of the molten pool increase from 310  $\mu m$  to 350  $\mu m$ . These values show that the product's dimensions depend only slightly on the laser power.

### 3.6.2 SLS process with PA12

Table 3.6: PA12 Powder bed, SLS parameters and material properties used in model.

Parameter and Property	Value
Diameter of the laser beam, [ $\mu m$ ]	400
Thickness of the powder layer, [ $\mu m$ ]	60
Total attenuation coefficient, [ $m^{-1}$ ]	1.7e4
Extinction coefficient, [ $m^{-1}$ ]	7500
Anisotropy factor, $g$	0.87
Laser power, [ $W$ ]	1.1,3.3,5.6,7.8
Relative density	0.7
Average diameter of the grain [ $\mu m$ ]	60
Reflective	0.1
Preheating temperature [ $K$ ]	445
Starting melting temperature [ $K$ ]	454
Final melting temperature [ $K$ ]	461
Ambient temperature [ $K$ ]	454



(a) Width of the sample.

(b) Depth of the sample.

Figure 3.26: Dimensions of the samples: comparison between experimental and numerical results for different cases.

Table 3.7: Process parameters for simulation.

Test case	Power [ $W$ ]	$V_s$ [ $m/s$ ]
1	3.3	0.5
2	3.3	1.0
3	7.8	0.5
4	7.8	1.0
5	7.8	1.5
6	7.8	2.0

As stated early in the chapter, the original work of Riedlbauer et al [145] on a semi-crystalline polymer PA12 (PA2200) is both numerical and experimental. Their experimental results are the rare data that can be used from literature to qualify numerical modeling. Mokrane [93] used these experimental data in the case without scattering. In this work, we revisit numerically the PA12 configurations in the scope of scattering. The polymer properties and process parameters are extracted from Riedlbauer et al. [145] and presented in Tab. 3.6 and Tab. 3.7. Figs. 3.26b and 3.26a summarize the product's width and depth measured by Riedlbauer et al. [145] and calculated in our simulations. We use the contact length rate of 13 % to determine a firm bond and calculate therefore the product's dimension. The comparison indicates a good agreement between numerical and experimental results, excellent agreement is observed for cases 1, 3, 4, and 6 (Fig. 4.7), where the errors are smaller than 8 %.

### 3.7 Summary

In this chapter, we studied how a laser beam interacts with a powder bed. We are interested in Beer-Lambert model in the case without scattering and a scattering model obtained by combining the modified Monte-Carlo method and the Mie theory. The effects of scattering on the laser photons travel in the powder bed were evaluated in terms of the scattering anisotropy factors ( $g$ ) and the density of the initial powder bed. We also simulated single-sweep SLS processes and analysed temperature distribution in the powder bed and the product's dimensions.

Although no result is available to validate directly the scattering effects observed and the scattering model established in this chapter, numerical results obtained using the scattering model are compared with the experimental results in the literature and our own experiments. The comparison shows good agreement between numerical and experimental results. This supports completely the idea that the scattering model established is well founded and can be used to study more complex SLS processes.

# Chapter 4

## Single layer SLS processes

### Contents

---

4.1	Calibration of the IR camera . . . . .	81
4.2	Complementary results of single-sweep processes . . . . .	85
4.3	Multi-sweep and single-layer processes . . . . .	89
4.3.1	Influence of laser moving direction and laser power model . . . . .	89
4.3.2	Parametric analysis . . . . .	97
4.3.3	Comparison with experimental results . . . . .	101
4.4	Summary . . . . .	106

---

In this chapter we are interested in single-layer SLS processes. In comparison with the previous chapter, the only complexity comes from multi-sweep of the laser beam.

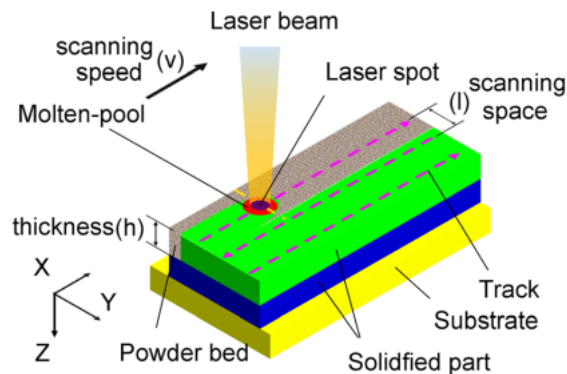


Figure 4.1: Schematic diagram of a multi-sweep SLS process [147]. The laser beam is scanning forward and backward and the heating overlap is controlled by the scanning space.

A multi-sweep SLS process is shown in Fig 4.1 and the laser displacements are defined as:

$$\begin{aligned}x_L &= x_0 + v_x t \\y_L &= y_0 + v_y t\end{aligned}$$

where  $x_0$  and  $y_0$  are the initial position of the laser beam,  $v_x$  and  $v_y$  are the beam speeds in  $x$  and  $y$  directions,  $x_L$  and  $y_L$  are the position of the laser beam centre.

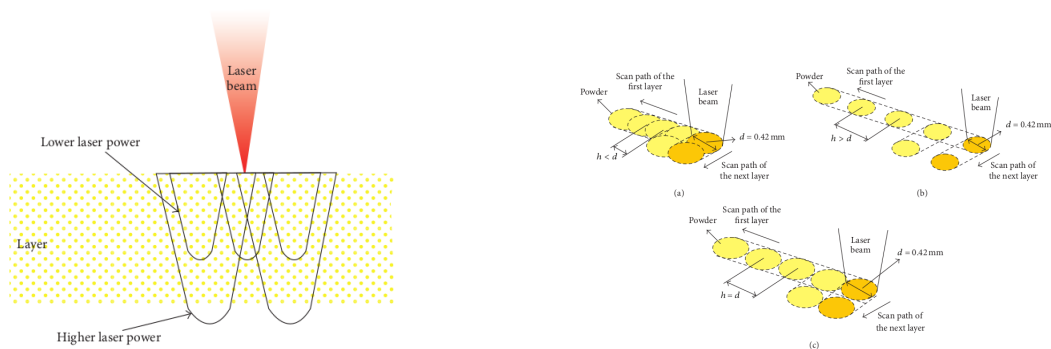


Figure 4.2: Scheme of the powder particles sintering [148].

The energy density is the main factor of a multi-sweep SLS process and related to the scanning space, laser moving speed and laser power, as is shown in Fig. 4.2. If the scanning space is much smaller than the laser beam diameter or the laser moving speed is much lower, the overlap heating will cause much high energy density at this position. Too high manufacture temperature disrupts molecular structure, reduces the mechanical properties, and increases the surface roughness. In the inverse, too low energy density produces in the manufacturing part unsintered materials, which also reduce the mechanical properties of the sample [148] [149]. Therefore, it is important to choose suitable process parameters and especially the energy density. Energy density can be calculated, according to [149], as:

$$ED = \frac{P}{ve} \quad (4.1)$$

where ED is the energy density ( $J/m^2$ ),  $P$  is the laser power ( $W$ ),  $e$  is the the laser scan space ( $m$ ) and  $v$  ( $m/s$ ) is the laser scan moving speed.

In multi-sweep SLS processes, the heating overlap causes the temperature evolution different from the single-sweep ones. We will use the laser models with and without scattering to do numerical simulations and study heat conduction in the powder bed in multi-sweep situations. A parametric analysis will be done using the scattering model and a comparison between numerical and experimental results will be performed. In the next section we detail the calibration of the IR camera which is used to measure surface temperature. It is followed by complementary results of single-sweep processes before presenting the numerical results and comparing them with the experimental measurements.

## 4.1 Calibration of the IR camera

Several standard methods can be used to measure temperature distribution in the powder bed, including thermocouples, probes, thermochromic liquid crystals, infrared thermography, micro-cantilevers, thermorefectance and thermography. Among these methods, infrared thermography is a popular, easy to use and accurate measurement technique, especially for inspecting surface temperature evolution during the SLS process. The digital camera (Fig. 4.4) can act as a luminance meter and is used to measure the infrared thermography of materials, it turns an image into an array of pixels. Ignoring the complication of color in the digital camera, the value in each pixel represents the brightness at this point. The digital camera captures the luminance of the whole scene, including the surrounding, and its one pixel can measure a small area. The advantage of thermographic systems is that they provide without any contact a full field of surface temperature. The use of infrared techniques in testing the thermal behavior, mechanics, and structures of materials has been considerably extended over the last 30 years in academic laboratories and industrial research. The IR cameras allow storage of thermal images of about 80 000 pixels at frame rates reaching up to several hundred Hertz under certain conditions. However, the results are not very accurate because a subtle change of the material emissivity with material phase change affects the results and is hard to measure.



Figure 4.3: IR camera-TITANIUM 520.

The calibration of thermal infrared (IR) cameras from raw measurement of luminance signals to an absolute temperature or thermal image is a complicated and time-consuming process especially for the situation in which temperature is not stabilized. To establish the relationship between the pixel luminance signal and the target object's temperature through the object's surface emissivity, the process needs to consider both the non-uniformity of the pixel temperature and the temperature dependence of the sensor [150]. In a stable temperature and stable phase situation, the measurement of absolute temperatures can be obtained with a minimum measurement uncertainty after a precise calibration. In the situations of extreme

unstable temperature, the camera measures high variations between the shutter cycles, and the variations are more important if the material phase change is involved.

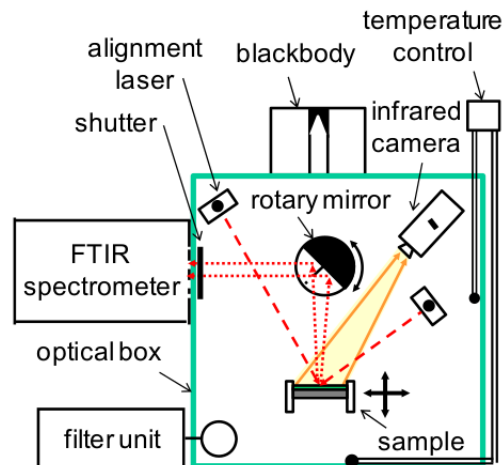


Figure 4.4: Schematic of camera installation [151].

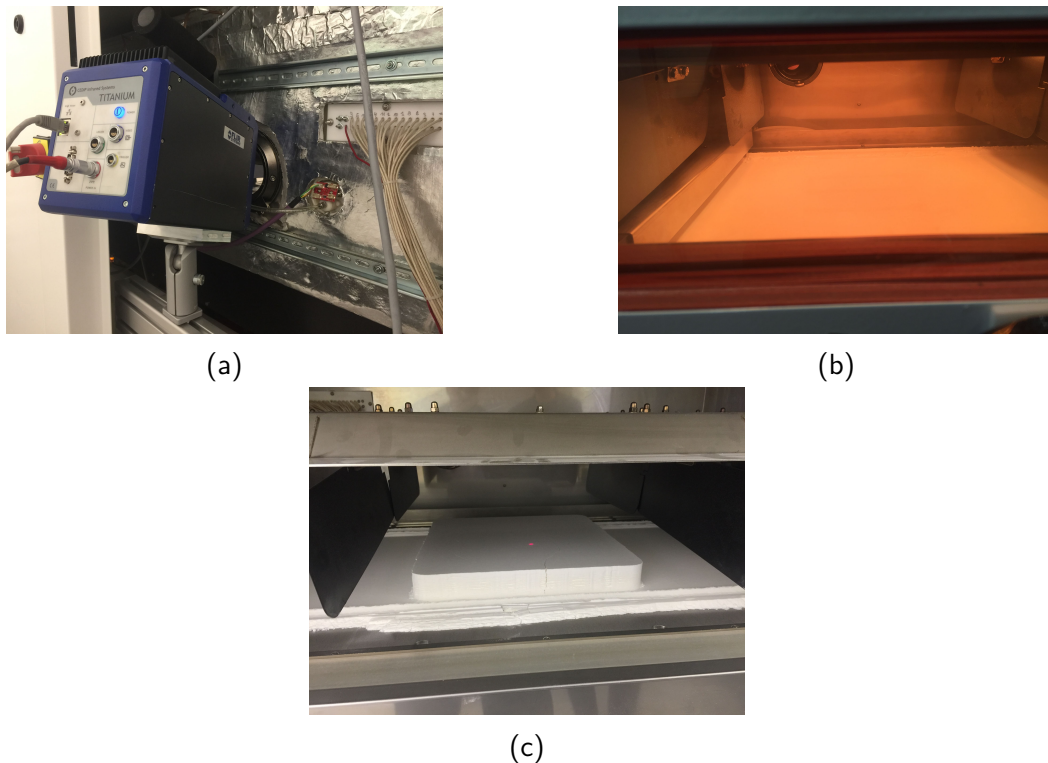


Figure 4.5: Photos of SLS experimental set up. (a) The IR camera. (b) View of the manufacturing room (manufacturing). (c) View of the manufacturing room (after manufacturing).

For monitoring the thermal distribution and acquiring absolute temperature of the part's surface, IR camera has been installed in a SLS system, the measuring apparatus installation is shown in Fig. 4.4. The emissivity is the connection between IR images and absolute temperature. The emissivity is affected by the part's surface temperature, microstructural properties, and instantaneous phase change [152]. A schematic diagram for using an IR camera to monitor the temperature evolution during the SLS process for PA6 polymer is shown in Fig. 4.5, the camera is installed on the outer wall. Fig. 4.7a and Fig. 4.7b are the views inside the working room. The brightness of the final image is proportional to the number of electrons released by the photons during the exposure time. The value of brightness and the

luminance (light radiating from per square meter) is not the same, the brightness increases as a 0.33 power of the luminance according to Steven's Law [153],

$$S = KL_v^{0.33} \quad (4.2)$$

where  $S$  is the brightness perceived by the sensor,  $K$  is a constant and  $L_v$  is the luminance of the pixel in the image, that is also called as digital level. These values depend on the exposure time, film speed, aperture number, ISO sensitivity of the film and other camera parameters. The luminance can be calculated as follows [153],

$$L_v = K_c \left( \frac{tS_v}{f_s^2} \right) L_s \quad (4.3)$$

where  $K_c$  is the calibration constant for the camera,  $t$  is the exposure time (5.6 ms),  $S_v$  is the ISO sensitivity of the film, and  $L_s$  is the luminance of the scene.

Luminance is photometric brightness of the luminous intensity per unit surface area of light traveling in a given direction. It describes the amount of light that passes through, is emitted from, or is reflected from a particular area, and falls within a given solid angle (Fig. 4.6).

$$L_v = \frac{d^2\phi_v}{d\omega dS \cos\theta} \quad (4.4)$$

where  $d\phi_v$  is the luminous flux ( $\phi_v$ ) leaving the infinitesimal area  $dS$  ( $m^2$ ) with any direction contained inside a solid angle ( $d\omega$ ),  $\theta$  is the angle between the normal  $n_\omega$  to the surface and the specified direction.

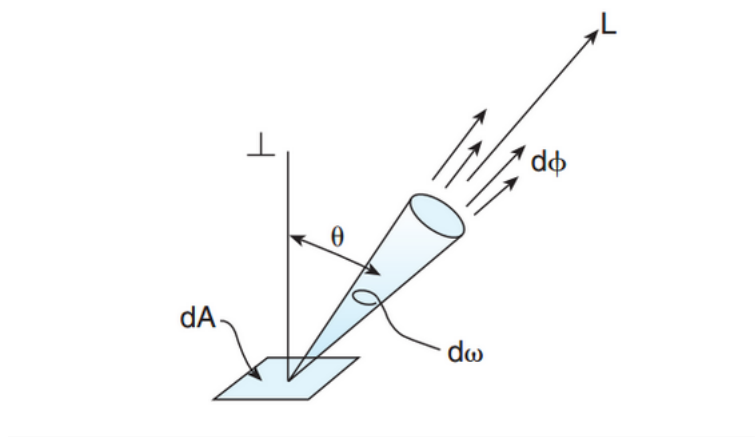


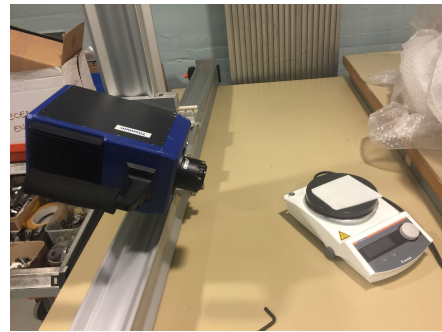
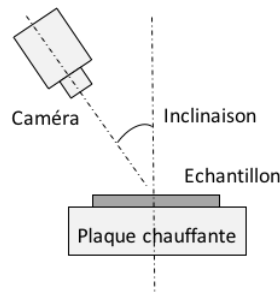
Figure 4.6: Luminance of the sources.

In common usage, luminance is determined by the measurement of absolute luminance and the condition of the photosensitive receptors, which is usually referred to as the sensation results from the viewing surface. The digital level ( $DL$ ) is used to represent the luminance emitted by the samples and captured the IR camera, the digital level is represented as follows:

$$DL = F\varepsilon\sigma AT^4 \quad (4.5)$$

$$C = FA \quad (4.6)$$

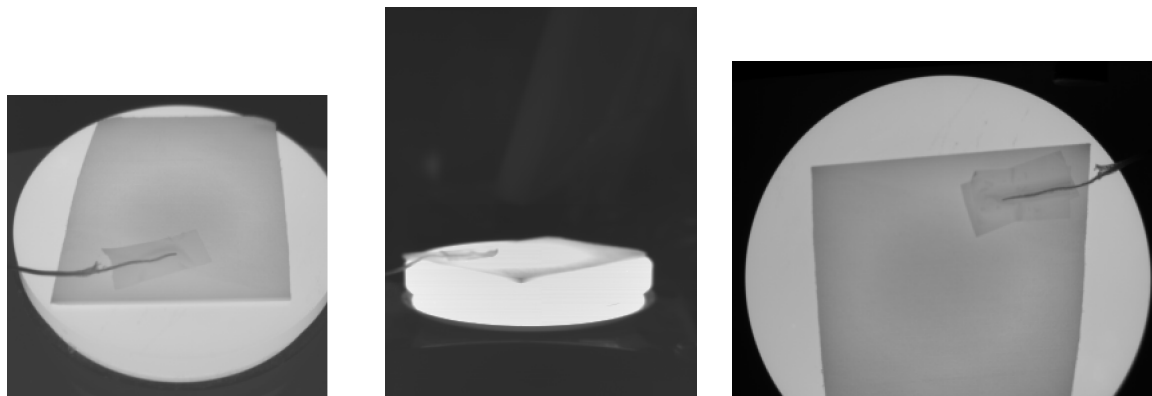
where  $DL$  is the digital level from the IR camera,  $T$  is the temperature of the sample,  $F$  is the test error correction factor caused by the window's temperature, camera setting factors, inclined angle and another external factors,  $A$  is the emissive surface area,  $\varepsilon$  is the emissivity of powder bed and  $\sigma$  is Stefan-Boltzmann constant equal to  $5.68 \times 10^{-8} W/K^4m^2$ .



(a) Schematic representation of inclination angle. (b) Experimental view of inclination angle.

Figure 4.7: Schematic of the experimental installation for testing the inclination angle.

As camera angles may influence the accuracy of measurements, an experiment is used to observe how the camera inclination angle affects the measured digital level. In this test, the emissivity is constant because all the experiments are performed at constant ambient temperature and neither material phase nor surface roughness changes. The camera parameters are also fixed in this test. Therefore, the tilting angle is the only factor that influences the measured digital level. The schematic of experimental test is shown in Fig 4.7. The thin polymer sheets are placed on the heating plate which is heated to different setting temperature,  $70\text{ }^{\circ}\text{C}$ ,  $90\text{ }^{\circ}\text{C}$  and  $120\text{ }^{\circ}\text{C}$ , respectively. A thermocouple is put on the polymer sheet to measure its surface temperature ( $T_{therm}$ ). The IR camera is used to monitor the surface of PA sheet by capturing the digital level ( $DL$ ) of polymer surface. At each temperature, the IR camera is set with different inclination angles from  $0^{\circ}$  to  $82^{\circ}$ , as is shown in Fig. B.4. These parameters are summarized in Tab. 4.1.  $T_{therm}$  is the surface temperature measured by the thermal couple, and the value of  $DL$  is the luminance measured by the IR camera and will be transformed into the temperature by using the conversion coefficient  $C$ , Eq. (4.5).



(a) Inclination angle of  $38.7^{\circ}$ . (b) Inclination angle of  $81.9^{\circ}$ . (c) Inclination angle of  $0^{\circ}$ .

Figure 4.8: IR images with different inclination angles.

Tab. 4.1 summarises the setting temperature, temperature measured by thermal couple, the digital value ( $DL$ ) and the corresponding conversion coefficient  $C$  for the inclination angles tested. The value of  $C$  is calculated by using  $DL$  values and the plate's temperature provided by the thermal couple, it is only influenced by the inclination angle because the surface condition and the material phase do not change in the experiments. From Tab. 4.1, we see that at the setting temperature of  $120\text{ }^{\circ}\text{C}$  the values of  $DL$  are equal to about 14400, no matter how the inclination angle change. The values of  $DL$  varies between 9480 and 10700 when the setting temperature is equal to  $70\text{ }^{\circ}\text{C}$ , and its values are equal to around 7000 for

Table 4.1: Parameters used for testing how the inclination angles affect the experimental results.

inclination angle ( $^{\circ}$ )	Temperature setting ( $^{\circ}C$ )	Temperature from thermal-sensors ( $^{\circ}C$ )	DL mean value	$C$
0	120	88.1	14453.7	18.78
0	90	74.3	10692.2	16.17
24.7	90	73.3	11295.7	17.28
24.7	120	88.8	14641.8	18.85
38.7	70	60.5	7044.4	12.6
59.3	70	61	6862.4	12.2
59.3	90	60.5	10098.6	17.8
76	90	72.7	9460.2	14.66
81.56	120	96.1	14022.8	16.67
81.56	90	77.2	9489.5	13.88

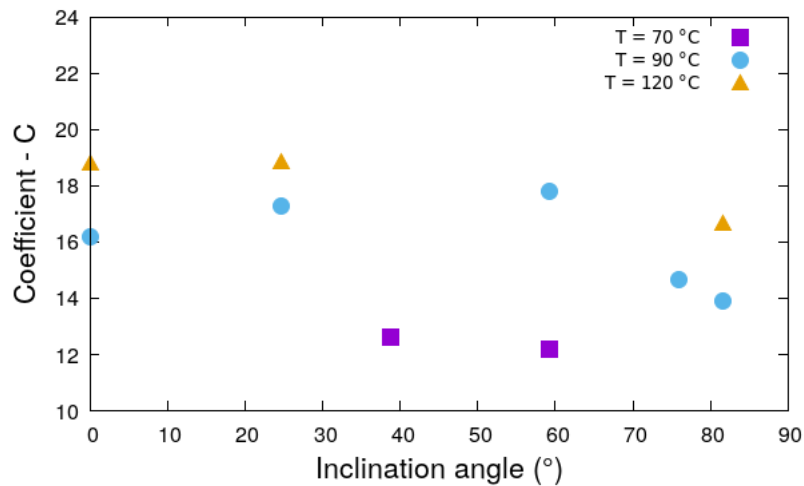


Figure 4.9: Angle of inclination versus temperature

the setting temperature of  $90^{\circ}C$ . Fig. 4.9 shows the evolution of the conversion coefficient  $C$  with inclination angle. At the setting temperature of  $90^{\circ}C$ , the coefficient  $C$  is about 17 for the inclination angle from  $0^{\circ}$  to  $70^{\circ}$ , and its value is slightly decreasing for inclination angle higher than  $70^{\circ}$ . Similar behavior is also observed for the setting temperature of  $120^{\circ}C$ . We can conclude that for inclination angle less than  $70^{\circ}$  it does not influence temperature measured by IR camera. This suggests that in practice inclination angle used should be less than  $70^{\circ}$ , what we will do in the present work.

## 4.2 Complementary results of single-sweep processes

The IR camera technique is used for inspecting the temperature evolution at the powder bed's surface during the whole single-sweep SLS process. Three experimental cases studied are characterized by different laser power and they are listed in Tab. 4.2. Only one result was presented in Chapter 3 to qualify the scattering model. More details are given in this section.

Table 4.2: Manufacturing parameters.

Case	Power ( $W$ )	laser speed ( $m/s$ )
1	15	3.5
2	14	3.5
3	13	3.5

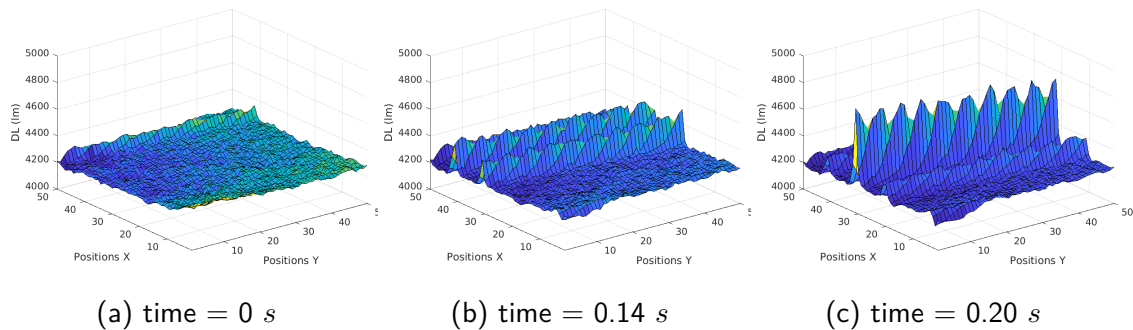
Figure 4.10:  $DL$  of a laser path measured by an IR camera.

Fig. 4.10 shows the digital level ( $DL$ ) at the layer surface at three time points. The laser moving path is monitored by the IR camera with a single sweep condition, it concerns the laser power equal of  $13 W$  and the laser speed of  $3.5 m/s$  (Case 3). The adjacent laser paths do not influence each other because the space between the sweeps is large enough. But before the laser passes through the position (Fig. 4.10c), a low energy is observed by the IR camera (Fig. 4.10b). Although we do not understand the reason for this laser preheating, the accuracy of the 3D print machine is inevitably reduced.

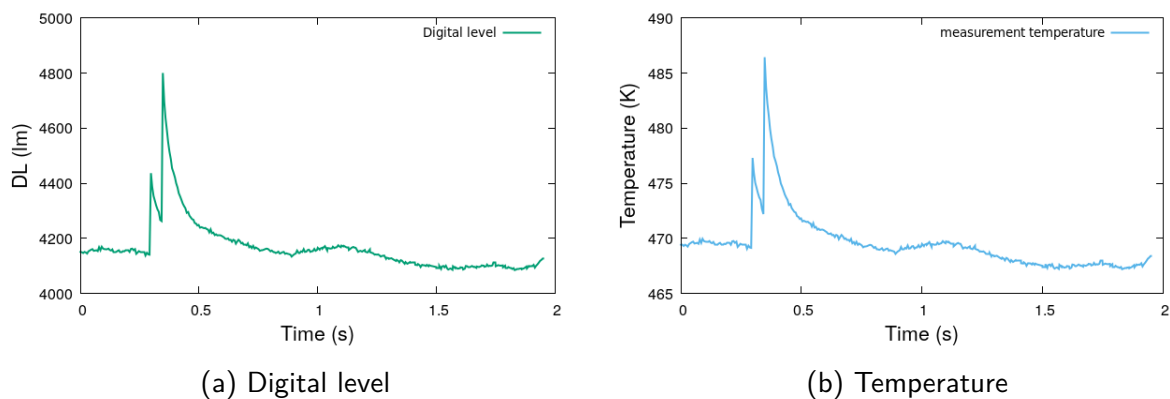


Figure 4.11: Digital level and temperature evolution with time (Case 3).

Fig. 4.11a presents the  $DL$  time evolution measured by the IR camera, which needs to be converted into the time evolution of temperature for comparison with the corresponding simulation results. Eq. (4.5) is used to transform  $DL$  into temperature. We know that the base  $DL$  average is equal to 4200 according to Fig. 4.11a, and the preheating temperature of the machine manufacturing room is set as  $198 \pm 7 ^\circ C$  in the experiment. The emissivity of the powder bed is contributed by polymer particles and the holes between the particles. The emissivity of the holes is equal to 1 because the holes are black and that of the PA polymer is equal to 0.8. The powder bed's emissivity calculated by the models shown in Chapter 2 is equal to 0.86. According to the value of powder bed's emissivity, the preheating temperature, and the value of  $DL$ , we finally obtain the coefficient  $C$  which is, according to Eq. (4.5), equal to 1.75. The time evolution of surface temperature is shown in Fig. 4.11b. The powder bed's

surface temperature sharply increases when the laser arrives, reaches the maximum of about  $488\text{ K}$  and comes back to the preheating temperature within  $0.1\text{ s}$ . In this figure, we see before the maximum temperature another temperature peak that corresponds to the unknown heating laser power. As it influences the temperature at a lever of  $2 - 4\text{ K}$ , we chose to ignore this phenomenon in the comparisons.

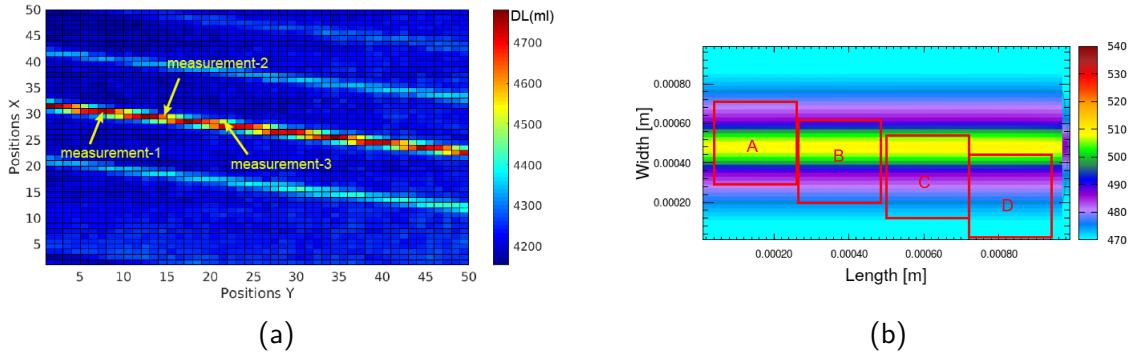


Figure 4.12: Numerical and experimental results at the chosen positions in the single-sweep situation (Case 3). (a) Three positions chosen in experimental photo. (b) Four positions chosen in simulation points for comparison.

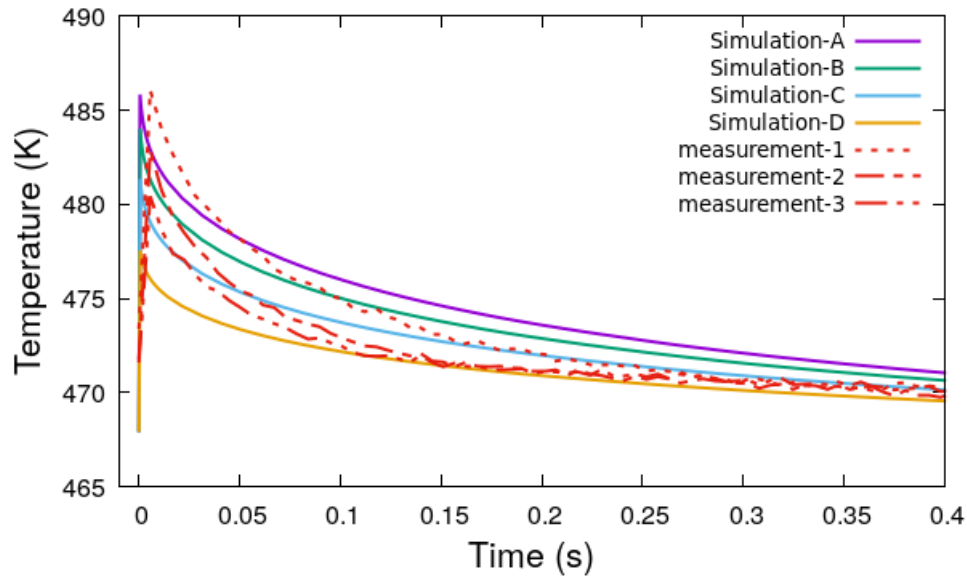


Figure 4.13: Numerical results at the chosen positions in the single-sweep situation (Case 3) : Time evolution of temperature.

As is explained in Chapter 3, the Finite volume method (FVM) is used for solving the heat equation in the simulation process and the dimension of each mesh is of  $20\ \mu\text{m} \times 20\ \mu\text{m} \times 10\ \mu\text{m}$ . But the IR camera used works with a pixel area of  $460\ \mu\text{m} \times 460\ \mu\text{m}$  which is much larger than the mesh size. In order to compare the numerical and experimental results, we average the numerical surface temperature over 529 meshes which cover the same surface as one pixel area of the IR camera. In Case 3, for an initial porosity of the powder bed equal to 0.3, Fig. 4.13 presents both the experimental results and numerical data of temperature time evolution. The curves Measurements-1, Measurements-2, and Measurements-3 are measurements of the IR camera at three positions, in which the pixel central has different

distance to laser center, which are shown in Fig. 4.12a. The curves A, B, C and D are the simulation results for the equivalent pixels shown in Fig. 4.12b. The comparison shows that the temperature kinetics during laser heating is more rapid in the numerical simulation than in the experiment and that of cooling phase is slower in the numerical simulation. But numerical results agree qualitatively with the measurements. One factor that influences the agreement is the powder bed's emissivity because the powder bed's surface changes from a rough surface before laser heating to a smooth surface after the melting. Also polymer emissivity depends on the polymer phase and changes during the sintering. Up to now, the evolution of the powder bed's emissivity is not considered. Uncertainty on the pixel's position also influences the agreement as a pixel with maximal  $DL$  value may not be centered on the laser axis.

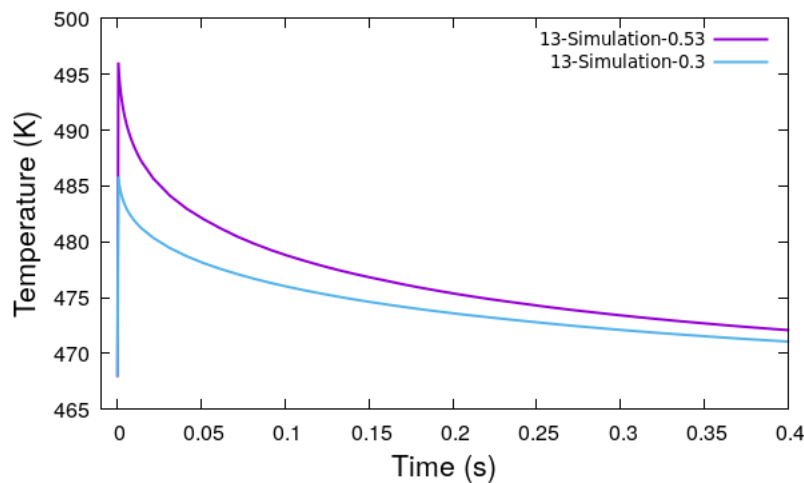


Figure 4.14: Influence of the initial porosity of the powder bed on temperature evolution.

The initial porosity of the powder bed is an important factor influencing the agreement. In the simulations, we consider the powder bed as a homogeneous medium where the initial porosity of the powder bed is in the range from 0.26 to 0.56, depending on the packing presser of the roller, the thickness of powder layers, the polymer particle surface, particle diameter, the aging degree of polymer and so on. As is shown in Fig. 4.14, the initial powder bed's porosity as an important parameter highly influences the temperature evolution during the SLS process. The maximum temperature and the cooling time increase with increasing the powder bed's initial porosity, because the melting process as a heat sink process is slower under lower porosity condition and surface temperature of the manufacturing part is lower.

Fig. 4.15 displays temperature time evolution obtained from numerical simulations and experiments for Cases 1, 2 and 3 with an initial porosity of 0.3. Again numerical results agree approximately the experimental measurements, which seems to indicate the viability of the model. Numerical results show that the maximum temperature increases from 493 K to 499 K when laser power is increased from 13 W (Case 3) to 15 W (Case 1), while in the experiments the maximum temperature does not seem to depend on the laser power and remains about 485 K. This can be caused by the uncertainty on the pixel position as is explained in Fig. 4.36a. The shutter time is another possible reason, the camera shutter time of 0.0056 s is not small enough to capture the transient maximum temperature.

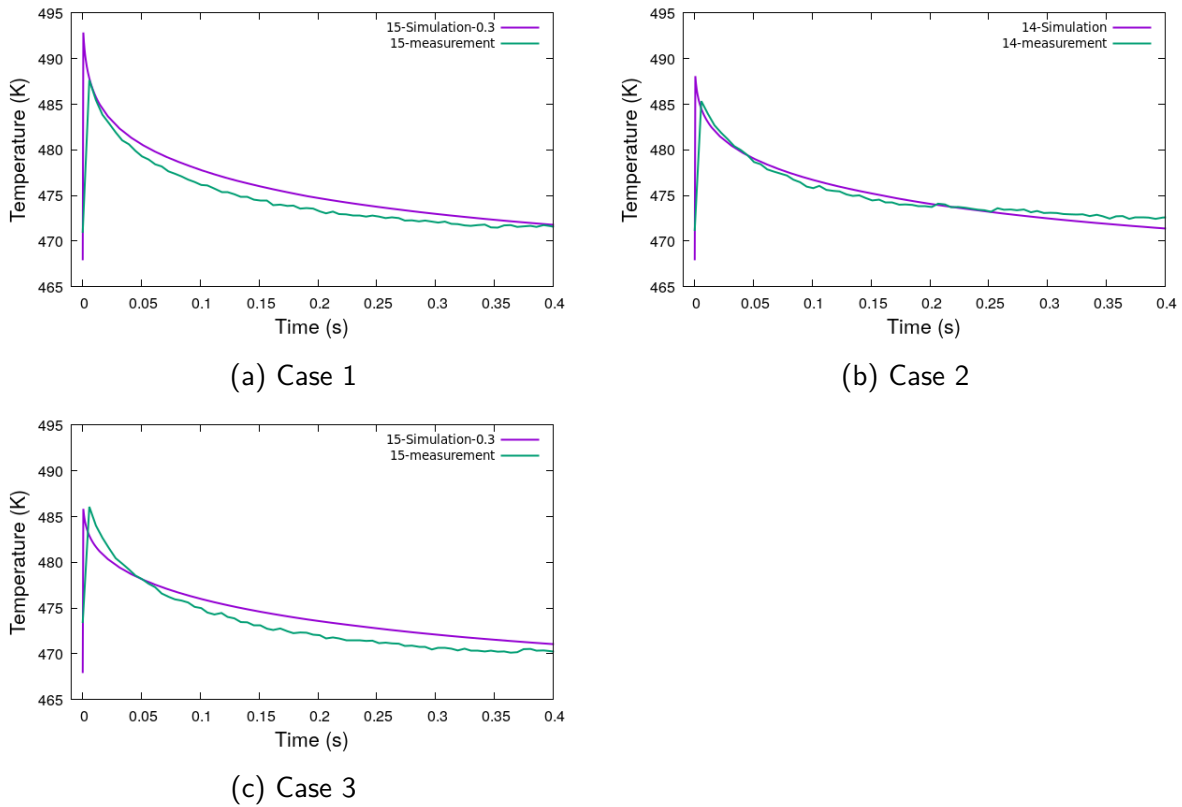


Figure 4.15: Comparison of temperature time evolution between measurements and simulations.

### 4.3 Multi-sweep and single-layer processes

Fig. 4.16 shows a picture of the powder bed with 4 working samples of  $0.05\text{ m} \times 0.01\text{ m}$ : time evolution of surface temperature is recorded by an IR camera and the dimension of the samples are also measured (Fig. 4.17 displays a photo showing the sample's thickness and Fig. 4.18 shows the samples' length and width.). In multi-sweep cases, we focus on studying how the scanning space and scanning length affect heating overlap, heat transfer and sintering process, In a multi-sweep process, laser scanning can be both horizontal and vertical and scanning lengths are determined according to the dimension of the manufactured parts. A scheme of laser scanning is shown in Fig. 4.19.

In a multi-sweep SLS situation, the influential parameters include the scanning length, laser scanning space, laser power and laser moving speed. We study nine experimental cases with different energy densities as is listed in Tab. 4.3, an IR camera is used to capture the digital level ( $DL$ ) of the heated area part and time evolution of surface temperature is obtained for the SLS process. Comparison of the experimental results with the numerical ones allows to qualify the ability of our models.

#### 4.3.1 Influence of laser moving direction and laser power model

Fig. 4.19 shows two typical sweeping methods in our experiments, the horizontal type (Fig. 4.19b) with a longer scanning length and the vertical type (Fig. 4.19a) with a shorter scanning length. How the scanning type influences the heat transfer in the SLS process is shown in the following.

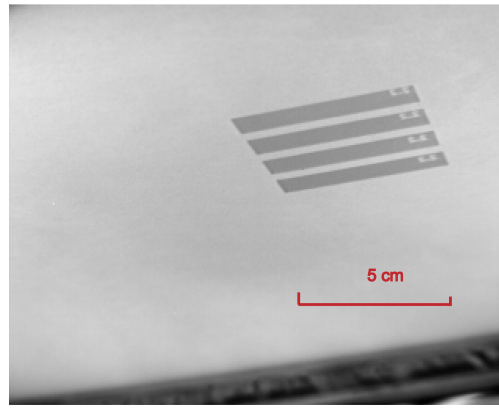


Figure 4.16: Picture during a SLS manufacturing process. A multi-sweep process allows to melt polymer powder in the controlled areas in one single-layer and manufacture multiple pieces. This process can be repeated for multi-layers and allows to produce parts of bigger dimensions.

Table 4.3: Summary of nine experimental cases.

Case	Power ( $W$ )	laser speed ( $m/s$ )	scanning space ( $mm$ )	Energy density ( $J/cm^2$ )
1	15	3.5	0.22	1.95
2	14	3.5	0.22	1.8
3	13	3.5	0.22	1.7
4	15	3.6	0.22	1.9
5	15	3.3	0.22	2.06
6	15	3.1	0.22	2.2
7	15	3.5	0.23	1.86
8	15	3.5	0.21	2.04
9	15	3.5	0.20	2.14

Figs. 4.20 and Fig. 4.21 present the  $DL$  evolution with time recorded by the IR camera for both the vertical and horizontal scanings. The  $DL$  evolution in the vertical situation is shown in Fig. 4.20, and the one in the horizontal situation is shown in Fig. 4.21. The  $DL$  for the horizontal scanning is equal to  $6000\text{ ml}$  and less than  $6700\text{ ml}$  for the vertical scanning. In Fig. 4.20, for the vertical scanning the  $DL$  at the edge of the samples is much higher than in the middle of the samples. This phenomenon is not clear in the horizontal scanning situation (Fig. 4.21). The heating history at the edge of a sample is more complex in the vertical scanning situation. The edge part is easy to get more preheating energy because the previous sweeps do not have time to be cooled down and this leads to a higher preheating temperature. Also at the edge and the corners of a sample, complex laser moving traces result in repeated local heating and leads to more energy input in these positions when vertical scanning is used. In the horizontal scanning situation, a longer time is left for cooling: this reduces the overlap heating impact and makes more stable the temperature in the middle part and at the edge of a sample. In our numerical work, we choose to get rid of the end parts of a sample and simulate only its central part. The computational domain chosen is of dimension  $1.5\text{ mm} \times 2\text{ mm} \times 0.5\text{ mm}$ , which corresponds to only a small central part of the samples manufactured. Furthermore, laser power is applied only to part of the domain: for example it is applied to a length of  $1.2\text{ mm}$  because of the adiabatic boundary conditions. We checked that this length is longer enough so that time evolution of temperature presented in the present work does not depend on it. The initial porosity of the powder bed is equal to 0.3 except for the case of studying the influence of the initial porosity.

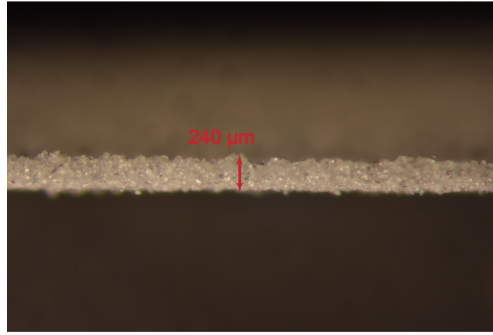


Figure 4.17: Sample picture showing its thickness.

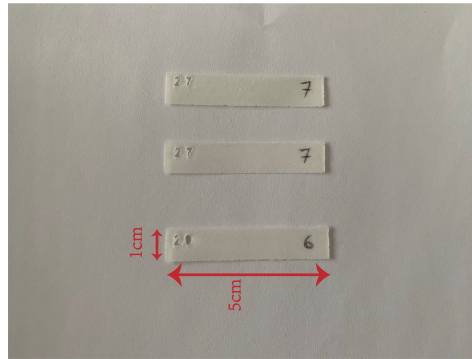
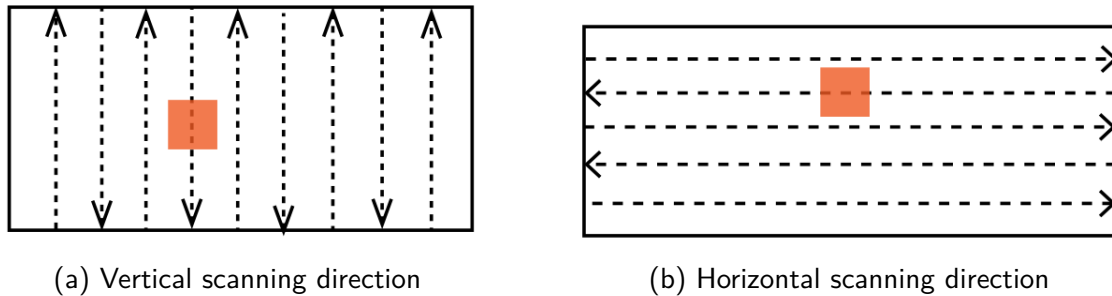
Figure 4.18: Sample picture in  $X - Y$  plane.

Figure 4.19: Scheme of laser moving directions.

Fig. 4.22 shows, using a scattering model, the numerical results of surface temperature in the  $x - y$  plane for 6 sweeps during a multi-sweep and one-layer process. It concerns Case 1 in a horizontal scanning situation with a preheating temperature of  $465\text{ K}$ , the scanning length considered is equal to  $50\text{ mm}$  and only six laser tracks are simulated because trac-1 and trac-6 are almost independent. Given the scanning length of  $50\text{ mm}$  and the laser moving speed of  $3.5\text{ m/s}$ , the laser sweeps in the simulated domain are separated by  $0.05/3.5\text{ s} = 0.0145\text{ s}$ . Figs. 4.22a-4.22i show time evolution of surface temperature and the molten area. After the first laser sweep Fig. 4.22a shows that surface temperature along trac-1 is increased and just after the second sweep surface temperature along trac-1 and trac-2 is increased further (Fig. 4.22b) before being decreased (Fig. 4.22c). The third sweep increases again surface temperature along trac-1, trac-2 and trac-3 (Fig. 4.22d) and this confirms that the three successive sweeps influence each other. It is difficult to see from Fig. 4.22e if the fourth sweep influences temperature on trac-1. After the sixth sweep surface temperature along all the tracks decreases (Figs. 4.22h and 4.22i).

Fig. 4.23 illustrates the heat diffusion in the  $y - z$  plane of the powder bed for Case-1

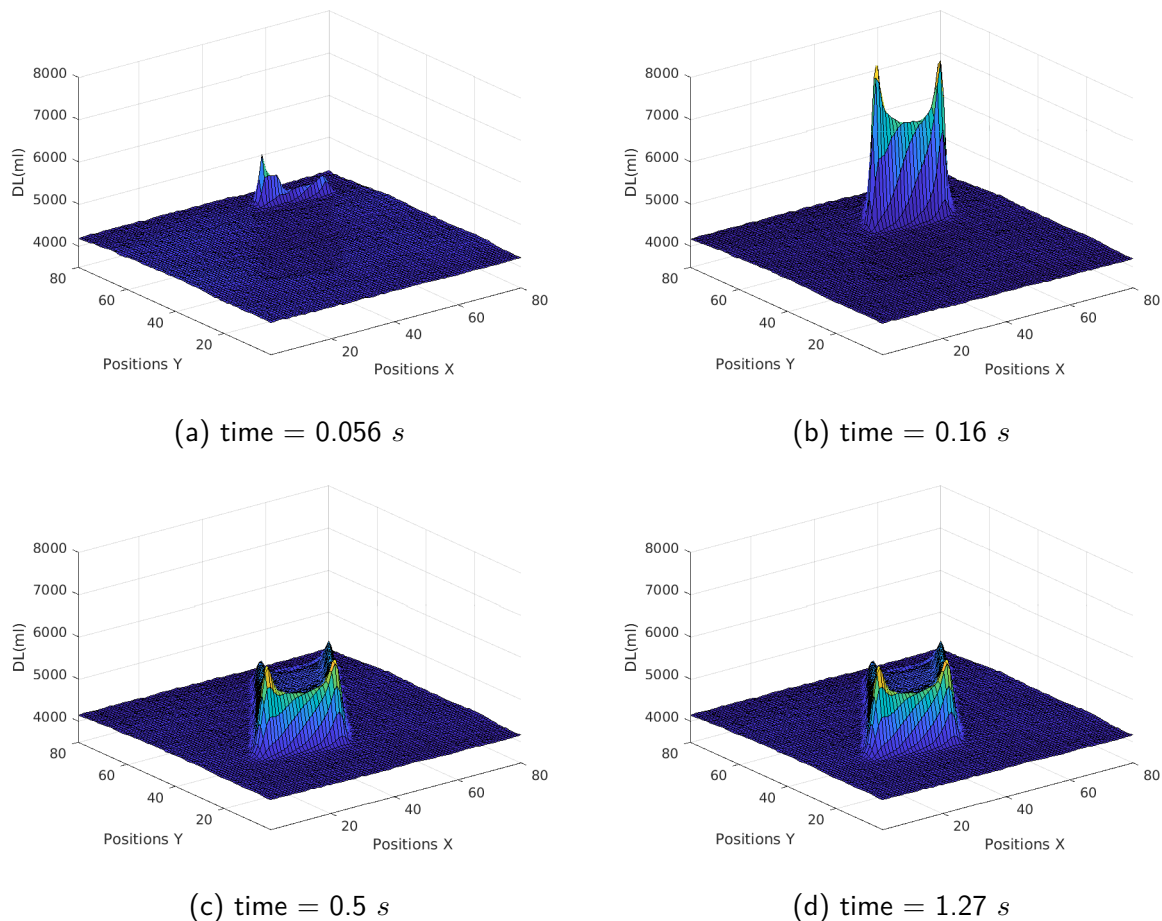


Figure 4.20: Vertical scanning type:  $DL$  distributions during the scanning.

with horizontal scanning. These figures show not only heat diffusion in depth direction but also the shrinkage resulted from coalescence and densification. The diffusion depth is not really influenced by the laser sweeps although a slight difference is observed. The heat diffusion's depth, about  $200 \mu m$ , is in the same order as in the single-sweep cases. But the shrinkage in the powder bed is obvious and is about  $50 \mu m$  in Fig. 4.23i, which is very important compared with a heat diffusion's depth of about  $200 \mu m$ . Shrinkage is therefore an important element for reliable prediction of SLS manufacturing process.

For a better understanding of the temperature distribution in the powder bed, we choose about the domain mid-width 10 points to study the time evolution of surface temperature, their positions are shown in Fig. 4.24. The 5 points from trac-1 to trac-5 are at the central line of each laser sweep and the 5 points from position-1 to position-5 are chosen between trac-3 to trac-4.

Fig. 4.25 shows temperature time evolution at different positions: 5 points from trac-1 to point trac-5, 5 points from positions-1 to point positions-5 and 5 depth positions under trac-3. Compared with a single-sweep situation illustrated previously, temperature of each point at the central line of a laser track has a higher level. This is caused by the heating overlap. Any laser sweep influences temperature distributions in the neighbouring tracks, keeps the maximum temperature for a longer time, promotes the coalescence of polymer particles, and helps air escaping from the powders. As laser moving speed, laser scanning length and scanning space affects strongly the heating overlap, they are the main parameters that influence the temperature distribution in a multi-sweep SLS process.

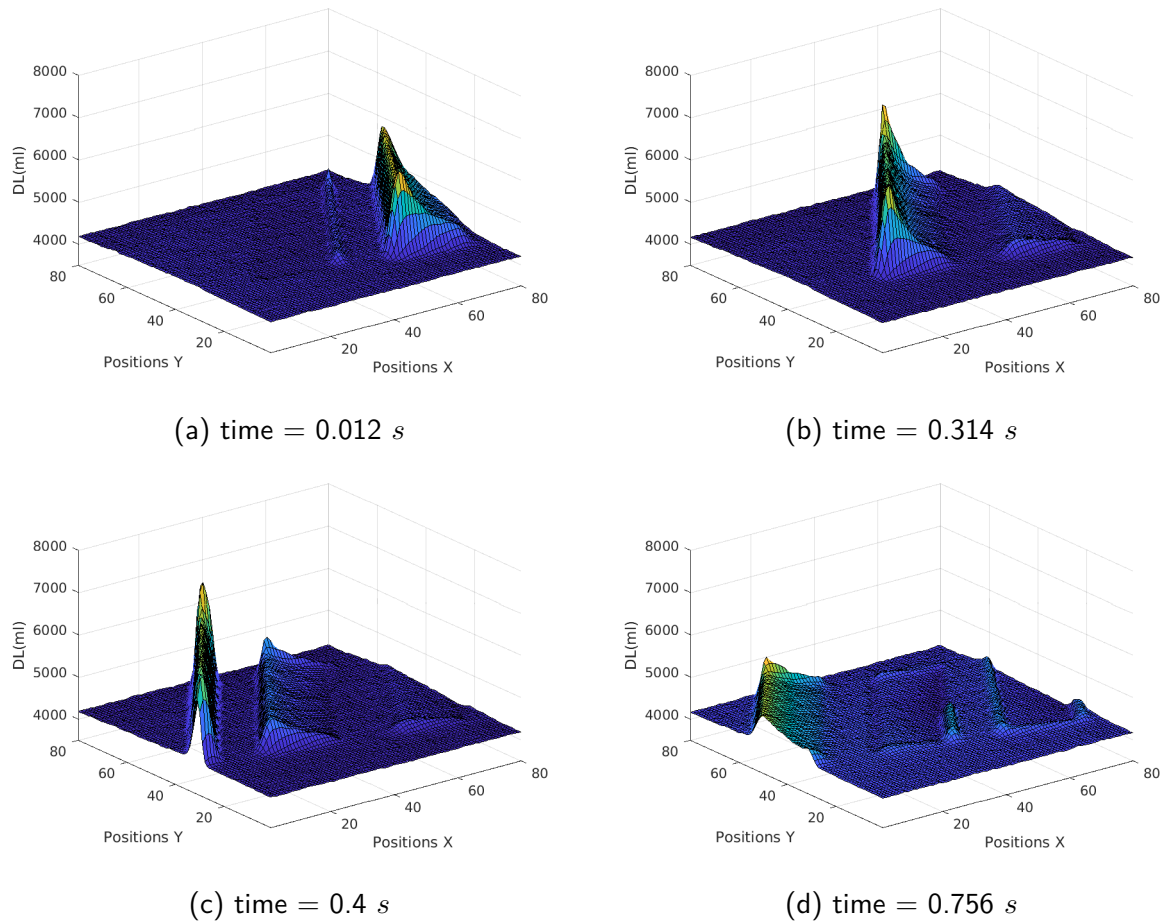


Figure 4.21: Horizontal scanning type:  $DL$  distributions during the scanning.

Fig. 4.25a shows the time evolution of surface temperature at the positions from trac-1 to trac-5. It is clear that the first laser sweep influences temperature traces at the positions trac-2 and trac-3 and that it does not seem to influence temperature at the positions trac-4 and trac-5. In the same way the fourth sweep does not seem to influence temperature at the position trac-1. For each laser track, the maximum temperature occurs when the next sweep is applied: for example, at the position trac-1 temperature is maximal after the application of the second sweep, at the position trac-2 the maximum is observed when the third sweep is realised, etc. Furthermore, time traces of temperature at the positions trac-3, trac-4 and trac-5 are similar in the sense that their maximum temperature is about  $539\text{ K}$  and that there seems to be only a time delay between them. This is confirmed by Fig. 4.25b when time delays are removed:  $T_3(t)$  at trac-3,  $T_4(t - 0.0145)$  at trac-4 and  $T_5(t - 0.029)$  at trac-5 behave exactly in the same way. This suggests that time traces of temperature at the positions trac-3 and trac-4 are recurrent and could represent the general behaviour of most of the sweeps (excluding the first two and the last two sweeps) in multi-sweep SLS processes. For the laser track  $n$ , the laser sweep  $n - 2$  begins to influence its temperature distribution (increase its maximum temperature). The increase of its maximum temperature continues with the laser sweeps  $n - 1$ ,  $n$  and  $n + 1$ . Although the sweep  $n + 2$  modifies its temperature distribution, the maximum does not increase anymore. This means that maximum temperature on the track  $n$  is observed when the laser sweep  $n + 1$  is applied. If we take trac-2 as an example, the first peak is caused by the first laser sweep that heats trac-2, the second temperature peak of  $518\text{ K}$  corresponds to the second laser sweep. When the third laser sweep arrives, temperature at track-2 increases to a peak value of  $530\text{ K}$ . Although the fourth laser sweep

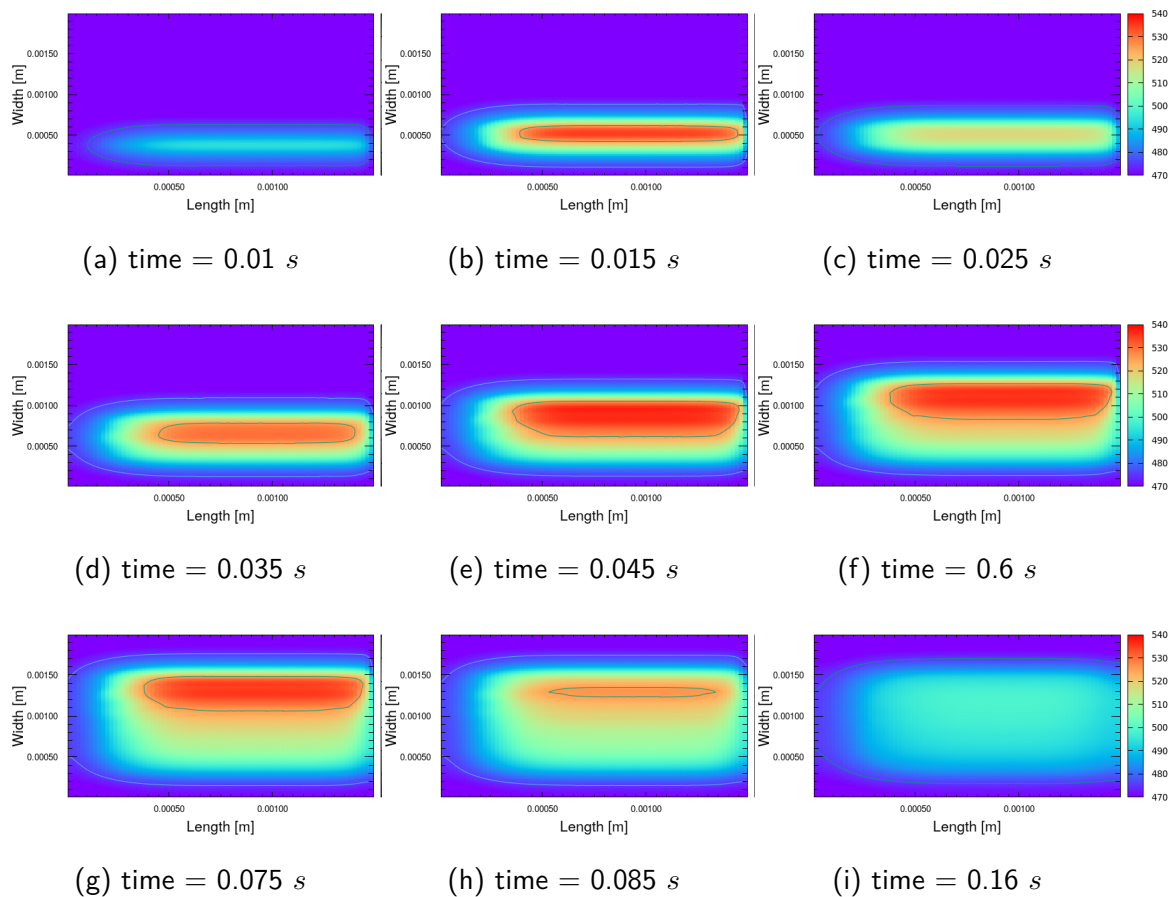


Figure 4.22: Surface temperature distribution during a multi-sweep SLS process (Case 1) using a scattering model: a scanning length of  $0.05\text{ m}$  is considered and the studied scanning is horizontal, but note that in the simulation laser power is only applied to a length of  $1.2\text{ mm}$ .

influences its temperature distribution, the peak value never exceeds  $530\text{ K}$ . The fifth and sixth laser sweeps do not seem to influence temperature at trac-2.

Fig. 4.25c shows the time evolution of surface temperature at the positions from position-1 to position 5 (Fig. 4.24). In the region of heating overlap, temperature has different time traces for short time  $t < 0.1\text{ s}$  but for  $t > 0.1\text{ s}$ , it has the same behaviour. We choose several depth positions under trac-3 to study temperature evolution in the depth direction: the results are shown in Fig. 4.25d and the heating influenced depth is around  $200\text{ }\mu\text{m}$ .

In a multi-sweep SLS process, it is also interesting to understand the effect of scattering on heat transfer. We use again the BL model without scattering to study heat transfer in the powder bed for Case 1 by using an initial porosity of 0.3. Apart from the BL model, all the parameters remain unchanged in comparison with the case using a scattering model.

Fig. 4.26 shows time evolution of temperature in a multi-sweep process under the non-scattering condition. Without scattering, time traces of temperature all increase sharply to a maximum at the beginning of its own laser sweep: at trac-1 the maximum temperature is observed immediately after the first laser sweep, the second laser sweep influences only slightly its temperature evolution and other laser sweeps do not seem to have any effect. Compared with the case using a scattering model, the maximum temperature on each laser track, between  $570\text{ K}$  and  $580\text{ K}$ , is much higher. Similar result is also observed for other tracks. It can be

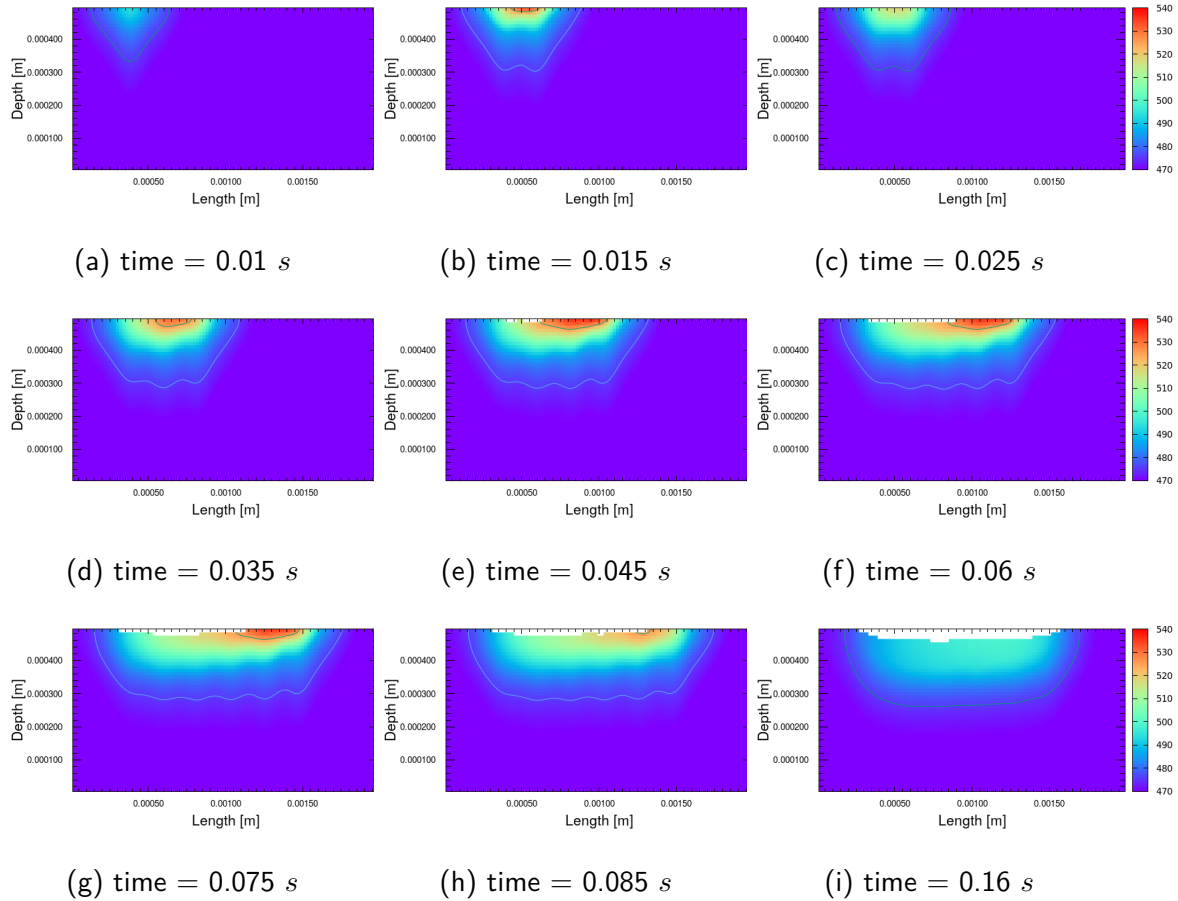


Figure 4.23: Temperature distribution in the  $y-z$  plane at the mid-width during a multi-sweep SLS process (Case 1) using a scattering model: a scanning length of  $0.05\text{ m}$  is considered and the studied scanning is horizontal, but note that in the simulation laser power is only applied to a length of  $1.2\text{ mm}$ .

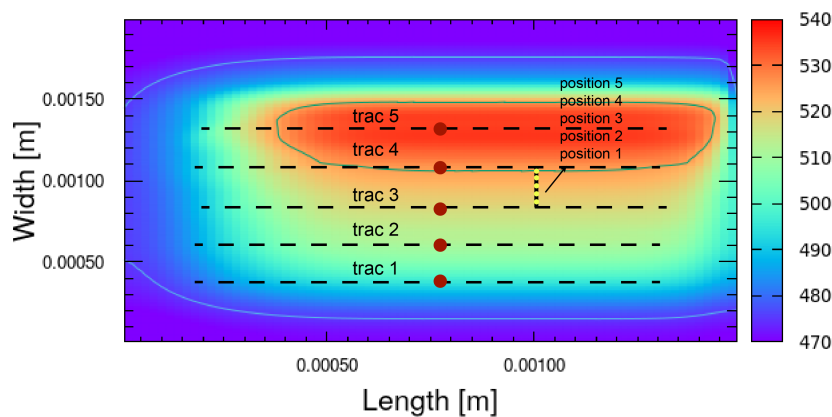


Figure 4.24: 10 points in the central part of the computational domain are chosen for the comparison of temperature time traces. One point is chosen for each of the first 5 tracks and another 5 points are chosen between trac-3 and trac-4.

said that along the central line of a laser track temperature evolution is almost not influenced by other laser sweeps. In the region of heating overlap, temperature evolution is influenced

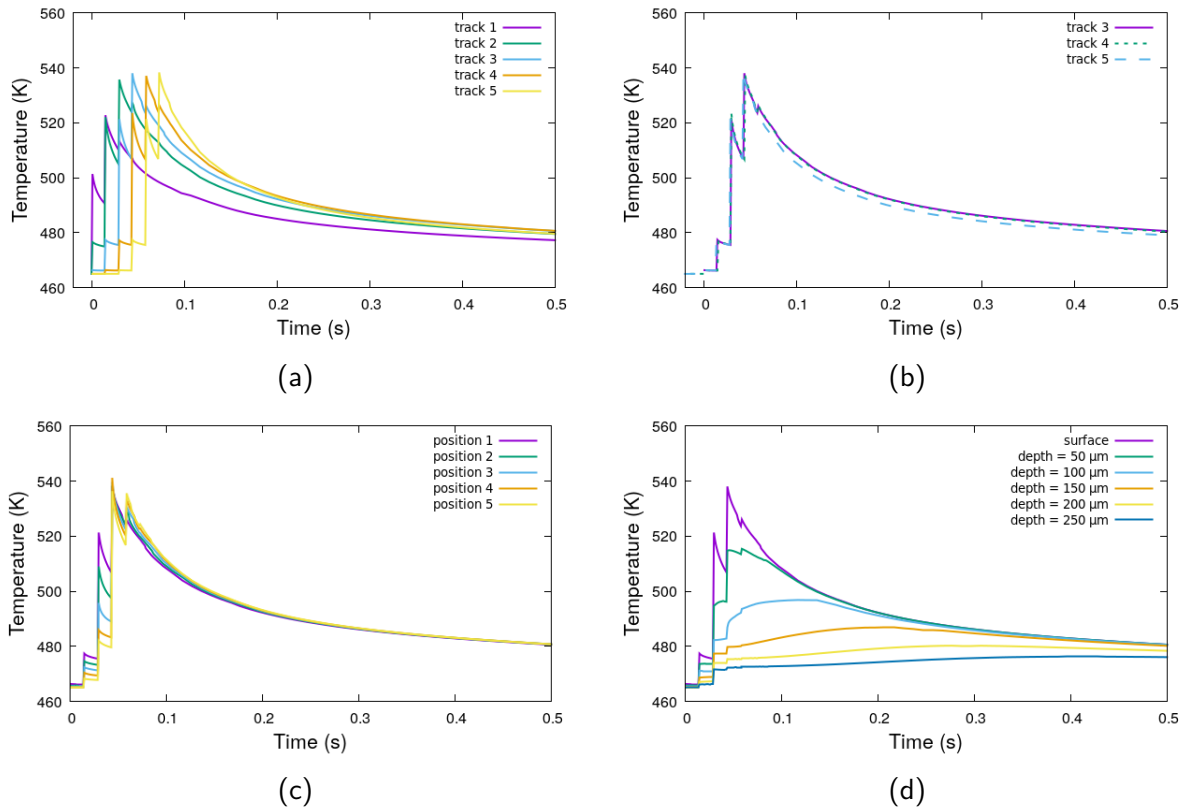


Figure 4.25: Time evolution of temperature at various positions about the domain mid-width (Case 1) and numerical simulation is performed using a scattering model. (a) (b) At the tracks' centers. (c) At positions from position-1 to position-5. (d) At different depth positions under trac-3. Note that in (b) time delays between trac-3, trac-4 and trac-5 are removed by drawing  $T_3(t)$ ,  $T_4(t - 0.0145)$  and  $T_5(t - 0.029)$ .

by the two neighbouring sweeps (Fig. 4.26b): huge temperature difference is observed at the points from position 1 to position 5 for  $t < 0.1$  s, but for  $t > 0.1$  s temperature evolution is similar. Fig. 4.26c presents time evolution of temperature at 5 depth positions. Temperature decreases with depth increasing because of the energy decay and the heating influenced depth around  $250 \mu\text{m}$  is slightly larger than in the scattering case.

Fig. 4.27 compares time evolution of temperature obtained in the cases with and without scattering. Two surface points (trac-1 and trac-2) and two depth positions (depth of  $200 \mu\text{m}$ ) under trac-1 and trac-4 are chosen. Bot Fig. 4.27a and Fig. 4.27b show that the BL model yields higher maximum temperature while maximum temperature is lower with the scattering model. Furthermore, with the BL model temperature evolution on each point (trac-1 or trac-4) depends only on its own laser sweep (the first laser sweep for trac-1 and the forth laser sweep for trac-4) while using the scattering model temperature evolution at each point depends on the neighbouring laser sweeps. In the depth direction Figs. 4.27c and 4.27d indicate that at the depth position of  $200 \mu\text{m}$  the BL model yields always higher temperature than the scattering model. This leads to the same conclusion of a single-sweep process that the BL model predicts a larger thickness of the final parts.

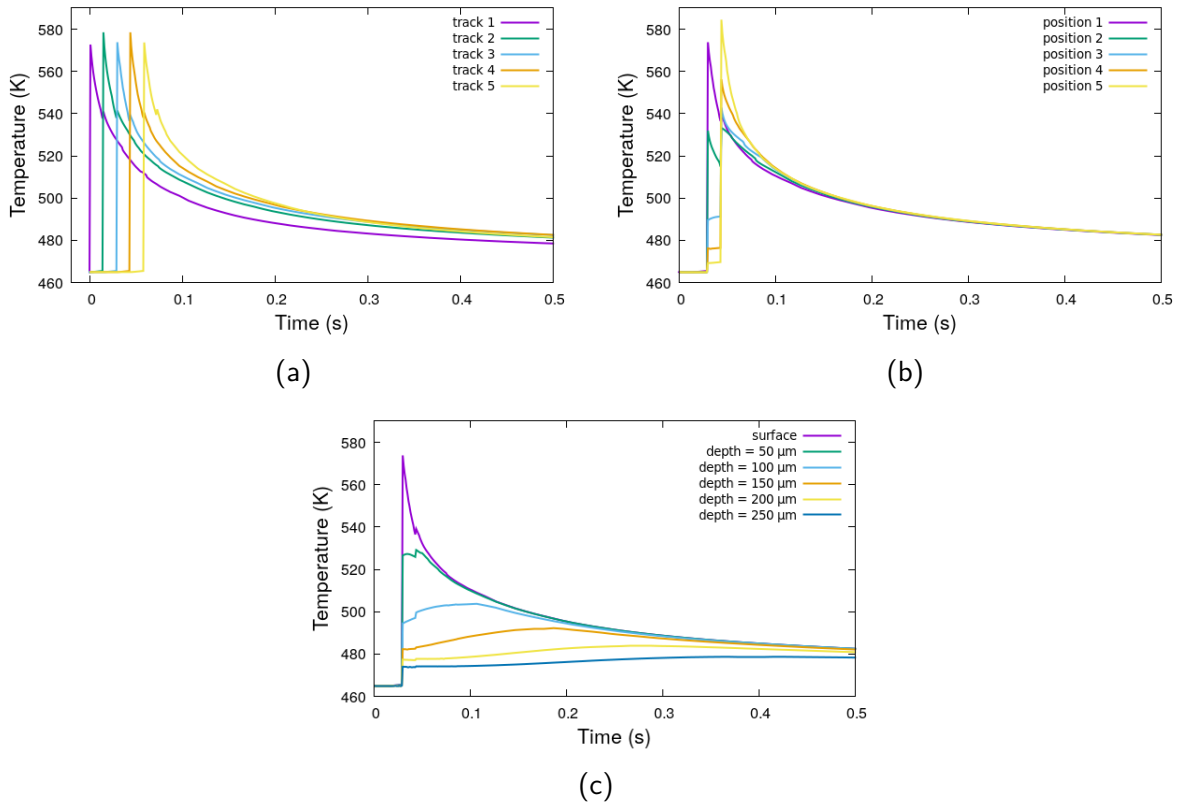


Figure 4.26: Time evolution of temperature at various positions about the domain mid-width (Case 1) and numerical simulation is performed using BL model without scattering. (a) At the tracks' centers. (b) At positions from position-1 to position-5. (c) At different depth positions under trac-3.

### 4.3.2 Parametric analysis

Laser power, scanning speed, and scanning space define laser energy density, an important factor in a multi-sweep process. Scanning length, initial porosity of the powder bed and preheating temperature also influence the process. We are trying to understand how scanning length, scanning speed, laser power and scanning space, powder bed's preheating temperature and initial porosity influence the thermal history in the powder bed during multi-sweep SLS processes. From now on only scattering model is considered. Furthermore, numerical results of temperature presented are averaged temperature over one pixel area of the IR camera.

#### Scanning length

In a multi-sweep situation, temperature evolution at a point is a result of several sweeps because the previous neighbouring laser sweeps preheat the powders and the following laser sweeps reheat this area. The scanning length decides the cooling time between laser sweeps which influence the preheating and reheating phenomena.

Fig. 4.28 shows time evolution of surface temperature averaged over one IR pixel area about trac-4 for scanning length ranging from 0.01  $m$  to 0.05  $m$  (case-1). Note that the averaged temperature has a slightly lower maximum compared with the temperature localised at trac-4. In fact, a length of 0.05  $m$  which is the sample length corresponds to the horizontal

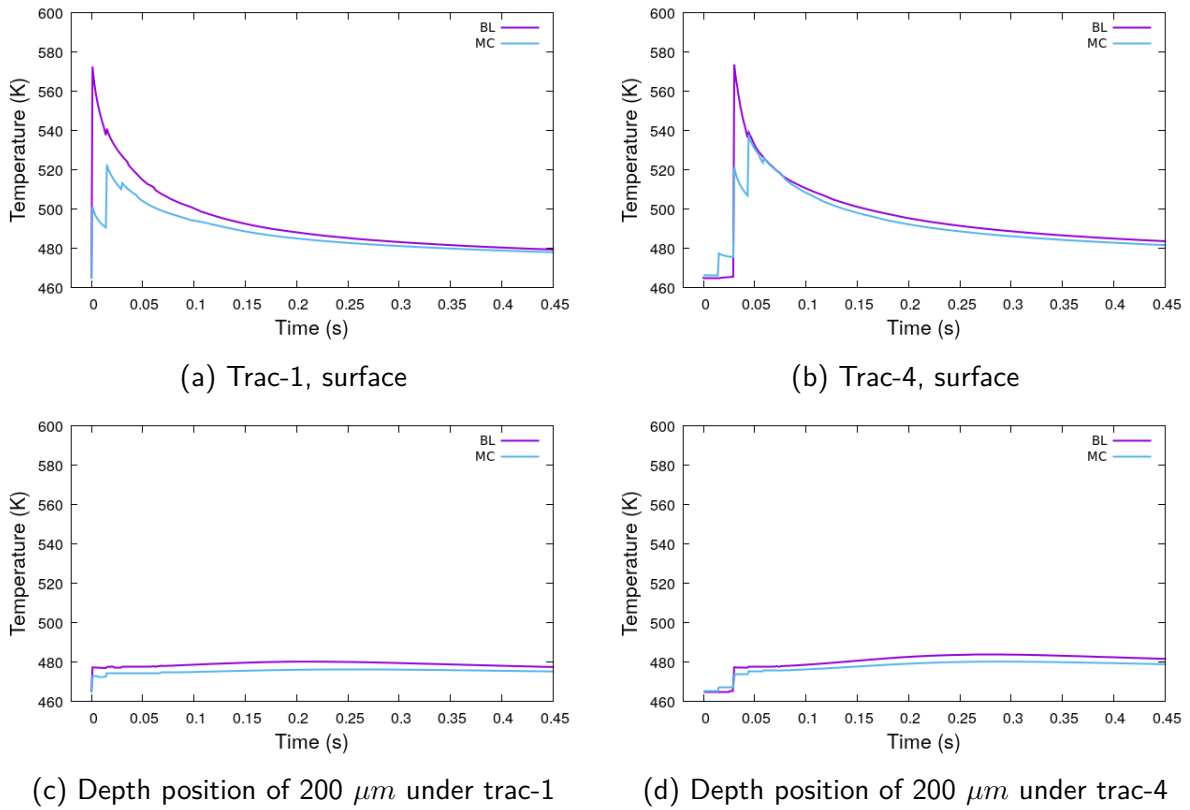


Figure 4.27: Comparison of the results between the cases with and without scattering. Potions chosen are trac-1 and trac-4 on the bed surface and at a depth position of 200  $\mu\text{m}$ .

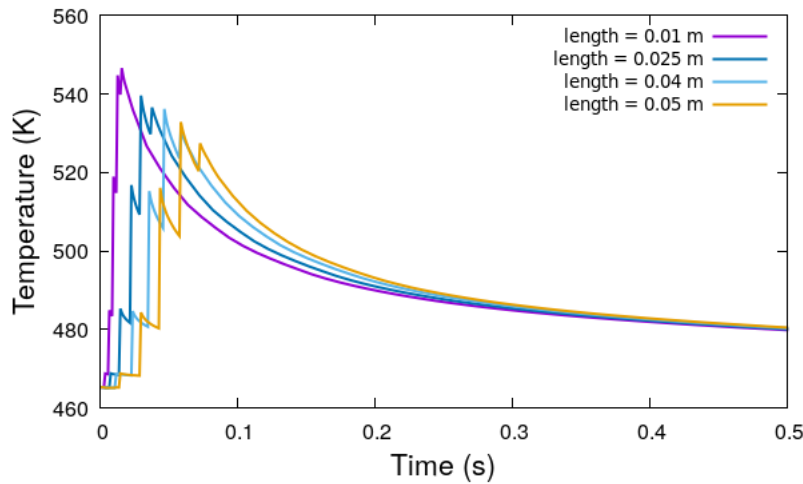


Figure 4.28: Influence of scanning length: time evolution of temperature averaged over one IR pixel area centered on trac-4 (case-1). Scanning length specifies laser scanning frequency and therefore cooling time at a local position.

scanning and a length of 0.01  $m$  which is the sample width approaches the vertical scanning case. For the smallest scanning length of 0.01  $m$ , the cooling time is the shortest, temperature increase is the fastest and the maximum peak temperature of 544  $K$  is the highest. With increasing scanning length and cooling time, temperature increase is slowed down and the maximum temperature reached is decreased. Apart from the influence on short time behaviour and maximum temperature, for  $t > 0.2$   $s$  the curves are similar and the temperature drops to the preheating temperature within 1  $s$ .

### Scanning space between laser sweeps

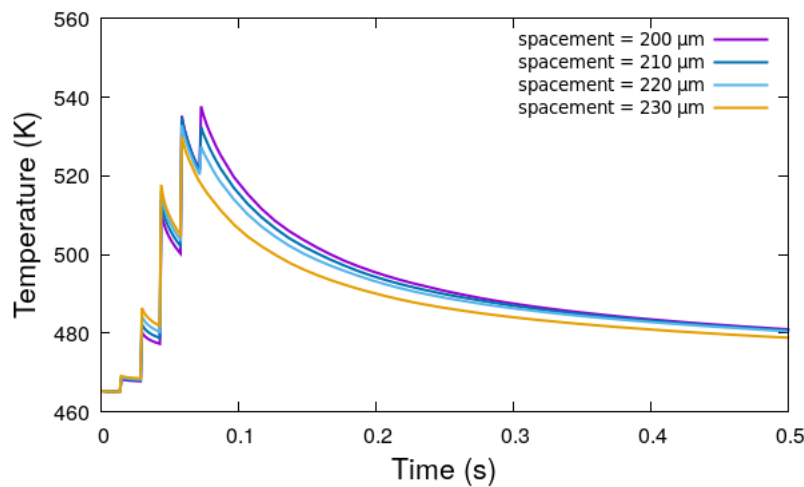


Figure 4.29: Influence of scanning space: time evolution of temperature averaged over one IR pixel area about the surface center.

When laser scanning space is varied from  $200 \mu m$  to  $230 \mu m$  (cases 9, 8, 1 and 7 respectively), temperature profiles obtained are shown in Fig. 4.29. As other parameters (laser power, laser moving speed and scanning length) remain the same, the increase in scanning space decreases energy density and the maximum temperature from  $536 K$  for the scanning space equal to  $200 \mu m$  and  $517 K$  for the scanning space of  $230 \mu m$ . Higher maximum temperature means longer keeping time of the molten part, there is therefore more time for air escape and the porosity of the final part would be smaller.

### Laser power

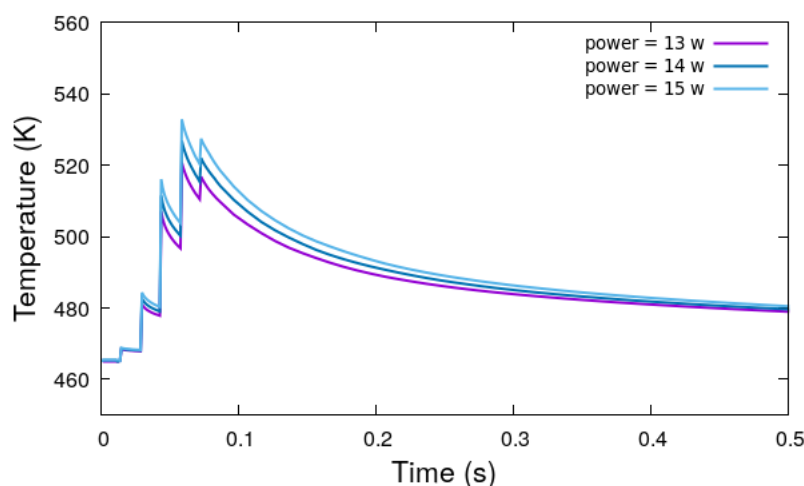


Figure 4.30: Influence of laser power: time evolution of temperature averaged over one IR pixel area about the surface center.

Fig. 4.30 presents the time evolution of surface temperature at the surface center of the computation domain for 3 laser powers ( $13 W$ ,  $14 W$  and  $15 W$ ). The scanning length, the laser moving speed and the scanning space are equal to respectively  $0.05 m$ ,

3.5  $m/s$  and 220  $\mu m$ . With increasing laser power, The maximum temperature increases from 520  $K$  to 535  $K$ , but time traces of surface temperature are similar. Comparing with the single-sweep case, surface temperature is higher and the corresponding coalescence and crystallization processes are different in multi-sweep cases.

### Scanning speed

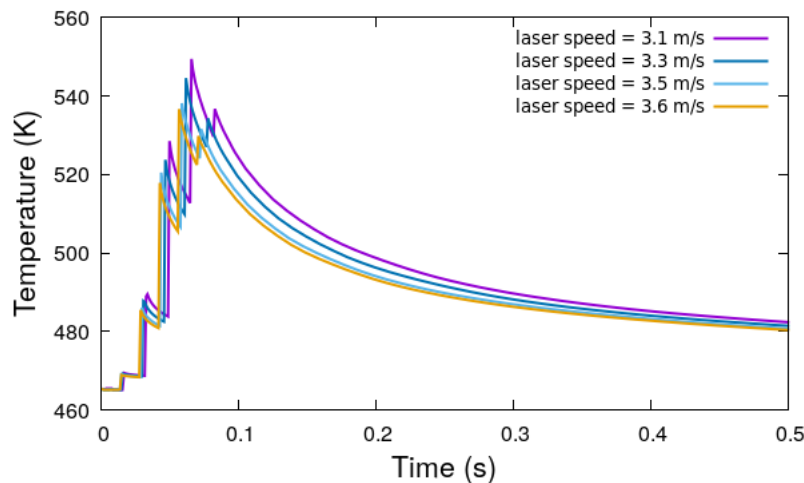


Figure 4.31: Influence of scanning speed: time evolution of temperature averaged over one IR pixel area about the surface center

To understand the influence of the laser moving speed, cases 6, 5, 1 and 4 are studied: laser moving speed increases from 3.1  $m/s$  to 3.6  $m/s$ . This means that energy density is decreased. The results of temperature evolution with time are shown in Fig. 4.31. The maximum temperature with 3.1  $m/s$  is equal to 558  $K$  and is decreased to 540  $K$  when the laser moving speed increases to 3.6  $m/s$ , this is also due to the decrease in energy density. Higher maximum temperature means also longer keeping time in the molten state and longer cooling period.

### Initial porosity of powder bed

Fig. 4.32 displays time evolution of surface temperature obtained for two initial porosities of the powder bed (0.3 and 0.53). The maximum temperature reached increases from 530  $K$  for the porosity of 0.3 to 560  $K$  for the porosity of 0.53. The conclusion is in agreement with that drawn in a single-sweep case. As is seen in Chapter 3, particles' arrangement and the morphology of the powders influence laser photons transmission in the powder bed. The attenuation coefficient is highly dependent on the particles' arrangement: it is higher for lower initial porosity. This leads to more energy absorption by the topper layers at lower porosity. However, as the powder bed at higher porosity has lower  $\rho$  and  $C_p$  and lower melting latent heat, the maximum temperature at higher porosity is not lower but higher.

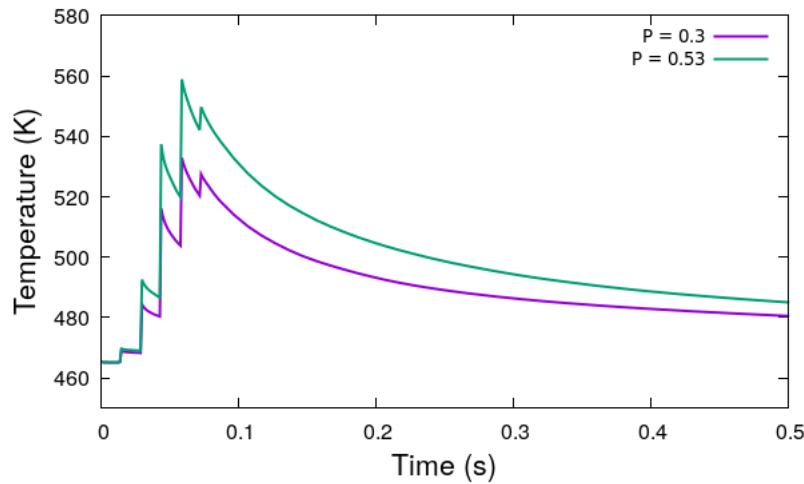


Figure 4.32: Influence of initial porosity: time evolution of temperature averaged over one IR pixel area about the surface center.

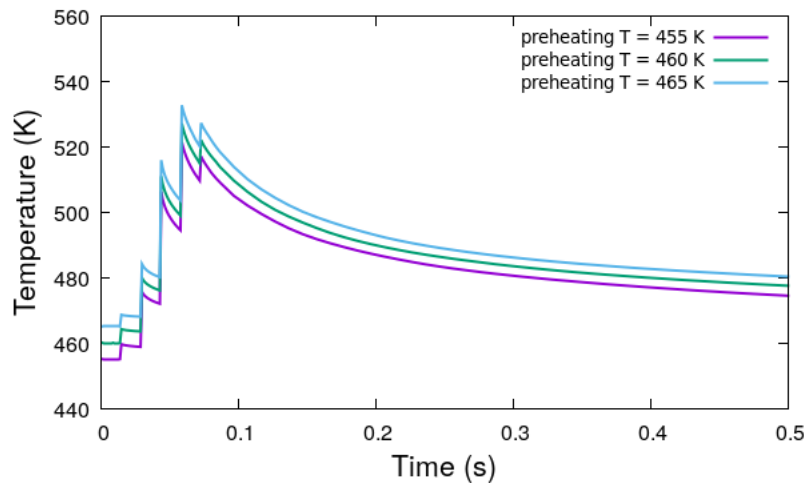


Figure 4.33: Influence of preheating temperature: time evolution of temperature averaged over one IR pixel area about the surface center.

### Preheating temperature

Fig. 4.33 displays time evolution of surface temperature at the surface center of the computation domain for Case 1. The maximum temperature is higher for higher preheating temperature. In practice, the preheating temperature for PA6 polymer is set just below the melting temperature to reduce the thermal stress and increase the keeping time of the molten state.

### 4.3.3 Comparison with experimental results

Although the calibration of the IR camera was explained previously, we stress again the complexity in converting the digital level into temperature. The digital level or the luminance  $L_v$  is recorded by the IR camera. An example of its time evolution is shown in Fig. 4.34a. We use the equation  $L_v = FA\varepsilon\sigma T^4$  to calculate temperature from the luminance with  $\varepsilon$  emissivity and  $\sigma$  Stefan-Boltzmann constant. In a multi-sweep situation, we assume that the emissivity

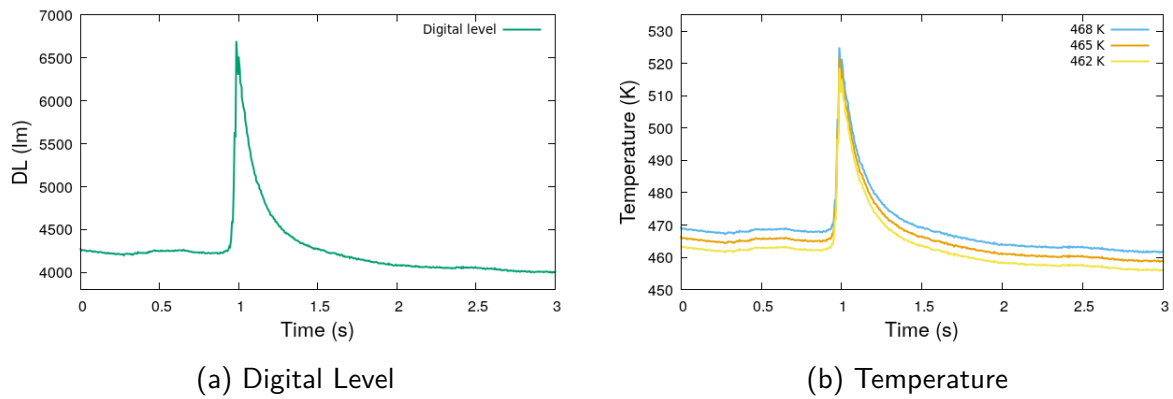


Figure 4.34: Digital level and conversion into temperature using various adjustment parameters (case 7 with energy density of  $1.86 \text{ J/cm}^2$ ).

of the heated part is equal to 0.82 and that any variation due to polymer phase change, porosity evolution and surface evolution is neglected. The adjustment coefficient  $C$  ( $C = FA$ ) is calculated according to the machine's room temperature which is in the range of  $460 \text{ K}$  and  $470 \text{ K}$  and is taken as from 1.9 to 2.0. Fig. 4.34b displays the influence of the preheating room temperature. With the preheating room temperature of  $465 \text{ K}$ , the maximum temperature is equal to  $521 \text{ K}$ . The preheating room temperature of  $470 \text{ K}$  leads to a maximum temperature equal to  $525 \text{ K}$ . As more uncertainty related to the emissivity should be added, the comparisons which are and will be performed remains unfortunately qualitative. This indicates that measuring accurately surface temperature in any SLS processes still remains challenging.

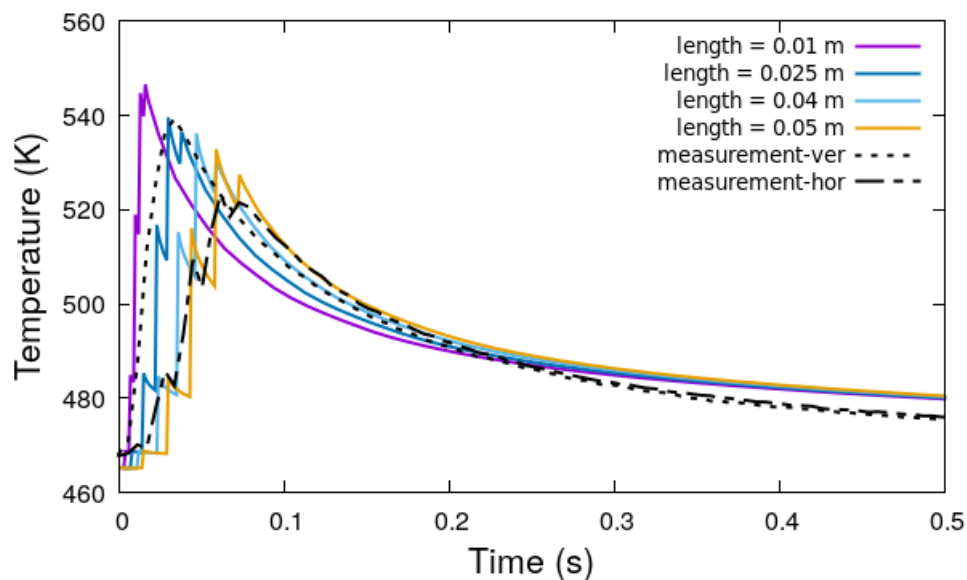


Figure 4.35: Comparison between numerical and experimental results: time evolution of temperature about trac-4. Experimental results are obtained for both the horizontal and the vertical scanings. Numerical simulations are performed for scanning length varying from  $0.05 \text{ m}$  (experiment of horizontal scanning) to  $0.01 \text{ m}$  (experiment of vertical scanning).

The scanning length influences the maximum temperature because longer scanning length increases locally the cooling time and decreases the heating overlap. The dimension of the manufactured samples is of  $50 \text{ mm} \times 10 \text{ mm}$ , the horizontal scanning uses a scanning length of  $50 \text{ mm}$  and the vertical scanning uses a scanning length of  $10 \text{ mm}$ . In the experiments,

both scanings are realised as is shown in Fig. 4.20 and Fig. 4.21. Numerical simulations are performed for scanning lengths varying from 10 *mm* to 50 *mm*. In Fig. 4.35 the time evolution of temperature measurement is named as "measurement-ver" and "measurement-hor". They should be compared with the numerical curves obtained with respectively the scanning lengths of 10 *mm* and 50 *mm*. With the horizontal scanning, the maximum temperature measured is lower than that obtained with the vertical scanning. When compared with the numerical results, the experimental maximum temperature is lower for both the horizontal and the vertical scanings. For the horizontal scanning, both the experimental and the numerical curves are similar. But for the vertical scanning, the maximum temperature in numerical simulation occurs earlier than in the experiment. Note that the time necessary for laser to change its direction at the end of a scanning is not considered in the simulations, this time may be important for short scanning length and future work is therefore necessary.

In order to compare the numerical and experimental results, 8 of 9 cases listed in Tab. 4.3 are chosen: cases 1-3 and 5-9. In the numerical simulations, the initial porosity of the powder bed is supposed to be equal to 0.3, the scanning type is horizontal with a scanning length of 0.05 *m*, the energy density applied, depending on laser energy, scanning speed, and scanning space, varies from 1.7 *J/cm<sup>3</sup>* to 2.2 *J/cm<sup>3</sup>*, and the surface center of the computation domain is chosen to do the comparison. Fig. 4.36 shows the comparison of time evolution of surface temperature for the 8 cases.

Generally speaking, agreement between the numerical and experimental results is reasonable: similar curve behaviour is observed. In both experiments and numerical simulations, the maximum temperature takes place at similar moments and increases with increasing energy density. Apart from the highest energy density, the difference between the numerical and experimental results of maximum temperature is less than 10 *K*. This is fairly satisfying given the experimental uncertainties mentioned previously on the IR measurements, the inaccurate knowledge on the parameters of the SLS machine (for example, the small preheating observed in Fig. 4.10) and the limitation introduced by the camera shutter time of about 0.0056 *s*. In fact, in the studied SLS process the sample temperature reaches, during a laser sweep, a high level with a short period, usually smaller than 0.001 *s* and then quickly decreases after the sweep. The keeping time of the maximum temperature is thus very short. The shutter time of the IR camera used, about 0.0056 *s*, does not allow to capture the rapid temperature increase and may not allow to capture correctly the luminance of the maximum temperature. The agreement leads to the conclusion that the models we used, especially the scattering model used, are satisfying in predicting heat transfer in the powder bed and hence its surface temperature.

Fig. 4.37 presents the time evolution of surface temperature obtained for a vertical scanning with the scanning length of 10 *mm*. The studied case is case 1 with  $E_p = 1.95 \text{ J/cm}^2$ . As shown in Fig. 4.20, for the vertical scanning the maximum temperature at the sample's edges and in the central part has a huge difference. To simplify the problem and do comparison we study only the central part in our simulations. As the *DL* surface is not smooth enough, three experimental points are chosen for comparison. Fig. 4.37 displays three experimental curves and one numerical curve: for short time ( $t < 0.2 \text{ s}$ ) the three experimental curves show a temperature difference of more than 30 *K* and for longer time they display only a slight difference; the numerical result remains among the experimental curves. It means that, for the vertical scanning with very short time delay between the two neighbouring sweeps, surface temperature depends heavily on the positions for short time and that for longer time it becomes independent of the positions. Nonetheless, qualitative agreement is observed between the numerical and experimental results.

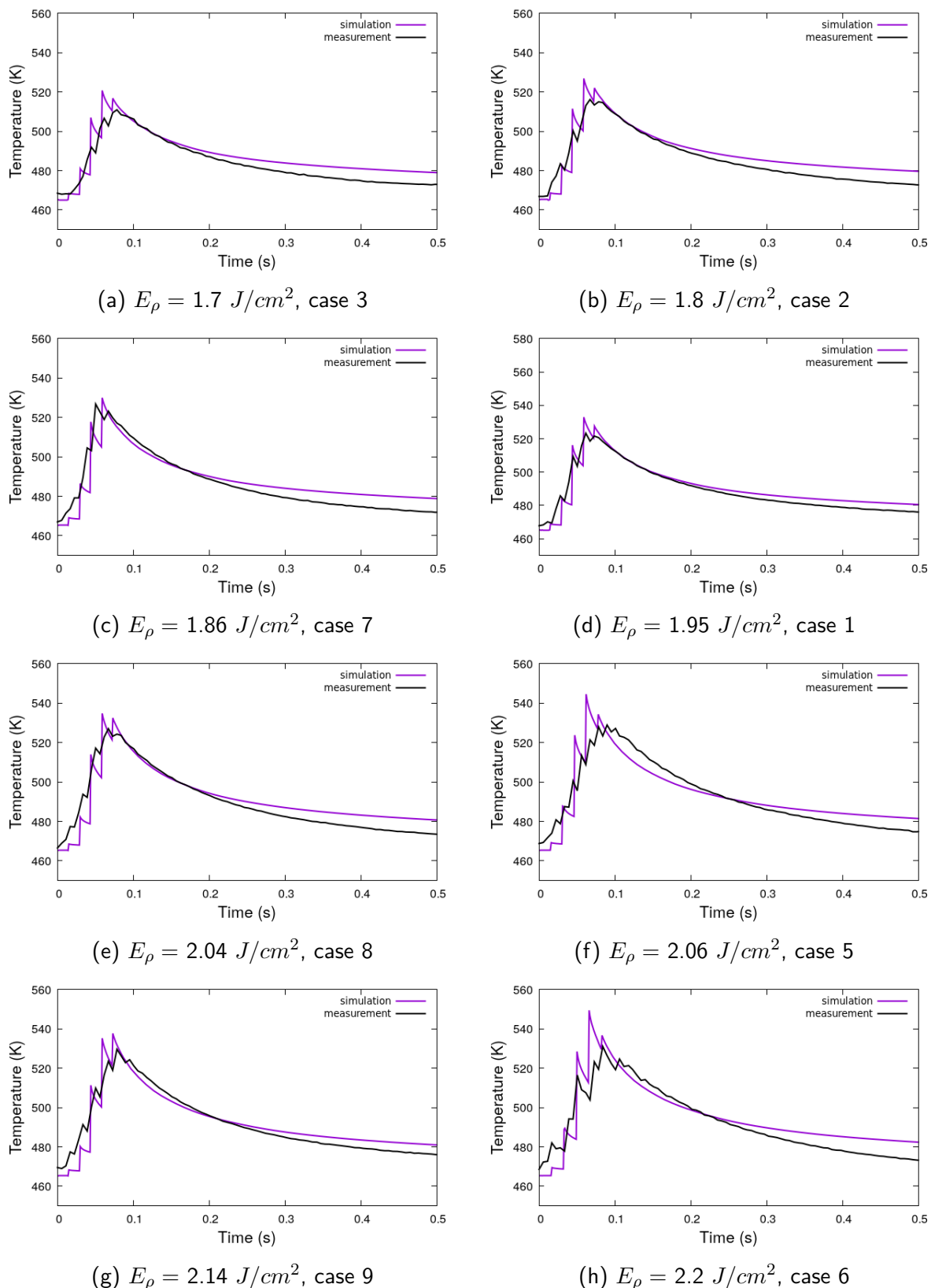


Figure 4.36: Comparison between experimental and numerical results obtained for the horizontal scanning with the scanning length of  $50 \text{ mm}$ : time evolution of surface temperature. 8 cases are compared.

Dimension of the samples is an important result of a SLS process. Based on Fig. 3.22, if the temperature keeping time is longer than  $0.05 \text{ s}$  at  $474 \text{ K}$  or higher temperature, the

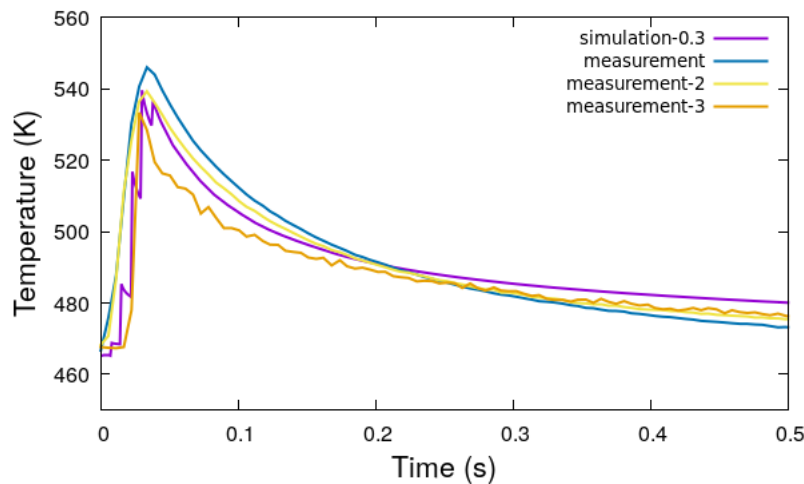


Figure 4.37: Comparison between experimental and numerical results obtained for the vertical scanning: time evolution of surface temperature. Three experimental curves are presented.

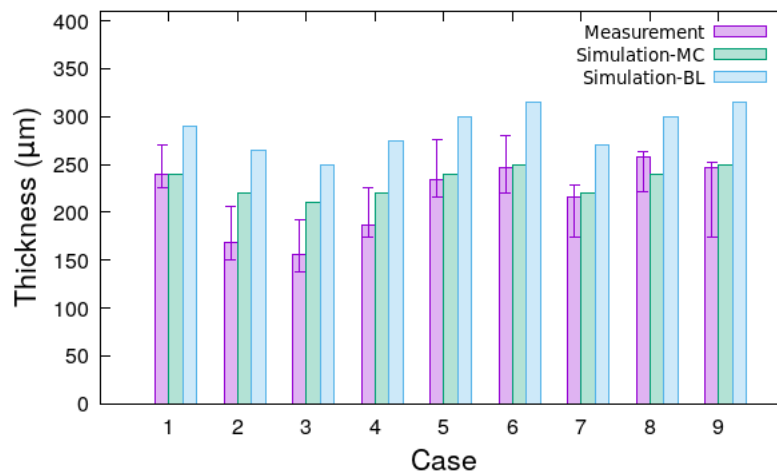


Figure 4.38: Thickness of the sintering samples for the cases 1-9: comparison of the experimental results with the numerical results yielded by both the scattering model and the BL model without scattering.

adjacent particles are considered as well fused together. In a multi-sweep situation, we continue to use this condition. Fig. 4.38 shows the samples' thickness for two types of simulations and the experiments: it is clear that the scattering model yields comparable results with the measurements while the BL model without scattering provides higher thickness as is in the single-sweep cases. This seems to indicate the superiority of the scattering method.

Fig. 4.39 presents the shrinkage size predicted by the two types model for the 9 cases. It can be seen that higher energy density leads to a more important shrinkage. The averaged shrinkage size is about  $45 \mu\text{m}$  with the scattering model, and is  $60 \mu\text{m}$  with the unscattering BL model. Even with lower shrinkage predicted by scattering model, the final thickness of the sample is still smaller than the prediction obtained under the un-scattering condition. Compared with the averaged thickness of  $220 \mu\text{m}$ , the shrinkage which is more than 20 % of the thickness is very important. Without taking into account the shrinkage, any modeling of SLS processes would predict wrong thickness.

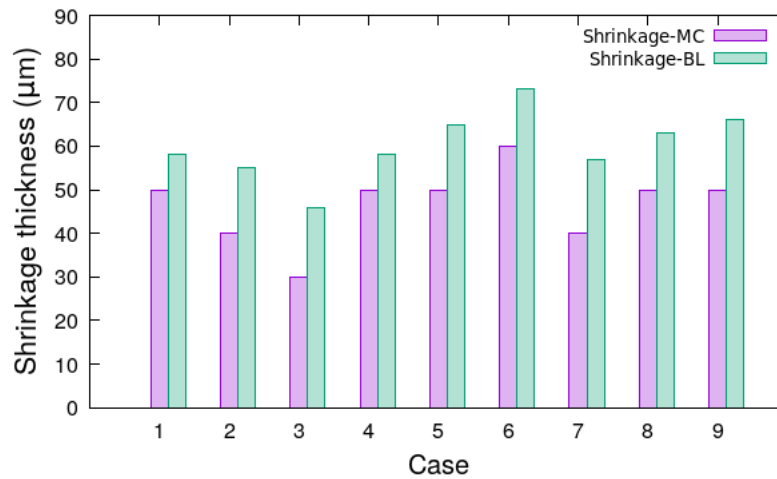


Figure 4.39: Shrinkage size for the test cases 1-9: numerical results using the scattering model.

## 4.4 Summary

In this chapter, single-layer SLS processes are analysed: complementary results are presented for single-sweep cases and main studies are concentrated on the multi-sweep cases.

Numerical results obtained show that any parameter, among laser power, laser moving speed and scanning space, contributing to increase of energy density will increase the maximum surface temperature and the keeping time of the molten state and affect the SLS processes because higher maximum surface temperature and longer keeping time of the molten state influence the coalescence and air escaping. Decreasing the scanning length, increasing the initial porosity of the powder bed and increasing the preheating temperature lead to higher maximum temperature and longer keeping time of the molten state.

Apart from analysing the numerical results obtained, they are also compared, when it is possible, with experimental results which are mainly surface temperature measured by an IR camera. As the conversion of digital level measured by an IR camera into temperature is complex and becomes more complex with a powder bed undergoing phase change, porosity change and surface evolution, calibration of the IR camera is emphasized.

Despite of the good agreement between the measured surface temperature and the numerical prediction obtained by the scattering model, the agreement is still considered as qualitative because of uncertainties related to phase change, porosity change and surface evolution. Further to the agreement on the samples' dimensions between the measurements and the numerical results obtained by the scattering model, the scattering model seems to be better than the BL model without scattering, which yielded higher surface temperature and larger sample's thickness. It can be concluded that scattering in the polymer powder bed is an important phenomenon and must be considered in the modeling of SLS processes.

The simulations performed in multi-sweep cases revealed an important shrinkage representing 20 % of the sample's thickness. This indicates that shrinkage is an important phenomenon in a polymer SLS process and should be part of SLS modeling.

# Chapter 5

## Multi-layer SLS processes

### Contents

---

<b>5.1 Thermal history in multi-layer processes . . . . .</b>	<b>108</b>
5.1.1 Layer thickness of 100 $\mu m$ . . . . .	109
5.1.2 Layer thickness of 80 $\mu m$ . . . . .	111
<b>5.2 Porosity of the manufactured parts . . . . .</b>	<b>113</b>
5.2.1 Experimental results . . . . .	114
5.2.2 Porosity analysis using numerical simulations . . . . .	115
5.2.2.1 Global description and analyses . . . . .	117
5.2.2.2 Effects of the parameters . . . . .	123
5.2.2.3 Comparison between the experimental and numerical results . . . . .	129
<b>5.3 Summary . . . . .</b>	<b>131</b>

---

After studying single-layer SLS processes, we are interested in multi-layer processes in which polymer will be repeatedly heated by laser sweeps and the heating cycles affect the micro-structure of the fabricated parts. In this chapter, we focus on analyzing the thermal histories of multi-layer situation and predicting the porosity of the fabricated parts. Viscosity of the molten polymer decreases with increasing temperature and this decreases the coalescence period in a SLS process. The porosity evolution is connected to the polymer viscosity and the thermal history of the powder bed, the porosity distribution in the samples is simulated and compared with the experimental results.

## 5.1 Thermal history in multi-layer processes

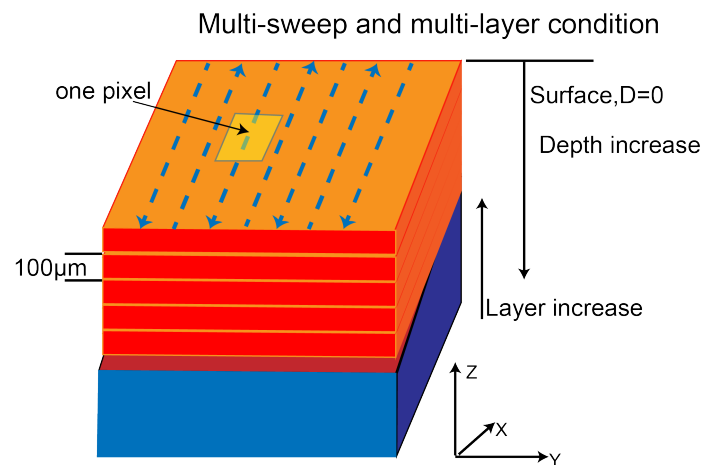


Figure 5.1: Schematic of successive layers heated by multiple laser sweeps.

In multi-layer SLS processes, new polymer powder is deposited successively layer by layer (Fig. 5.1). The time interval between two lasers is long (usually larger than 14 s), it is longer enough to wait for the heated polymers to be cooled down to the preheating temperature. Therefore, surface temperature of the new powder layer will not be influenced by the old layer's heating cycles. Surface temperature depends only on the way that the new layer is heated. Multi-layer processes depend on not only the parameters like laser power, laser moving speed, laser scanning and scanning space but also the thickness of the new layers. In fact, laser scanning in multi-layer processes depends on the scanned layers. It is not the same for all the layers: the first layer is scanned horizontally (Fig. 4.21), the second layer is scanned vertically (Fig. 4.20) and so on. Therefore, in order to be compatible with the experiments the scanning length for the odd number of the layers is set to 50 mm and for the even number of the layers it is equal to 10 mm in the simulations.

Decreasing the thickness of the added layers is a good way for SLS processes to increase the samples' density and improve the products' quality. However, in a SLS process, smaller thickness leads to longer manufacturing time and decrease in efficiency and productivity. In general, the minimum thickness of layers is limited by the particle size, and the mechanical process of adding layers is also a technical problem, so the minimum adding thickness is not easy to be decreased in real fabricating condition. For improving the mechanical quality of the product, suitable laser power, layer thickness and manufacture time need to be found. In the following, we are interested in the layer thicknesses of 100  $\mu\text{m}$  and 80  $\mu\text{m}$  and their effects on the thermal history.

### 5.1.1 Layer thickness of $100 \mu m$

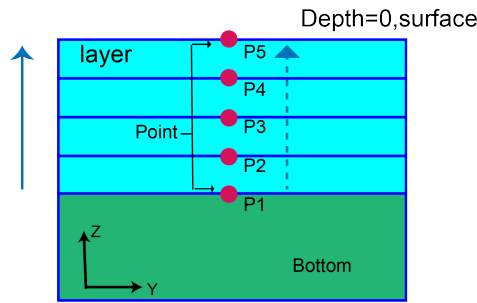


Figure 5.2: Schematic of the monitoring positions. The IR camera is measuring surface temperature of the powder bed. After adding the second layer, the monitoring point is switched from P1 to P2, the third layer switches it from P2 to P3, etc. One signal of an IR camera contains time evolution of surface temperature at several points.

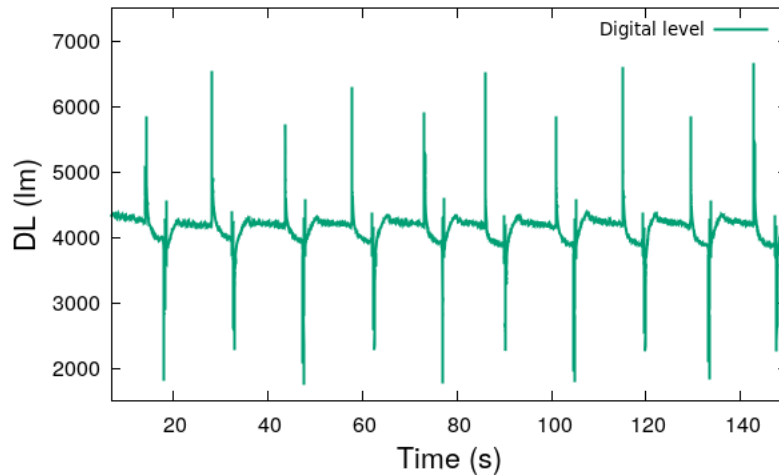
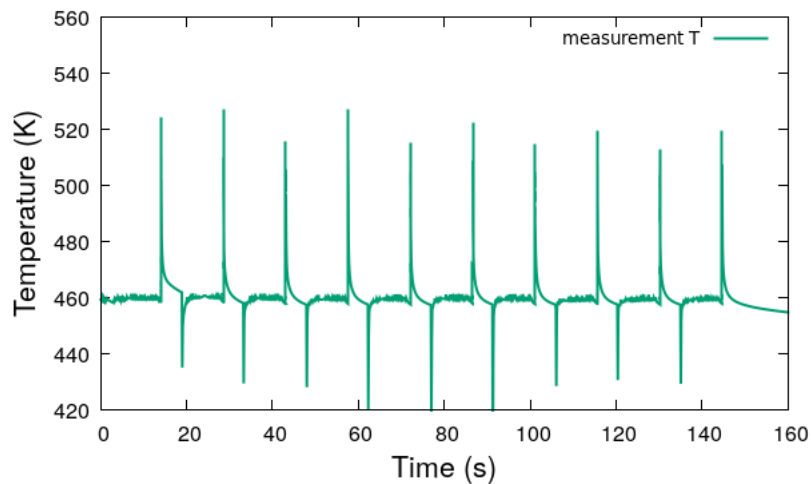


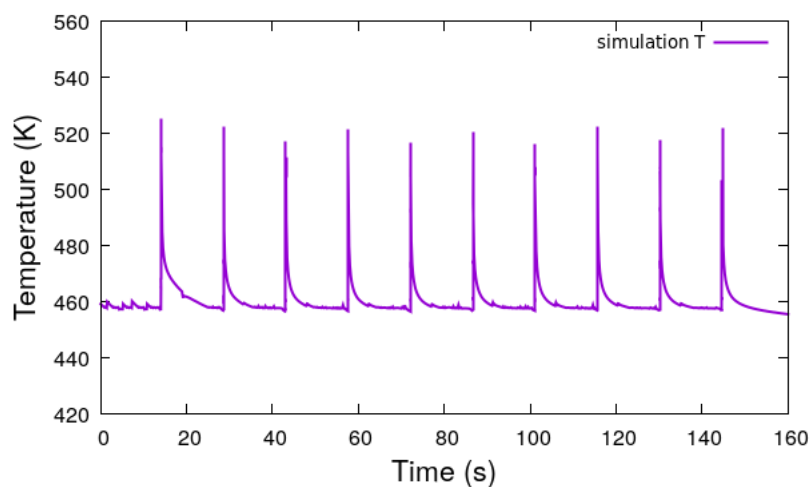
Figure 5.3: Digital level measured by the IR camera. The peaks about  $DL = 2500$  correspond to adding a new layer and it is at these moments that the monitoring point is switched from one to another.

We choose case 3 in Tab. 4.3 as an example to study the thermal history in a multi-layer SLS process. The simulation condition is: the initial thickness of the powder bed of  $1200 \mu m$ , the thickness of new layers of  $100 \mu m$ , the laser power of  $13 W$ , the scanning space of  $220 \mu m$  and the laser moving speed of  $3.5 m/s$ , and the scanning lengths alternated between  $50 mm$  and  $25 mm$ . Fig. 5.3 presents the digital level ( $DL$ ) measured by the IR camera. The two scanning directions are alternated from one to another. The maximum  $DL$  values are about  $5800 ml$  if the laser scans horizontally and they are equal to about  $6800 ml$  with a vertical scanning. In multi-layer situations, the surface temperature of each newly added layer is independent and is not influenced by other layers because of the long cooling time. Therefore, the temperature evolution is similar to that observed in multi-sweep and single-layer situations.

The  $DL$  values are converted into temperature by using an correction factor  $C = 2.05$  and an emissivity of  $0.82$ . This value is slightly smaller than the one used in Chapter 4 because it intends to take into account the effects of polymer phase change, porosity evolution and surface evolution of the powder bed. Fig. 5.4a presents the time evolution of surface temperature measured by the IR camera. The sharp decreases down to  $420 K$  corresponds to



(a) Time evolution of surface temperature converted from the  $DL$  profile measured by the IR camera.



(b) Time evolution of surface temperature provided by the numerical simulation.

Figure 5.4: Experimental and numerical results of surface temperature in a multi-layer process.

adding the new layers and is caused by the powder roller which has extremely lower surface emissivity. It is also at these moments that the monitoring point is switched from the old layer's surface to the new layer's surface. The time profile of temperature given by the numerical simulation is shown in Fig. 5.4b. As new layers are added numerically without the powder roller, the preheating temperature is always observed when adding a new layer. In both Fig. 5.4a and Fig. 5.4b, the first peak of the maximum temperature represents the laser heating of the initial powder bed and concerns the point P1, the second peak describes the laser heating of the newly added layer and concerns the point P2, and so on. The numerical simulation provides a maximum temperature about  $518\text{ K}$  for the odd number of the points and about  $525\text{ K}$  for the even number of the points.

Fig. 5.5 displays the comparison between the results of the simulation and the experiment. Agreement is observed on the maximum temperature and the time evolution.

Fig. 5.6 presents time evolution of temperature at 10 points in the case of 10 layers: one point on each layer. Different from Fig. 5.4a which always shows the temperature on the top layer, Fig. 5.6 selects one point on each layer and shows the corresponding temperature evolution. For example, Fig. 5.6a concerns the temperature evolution at the position P1

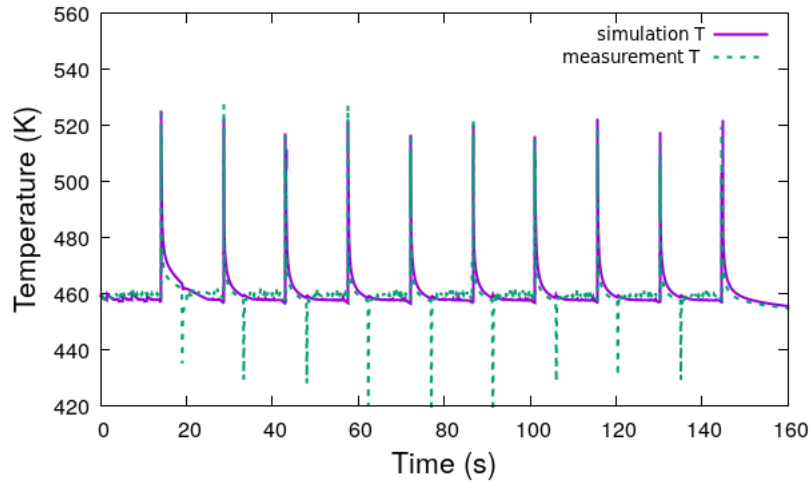


Figure 5.5: Comparison between the numerical and experimental results: time evolution of surface temperature.

(see Fig. 5.2) during the whole SLS process. Adding the a new layer creates point P2, the corresponding temperature evolution is shown in Fig. 5.6b. Other layers are added afterwards and the points P3 - P10 are established. From these curves we see that the laser influences about 5 layers. The shape of these temperature curves and the maximum temperature at each point are similar. Fig. 5.7 groups all the curves together by canceling the time delays between them. The curves collapse into two groups: one group for the horizontal scanning and another for the vertical scanning. It means that temperature evolution does not depend on the layer and that it depends only on the scanning length applied to the layer as the waiting time is long enough to make the thermal histories of the layers independent.

One of the consequences of the thermal history is the thickness of the manufactured samples. The thicknesses of the samples manufactured by multi-layer SLS processes using the parameters listed in Tab. 4.3 are measured. Numerical simulations of the corresponding processes are performed. The measured and predicted dimensions of the manufactured are shown in Fig. 5.8. The good agreement between the results proves the reliability of our model.

### 5.1.2 Layer thickness of $80 \mu m$

As the thickness of the added layers is a control parameter of the multi-layer SLS processes, we modify slightly the thickness to observe its influence. Fig. 5.9 shows the time evolution of temperature at the point P1 on the first layer's surface for both thicknesses ( $100 \mu m$  and  $80 \mu m$ ). The first heating cycle is exactly the same because the preheating temperature is the same for the initial powder bed. The differences are observed since the second heating cycle: the maximum temperature is higher for the thin layers of  $80 \mu m$  because more heating power of other layers arrives at the surface of the first layer. The differences of several degrees in temperature influence the material's thermal condition and hence the SLS process and the final porosity of the samples.

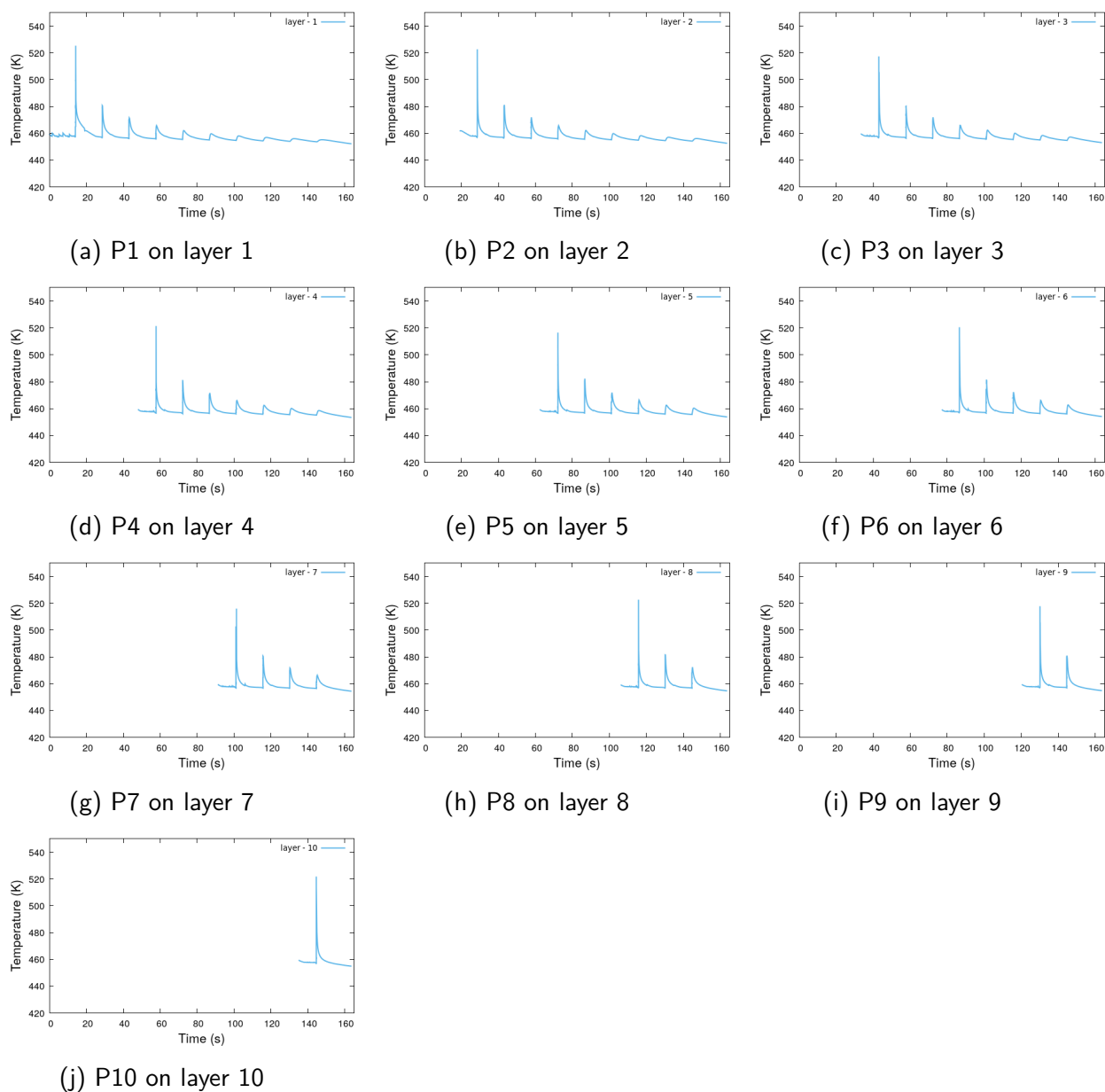


Figure 5.6: Temperature evolution at the positions from P1 to P10 for 10 layer case.

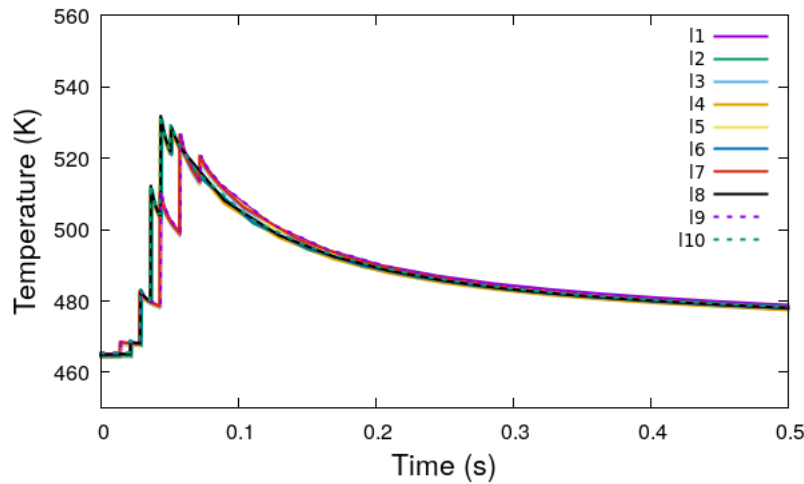


Figure 5.7: Time evolution of temperature on the top of each layer of  $100 \mu m$  thick: time delays or waiting times between the curves are cancelled.

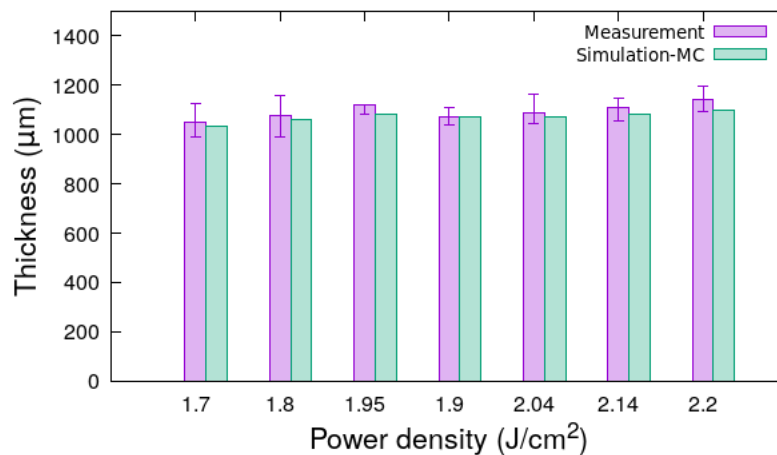


Figure 5.8: Thickness of the samples manufactured by multi-layer processes: comparison of the experimental results with the numerical results yielded by the scattering model,  $E_a = 58 kJ/mol$  with  $465 K$  preheating temperature.

## 5.2 Porosity of the manufactured parts

Porosity is one of the output parameters of any SLS process. It affects directly other output parameters such as density, roughness, strength and hardness. Characterising the porosity of the manufactured parts is an important issue, especially for the multi-layer cases because the samples provided by one-layer processes have very small thickness and are not representative of any manufactured part.

In this section we present the experimental results obtained by X-ray tomography, the numerical results of the simulations performed and the corresponding comparison.

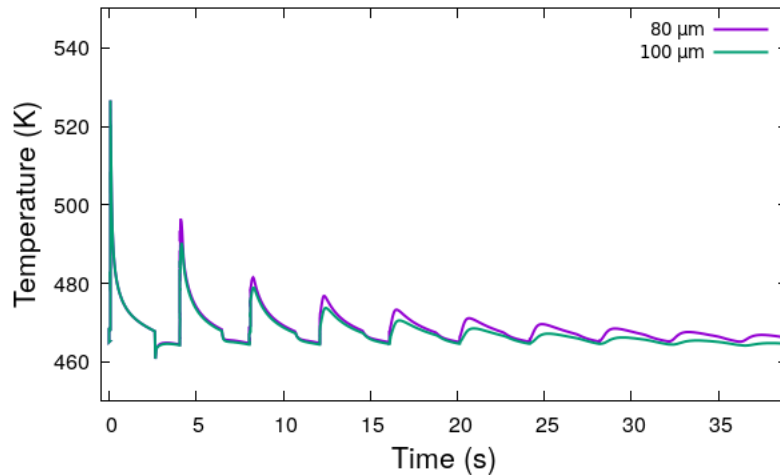


Figure 5.9: Temperature evolution at the point P1 on the first layer: comparison between the layer thicknesses of  $80 \mu m$  and  $100 \mu m$ .



Figure 5.10: X-ray tomography machine used.

## 5.2.1 Experimental results

Porosity distribution, pore shape, pore dimension and positions of the pores in the samples are investigated by X-ray computed tomography machine-Phoenix V|tome|x S240 (Fig.5.10). The X-ray beam energy was set to  $80 \text{ kV}$  and images of the tomography are reconstructed from 1500 projections. The spatial resolution of tomography for each cube is equal to  $6 \mu m$ , the measurement area is around  $1 \text{ cm} \times 1 \text{ cm}$ . Fig. 5.11 is the gray-scale image of a sample observed by X-ray tomography and the corresponding binarised image (Fig. 5.12) is obtained after the threshold. These mapping pictures are used to measure the pores and the porosity. The striking fact is that the aligned pores are observed and separate the images into layers. The gray-scale image indicates only 5 or 6 layers while the binarised image indicates clearly the 10 layers which are added in the SLS process. Fig. 5.13 presents a 3D view of the sample and indicates also clearly the 10 layers added in the process.

Fig. 5.14 displays the section images for different energy density. Pores of various sizes and shapes are observed. The aligned pores at low energy density indicate the layered structure of the parts. At higher energy density, the particles are well sintered together to

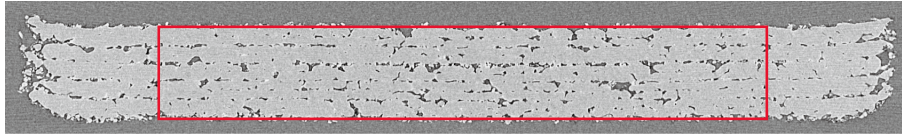


Figure 5.11: Grayscale image of a sample obtained by X-ray tomography for  $E_\rho = 1.7 \text{ J/cm}^2$ .



Figure 5.12: Binarised image of the sample obtained with  $E_\rho = 1.7 \text{ J/cm}^2$ : pores appear in white.

form a whole part and the layered structure is less clear. We chose the middle part (Fig. 5.11) to evaluate the porosity distribution in depth ( $z$ ) direction, the porosity in  $z$  direction is the averaged value in both  $x$  and  $y$  directions. Fig. 5.15 displays an example of the porosity profile in the depth direction. Again the oscillatory distribution reflects clearly the layered structure observed in Fig. 5.14.

If the porosity profile is averaged in the depth direction, we obtain an averaged porosity for the samples, the calculated area is shown in Fig. 5.11. Fig. 5.16 shows the averaged porosity of the samples for the energy densities used in the multi-layer SLS processes. The porosity decreases slowly with power density increase. The porosity measured is equal to 13 % when the energy density ( $E_\rho$ ) is equal to  $1.7 \text{ J/cm}^2$  and it is decreased to about 3.5 % when the energy density is increased to  $2.2 \text{ J/cm}^2$ . Higher energy density is therefore interesting in terms of decreasing the porosity and strengthening the mechanical properties of the manufactured parts. But as it increases also the maximum temperature, this may increase the aging effects.

## 5.2.2 Porosity analysis using numerical simulations

The porosity of the manufactured parts can be also studied by numerical simulations in which coalescence is modeled. In a SLS process, coalescence is the most important phenomenon responsible for air escape from the molten polymer particles. Coalescence is separated into two stages: free gas escape is followed by slow gas penetration. The first stage is much quicker than the second one and makes more contribution to the densification process. In the second stage of coalescence, the porosity is smaller than 0.03 and all the pores are closed. Air bubbles escape from powder bed through the slow gas diffusion in the polymer, it is a long and time-consuming process that happens in low temperature situation (temperature is still higher than the initial melting temperature.). Coalescence and hence porosity of the manufactured parts depend on the process parameters as preheating temperature, initial porosity of the powder bed, thickness of an added layer, laser power, laser moving speed, scanning space and scanning.

The powder bed is supposed to be a homogenized medium and a mixture of aging particles and new particles. The activation energy of polymer varies from  $24 \text{ kJ/mol}$  to  $105 \text{ kJ/mol}$ , and the viscosity varies from  $380 \text{ Pa.s}$  to  $1000 \text{ Pa.s}$ . Concerning the viscosity model, both Frenkel's model and MS model are used to simulate the coalescence process: for a relative density larger than 0.97 the MS model is used and for smaller relative density

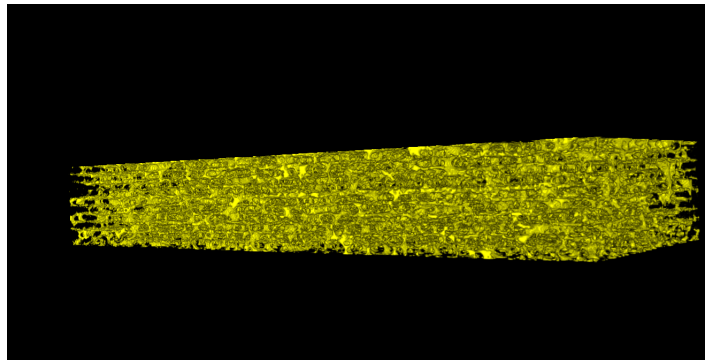


Figure 5.13: A 3D view of a sample.

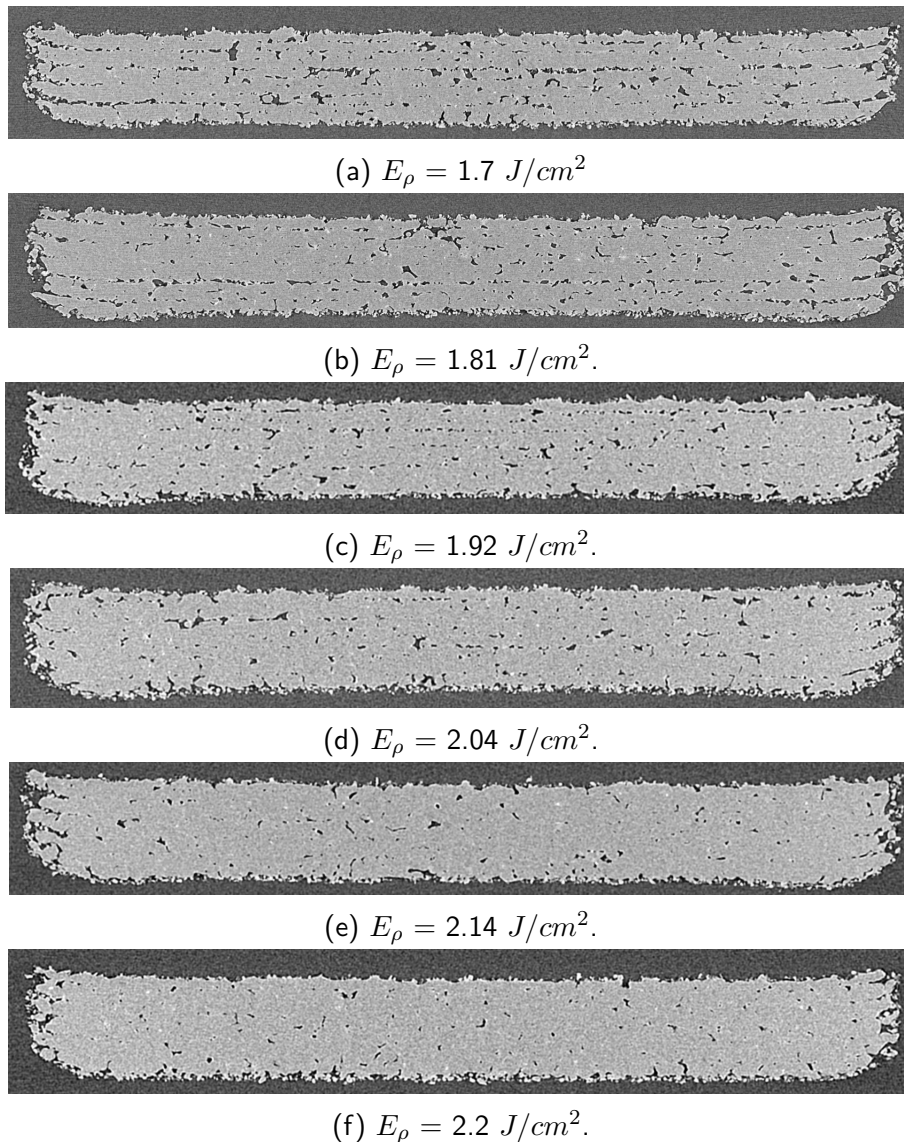


Figure 5.14: Section images of X-ray tomography: PA6 samples sintered using different energy density.

the coalescence is modeled by Frenkels' model. The process parameters used are shown in Tab. 5.1.

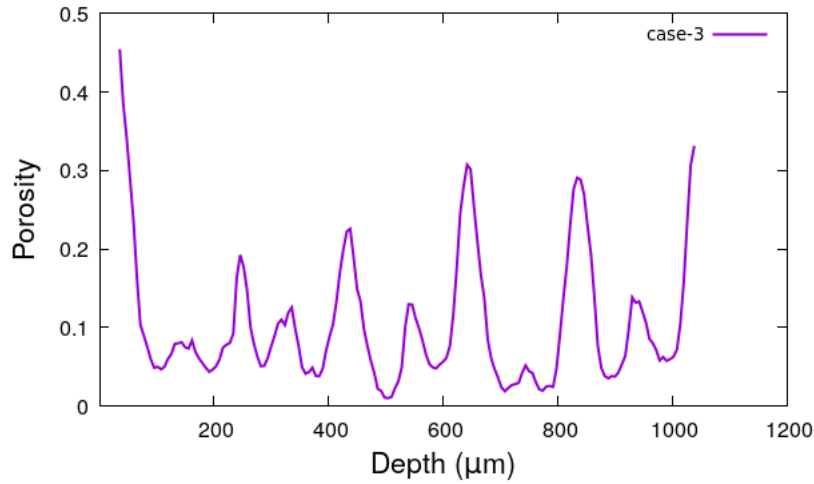


Figure 5.15: Porosity distribution in the depth direction for  $E_\rho = 1.7 \text{ J/cm}^2$ : the experimental profile is obtained by averaging the results in both  $x$  and  $y$  directions.

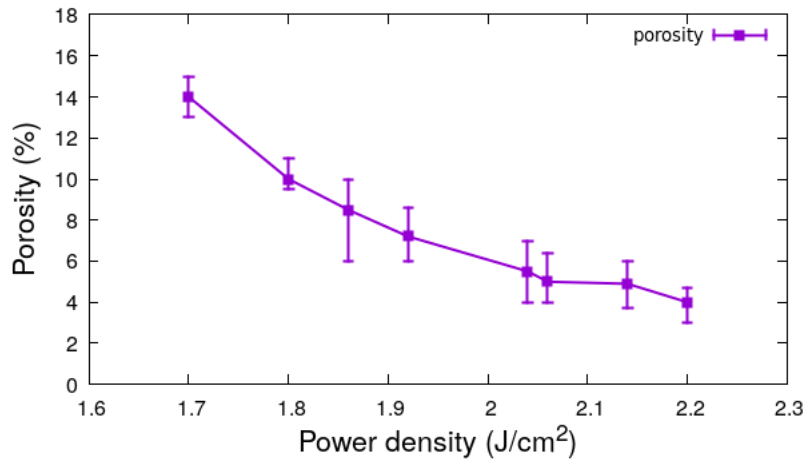


Figure 5.16: Porosity versus energy density.

Table 5.1: Summary of the process parameters.

Parameter and Property	Value
activation energy ( $E_a$ ) [ $kJ/mol$ ]	58, 24.1
Zero-shear viscosity ( $\eta_0$ ) at 513 K [ $Pa.s$ ]	650
Laser power [ $W$ ]	15, 14, 13
Preheating temperature [ $K$ ]	455, 460, 465
Thickness of adding layer [ $\mu m$ ]	100, 80
Polymer particles' radius [ $\mu m$ ]	30
Initial porosity of the powder bed	0.56, 0.47, 0.3

### 5.2.2.1 Global description and analyses

Fig. 5.17 shows a series of porosity distributions with successive 10 layers. Fig. 5.18 shows the porosity distribution following the  $z$  direction in the middle of laser scanning part shown in Fig. 5.17. The porosity of the sample is determined by the heat transfer process and the polymers' physical properties. In the simulations, the thickness of an added layer is set to

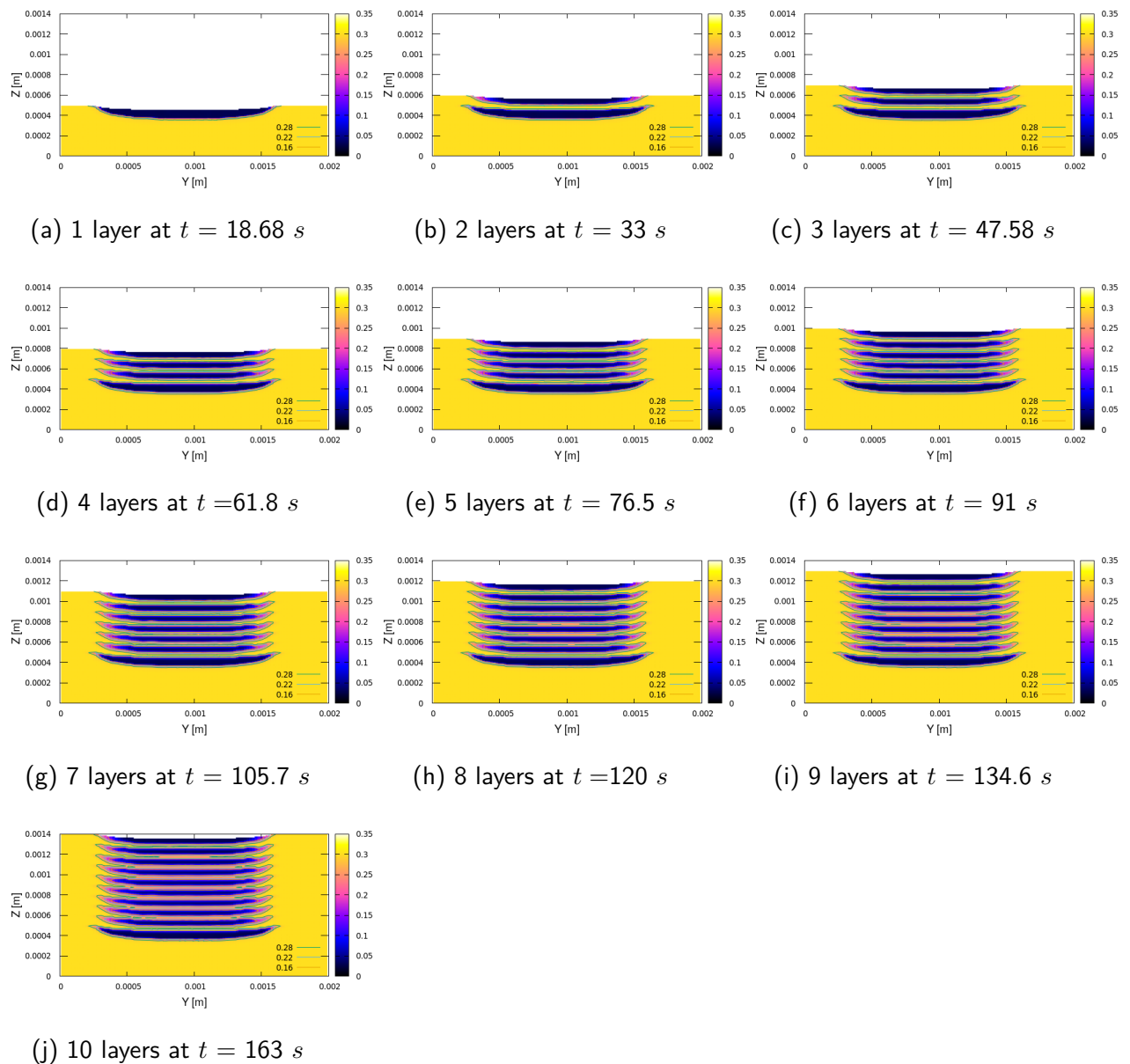


Figure 5.17: Illustration of porosity evolution in the  $y - z$  plane of the powder bed with the successively added layers.

$100 \mu\text{m}$ , the initial porosity of the powder is equal to 0.3, and the activation energy is equal to  $58 \text{ kJ/mol}$  with a viscosity of  $650 \text{ Pa}\cdot\text{s}$ . Once the melting takes place, coalescence of the polymer particles starts and air between the particles escapes and goes out of the polymer bed. The air escape results in densification of the powder bed and causes shrinkage. Therefore, in the simulation the thickness of a new added layer is usually higher than  $100 \mu\text{m}$ . The actual thickness of each added layer is shown in Fig. 5.19. The thickness of the first added layer of  $100 \mu\text{m}$  is theoretical, the thickness of the second added layer is equal to  $145 \mu\text{m}$  and it is higher than that of other added layers ( $135 \mu\text{m}$ ). It means that when the second layer is added the shrinkage of the first layer is equal to  $45 \mu\text{m}$  and that when other layers are added the shrinkage of the previous layers since the last scanning is equal to  $35 \mu\text{m}$ . But the total shrinkage of the 10 layers after adding the 10th layer and after the last laser scanning will be equal to  $50 \mu\text{m}$  (see Fig. 5.34). Porosity distributions show clearly the layered structure and the shrinkage phenomenon in the scanned zone on the top of each added layer. The porosity of the bottom (1st) and the top (10th) layers seems to be lower than that of other layers and

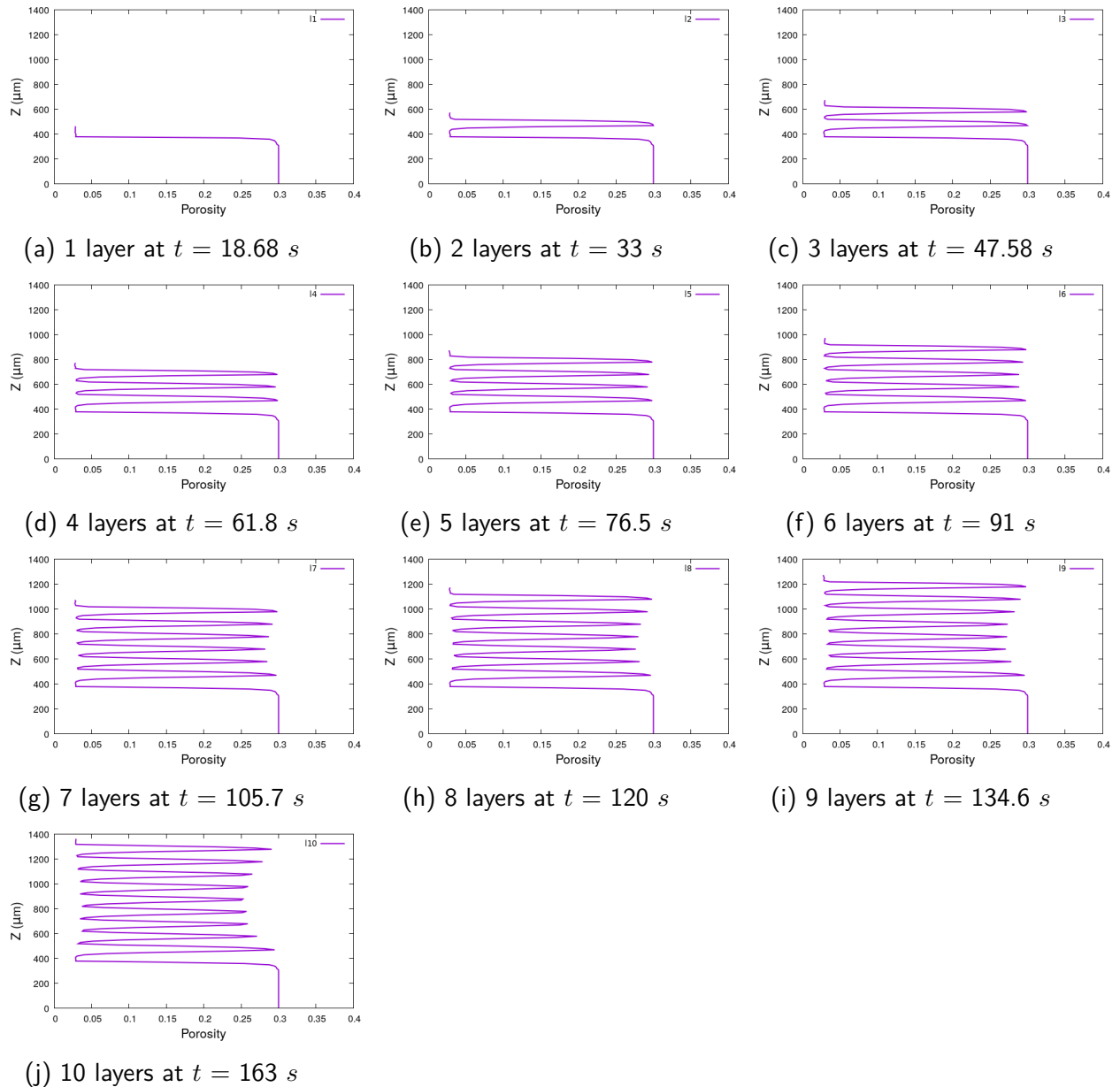


Figure 5.18: Illustration of porosity distribution in the  $z$  direction of the powder bed with the successively added layers.

the porosity distributions are similar in other layers. In each layer, the bottom part of the layer has higher porosity because the lower heating energy arriving at this depth can not provide enough time to help the polymer particles finish the coalescence process. Even though the coalescence at the bottom of each layer is not as sufficient as on the top, these layers are still well connected because the liquid fraction of these parts is still higher than 50 %.

Fig. 5.20 displays the porosity distributions in the depth direction at the positions shown in Fig. 4.24. The initial porosity of the powder bed is equal to 0.3, laser power is set to 13 W with a preheating temperature of 468 K. The porosity distributions in the depth direction at five central points of the laser tracks are shown in Fig. 5.20a. The  $x$  coordinate starts on the position of the top surface of the 10th layer. Because of the shrinkage after sintering, the top surface goes down and the distance between 0 and the first point of the porosity profile is the shrinkage size. The porosity profiles are oscillatory: they start with flat distributions, continue with sharp peaks at the bottom of the 10th layer which is followed

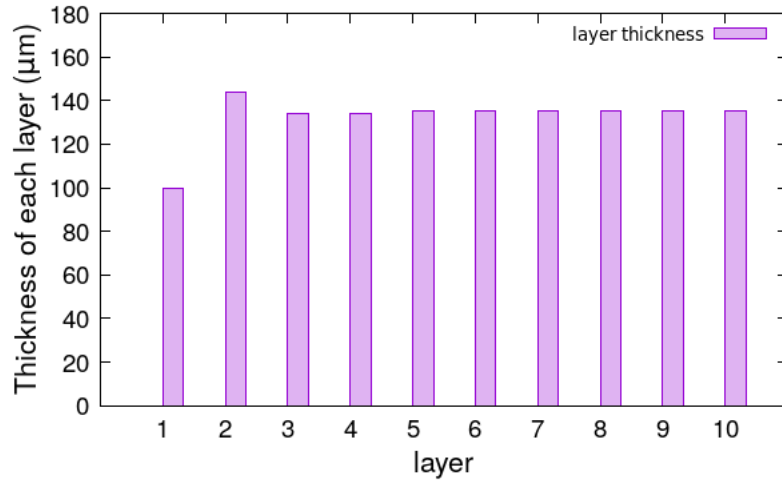


Figure 5.19: Actual thickness of layers added during manufacturing, in the Case 3 ( $E_p = 1.7 \text{ J/cm}^2$ ) with the  $58 \text{ kJ/mol}$  activation energy, the viscosity is  $1000 \text{ Pa}\cdot\text{s}$  and the pre-heating temperature of  $465 \text{ K}$ .

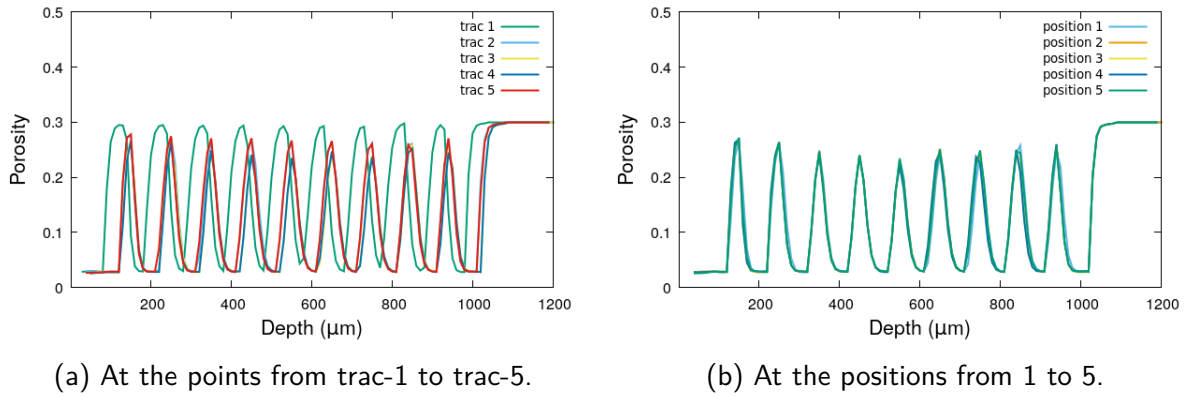


Figure 5.20: Porosity distributions in the depth direction at the points defined in Fig. 4.24.

repeatedly by flat distributions and peaks and end with a plateau of 0.3 (initial powder bed). All the peaks correspond to the junctions of the added layers and represent values about 0.27 indicating incomplete melt. There is a shift between the profile at trac-1 and the others because of the weaker shrinkage and the faster cooling there. The porosity distributions at the positions from 1 to 5 are shown in Fig. 5.20b. Recall that the five points are located between trac-3 and trac-4. The porosity profiles are almost the same, this agrees with the fact that the profiles at trac-3 and trac-4 are almost the same not only for porosity (Fig. 5.20) but also for temperature (Fig. 4.25).

In order to understand the porosity distribution, seven points in the first layer are selected for monitoring the time evolution of the porosity. The points selected range from the surface to to  $150 \mu\text{m}$  and are displayed in Fig. 5.21. The time evolution of temperature and porosity at these points is shown in Fig.5.22, respectively. Laser sweeps increase temperature at the monitored points, even at P7 temperature goes beyond  $480 \text{ K}$ , which is higher than the melting start temperature. As the staying time is not longer enough, the porosity at P6 and P7 changes only slightly and remains about 0.3. Fig. 5.22b indicates that the porosity evolution at other points is fast: it needs less than  $0.3 \text{ s}$  to decrease to 0.03. Note nevertheless that at deeper positions (P4 and P5 for example) the porosity evolution is slightly slower and that more time ( $<0.1 \text{ s}$ ) is needed to reach the level of 0.03. Porosity evolution becomes

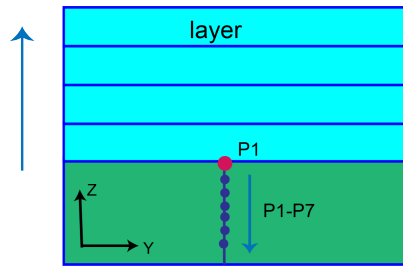
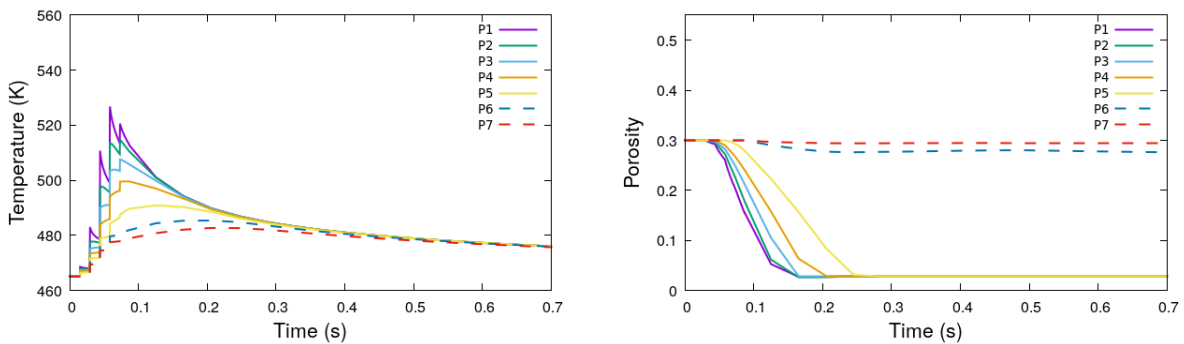


Figure 5.21: The positions monitored in the first layer in order to understand the porosity evolution. P1 is on the layer surface, P2 at the depth position of  $30 \mu m$ , P3 at the position of  $50 \mu m$ , P4 at the position of  $70 \mu m$ , P5 at the position of  $100 \mu m$ , P6 at the position of  $130 \mu m$  and P7 at the position of  $150 \mu m$ .

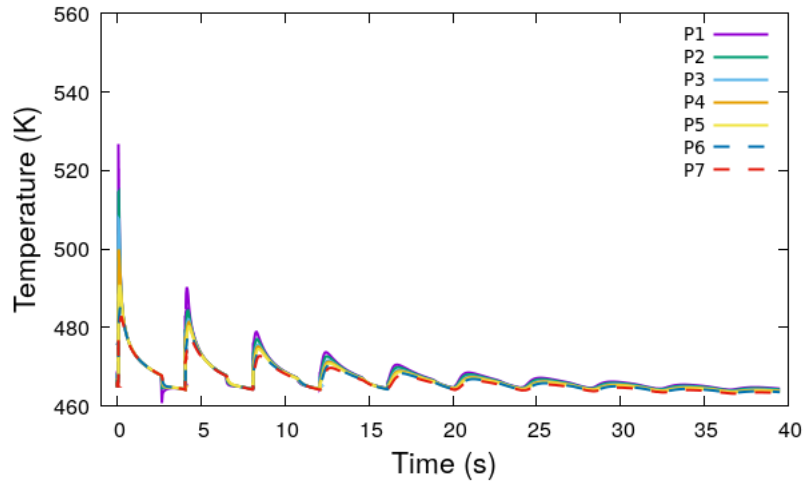


(a) Temperature evolution at the points P1-P7. (b) Porosity evolution at the points P1-P7.

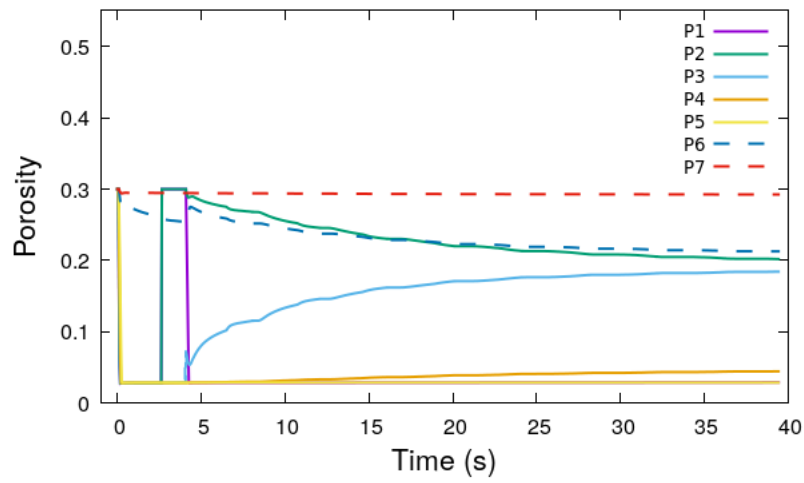
Figure 5.22: Time evolution of temperature and porosity at the points P1-P7 in the first layer for Case 3 ( $E_p = 1.7 J/cm^2$ ) with the initial porosity of 0.3, the preheating temperature of  $465 K$  and the thickness of  $100 \mu m$  for the added layer.

extremely slow once it reaches the level of 0.03 because air is only contained by closed pores and diffused slowly out of the polymer.

Figs. 5.23a and 5.23b present the time evolution of temperature and porosity at the points P1 - P7 in the 10-layer case. Let's stress that the present simulation is performed with a waiting time of  $4 s$ , which is more than three times smaller than the previous one. As can be seen, a new layer is added before the surface temperature reaches the preheating temperature and a sudden drop of temperature is observed when the new layer is added. We think that the waiting time is longer enough to reveal what happens in a multi-layer SLS process. Temperature curves indicate that the points P1 - P7 (Fig. 5.23a) are sensitive at least to the laser sweeps of the four following layers. It is these temperature variations that continue to contribute to the porosity evolution. In fact, before adding the second layer, shrinkage takes place at P1 and P2: this is why porosity at P1 and P2 takes the value of 0.3 (at  $t = 2.5s$  in Fig. 5.23b) when the second layer is added. When the laser sweeps scan the computed zone, porosity at P1 decreases rapidly to the level of 0.03 with an efficient coalescence process while porosity at P2 decreases very slowly in time because of a slow coalescence. Porosity at P3 was at the level of 0.03 when the second layer was added, but the laser sweeps of the second layer modifies suddenly its value which increases slowly in time. Very slow evolution of porosity is observed at P4 and P5, but significant decrease of porosity is observed at P6. In terms of long time behaviour, decrease of porosity at P2 and P6, increase of porosity at P3 and stable porosity of 0.3 at P7 are observed.

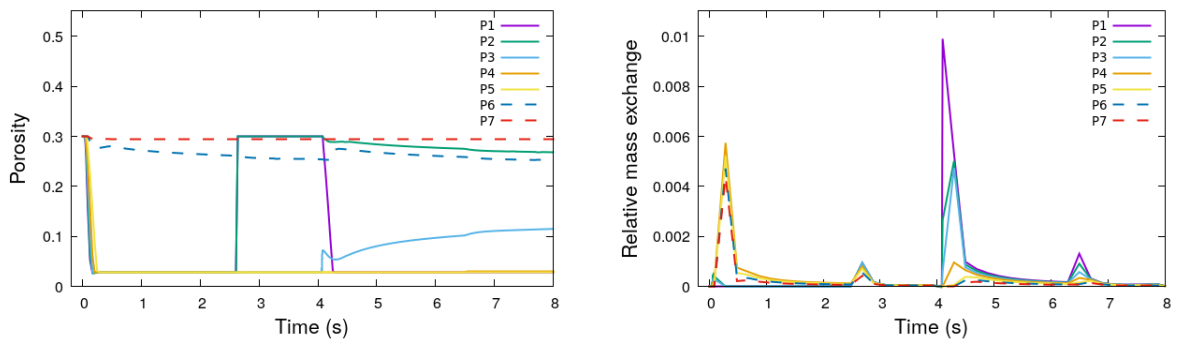


(a) temperature



(b) Porosity

Figure 5.23: Time evolution of temperature and porosity at P1-P7 in a ten-layer process for case 3 ( $E_\rho = 1.7 \text{ J/cm}^2$ ) with the initial porosity of 0.3, the preheating temperature of 465 K and the thickness of 100  $\mu\text{m}$  for the added layer.



(a) Porosity evolution at the points P1-P7.

(b) Relative mass exchange at the points P1-P7.

Figure 5.24: Zoom on the first 8 seconds: time evolution of porosity and mass exchange at the points P1-P7 for Case 3 ( $E_\rho = 1.7 \text{ J/cm}^2$ ) with the initial porosity of 0.3, the preheating temperature of 465 K and the thickness of 100  $\mu\text{m}$  for the added layer.

To better understand the porosity evolution, time evolution of the porosity and the mass exchange in the control volumes are presented for the first 8 seconds in Fig. 5.24. The space freed by air escape in each control volume is filled by the polymer coming from the upper neighbouring control volumes. The mass exchange happens almost all the times, especially during the melting process. We only consider the collapse and mass exchange in depth direction in our simulation, therefore, the porosity calculated in the simulations is determined by not only the coalescence processes but also the porosity of the upper neighbouring control volumes. From Fig. 5.24b we observe that after the scanning of the first layer the mass exchange is weak at P1, P2 and P3 due to air escape and shrinkage and important at other points. After the scanning of the second layer, very important mass exchange is observed at the points P1, P2 and P3. We know that at P1 the melting/coalescence process is efficient and that it is not the case at P2 and P3. As we observe also a smaller mass exchange at P4, the porosity evolution at P2 and P3 is more likely due to the shrinkage and the fact that polymer of the second layer goes down to P3. The important mass exchange is followed by a longer period of weak mass exchange explaining the slow evolution of the porosity.

### 5.2.2.2 Effects of the parameters

The parameters of interest are laser power, thickness of the added layers, preheating temperature, initial porosity of the powder bed and viscosity of the molten polymer.

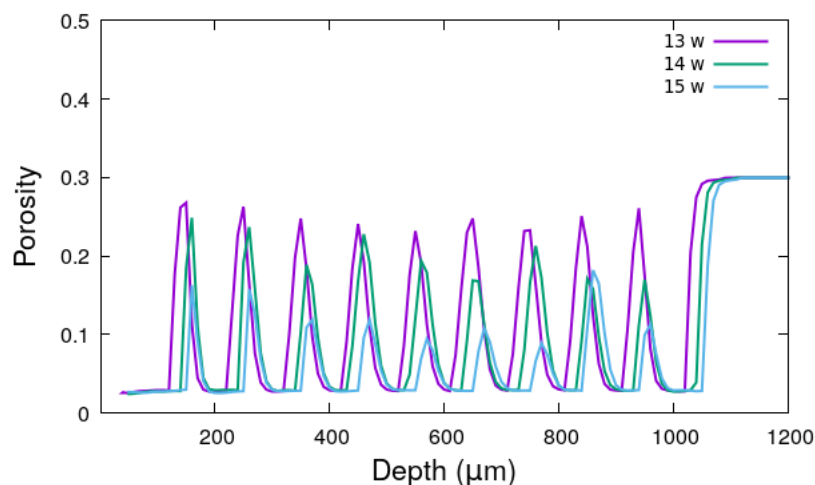


Figure 5.25: Influence of laser power (13 W/14 W/15 W) on the porosity distribution

Laser power of 13 W, 14 W, and 15 W is applied to a powder bed with an initial porosity of 0.3. Fig. 5.25 shows the porosity distributions obtained: the layered structure of the porosity distribution remains. Higher laser power gives rise to smaller porosity because increase in laser power results in an increase of energy density, a higher maximum temperature, a larger influential zone, and therefore more efficient melting/coalescence processes.

To understand how the thickness of the added layers affects the coalescence process, the thickness of 80  $\mu m$  is chosen and studied with the laser power of 13 W and the preheating temperature of 465 K. The porosity distribution is displayed in Fig. 5.26. Compared with Fig. 5.20 obtained with a thickness of 100  $\mu m$ , porosity has smaller amplitude especially for the even layers which are scanned vertically. In terms of the averaged porosity, it decreases to 6 % to be compared with 13 % for the thickness of 100  $\mu m$ .

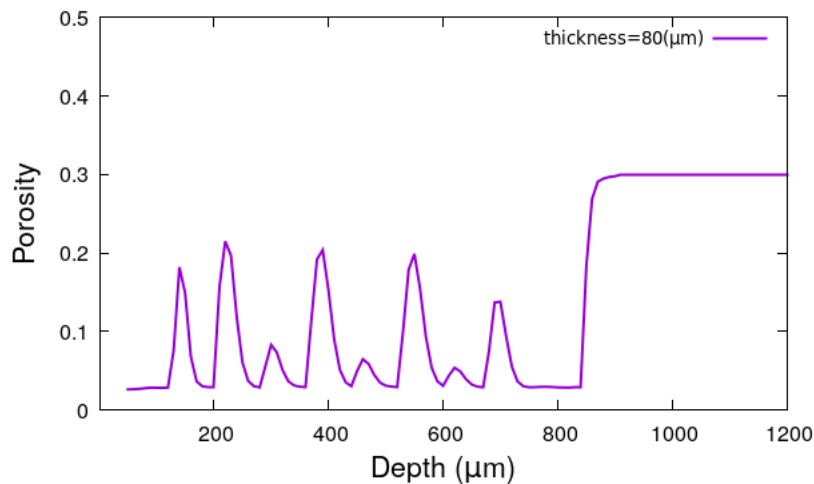
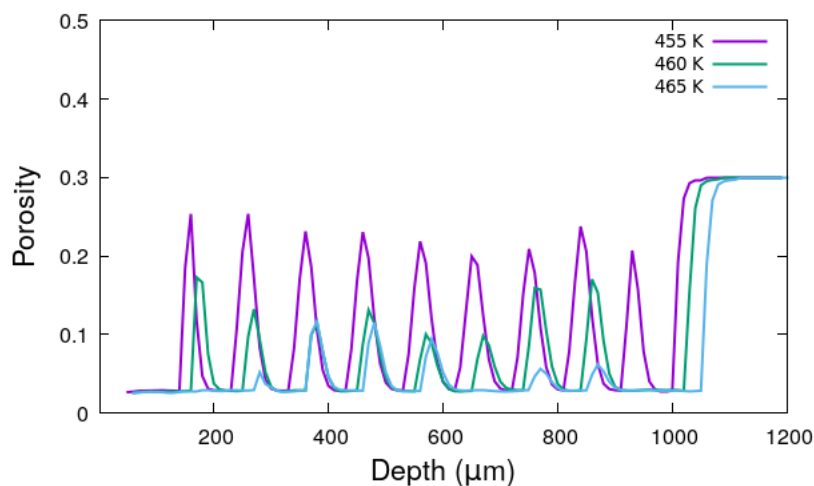


Figure 5.26: Porosity distribution obtained with .

Figure 5.27: Influence of the preheating temperature on the porosity with  $E_p = 1.92 \text{ J/cm}^2$ .

Preheating temperature is an essential parameter to minimize the residual stress and improve the quality of the products. The SLS processes use three preheating methods which are built chamber preheating, base-plate preheating, and laser pre-scanning heating. Higher preheating temperature improves the products' quality, however, it increases the energy consumption and in some cases the preheating increases the energy consumption up to 40 %. In our simulations, we are only interested in the influences of the preheating temperature on the thermal history in the powder bed, the shrinkage and the final porosity of the samples. Fig. 5.27 shows the porosity distribution results in the depth direction with the preheating temperature varying from 455 K to 465 K. In the previous analysis, we know that the maximum temperature and high temperature keeping time are increasing with preheating temperature increasing. Increasing the preheating temperature allows therefore to complete the coalescence process and decrease the samples' porosity, which is clearly indicated by Fig. 5.27

The initial porosity of the powder bed is usually in the range from 0.26 to 0.6. As it influences the photons' transmission in the powder bed, the final porosity of the samples highly depends on it. For an initial porosity is equal to 0.56, the porosity distribution for a 10-layer SLS process is shown in Fig. 5.28. The porosity distribution in the sample has a similar oscillatory behaviour with higher peak and averaged values. The averaged final porosity

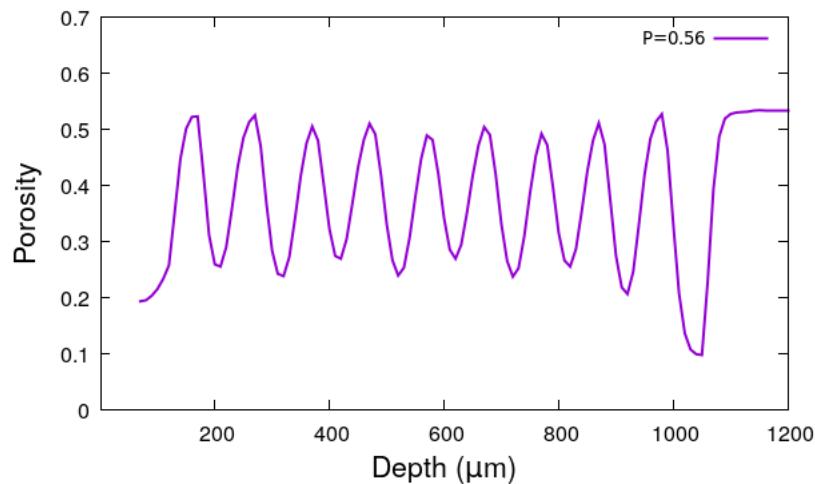


Figure 5.28: Porosity distribution obtained with an initial porosity of 0.56.

is equal to 36 % (much higher than 13 % obtained for the thickness of 100  $\mu m$ ). The lowest porosity equal to 10 % is observed in the first layer. For other layers, porosity ranges from 25 % to 50 %.

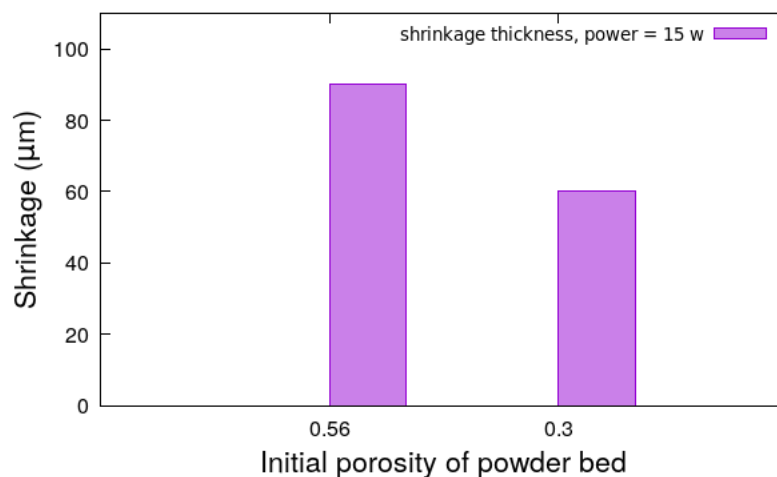


Figure 5.29: Influence of the initial porosity on shrinkage

Fig. 5.29 shows the shrinkage obtained with two initial porosity of the powder bed. The dimension of the shrinkage is higher for higher initial porosity. There are two possible reasons: The loose iterative structure with higher initial porosity collapses more easily and more space is freed by the coalescence process; high porosity results in higher maximum temperature and longer staying time at high temperature promote efficient coalescence process and leave more time for inserted air to escape from the molten polymer.

As far as is concerned the experiment that used similar process parameters, the averaged porosity of the measured sample is about 14 %. This is much smaller than 37 % yielded by the numerical simulation performed for the initial porosity of 0.56. With an initial porosity of 0.30 and a laser power of 13 W, the corresponding porosity distribution shown in Fig. 5.25 leads to an averaged final porosity equal to 11%. An initial initial porosity of 0.3 seems to be more reasonable for the powder bed studied experimentally. In our simulations, the thicknesses of each layer is equal to 100  $\mu m$  and the averaged particles' diameter is equal to 60  $\mu m$ . It is possible to have the models b and c (in Fig. 1.11) and get a volume fraction of

voids about 37 %. Given the variability of particles' size and shape, smaller particles can easily fill the empty space and one get smaller porosity. In the numerical simulations, we choose the initial porosity equal to 0.3 for the powders used in the experimnts.

The viscosity calculation follows the Carreau-Yasuda model and the shear viscosity ( $\eta$ ) can be calculated as:

$$\eta(T) = \eta(T_0) \exp\left(\frac{E_a}{R} \left(\frac{1}{T} - \frac{1}{T_0}\right)\right) \quad (5.1)$$

where the value of  $E_a$  for PA6, varying from 24.1  $kJ/mol$  to 105  $kJ/mol$ , depends on the state of polymer,  $\eta(T_0)$  is the zero shear viscosity of the polymer, varying from 380  $Pa.s$  to 1000  $Pa.s$ .

According to Veberlen et al. [52], the activation energy of virgin PA6 Sinterline is equal to around 24.1  $kJ/mol$ , lower than the typical values of polyamides that range up to 58  $kJ/mol$ , and the activation energy for an extremely aging polymer may increase to more than 105  $kJ/mol$ . The aged powders thus have higher viscosity and longer relaxation time than new polymer particles because they go through a solid state post condensation process.

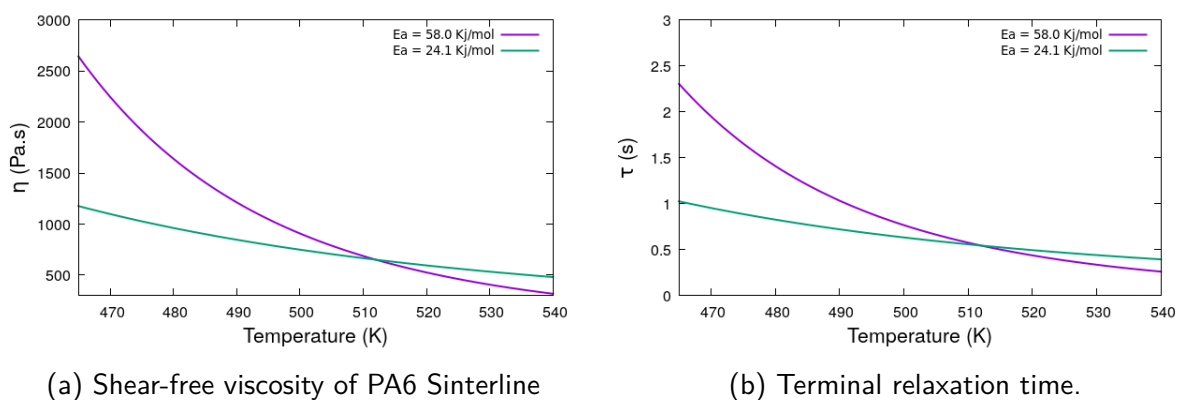


Figure 5.30: Viscosity and terminal relaxation time versus temperature obtained for two  $E_a$  values and  $\eta_0 = 580 \text{ Pa.s}$ .

Figs. 5.30a and 5.30b show viscosity and relaxation time versus temperature for two values of activation energy. For high activation energy, viscosity is larger and terminal relaxation time is longer at lower temperature condition ( $T > 510 \text{ K}$ ). For higher temperature, viscosity is smaller and terminal relaxation time is shorter. During the manufacturing processes, if temperature is higher than 510  $K$ , the aged particles with higher activation energy is connected together more easily because of a slightly high flowability of the melting polymer. However, at lower manufacture temperature ( $T < 510 \text{ K}$ ), the new powders having high flowability are connected more easily together to form a whole object.

In SLS processes using PA6, temperature is in the range from 470  $K$  to 560  $K$ . Two values of temperature of 490  $K$  and 540  $K$  are chosen as coalescence temperature to study the coalescence process, the characteristic used is the contact length. Figs. 5.31a and 5.31b present time evolution of the contact length with two different values of activation energy. At higher coalescence temperature, the coalescence process is faster than at lower coalescence temperature: at  $T = 540 \text{ K}$  it ends within 2  $s$  while at  $T = 490 \text{ K}$  it lasts at least 4  $s$ . From the figures we see also that at  $T = 540 \text{ K}$  the aged particles with higher activation energy is more interesting and that at  $T = 490 \text{ K}$  the new powders are more interesting because of a shorter coalescence process.

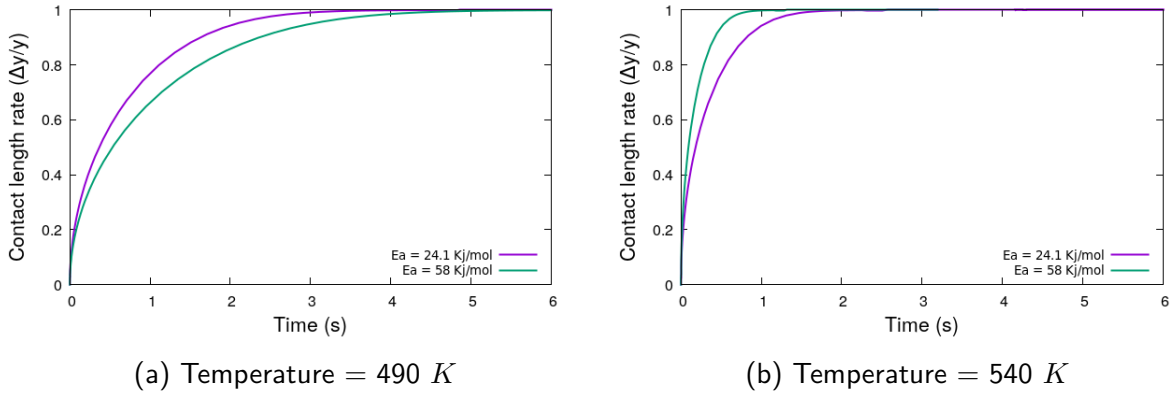


Figure 5.31: Time evolution of contact length for  $E_a = 58$  kJ/mol and 24 kJ/mol at temperature of 490 K and 540 K.

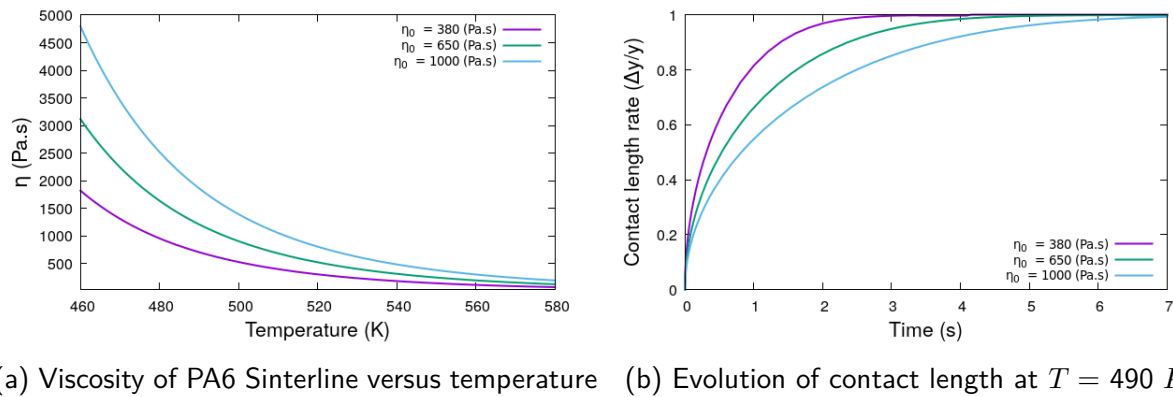


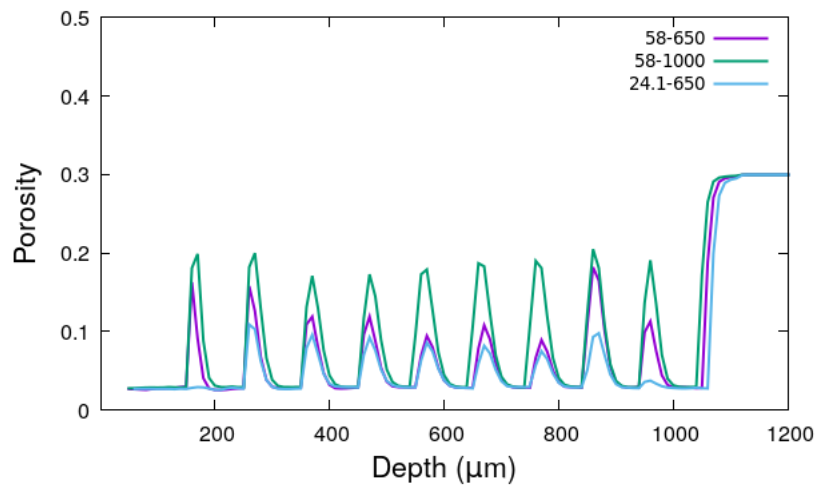
Figure 5.32: Influence of  $\eta(T_0)$  on polymer viscosity and contact length with  $E_a = 58$  kJ/kg.

The  $\eta(T_0)$  is influenced by the material properties and depends therefore on aging. As  $\eta$  is linear with  $\eta(T_0)$ , the increase in  $\eta(T_0)$  will increase  $\eta$  (Fig. 5.32a). The fact that higher viscosity slows down the coalescence process leads to a slowing down of the coalescence process with increasing  $\eta(T_0)$ .

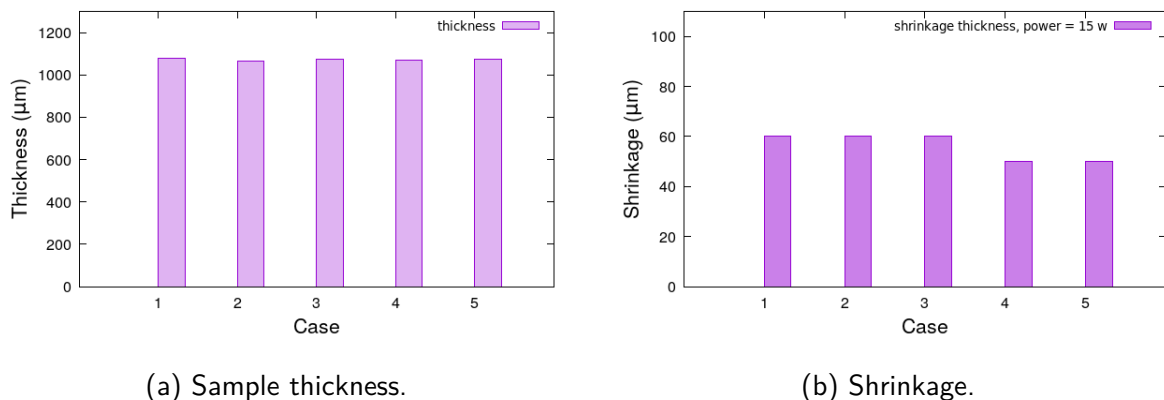
Table 5.2: Summary of the polymer properties.

Case	activation energy ( $E_a$ ), [kJ/mol]	Zero-shear viscosity ( $\eta(T_0)$ ) at $T_0 = 513$ K (Pa.s)
1	24.1	380
2	58	380
3	24.1	650
4	58	650
5	58	1000

As is illustrated above and in Chapter 2, polymer viscosity, an important parameter affecting the coalescence process, affects therefore the shrinkage process and the final porosity distribution of the sample. Fig. 5.33 shows the final porosity distribution in the samples under three conditions (cases 3, 4 and 5 listed in Table 5.2) using the energy density of  $1.92$  J/cm<sup>2</sup>, the scanning length of  $0.05$  m and the initial porosity of 0.3. These results illustrate that decreasing the activation energy and the zero-shear viscosity will promote the flowability of liquid polymer and therefore the coalescence process and the connection of particles to get a higher density sample. For fixed zero-shear viscosity, decrease in the activation energy leads to

Figure 5.33:  $E_p=1.92 J/cm^2$ .

a lower porosity and, for fixed activation energy, decrease zero-shear viscosity leads also to a lower porosity. This indicates that, in terms of air escape or shrinkage, the multi-layer processes is mainly dominated by the coalescence process happening between 474 K to 510 K. The reason is that if the merging process happened mainly at higher temperature ( $> 510 K$ ), the lower activation energy of 24.1 kJ/mol would result in higher porosity according to Fig. 5.31.



(a) Sample thickness.

(b) Shrinkage.

Figure 5.34: Dimension of the thickness and shrinkage for the cases listed in Table 5.2.

Tab. 5.2 lists five cases combining two values of activation energy with three values of zero-shear viscosity. Numerical simulations of the five cases are performed with laser power of 15 W, scanning length of 0.05 m, energy density of 1.92 J/cm<sup>2</sup> and initial porosity of 0.3. The samples' thickness obtained for the cases 1 - 5 is shown in Fig. 5.34a. The shrinkage obtained for the cases 1 - 5 is shown in Fig. 5.34b: lower zero-shear viscosity and lower activation energy (Cases 1 - 3) result in a higher shrinkage (60 μm) and a smaller shrinkage is observed for the cases 4 - 5. In fact, the thickness of the sample is between 1170 μm and 1180 μm, the shrinkage observed is between 50 μm and 60 μm and it is in the same order of the shrinkage obtained for one-layer processes. This result is not surprising because in multi-layer processes the shrinkage of the layers before the last one is all covered by the added layers and only the shrinkage of the last layer remains at the end.

In the SLS process, the powders usually consists of aging powders and new powders. In multi-layers and multi-sweeps cases, even if all the powders consist of new polymer particles, near the laser scanning zone the particles which are not melted are still through the preheating

and heating cycle: the chain structure of polymers have been changed and the same remains true for the physical properties of the polymer. Therefore, we chose an average activation energy for the working powder bed, which is equal to  $58 \text{ kJ/mol}$ , and  $\eta(T_0)$  equal to  $650 \text{ Pa.s}$  at  $T_0 = 513 \text{ K}$  for PA6 Sinterline, because new particles are assumed mixed with used polymer particles.

### 5.2.2.3 Comparison between the experimental and numerical results

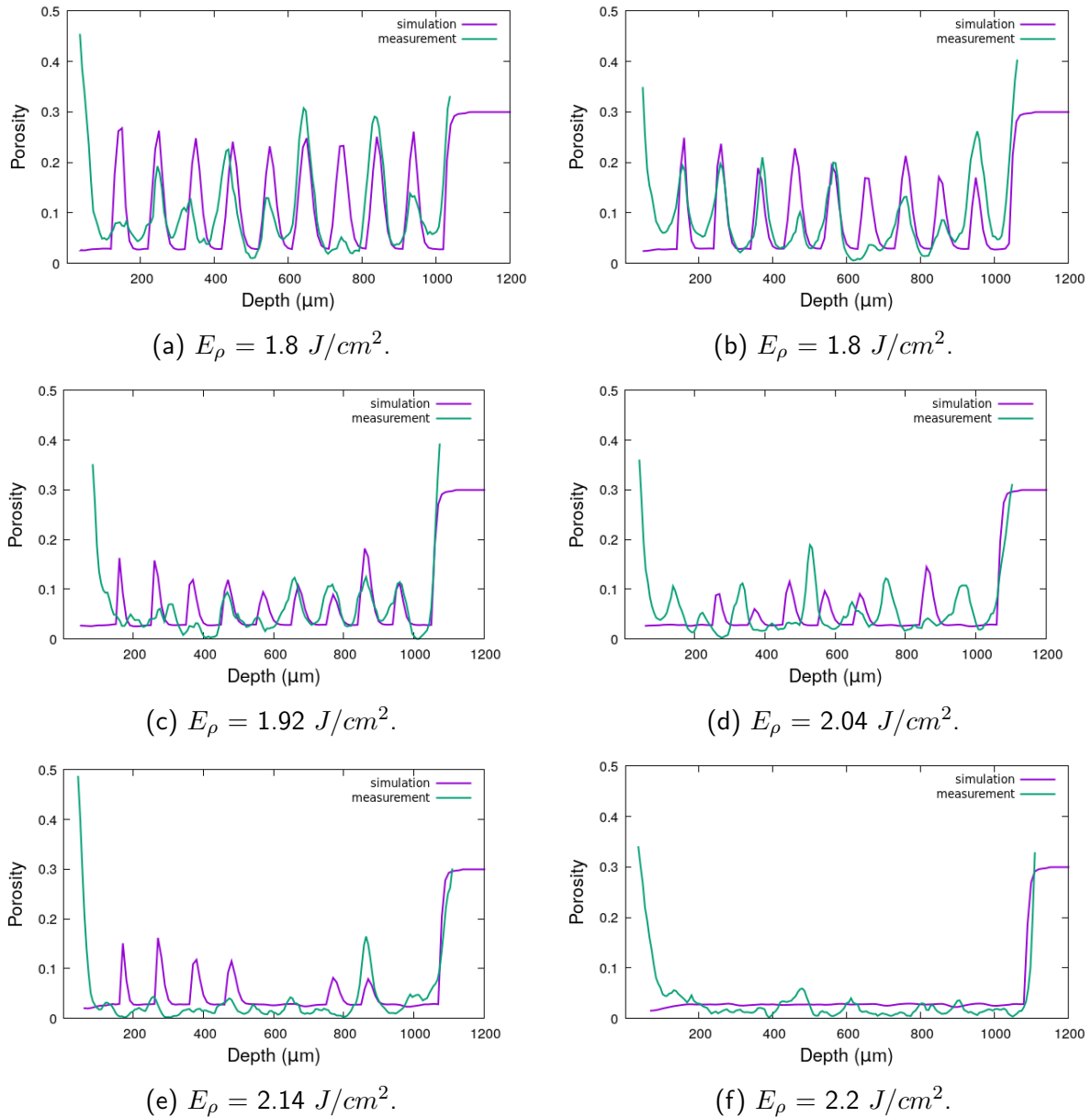


Figure 5.35: Porosity distribution versus energy density: comparison of measurements with numerical results.

We are going to qualify our modeling approach by comparing tomography measurements of porosity with numerical predictions of porosity. Many factors affect porosity of the powder bed, the main factors considered in the numerical simulations include laser power, energy density, preheating temperature, thickness of the added layers and polymer viscosity. This is why, in the simulations, we choose the mid-values of viscosity and activation energy:

zero-shear viscosity is equal to  $650 \text{ Pa}\cdot\text{s}$  and  $E_a$  is equal to  $58 \text{ kJ/mol}$ . The polymer powder bed is seen as a homogeneous medium with an initial porosity equal to 0.3 because of the even distribution of the particle size and the pressure applied to the thin polymer layers by the roller. To better describe the experimental conditions, numerical simulations are performed by using the horizontal scanning for the odd layers (1, 3, etc.) and the vertical scanning for the even layers (2, 4, etc.).

Porosity distributions in the depth direction are displayed in Fig. ?? for various energy densities: for each energy density numerical porosity profile is plotted against the experimental measurement. The global observation is the following: both experiments and simulations show the oscillatory distribution of the porosity, the layered structure of the samples, the decrease of porosity peaks with increasing energy density, and an qualitative agreement between them. The oscillatory behaviour of the porosity is more pronounced for lower energy density (Figs. 5.35a and 5.35b), less pronounced for higher energy density because of the decrease of porosity peak values (Figs. 5.35c, 5.35d and 5.35e) and disappeared completely for the highest energy density of  $E_p=2.2 \text{ J/cm}^2$  (Fig. 5.35f).

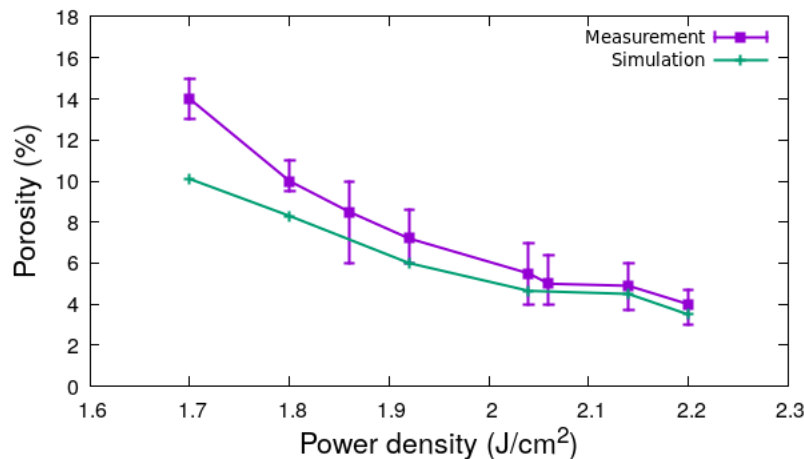


Figure 5.36: Comparison of the averaged Porosity

For the energy densities investigated, Fig. 5.36 shows the averaged porosity measured experimentally, the corresponding standard deviation and the averaged porosity of numerical simulations. The average porosity is decreasing as the energy density is increasing, this is observed in both the experiments and the simulations. Agreement between the measurements and the numerical results is good and encouraging for the numerical modeling. But note that for small energy density the difference between the experimental and numerical results is more important. The main reason for the discrepancy is the inaccurate knowledge on the sintering process and the properties of the materials. The preheating temperature is floating in the SLS machine while it is fixed in our simulations. Polymer viscosity depends on the aging degree of the powder and it is difficult to monitor the polymer aging in the SLS process. The initial porosity of the powder bed in the SLS machine is not well known and a value of 0.3 estimated from laboratory work is used in our simulations, furthermore the initial porosity under real particle packing conditions may not be homogeneous. Another possible reason is that we simulated only the central part of a sample: the end effects of the laser scanning are important for the vertical scanning and they are not considered in numerical simulations.

## 5.3 Summary

In this chapter, multi-layer processes are analysed. Time evolution of temperature and porosity distribution in the products are the highlight.

- In a multi-layer process, time evolution of surface temperature is not influenced by the previous layers because the waiting time is long enough to cool the scanned surface down to the preheating temperature.
- The laser scanning influences about 5 layers and repeatedly heats the polymer particles: it modifies slightly air escape, densification and hence porosity distribution. This modifies the conclusion drawn on the thermal influential zone of the laser scanning in one-layer cases.
- The porosity distribution in a manufactured sample is affected by the initial powder bed's porosity, the powder bed's preheating temperature, the thickness of the added layers, the laser power and the polymer viscosity. Decreasing the initial porosity and the thickness of the added layer and increasing the preheating temperature and the laser power decrease the sample's porosity and improve its density and its quality. Polymer viscosity plays a complex role because it depends on polymer aging degree and its effects depend on temperature.
- The X-ray computed tomography technique is used to measure the porosity distribution in the manufactured PA6 samples. The measurements are compared with the numerical results obtained with an initial porosity of 0.3, a zero-shear viscosity of 650 *Pa.s* and an activation energy ( $E_a$ ) of 58 *kJ/mol*. A good agreement observed on the porosity distribution, the averaged porosity and their evolution with respect to the energy density is encouraging and assesses the ability of our modeling.

# Conclusions and perspectives

## Conclusions

The SLS as a promising manufacturing method will be used in all the industry areas in the future industry. There are many defects existed in the sample comparing with traditional method and we need to control the manufacturing process for improving the samples' properties. The simulation methodology is used to better study the manufacturing process. This thesis focuses on simulating the whole SLS processes for PA material and more accurately heat transfer during the whole SLS processes. The phenomena involved in a SLS process or heat transfer in a SLS process include the laser-powder interaction, sintering and coalescence, powder bed's densification, and crystallisation. Details of these phenomena are discussed and modeled by the corresponding mathematical models. All the models are integrated in heat equation which is formulated under the assumption of an equivalent homogeneous medium to describe a SLS process. This assumption implies further models for thermo-physical properties, porosity, etc. Finite volume method is used to discretize the governing heat equation in space and the second-order semi-implicit Crank–Nicolson scheme is used to discretize it in time in order to obtain the transient thermal history in the powder bed. Note that the third-order Runge–Kutta method is used to discretize the coalescence model. The laser-powder interaction is first investigated: the scattering phenomenon is emphasized and analytical models are proposed. Temperature evolution, temperature distribution, thermally influenced area, dimension of the molten pool, and porosity of the samples are discussed in detail for both one-layer and multi-layer SLS cases.

We studied how the scattering phenomenon affects the distribution of laser power in a powder bed and heat transmission between laser and polymer particles. The modified Monte-Carlo method and the Mie theory are introduced to reflect the laser-polymer particles interaction. Different from the traditional Beer-Lambert method which only considers absorption and reflection, the MC model introduces also the scattering phenomenon. We analysed how the scattering factor ( $g$ ), the initial porosity of a powder bed and the particles' radius affect the distribution of laser power and heat transfer in the powder bed under scattering condition. Compared with the BL methods, the photons' distribution maps reveal that laser power is distributed in a larger and shallower zone under scattering condition and that the scattering leads to a wider and shallower molten pool. A larger distribution area for laser power which is caused by the fact that scattering modifies the photons' travel directions results in a lower maximum temperature on the bed surface. Surface temperature of the powder bed is measured by an IR camera and compared with the numerical results obtained by using both the scattering model and the BL model without scattering for laser power distribution. In single-sweep and single-layer SLS cases, time evolution of surface temperature using the scattering model fit better the experimental measurements of the IR camera. Finally, we calculated the dimension of the samples with our modeling and compared them with the existing

experimental results: a better prediction is observed when using the scattering model. These observations indicate the importance of the scattering phenomenon in laser-polymer powder interaction and hence the importance of the scattering model in simulating SLS processes.

We extended the studies to multi-sweep and single-layer cases. An IR camera is used to measure surface temperature of the powder bed and IR camera calibration is discussed. An IR camera captures the luminance signal emitted and reflected by the powder bed and outputs the Digital Level ( $DL$ ), then the  $DL$  value is converted into temperature. The factors influencing the conversion are camera correction factor, camera inclination angles and emissivity of the powder bed. The experimental results show that tilt angle has little influence on the results, especially when the angle is smaller than  $70^\circ$ . Emissivity of the powder bed depends on the emissivity of the polymer particles, the emissivity of the surface holes/pores and the porosity of the powder bed. As, during SLS processes, polymer particles change phase and the porosity and the surface roughness change too, it is very difficult to determine the emissivity of the powder bed and even less its time evolution which is necessary for the  $DL$  conversion. In the simulations performed, we chose 0.3 as the powder bed's initial porosity to better reflect the real condition. In the multi-sweep situation, surface temperature is higher than in the single-sweep situation because of the heating overlap. The numerical results reveal that shorter scanning length, smaller scanning space, lower scanning speed and higher preheating temperature increase the maximum temperature and prolong the high temperature keeping time. Higher initial porosity increases also the maximum temperature because of the lower melting sink. Comparison between numerical and experimental results shows a good agreement and assesses the ability of the scattering model and our modeling.

We applied the modeling to multi-layer cases, analyzed thermal history of the process and predicted the porosity distribution in the samples. In multi-layer processes, surface temperature and its time evolution are independent of other layers because the waiting time is very long and longer enough to cool the powder bed down to the preheating temperature. The porosity prediction is based on the sintering and coalescence model, which is highly affected by the preheating temperature, the initial porosity of the powder bed, the thickness of the added layers, laser power and polymer viscosity. Influences of these parameters are investigated and show that polymer viscosity depending on the aging degree is a complex parameter. An initial porosity of 0.3, a zero-shear viscosity of  $650 \text{ Pa}\cdot\text{s}$  and an activation energy ( $E_a$ ) of  $58 \text{ kJ/mol}$  are chosen for the numerical simulations. In order to assess the numerical results, the X-ray computed tomography technique is used to measure the porosity distribution in the manufactured PA6 samples. Comparison between the measurements and the numerical results shows a good agreement on the porosity distribution, the averaged porosity and their evolution with respect to the energy density.

## Perspectives

To evaluate heat transfer during a SLS process, we developed a detailed numerical modeling to predict thermal history (temperature), porosity distribution in the samples, averaged porosity, and dimension of the samples. Apart from pursuing the qualification/validation process of our modeling, the following points need to be improved:

- Crystallisation is the last phenomenon taking place in a SLS process, it determines another important output parameter, the crystallinity of the manufactured parts. Pre-

liminary experimental and simulation work has been done in the the present thesis and put in the appendix. We estimated roughly the values of melting latent heat of new polymer and aging polymer, simulated the crystallisation processes and estimated the crystallinity of the samples. The results obtained are interesting and in the future more work should be done both experimentally and numerically to improve the accuracy of the results.

- The computational cost of the numerical simulations performed is still too important although large time steps are used whenever it is possible. Therefore, we only simulated a small central part of the manufactured samples. To be able to simulate complete manufacturing products, more work needs to be done to simplify the simulation models and/or improve the computational efficiency. Model reduction could be a possibility.
- In the simulations performed, many model parameters of the polymer came from the experiments found in the literature. Given the fact that the materials used are provided by different suppliers and that the experiments are performed at different time periods, the model parameters chosen in the present work are not obtained for the same PA formulation and even less for the PA powder we used in the SLS machine. Future modeling progress relies heavily on the laboratory and process experiments performed for the polymer materials from the same formulation or at least from the same supplier. According to the current work, accurate knowledge on the preheating temperature and the initial porosity is privileged as none of the two parameters is measured up to now.
- We assume the powder bed is a uniformly homogeneous medium, but a real polymer powder bed may not be uniformly homogeneous. This leads to not only different equivalent local thermo-physical properties but also different laser-polymer powder interaction. Therefore, future experimental work is needed to characterise not only the porosity of a powder bed but also its spatial distribution and, if it is the case, the interaction of a laser with a non-uniformly homogeneous powder bed should be studied.

# References

- [1] C. W. Hull, *Apparatus for production of three-dimensional objects by stereolithography*, US Patent 4,575,330, 1986.
- [2] C. R. Deckard, *Method and apparatus for producing parts by selective sintering*, US Patent 4,863,538, 1989.
- [3] E. M. Sachs, J. S. Haggerty, M. J. Cima, and P. A. Williams, *Three-dimensional printing techniques*, US Patent 5,204,055, 1993.
- [4] *Smartechnology analysis issues new report on automotive additive manufacturing market, sees a 9 billion (usd) opportunity on the horizon*, SmarTech Markets Publishing, 2019.
- [5] A. P. "The complete guide to selective laser sintering (sls) in 3d printing." 3D printing news News. (2019).
- [6] D. Thomas, "Aiaa technical committee on management center overview and additive manufacturing at msfc," Tech. Rep., 2014.
- [7] T. Prater, "Study of material consolidation at higher throughput parameters in selective laser melting of inconel 718," in *The Materials Society (TMS) Annual Meeting & Exhibition*, 2016.
- [8] G. Liu, X. Zhang, X. Chen, *et al.*, "Additive manufacturing of structural materials," *Materials Science and Engineering: R: Reports*, vol. 145, p. 100 596, 2021.
- [9] B. Sun, Q. Ma, X. Wang, J. Liu, and M. Rejab, "Additive manufacturing in medical applications: A brief review," in *IOP conference series: materials science and engineering*, IOP Publishing, vol. 1078, 2021, p. 012 007.
- [10] M. Javaid and A. Haleem, "Additive manufacturing applications in medical cases: A literature based review," *Alexandria Journal of Medicine*, vol. 54, no. 4, pp. 411–422, 2018.
- [11] M. Cunha-Filho, M. R. Araújo, G. M. Gelfuso, and T. Gratieri, "Fdm 3d printing of modified drug-delivery systems using hot melt extrusion: A new approach for individualized therapy," *Therapeutic Delivery*, vol. 8, no. 11, pp. 957–966, 2017.
- [12] A. Butscher, M. Bohner, N. Doebelin, S. Hofmann, and R. Müller, "New depowdering-friendly designs for three-dimensional printing of calcium phosphate bone substitutes," *Acta biomaterialia*, vol. 9, no. 11, pp. 9149–9158, 2013.
- [13] B. Derby, "Printing and prototyping of tissues and scaffolds," *science*, vol. 338, no. 6109, pp. 921–926, 2012.

- [14] R. E. Saunders, J. E. Gough, and B. Derby, "Delivery of human fibroblast cells by piezoelectric drop-on-demand inkjet printing," *Biomaterials*, vol. 29, no. 2, pp. 193–203, 2008.
- [15] Y. Yap and W. Yeong, "Additive manufacture of fashion and jewellery products: A mini review: This paper provides an insight into the future of 3d printing industries for fashion and jewellery products," *Virtual and Physical Prototyping*, vol. 9, no. 3, pp. 195–201, 2014.
- [16] R. Brighenti, M. P. Cosma, L. Marsavina, A. Spagnoli, and M. Terzano, "Laser-based additively manufactured polymers: A review on processes and mechanical models," *Journal of Materials Science*, vol. 56, no. 2, pp. 961–998, 2021.
- [17] J. J. Beaman and C. R. Deckard, *Selective laser sintering with assisted powder handling*, US Patent 5,053,090, 1991.
- [18] B. Mueller, "Additive manufacturing technologies—rapid prototyping to direct digital manufacturing," *Assembly Automation*, 2012.
- [19] H. Lee, C. H. J. Lim, M. J. Low, N. Tham, V. M. Murukeshan, and Y.-J. Kim, "Lasers in additive manufacturing: A review," *International Journal of Precision Engineering and Manufacturing-Green Technology*, vol. 4, no. 3, pp. 307–322, 2017.
- [20] J.-P. Kruth, G. Levy, F. Klocke, and T. Childs, "Consolidation phenomena in laser and powder-bed based layered manufacturing," *CIRP annals*, vol. 56, no. 2, pp. 730–759, 2007.
- [21] B. T. Phillips, J. Alder, G. Bolan, *et al.*, "Additive manufacturing aboard a moving vessel at sea using passively stabilized stereolithography (sla) 3d printing," *Additive Manufacturing*, vol. 31, p. 100969, 2020.
- [22] S. F. S. Shirazi, S. Gharekhani, M. Mehrali, *et al.*, "A review on powder-based additive manufacturing for tissue engineering: Selective laser sintering and inkjet 3d printing," *Science and technology of advanced materials*, vol. 16, no. 3, p. 033502, 2015.
- [23] P. Shakor, S. Nejadi, G. Paul, and J. Sanjayan, "Dimensional accuracy, flowability, wettability, and porosity in inkjet 3dp for gypsum and cement mortar materials," *Automation in Construction*, vol. 110, p. 102964, 2020.
- [24] B. N. Turner and S. A. Gold, "A review of melt extrusion additive manufacturing processes: li. materials, dimensional accuracy, and surface roughness," *Rapid Prototyping Journal*, 2015.
- [25] O. S. Carneiro, A. Silva, and R. Gomes, "Fused deposition modeling with polypropylene," *Materials & Design*, vol. 83, pp. 768–776, 2015.
- [26] M. Schmidt, M. Merklein, D. Bourell, *et al.*, "Laser based additive manufacturing in industry and academia," *Cirp Annals*, vol. 66, no. 2, pp. 561–583, 2017.
- [27] B. Mueller and D. Kochan, "Laminated object manufacturing for rapid tooling and pattern-making in foundry industry," *Computers in Industry*, vol. 39, no. 1, pp. 47–53, 1999.
- [28] B. Cox, M. Saari, B. Xia, E. Richer, P. S. Krueger, and A. L. Cohen, "Fiber encapsulation additive manufacturing: Technology and applications update," *3D Printing and Additive Manufacturing*, vol. 4, no. 2, pp. 116–119, 2017.
- [29] W. Gao, Y. Zhang, D. Ramanujan, *et al.*, "The status, challenges, and future of additive manufacturing in engineering," *Computer-Aided Design*, vol. 69, pp. 65–89, 2015.

- [30] R. Goodridge, C. Tuck, and R. Hague, "Laser sintering of polyamides and other polymers," *Progress in Materials science*, vol. 57, no. 2, pp. 229–267, 2012.
- [31] J. Beaman and C. Deckard, *Selective laser sintering with assisted powder handling: Us4938816*.
- [32] A. Gisario, M. Kazarian, F. Martina, and M. Mehrpouya, "Metal additive manufacturing in the commercial aviation industry: A review," *Journal of Manufacturing Systems*, vol. 53, pp. 124–149, 2019.
- [33] J. P. Schultz, "Modeling heat transfer and densification during laser sintering of viscoelastic polymers," Ph.D. dissertation, Virginia Polytechnic Institute and State University, 2003.
- [34] C. Cai, W. S. Tey, J. Chen, *et al.*, "Comparative study on 3d printing of polyamide 12 by selective laser sintering and multi jet fusion," *Journal of Materials Processing Technology*, vol. 288, p. 116882, 2021.
- [35] J. M. Stujenske, T. Spellman, and J. A. Gordon, "Modeling the spatiotemporal dynamics of light and heat propagation for in vivo optogenetics," *Cell reports*, vol. 12, no. 3, pp. 525–534, 2015.
- [36] E. Nisipeanu and P. Jones, "Comparison of monte carlo surface exchange with radiative continuum results in large particle dispersions," *J. Heat Transfer*, vol. 122, no. 3, pp. 503–508, 2000.
- [37] J. Zhou, Y. Zhang, and J. Chen, "Numerical simulation of laser irradiation to a randomly packed bimodal powder bed," *International Journal of Heat and Mass Transfer*, vol. 52, no. 13–14, pp. 3137–3146, 2009.
- [38] M. Ilie, J.-C. Kneip, S. Mattei, A. Nichici, C. Roze, and T. Girasole, "Laser beam scattering effects in non-absorbent inhomogenous polymers," *Optics and Lasers in Engineering*, vol. 45, no. 3, pp. 405–412, 2007.
- [39] L. Xin, M. Boutaous, S. Xin, and D. A. Siginer, "Numerical modeling of the heating phase of the selective laser sintering process," *International Journal of Thermal Sciences*, vol. 120, pp. 50–62, 2017.
- [40] R. M. German, "Coarsening in sintering: Grain shape distribution, grain size distribution, and grain growth kinetics in solid-pore systems," *Critical reviews in solid state and materials sciences*, vol. 35, no. 4, pp. 263–305, 2010.
- [41] B. Haworth, J. R. Tyrer, and Z. Zhou, "Selective laser melting using holographic beam manipulation: Influence of polypropylene molecular weight," *Rapid Prototyping Journal*, 2018.
- [42] Z. Mierzejewska and W. Markowicz, "Selective laser sintering-binding mechanism and assistance in medical applications," *Advances in materials science*, vol. 15, no. 3, p. 5, 2015.
- [43] J.-P. Kruth, X. Wang, T. Laoui, and L. Froyen, "Lasers and materials in selective laser sintering," *Assembly Automation*, 2003.
- [44] T. Laoui, X. Wang, T. Childs, J.-P. Kruth, and L. Froyen, "Laser penetration in a powder bed during selective laser sintering of metal powders: Simulations versus experiments 453," in *2000 International Solid Freeform Fabrication Symposium*, 2000.

- [45] Y Shi, Z Li, H Sun, S Huang, and F Zeng, "Effect of the properties of the polymer materials on the quality of selective laser sintering parts," *Proceedings of the Institution of Mechanical Engineers, Part L: Journal of Materials: Design and Applications*, vol. 218, no. 3, pp. 247–252, 2004.
- [46] D. Schulze, "Powders and bulk solids," *Behaviour, characterization, storage and flow*. Springer, vol. 22, 2008.
- [47] S. Haeri, Y Wang, O Ghita, and J Sun, "Discrete element simulation and experimental study of powder spreading process in additive manufacturing," *Powder Technology*, vol. 306, pp. 45–54, 2017.
- [48] C. Boley, S. A. Khairallah, and A. M. Rubenchik, "Calculation of laser absorption by metal powders in additive manufacturing," *Applied optics*, vol. 54, no. 9, pp. 2477–2482, 2015.
- [49] W. E. King, A. T. Anderson, R. M. Ferencz, *et al.*, "Laser powder bed fusion additive manufacturing of metals; physics, computational, and materials challenges," *Applied Physics Reviews*, vol. 2, no. 4, p. 041304, 2015.
- [50] J. Lim and N. Khan, "Effects of particle size distribution on surface finish of selective laser melting parts," in *2019 International Solid Freeform Fabrication Symposium*, University of Texas at Austin, 2019.
- [51] M. Naftaly, G. Savvides, F. Alshareef, *et al.*, "Non-destructive porosity measurements of 3d printed polymer by terahertz time-domain spectroscopy," *Applied Sciences*, vol. 12, no. 2, p. 927, 2022.
- [52] L. Verbelen, S. Dadbakhsh, M. Van den Eynde, J.-P. Kruth, B. Goderis, and P. Van Puyvelde, "Characterization of polyamide powders for determination of laser sintering processability," *European Polymer Journal*, vol. 75, pp. 163–174, 2016.
- [53] P. Chen, H. Wu, W. Zhu, *et al.*, "Investigation into the processability, recyclability and crystalline structure of selective laser sintered polyamide 6 in comparison with polyamide 12," *Polymer Testing*, vol. 69, pp. 366–374, 2018.
- [54] M. Schmid, A. Amado, and K. Wegener, "Polymer powders for selective laser sintering (sls)," in *AIP Conference proceedings*, AIP Publishing LLC, vol. 1664, 2015, p. 160009.
- [55] —, "Materials perspective of polymers for additive manufacturing with selective laser sintering," *Journal of Materials Research*, vol. 29, no. 17, pp. 1824–1832, 2014.
- [56] M. I. Kohan, "Nylon plastics handbook, hanser," *Munich (Germany)*, 1995.
- [57] S. Dupin, O. Lame, C. Barrès, and J.-Y. Charneau, "Microstructural origin of physical and mechanical properties of polyamide 12 processed by laser sintering," *European Polymer Journal*, vol. 48, no. 9, pp. 1611–1621, 2012.
- [58] F. Yang, T. Jiang, G. Lalier, J. Bartolone, and X. Chen, "Process control of surface quality and part microstructure in selective laser sintering involving highly degraded polyamide 12 materials," *Polymer Testing*, vol. 93, p. 106920, 2021.
- [59] J. R. White, "Polymer ageing: Physics, chemistry or engineering? time to reflect," *Comptes Rendus Chimie*, vol. 9, no. 11-12, pp. 1396–1408, 2006.

- [60] H. Zarringhalam, N. Hopkinson, N. Kamperman, and J. De Vlieger, "Effects of processing on microstructure and properties of sls nylon 12," *Materials Science and Engineering: A*, vol. 435, pp. 172–180, 2006.
- [61] B. Haworth, N. Hopkinson, D. Hitt, and X. Zhong, "Shear viscosity measurements on polyamide-12 polymers for laser sintering," *Rapid Prototyping Journal*, 2013.
- [62] R. Goodridge, R. Hague, and C. Tuck, "Effect of long-term ageing on the tensile properties of a polyamide 12 laser sintering material," *Polymer Testing*, vol. 29, no. 4, pp. 483–493, 2010.
- [63] B. Wunderlich and J. Grebowicz, "Thermotropic mesophases and mesophase transitions of linear, flexible macromolecules," *Liquid crystal polymers II/III*, pp. 1–59, 1984.
- [64] M. Di Lorenzo and C. Silvestre, "Non-isothermal crystallization of polymers," *Progress in Polymer Science*, vol. 24, no. 6, pp. 917–950, 1999.
- [65] T. Ozawa, "Kinetics of non-isothermal crystallization," *Polymer*, vol. 12, no. 3, pp. 150–158, 1971.
- [66] A. Jeziorny, "Parameters characterizing the kinetics of the non-isothermal crystallization of poly (ethylene terephthalate) determined by dsc," *Polymer*, vol. 19, no. 10, pp. 1142–1144, 1978.
- [67] K. Nakamura, K. Katayama, and T. Amano, "Some aspects of nonisothermal crystallization of polymers. ii. consideration of the isokinetic condition," *Journal of Applied Polymer Science*, vol. 17, no. 4, pp. 1031–1041, 1973.
- [68] K. Nakamura, T. Watanabe, K. Katayama, and T. Amano, "Some aspects of nonisothermal crystallization of polymers. i. relationship between crystallization temperature, crystallinity, and cooling conditions," *Journal of Applied Polymer Science*, vol. 16, no. 5, pp. 1077–1091, 1972.
- [69] J. D. Hoffman, G. T. Davis, and J. I. Lauritzen, "The rate of crystallization of linear polymers with chain folding," in *Treatise on solid state chemistry*, Springer, 1976, pp. 497–614.
- [70] Y. Furushima, C. Schick, and A. Toda, "Crystallization, recrystallization, and melting of polymer crystals on heating and cooling examined with fast scanning calorimetry," *Polymer Crystallization*, vol. 1, no. 2, e10005, 2018.
- [71] N. Dencheva, Z. Denchev, M. J. Oliveira, and S. S. Funari, "Relationship between crystalline structure and mechanical behavior in isotropic and oriented polyamide 6," *Journal of applied polymer science*, vol. 103, no. 4, pp. 2242–2252, 2007.
- [72] L. S. Loo and K. K. Gleason, "Insights into structure and mechanical behavior of  $\alpha$  and  $\gamma$  crystal forms of nylon-6 at low strain by infrared studies," *Macromolecules*, vol. 36, no. 16, pp. 6114–6126, 2003.
- [73] R. Puffr and V. Kubanek, "Lactam-based polyamides," *Vol. II, CRC Press, Ann Arbor MI*, pp. 145–162, 1991.
- [74] S. M. Aharoni, *n-Nylons: their synthesis, structure, and properties*. John Wiley & Sons Incorporated, 1997.
- [75] J. Pepin, V. Miri, and J.-M. Lefebvre, "New insights into the brill transition in polyamide 11 and polyamide 6," *Macromolecules*, vol. 49, no. 2, pp. 564–573, 2016.

- [76] D. Holmes, C. Bunn, and D. Smith, "The crystal structure of polycapraamide: Nylon 6," *Journal of Polymer Science*, vol. 17, no. 84, pp. 159–177, 1955.
- [77] X. Duan, Y. Wu, Z. Chen, *et al.*, "In-situ polymerization of high-molecular weight nylon 66 modified clay nanocomposites with low apparent viscosity," *Polymers*, vol. 11, no. 3, p. 510, 2019.
- [78] Y. Li and D. Gu, "Thermal behavior during selective laser melting of commercially pure titanium powder: Numerical simulation and experimental study," *Additive Manufacturing*, vol. 1, pp. 99–109, 2014.
- [79] E. Malekipour and H. El-Mounayri, "Common defects and contributing parameters in powder bed fusion am process and their classification for online monitoring and control: A review," *The International Journal of Advanced Manufacturing Technology*, vol. 95, no. 1, pp. 527–550, 2018.
- [80] P. Bacchewar, S. Singhal, and P. Pandey, "Statistical modelling and optimization of surface roughness in the selective laser sintering process," *Proceedings of the Institution of Mechanical Engineers, Part B: Journal of Engineering Manufacture*, vol. 221, no. 1, pp. 35–52, 2007.
- [81] A. Sachdeva, S. Singh, and V. S. Sharma, "Investigating surface roughness of parts produced by sls process," *The International Journal of Advanced Manufacturing Technology*, vol. 64, no. 9, pp. 1505–1516, 2013.
- [82] Z. Zhu, S. Lou, and C. Majewski, "Characterisation and correlation of areal surface texture with processing parameters and porosity of high speed sintered parts," *Additive Manufacturing*, vol. 36, p. 101402, 2020.
- [83] M. Vlasea, R. Pilliar, and E. Toyserkani, "Control of structural and mechanical properties in bioceramic bone substitutes via additive manufacturing layer stacking orientation," *Additive Manufacturing*, vol. 6, pp. 30–38, 2015.
- [84] D. Gu and Y. Shen, "Effects of processing parameters on consolidation and microstructure of w–cu components by dmls," *Journal of Alloys and Compounds*, vol. 473, no. 1-2, pp. 107–115, 2009.
- [85] C. Hauser, "Selective laser sintering of a stainless steel powder," Ph.D. dissertation, University of Leeds, 2003.
- [86] O. Lopez-Botello, U. Martinez-Hernandez, J. Ramírez, C. Pinna, and K. Mumtaz, "Two-dimensional simulation of grain structure growth within selective laser melted aa-2024," *Materials & Design*, vol. 113, pp. 369–376, 2017.
- [87] K Dai and L Shaw, "Thermal and mechanical finite element modeling of laser forming from metal and ceramic powders," *Acta Materialia*, vol. 52, no. 1, pp. 69–80, 2004.
- [88] F. Liu, Q Zhang, W. Zhou, J. Zhao, and J. Chen, "Micro scale 3d fem simulation on thermal evolution within the porous structure in selective laser sintering," *Journal of Materials Processing Technology*, vol. 212, no. 10, pp. 2058–2065, 2012.
- [89] J. C. Steuben, A. P. Iliopoulos, and J. G. Michopoulos, "Discrete element modeling of particle-based additive manufacturing processes," *Computer Methods in Applied Mechanics and Engineering*, vol. 305, pp. 537–561, 2016.

- [90] S. Luding, "Cohesive, frictional powders: Contact models for tension," *Granular matter*, vol. 10, no. 4, pp. 235–246, 2008.
- [91] R. Kačianauskas, A. Maknickas, A. Kačeniauskas, D. Markauskas, and R. Balevičius, "Parallel discrete element simulation of poly-dispersed granular material," *Advances in Engineering Software*, vol. 41, no. 1, pp. 52–63, 2010.
- [92] P. Yuan and D. Gu, "Molten pool behaviour and its physical mechanism during selective laser melting of tic/alsi10mg nanocomposites: Simulation and experiments," *Journal of Physics D: Applied Physics*, vol. 48, no. 3, p. 035 303, 2015.
- [93] A. Mokrane, M. Boutaous, and S. Xin, "Process of selective laser sintering of polymer powders: Modeling, simulation, and validation," *Comptes Rendus Mécanique*, vol. 346, no. 11, pp. 1087–1103, 2018.
- [94] A. Okunkova, M. Volosova, P. Peretyagin, Y. Vladimirov, I. Zhirnov, and A. Gusarov, "Experimental approbation of selective laser melting of powders by the use of non-gaussian power density distributions," *Physics Procedia*, vol. 56, pp. 48–57, 2014.
- [95] P.-k. BAI, J. CHENG, L. Bin, and W.-f. WANG, "Numerical simulation of temperature field during selective laser sintering of polymer-coated molybdenum powder," *Transactions of Non-ferrous Metals Society of China*, vol. 16, s603–s607, 2006.
- [96] Z. Jiang, X. Chen, H. Li, *et al.*, "Grain refinement and laser energy distribution during laser oscillating welding of invar alloy," *Materials & Design*, vol. 186, p. 108 195, 2020.
- [97] L Dong, A Makradi, S Ahzi, and Y Remond, "Three-dimensional transient finite element analysis of the selective laser sintering process," *Journal of materials processing technology*, vol. 209, no. 2, pp. 700–706, 2009.
- [98] J. D. Williams and C. R. Deckard, "Advances in modeling the effects of selected parameters on the sls process," *Rapid Prototyping Journal*, 1998.
- [99] P. F. Jacobs, *Rapid prototyping & manufacturing: fundamentals of stereolithography*. Society of Manufacturing Engineers, 1992.
- [100] F. Osmanlic, K. Wudy, T. Laumer, M. Schmidt, D. Drummer, and C. Körner, "Modeling of laser beam absorption in a polymer powder bed," *Polymers*, vol. 10, no. 7, p. 784, 2018.
- [101] G Zak, L Mayboudi, M Chen, P. J. Bates, and M Birk, "Weld line transverse energy density distribution measurement in laser transmission welding of thermoplastics," *Journal of Materials Processing Technology*, vol. 210, no. 1, pp. 24–31, 2010.
- [102] G. Mie, "Beiträge zur optik trüber medien, speziell kolloidaler metallösungen," *Annalen der physik*, vol. 330, no. 3, pp. 377–445, 1908.
- [103] L. Xin, M. Boutaous, S. Xin, and D. A. Siginer, "Multiphysical modeling of the heating phase in the polymer powder bed fusion process," *Additive Manufacturing*, vol. 18, pp. 121–135, 2017.
- [104] S. L. Jacques and L. Wang, "Monte carlo modeling of light transport in tissues," in *Optical-thermal response of laser-irradiated tissue*, Springer, 1995, pp. 73–100.
- [105] X. Liu, "Numerical modeling and simulation of selective laser sintering in polymer powder bed," Ph.D. dissertation, Université de Lyon, 2017.

- [106] N. K. Tolochko, Y. V. Khlopkov, S. E. Mozzharov, M. B. Ignatiev, T. Laoui, and V. I. Titov, "Absorptance of powder materials suitable for laser sintering," *Rapid Prototyping Journal*, 2000.
- [107] R West, D Gibbs, L Tsang, and A. Fung, "Comparison of optical scattering experiments and the quasi-crystalline approximation for dense media," *JOSA A*, vol. 11, no. 6, pp. 1854–1858, 1994.
- [108] T Laumer, T Stichel, K Nagulin, and M Schmidt, "Optical analysis of polymer powder materials for selective laser sintering," *Polymer Testing*, vol. 56, pp. 207–213, 2016.
- [109] E. E. Gonzo, "Estimating correlations for the effective thermal conductivity of granular materials," *Chemical Engineering Journal*, vol. 90, no. 3, pp. 299–302, 2002.
- [110] J. C. Maxwell, *A treatise on electricity and magnetism*. Clarendon press, 1873, vol. 1.
- [111] Y. Chiew and E. Glandt, "The effect of structure on the conductivity of a dispersion," *Journal of colloid and interface science*, vol. 94, no. 1, pp. 90–104, 1983.
- [112] Z. Hashin and S. Shtrikman, "A variational approach to the theory of the effective magnetic permeability of multiphase materials," *Journal of applied Physics*, vol. 33, no. 10, pp. 3125–3131, 1962.
- [113] T. Bauer, "A general analytical approach toward the thermal conductivity of porous media," *International journal of heat and mass transfer*, vol. 36, no. 17, pp. 4181–4191, 1993.
- [114] J. A. Eastman, S. Choi, S. Li, W Yu, and L. Thompson, "Anomalously increased effective thermal conductivities of ethylene glycol-based nanofluids containing copper nanoparticles," *Applied physics letters*, vol. 78, no. 6, pp. 718–720, 2001.
- [115] R. L. Hamilton and O. Crosser, "Thermal conductivity of heterogeneous two-component systems," *Industrial & Engineering chemistry fundamentals*, vol. 1, no. 3, pp. 187–191, 1962.
- [116] Y. Zhao, Y. Koizumi, K. Aoyagi, K. Yamanaka, and A. Chiba, "Thermal properties of powder beds in energy absorption and heat transfer during additive manufacturing with electron beam," *Powder Technology*, vol. 381, pp. 44–54, 2021.
- [117] S. S. Sih and J. W. Barlow, "Emissivity of powder beds," in *1995 International Solid Freeform Fabrication Symposium*, 1995.
- [118] V. Voller and C. Swaminathan, "General source-based method for solidification phase change," *Numerical Heat Transfer*, no. Part B, pp. 175–189,
- [119] A. Amado, M. Schmid, and K. Wegener, "Simulation of warpage induced by non-isothermal crystallization of co-polypropylene during the sls process," in *AIP Conference Proceedings*, AIP Publishing LLC, vol. 1664, 2015, p. 160 002.
- [120] R. J. Gaymans, J. Amirtharaj, and H. Kamp, "Nylon 6 polymerization in the solid state," *Journal of applied polymer science*, vol. 27, no. 7, pp. 2513–2526, 1982.
- [121] A. Birley, B Haworth, and J Batchelor, *Physics of plastics: Processing, properties and materials engineering*, 1991.
- [122] S. Dadbakhsh, L. Verbelen, O. Verkinderen, D. Strobbe, P. Van Puyvelde, and J.-P. Kruth, "Effect of pa12 powder reuse on coalescence behaviour and microstructure of sls parts," *European Polymer Journal*, vol. 92, pp. 250–262, 2017.

- [123] S. Dupin, "Etude fondamentale de la transformation du polyamide 12 par frittage laser: Mécanismes physico-chimiques et relations microstructures/propriétés," Ph.D. dissertation, INSA de Lyon, 2012.
- [124] P. J. Carreau, "Rheological equations from molecular network theories," *Transactions of the Society of Rheology*, vol. 16, no. 1, pp. 99–127, 1972.
- [125] K. Yasuda, R. Armstrong, and R. Cohen, "Shear flow properties of concentrated solutions of linear and star branched polystyrenes," *Rheologica Acta*, vol. 20, no. 2, pp. 163–178, 1981.
- [126] D. Parisi, S. Costanzo, Y. Jeong, *et al.*, "Nonlinear shear rheology of entangled polymer rings," *Macromolecules*, vol. 54, no. 6, pp. 2811–2827, 2021.
- [127] W. W. Graessley, "Linear viscoelasticity in entangling polymer systems," *The Journal of Chemical Physics*, vol. 54, no. 12, pp. 5143–5157, 1971.
- [128] D. Ruggi, "Mise en œuvre de poudres de polyamides: Influence des conditions de transformation sur la microstructure et les propriétés. application à la fabrication additive par fusion laser.," Ph.D. dissertation, Lyon, 2019.
- [129] P. Hornsby and A. Maxwell, "Mechanism of sintering between polypropylene beads," *Journal of materials science*, vol. 27, no. 9, pp. 2525–2533, 1992.
- [130] M. Asgarpour, F. Bakir, S. Khelladi, A. Khavandi, and A. Tcharkhtchi, "3d model for powder compact densification in rotational molding," *Polymer Engineering & Science*, vol. 52, no. 9, pp. 2033–2040, 2012.
- [131] S.-P. Lyu, F. S. Bates, and C. W. Macosko, "Coalescence in polymer blends during shearing," *AIChE Journal*, vol. 46, no. 2, pp. 229–238, 2000.
- [132] J. Frenkel, "Viscous flow of crystalline bodies under the action of surface tension," *J. phys.*, vol. 9, p. 385, 1945.
- [133] M. O. Prado, E. D. Zanotto, and C. Fredericci, "Sintering polydispersed spherical glass particles," *Journal of materials research*, vol. 18, no. 6, pp. 1347–1354, 2003.
- [134] M. O. Prado, M. L. F. Nascimento, and E. D. Zanotto, "On the sinterability of crystallizing glass powders," *Journal of Non-Crystalline Solids*, vol. 354, no. 40-41, pp. 4589–4597, 2008.
- [135] F. B. Wadsworth, J. Vasseur, E. W. Llewellyn, *et al.*, "Sintering of viscous droplets under surface tension," *Proceedings of the Royal Society A: Mathematical, Physical and Engineering Sciences*, vol. 472, no. 2188, p. 20150780, 2016.
- [136] A. Hamidi, S. Farzaneh, F. Nony, *et al.*, "Modelling of sintering during rotational moulding of the thermoplastic polymers," *International Journal of Material Forming*, vol. 9, no. 4, pp. 519–530, 2016.
- [137] O. Pokluda, C. T. Bellehumeur, and J. Vlachopoulos, "Modification of frenkel's model for sintering," *AIChE journal*, vol. 43, no. 12, pp. 3253–3256, 1997.
- [138] G. W. Scherer, "Viscous sintering of a bimodal pore-size distribution," *Journal of the American Ceramic Society*, vol. 67, no. 11, pp. 709–715, 1984.

- [139] M. O. Prado, E. B. Ferreira, and E. D. Zanotto, "Sintering kinetics of crystallizing glass particles. a review," *Melt Chemistry, Relaxation, and Solidification Kinetics of Glasses*, vol. 170, pp. 163–179, 2006.
- [140] E. A. Giess, J. P. Fletcher, and L. W. Herron, "Isothermal sintering of cordierite-type glass powders," *Journal of the American Ceramic Society*, vol. 67, no. 8, pp. 549–552, 1984.
- [141] R Le Goff, G Poutot, D Delaunay, R Fulchiron, and E Koscher, "Study and modeling of heat transfer during the solidification of semi-crystalline polymers," *International Journal of Heat and Mass Transfer*, vol. 48, no. 25-26, pp. 5417–5430, 2005.
- [142] C. Ruan, "Kinetics and morphology of flow induced polymer crystallization in 3d shear flow investigated by monte carlo simulation," *Crystals*, vol. 7, no. 2, p. 51, 2017.
- [143] I. Hillier, "Modified avrami equation for the bulk crystallization kinetics of spherulitic polymers," *Journal of Polymer Science Part A: General Papers*, vol. 3, no. 9, pp. 3067–3078, 1965.
- [144] T. Choupin, B. Fayolle, G. Regnier, C Paris, J. Cinquin, and B. Brulé, "Isothermal crystallization kinetic modeling of poly (etherketoneketone)(pekk) copolymer," *Polymer*, vol. 111, pp. 73–82, 2017.
- [145] D Riedlbauer, M Drexler, D Drummer, P Steinmann, and J Mergheim, "Modelling, simulation and experimental validation of heat transfer in selective laser melting of the polymeric material pa12," *Computational Materials Science*, vol. 93, pp. 239–248, 2014.
- [146] P. Peyre, Y. Rouchausse, D. Defauchy, and G. Régnier, "Experimental and numerical analysis of the selective laser sintering (sls) of pa12 and pekk semi-crystalline polymers," *Journal of Materials Processing Technology*, vol. 225, pp. 326–336, 2015.
- [147] Z. Ling, J. Wu, X. Wang, X. Li, and J. Zheng, "Experimental study on the variance of mechanical properties of polyamide 6 during multi-layer sintering process in selective laser sintering," *The International Journal of Advanced Manufacturing Technology*, vol. 101, no. 5, pp. 1227–1234, 2019.
- [148] A. Pilipović, I. Drstvenšek, and M. Šercer, "Mathematical model for the selection of processing parameters in selective laser sintering of polymer products," *Advances in Mechanical Engineering*, vol. 6, p. 648 562, 2014.
- [149] A. Pilipović, T. Brajljih, and I. Drstvenšek, "Influence of processing parameters on tensile properties of sls polymer product," *Polymers*, vol. 10, no. 11, p. 1208, 2018.
- [150] H Budzier and G Gerlach, "Calibration of uncooled thermal infrared cameras," *Journal of Sensors and Sensor Systems*, vol. 4, no. 1, pp. 187–197, 2015.
- [151] M. Honner, P. Honnerová, M. Kučera, and J. Martan, "Laser scanning heating method for high-temperature spectral emissivity analyses," *Applied Thermal Engineering*, vol. 94, pp. 76–81, 2016.
- [152] E. Rodriguez, J. Mireles, C. A. Terrazas, D. Espalin, M. A. Perez, and R. B. Wicker, "Approximation of absolute surface temperature measurements of powder bed fusion additive manufacturing technology using in situ infrared thermography," *Additive Manufacturing*, vol. 5, pp. 31–39, 2015.

- 
- [153] P. D. Hiscocks and P Eng, "Measuring luminance with a digital camera," *Syscomp electronic design limited*, vol. 2, 2011.
- [154] A. D. K. KATTA, "Analysis of pa6 powder ageing during the selective laser sintering process," Ph.D. dissertation, Hochschule Aalen, 2019.
- [155] T Stiller, M Berer, A. K. Katta, *et al.*, "Powder ageing of polyamide 6 in laser sintering and its effects on powder and component characteristics," *Additive Manufacturing*, vol. 58, p. 102987, 2022.
- [156] N. Zaldua, J. Maiz, A. de la Calle, *et al.*, "Nucleation and crystallization of pa6 composites prepared by t-rtm: Effects of carbon and glass fiber loading," *Polymers*, vol. 11, no. 10, p. 1680, 2019.
- [157] C Majewski, H Zarringhalam, and N Hopkinson, "Effect of the degree of particle melt on mechanical properties in selective laser-sintered nylon-12 parts," *Proceedings of the Institution of Mechanical Engineers, Part B: Journal of Engineering Manufacture*, vol. 222, no. 9, pp. 1055–1064, 2008.

# Appendix A

## Crystallization analysis

In a SLS process, crystallisation happens during the last phase, the cooling phase, before getting the final samples/products. The crystallisation process influences one of the important output parameters, the final crystallinity of the final samples/products. As mechanical properties of the final samples/products depend on the final crystallinity, it is important to study crystallisation processes.

### A.1 DSC method and crystallinity

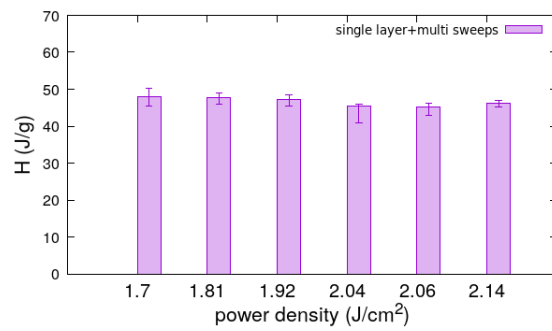
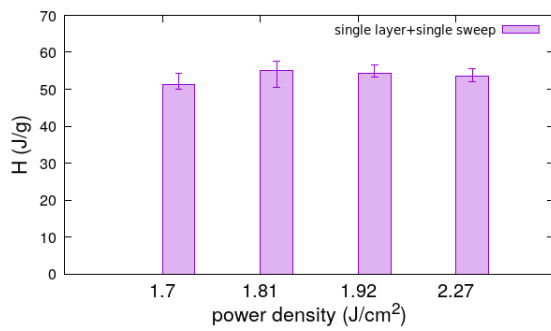
The thermal analysis experiments of laser samples are realised using a Diamond DSC machine, the DSC measurements are carried out with samples' weights between 5–10 *mg* under nitrogen flow. Samples are heated up from 20 °C to 240 °C, kept at 240 °C for 1 minute, and cooled down to 20 °C. All the steps are carried out with a rate of 10 °C/*min*, and the thermal programs of each step are recorded.

The degree of crystallinity  $X_c$  can be calculated by the following equation:

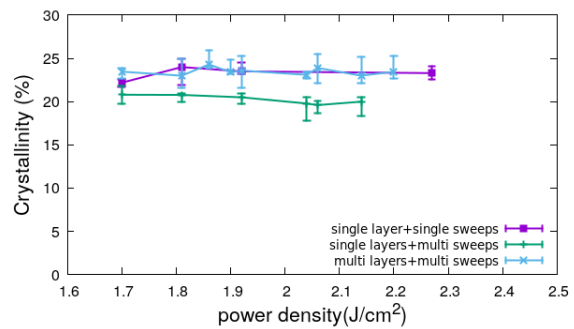
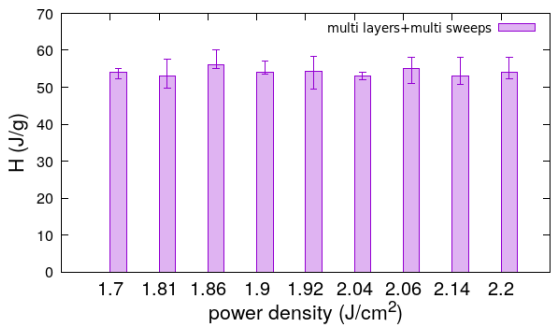
$$X_c = \frac{\Delta H_m}{\Delta H_m^0} \times 100\% \quad (\text{A.1})$$

where  $\Delta H_m$  is the melting enthalpy of the samples,  $\Delta H_m^0$  is the melting enthalpy of the perfect crystal, equal to 230 *J/g* for 100 % crystalline PA6 material [53] [75].

Fig. A.1 shows the melting enthalpy and the crystallinity of the samples that are manufactured with different processes. Fig. A.1a presents the melting enthalpy in single-sweep and single-layer situations: the melting enthalpy is between 52 *J/g* to 58 *J/g*. Fig. A.7a presents the melting enthalpy in multi-sweep and single-layer situations for energy density varying from 1.7 *J/cm<sup>2</sup>* to 2.14 *J/cm<sup>2</sup>*, the value of the melting enthalpy is in the range from 45 *J/g* to 50 *J/g*. Fig. A.7b presents the result in multi-layer cases and the averaged melting enthalpy is about 55 *J/g*. In the three groups of situations, the latent heat does not seem to depend on the energy density. But note that the melting enthalpy in multi-sweep and single-layer cases is smaller than the results obtained in single-sweep/single-layer and multi-sweep/multi-layer cases. The difference observed in the melting enthalpy may be due to the percentage of the molten polymer and the polymer aging during the corresponding processes. In fact, the molten polymer will crystallise partly during the cooling phase to



(a) Melting enthalpy in single-layer and single-sweep cases. (b) Melting enthalpy in single-layer and multi-sweep cases.



(c) Melting enthalpy in multi-layer and multi-sweep cases. (d) Crystallinity versus energy density

Figure A.1: Influence of SLS processes on melting enthalpy and crystallinity versus energy density with different fabrication condition.

form new crystalline and thermal aging modifies also thermo-physical properties of the aging powder.

Figs. A.2, A.3 and A.4 present the DSC curves of the samples manufactured in three SLS processes. In the single-sweep situation, the DSC curve shows two peaks for the fusion (Fig. A.2). They correspond to two types of crystalline: the peak at lower temperature corresponds to the crystallised aging polymer and the other one at higher temperature to the virgin or aging polymer powder. In the multi-sweep and single-layer case, the first peak of the crystallised aging polymer is lower and the second peak of the virgin or aging polymer powder is higher in comparison with the single-sweep/single-layer situation. In the single-sweep situation, the maximum heat flow takes place at the second peak temperature equal to about 208.5 °C, it decreases to 207 °C in the multi-sweep and single-layer situation. In the multi-sweep and multi-layer situation the maximum heat flow occurs at a higher temperature of 210 °C and the first peak of heat flow almost disappears.

The polymer aging of PA6 powders is studied experimentally by Katta [154] and Stiller et al. [155]: the effects of the aging and degradation phenomena on the properties are investigated for the virgin powders and the used powders during SLS processes manufacturing tensile samples. A SLS process producing 16 tensile samples is called one iteration: iteration 0 starts with virgin powders, at the end of iteration 0 the used powders are picked up from the thermally influenced but non molten zone. Then iteration 2 starts and at its end the used powders are picked up again. The procedure is followed till the end of iteration 7. The DSC experiments are conducted with the sample powders picked up after each iteration for two

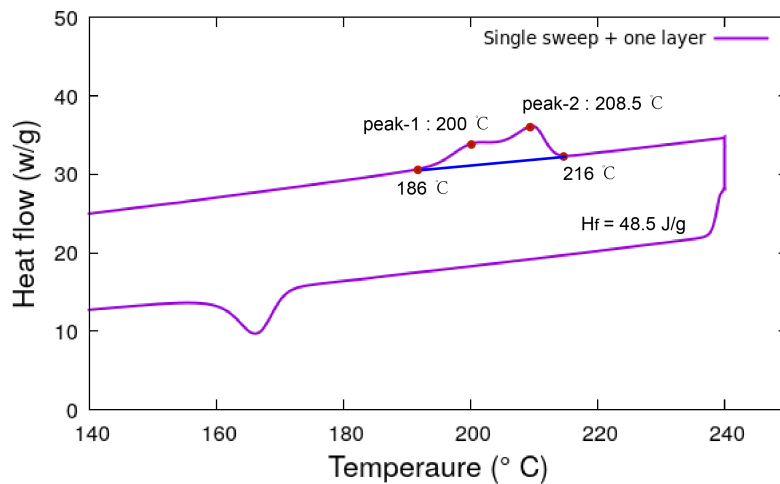


Figure A.2: DSC curve of a sample manufactured in a single-sweep and single-layer process.

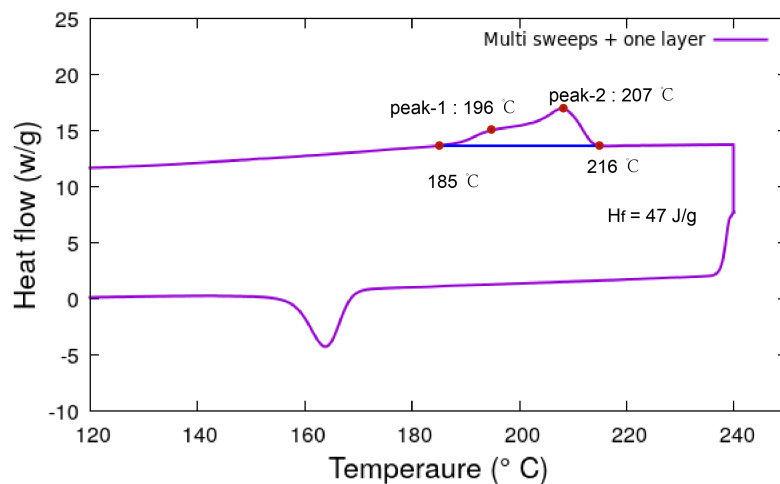


Figure A.3: DSC curve of a sample manufactured in a multi-sweep and single-layer process.

DSC heating cycles which are denoted respectively as the *1st* and *2nd* heating cycles. Fig. A.5 displays the crystallinity of PA6 powders from iteration 0 (unused powder) to iteration 7 (used powder) obtained after the *1st* and *2nd* heating cycles. For the experiments of the *1st* heating, sample powders are never melted before. As they are kept below the initial melting temperature, they are only aged. We see therefore that thermal aging either keeps or increases the melting enthalpy: DSC reveals the same crystallinity as the virgin powder after iteration 1 and a higher crystallinity of about 31 % after iteration 2 and other iterations (Fig. A.5a), the increase is induced by the thermo-oxidation, where the oxidative attack is preferentially localized on the C-H bonds of nitrogen atoms to decrease the molecular weight and increase the crystallinity. For the experiments of the *2nd* heating, DSC samples are cooled down to low temperature and crystallisation of the more or less aged polymer takes place under the DSC cooling conditions. The results indicate that crystallinity decreases for crystallisation under the DSC cooling conditions (Fig. A.5b). Another important result concerns the peak melting temperature: thermal aging decreases the peak melting temperature of PA6 powder from 210 °C for iterations 0 and 1 to 208 °C since iterations 2 (Fig. A.5c) on the one hand and on the other hand it increases the peak melting temperature of melted and crystallised aging PA6 powder to 209 °C since iteration 2.

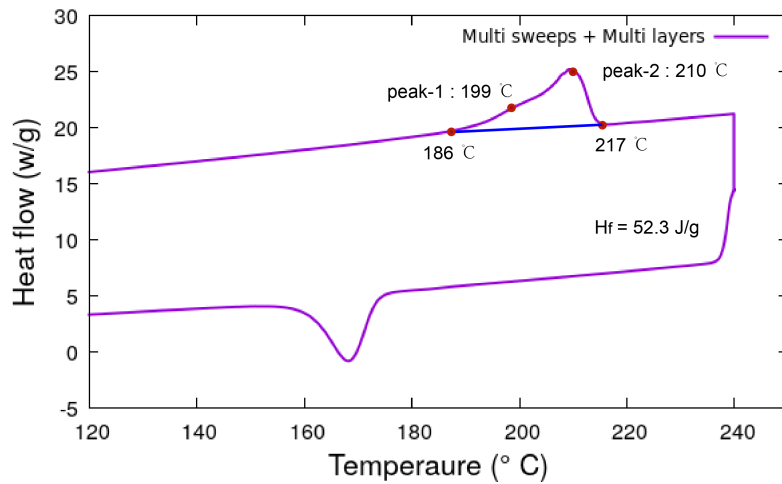


Figure A.4: DSC curve of a sample manufactured in a multi-sweep and multi-layer process

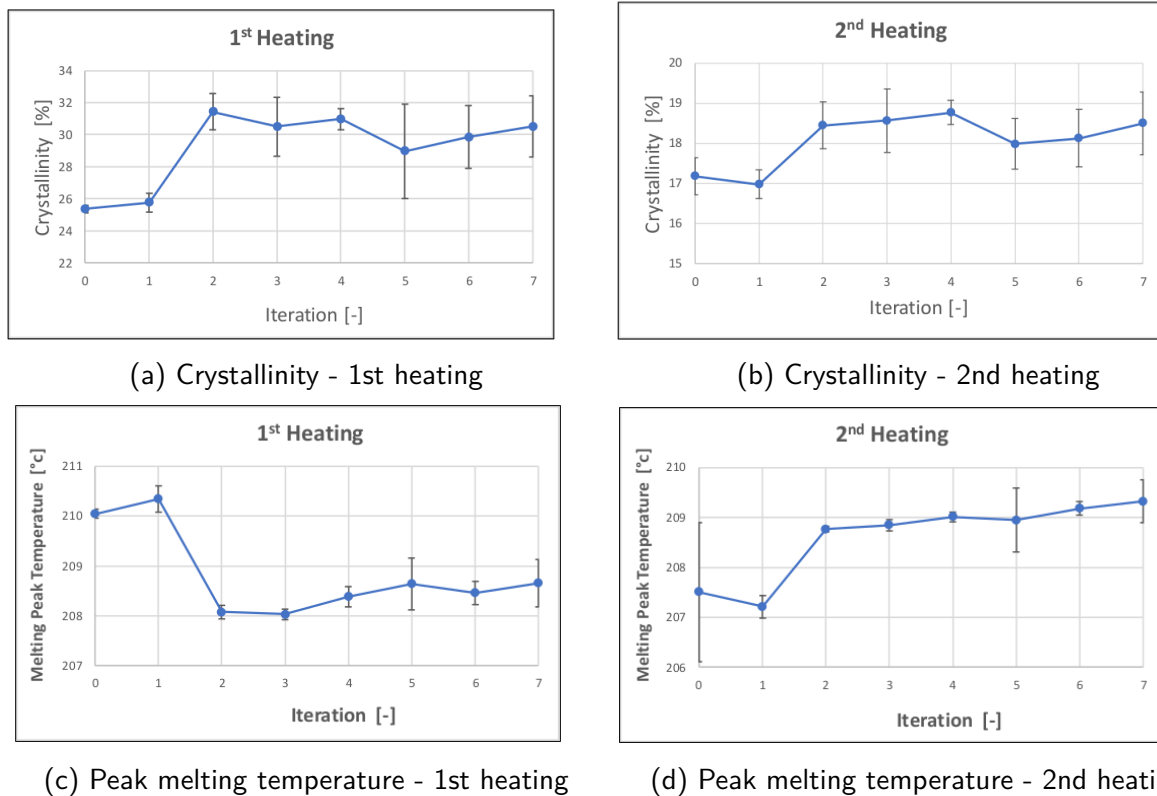


Figure A.5: Crystallinity ((a) and (b)) and peak melting temperature ((c) and (d)) of the PA6 powders for the 1st and 2nd heating runs with respect to the iteration number (iteration 0 is the virgin powder) [154].

Ruggi et al [128] measured, from the DSC melting and crystallisation curves, the initial melting temperature ( $T_{f\_debut}$ ), the temperature of melting peak ( $T_f$ ), the initial crystallization temperature ( $T_{c\_debut}$ ), the temperature of crystallization peak ( $T_c$ ), melting latent heat ( $\Delta H_f$  (J/g)) and crystallization enthalpy ( $\Delta H_C$  (J/g)) of PA6. They recorded these parameters at 1, 3 and 6 DSC testing cycles for a maximum arriving temperature of 240 °C and 280 °C. The corresponding results are shown in Tab. A.1. In the case of the maximum arriving temperature of 240 °C,  $T_f$  decreases from 209 °C at cycle 1 to 204 °C at cycle 6. We can see that the melting latent heat ( $\Delta H_f$ ) decreases from 68 J/g at cycle 1 to 35 J/g

at cycle 6.

Ruggi et al [128] also manufactured the PA6 tensile specimens according to ISO 527-1A using high energy density ( $3.65 \text{ J/cm}^2$ ) to totally melt the polymer and measured the crystallinity of the samples which are annealed at  $433 \text{ K}$  for increasing keeping time. The keeping times are  $0 \text{ h}$ ,  $1 \text{ h}$ ,  $10 \text{ h}$ , and  $24 \text{ h}$  and the corresponding crystallinities measured are equal to  $20 \%$ ,  $23 \%$ ,  $25 \%$  and  $28 \%$ , respectively. Because the repeated heating promotes the thermal degradation of the polymer and longer keeping time promotes crystallisation, the melting latent heat of the tensile specimens is higher than the melting latent heat of melted and crystallised PA6 material under DSC conditions.

Table A.1: Thermal characteristics recorded during cycles 1, 3, and 6, for a maximum temperature reach to  $240 \text{ }^\circ\text{C}/280 \text{ }^\circ\text{C}$  during the cycles [128].

Cycle number	$T_{fdebut} (^\circ\text{C})$	$T_f (^\circ\text{C})$	$T_{cdebut} (^\circ\text{C})$	$T_c (^\circ\text{C})$	$\Delta H_f (\text{J/g})$	$\Delta H_c (\text{J/g})$
$240 \text{ }^\circ\text{C}$						
1	200	209	169	159	68	45
3	195	205	168	159	42	38
6	192	204	168	159	35	35
$280 \text{ }^\circ\text{C}$						
1	200	209	167	156	68	36
3	192	201	167	156	34	34
6	192	200	167	156	33	33

Our experiments tested the manufactured samples. They should be compared with Katta's results obtained for the *2nd* heating cycle [154]. The results of the *1st* heating cycle are useful in terms of melting latent heat and crystallisation enthalpy. In our experiments,  $T_f$  of the single-layer cases is about  $208 \text{ }^\circ\text{C}$ . According to Katta [154], the PA6 powder used in our experiments is almost virgin because this agrees with the corresponding  $T_f$  of iterations 0 and 1 of the *2nd* heating cycle. In the multi-layers manufacturing cases, the measured  $T_f$  equal to  $210 \text{ }^\circ\text{C}$  agrees with the results of the *2nd* heating cycle since iteration 2. It means that in the multi-layers manufacturing cases the SLS process is much longer than the single-layer ones so that the PA6 powder used becomes thermally aged.

In terms of melting enthalpy and crystallinity, quantitative comparison of our results with the results of Katta [154] and Ruggi et al [128] remains difficult because crystallinity depends heavily on the cooling conditions while the cooling conditions in any SLS processes are completely different from those under DSC. Nevertheless we can compare qualitatively our results of multi-sweep and multi-layer cases with the study of Ruggi et al [128] on the annealing effects. Ruggi et al [128] showed that at the end of their SLS process the crystallinity obtained is about  $20\%$  and that at the end of  $1 \text{ h}$  annealing it increases to  $23\%$ . Given the difference between the manufactured samples, the crystallinities that we measured are equal to  $\sim 20\%$  in multi-sweep and single-layers cases and  $\sim 23\%$  in multi-sweep and multi-layer cases (Fig. A.1d) and agree reasonably with the results of Ruggi et al [128].

## A.2 Single-sweep and single-layer cases

We are interested in the kinetics of the crystallisation process and time evolution of the relative crystallization rate. The crystallization rate is calculated by the non-isothermal crystallization

Table A.2: Process parameters for simulation.

$K_0 (s^{-3})$	$U^{*a}$	$K_g (K^2)$	$T_f (K)$	$T_g (K)$
$7.1 \times 10^{18}$	7263	$2.9 \times 10^5$	496	330

model presented in Chapter 2, and the involved physical properties are calculated by the parallel model. The parameters used are listed in Table A.2.

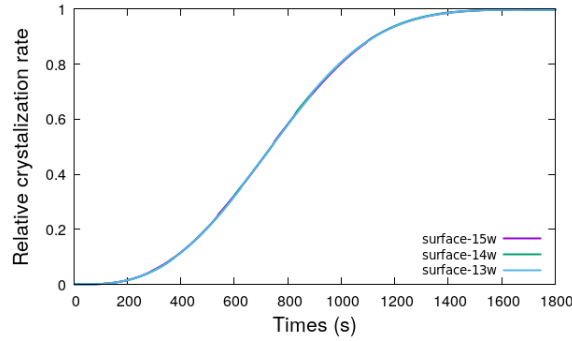


Figure A.6: Time evolution of relative crystallinity versus laser power (central of laser).

Time evolution of relative crystallization rate is displayed in Fig. A.9 for three laser powers (13 W, 14 W and 15 W) in a single-sweep situation. All the curves have an "S" shape, the relative crystallization rate is small and the crystallization process is slow at the beginning, the crystallization rate increases quickly in the middle part and it then slows down at the end. The three curves are similar: laser power has no influence on time evolution of crystallization rate.

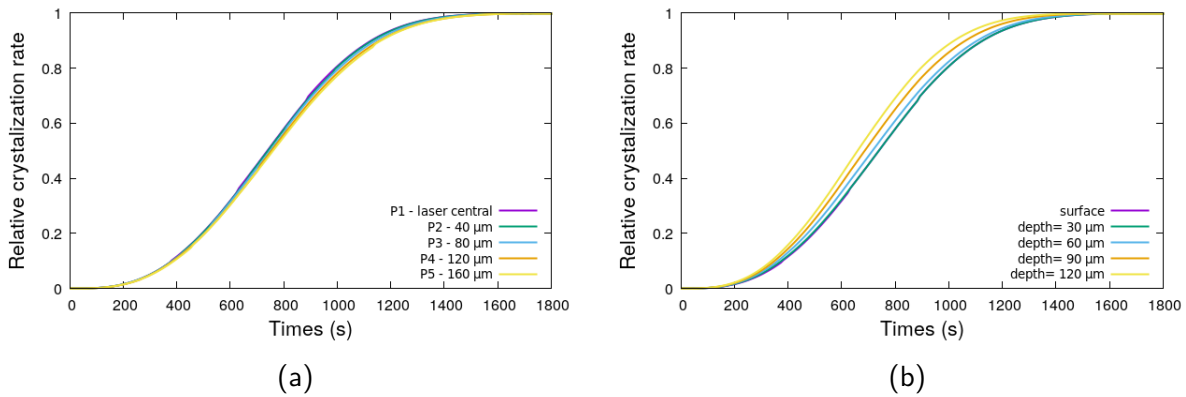


Figure A.7: Time evolution of relative crystallisation rate at (a) several surface positions with different distance to the path of laser center, (b) the laser central with different depths to the surface (laser power of 13 W).

Fig. A.7a displays time evolution of relative crystallization rate at several surface positions. Position 1 is located on the path of the laser beam center and positions 2-5 are off the center. Relative crystallization rate at the center of the laser indicates a crystallisation process slightly quicker than that at other surface positions. The maximum temperature is observed at position 1 and promotes the nucleation phenomenon. Fig. A.7b displays time evolution of relative crystallization rate at several depth positions below the path of the laser beam center, the the crystallisation kinetics is quicker at deeper position because of lower temperature.

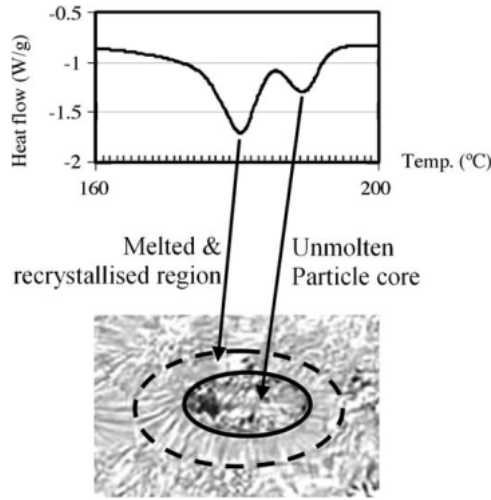


Figure A.8: Molten zone [156].

Two steps are necessary for estimating the crystallinity in a SLS process. It is necessary first to determine whether the crystallization process is finished and make sure that it is finished. It is then necessary to calculate the melting percentage in which the crystallization takes place. As shown in Fig. A.8, only the edge part of the particle is melted and the central part of the particle is not melted because energy supplied only melts the edge of the particle. The crystallinity of the manufactured samples depends on how the melted polymer crystallises and is also contributed by the non-melted particles incorporated in the samples. To predict the crystallinity of the product, one must know the molten percentage in the product, the polymer aging and the crystallisation process. Therefore, the heating cycles (heating time, maximum temperature, and high temperature keeping time) and the cooling cycles are important factors for predicting the crystallinity. According to the crystallinity isotherm curves, 1600 s is needed to reach 100 % of relative crystallization rate. In experiments, the SLS machine is kept for a time longer enough to finish the crystallization process. Therefore, the crystallinity of the samples depends on the percentage of the non-melted polymer ( $X_{nonmelted}$ ), the corresponding melting enthalpy, the percentage of the melted polymer ( $X_{melted}$ ) and the corresponding melting enthalpy [157]:

$$\Delta H = \Delta H_1 X_{melted} + \Delta H_2 X_{nonmelted} \quad (\text{A.2})$$

where  $H_1$  and  $H_2$  are respectively the melting enthalpy of the melted and crystallised polymer and the melting enthalpy of the non-melted polymer.

The percentage of the melted polymer corresponds, in the simulations, to the local maximum liquid volume fraction. With the linear relationship  $f_l(T) = (T - T_s)/(T_l - T_s)$  where  $T_s$ , the initial melting temperature, is equal to 471 K and  $T_l$ , the final melting temperature, is equal to 487 K,  $f_l$  is calculated in the simulations and the maximum during a SLS process can be easily calculated. We have then

$$\Delta H = \Delta H_1 f_l + \Delta H_2 (1 - f_l) \quad (\text{A.3})$$

$\Delta H_2$  is usually known for the virgin PA6 powder and equal to 68 J/g for PA6 powder and  $\Delta H_1$  is usually unknown as it depends heavily on the cooling or crystallisation process. The cooling process under a DSC is usually performed with 10 °C/min and the corresponding  $\Delta H_1$  in the range from 34 J/g to 48 J/g according to the work of Ruggi [128]. But the  $\Delta H_1$  corresponding to any SLS process is difficult to be obtained because the maximum of  $f_l$  is for most of the times different from 1.

As it is difficult to obtain  $\Delta H_1$  of the samples and we do have access to  $\Delta H$  of the samples, one idea is to use Eq. (A.3) and the numerical prediction of  $f_l$  maximum to estimate  $H_1$ .

### A.3 Multi-sweep : single-layer and multi-layer cases

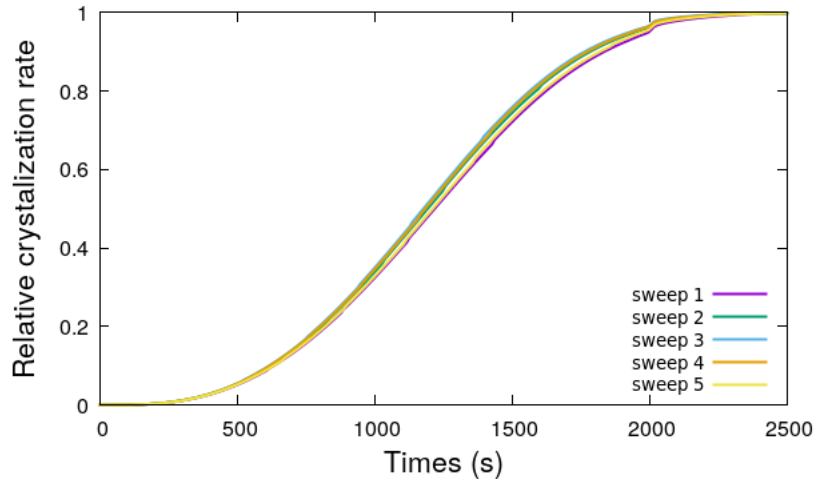


Figure A.9: Time evolution of relative crystallisation rate at the five surface positions in multi-sweep and single-layer cases.

In a multi-sweep and single-layer case, crystallisation process is modeled for an energy density of  $1.7 \text{ J/cm}^2$ . Fig. A.9 illustrates the time evolution of relative crystallization rate at the five surface positions: the curves are similar. The crystallization process ends at time about  $2500 \text{ s}$ , this is longer than  $1500 \text{ s}$  obtained in a single-sweep and single-layer case.

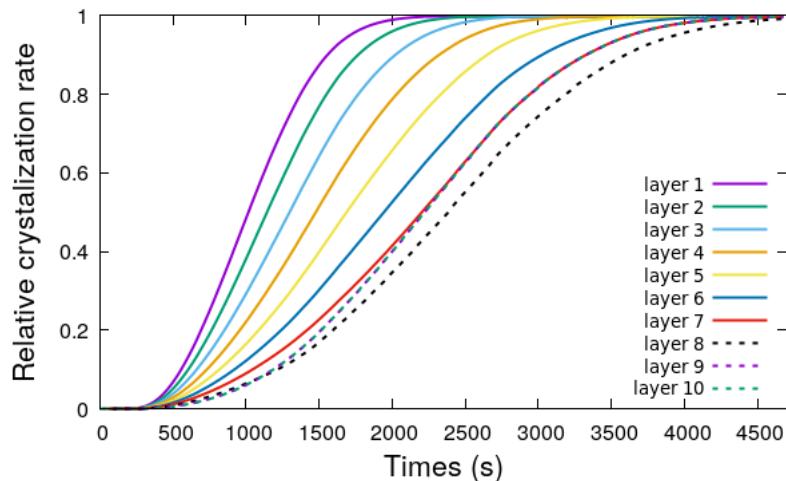


Figure A.10: Time evolution of relative crystallisation rate in the 10-layer case.

The crystallization simulation in multi-sweep and 10-layer cases is performed for the energy density of  $1.7 \text{ J/cm}^2$ . Fig. A.10 shows time evolution of relative crystallisation at each layer's surface, the relative crystallization rate decreases from layer-1 to layer-8 and increases slightly with layer-9 and layer-10. We see again that the crystallisation process becomes longer:  $4500 \text{ s}$  are necessary for finishing the crystallization.

# Appendix B

## Laser beam with $n_\sigma = 0.7071$

In the scattering section of Chapter 2, the photons' initial distribution was following the Gaussian relationship with  $n_\sigma$  equal to 1. This photons' initial distribution leads to a fraction of 63.2 % of the laser power transmitted within the laser's radius. This means that  $n_\sigma = 1$  defined a laser radius at 36.8 % of maximum. But the most used definition is the laser beam radius at  $1/e^2$  (13.5 %) of maximum. It means that 86.5 % of the laser power is transmitted within the laser's radius. This can be achieved with  $n_\sigma = 0.7071$ .

After considering the scattering phenomenon by using  $n_\sigma = 0.7071$ , we obtained a new map of the absorbed photons' final distribution, which indicates the region in which the energy brought by the laser beam is absorbed in the powder bed. From the new map we calculated the power distribution map and used data fitting to identify a similar but more complex expression to the Beer-Lambert law:

$$Q = \beta_1(1 - R_e)P\left(\frac{n}{\pi b^2}e^{-\frac{r^2}{b^2}} + \frac{c + az}{\pi b^2}e^{-\frac{9r^2}{b^2}}\right)e^{-\beta_1 z} \quad (\text{B.1})$$

where  $Q$ , the heating power of the laser beam, depends on the radial and vertical positions  $(r, z)$ ,  $P$  is the power of the laser beam. The least square fitting allowed to identify the parameters  $\beta_1$ ,  $a$ ,  $b$ ,  $c$  and  $n$  and obtain  $\beta_1 = 11130 \text{ m}^{-1}$ ,  $a = 9000 \text{ m}^{-1}$ ,  $b = 1.82e - 4 \text{ m}$ ,  $c = 0.93$  and  $n = 0.877$ .

Fig. B.1 displays, in symbols, the absorbed power distribution of the scattering model in the counting volumes and, in lines, that provided by the fitted model. Compared with Fig. 3.5, the laser affected region is smaller: it is limited to the 21st counting volume. The maximum absorbed power is higher in the  $n_\sigma = 0.7071$  case: for the first layer it is equal approximately to  $0.16 \text{ W}$  while in the  $n_\sigma = 1$  case it is equal to  $0.125 \text{ W}$ . The power absorbed by the first layer is equal approximately to  $1.65 \text{ W}$  in both cases.

In the following, we present briefly the main results obtained for a laser power of 15 with  $n_\sigma = 0.7071$  and reveal the differences compared with  $n_\sigma = 1$ .

### B.1 Single sweep case with laser beam of 15 W

Fig. B.2 shows the temperature profiles at several depth positions in a vertical plane normal to the laser trajectory at time equal to  $0.005 \text{ s}$  in both and  $n_\sigma = 1$  cases, they concern the time

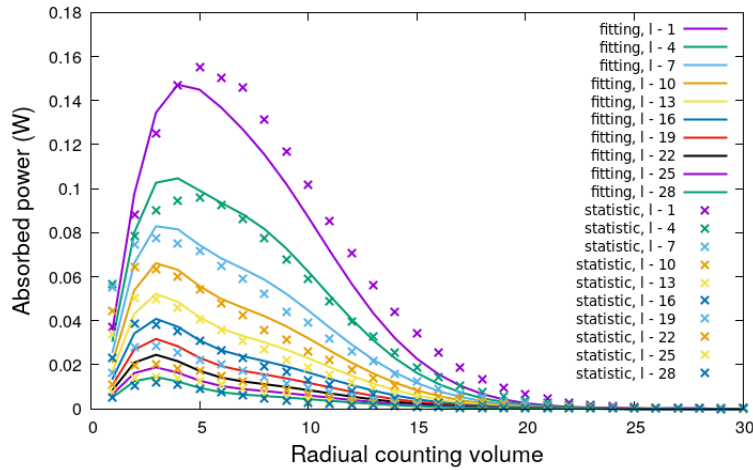


Figure B.1: Distribution of the absorbed power in the counting volumes for a laser beam radius defined at  $1/e^2$  (13.5 %) of maximum. The results of the scattering model and the fitted analytical model are displayed for different vertical layers.

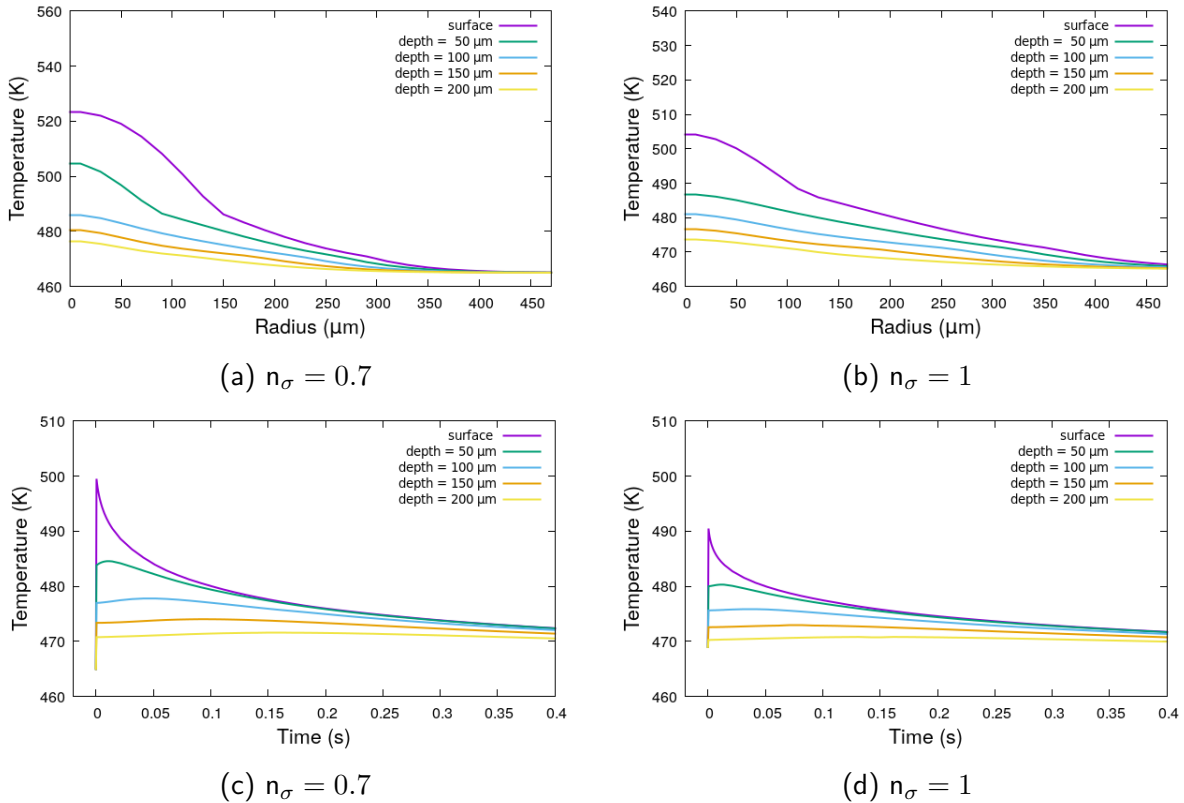


Figure B.2: (a) (b) Instantaneous temperature profiles at several depth positions in the vertical plane normal to the laser trajectory at time = 0.0005 s. (c) (d) Numerical results of averaged temperature in one camera pixel area centered about the trajectory of the laser axis.

evolution of both local temperature (Figs. B.2a and B.2b) and temperature averaged over one pixel area of the IR camera (Figs. B.2c and B.2d). In the case of  $n_\sigma = 0.7071$ , the maximum local temperature at the laser center is equal to 521 K and the horizontal size of influence area extends around 350  $\mu m$ , while for  $n_\sigma = 1$  the maximum local temperature at laser center is equal to 498 K and the influenced width is around 450  $\mu m$  at  $1n_\sigma$ . Fig. B.3 shows the time evolution of temperature averaged over one camera pixel area (460  $\mu m \times 460 \mu m$ ) centered

about the laser axis with  $n_\sigma = 0.7071$  and  $n_\sigma = 1$ . The averaged temperature is higher in the case of  $n_\sigma = 0.7071$  because the laser power is more concentrated within the laser radius with  $n_\sigma = 0.7071$  than with  $n_\sigma = 1$ . Using  $n_\sigma = 0.7071$ , the maximum local temperature is increased while the horizontal influence area of the laser beam is decreased.

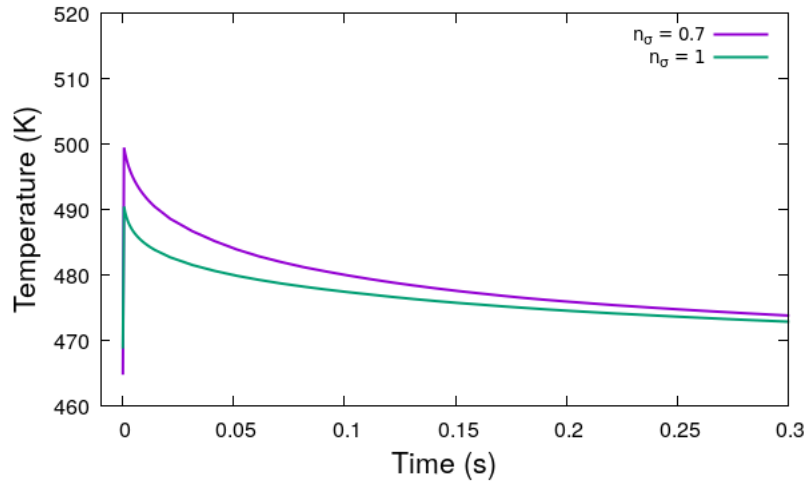
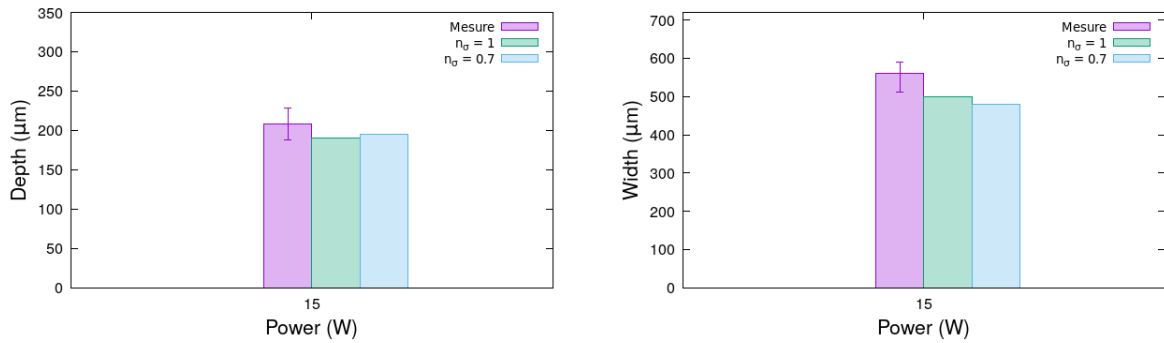


Figure B.3: Time evolution of temperature in one camera pixel area: comparison of the cases with  $n_\sigma = 0.7$  and  $n_\sigma = 1$ .



(a) Depth of the samples.

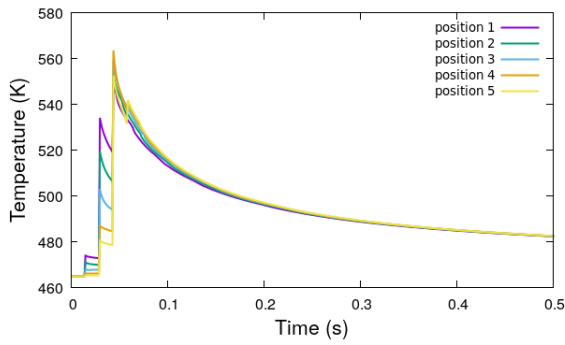
(b) Width of the samples.

Figure B.4: Dimensions of the samples under single-sweep conditions: comparison of numerical predictions with the measurements. Change from  $n_\sigma = 0.7071$  to  $n_\sigma = 1$  has very weak effect on sample dimensions.

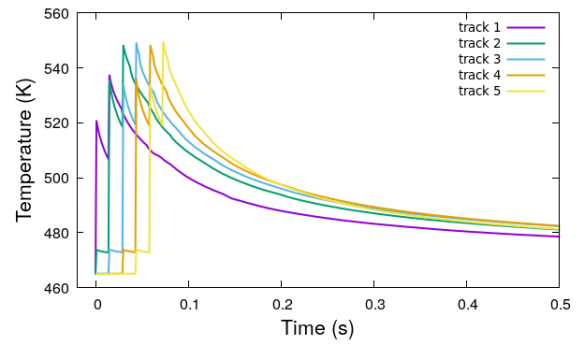
Figs. B.4a and B.4b show the dimensions of the samples obtained with  $n_\sigma = 0.7071$  and  $n_\sigma = 1$ . In the case of  $n_\sigma = 0.7071$ , the sample depth is equal to  $195 \mu m$ , and the sample width is equal to  $480 \mu m$ . In the case of  $n_\sigma = 1$ , the sample depth is equal to  $190 \mu m$ , and the sample width is equal to  $500 \mu m$ . It can be concluded that the width and depth of the samples are only modified slightly when  $n_\sigma$  is decreased from 1 to 0.7071.

## B.2 Multi-sweep case

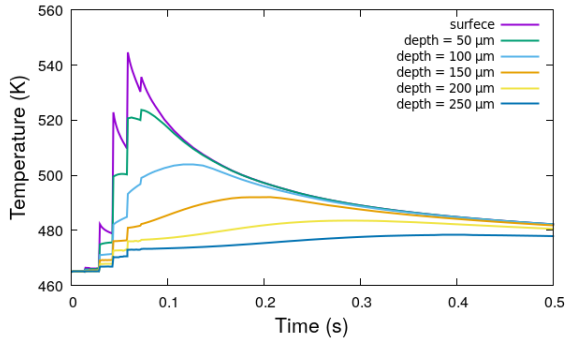
We revisit by using  $n_\sigma = 0.7071$  the case 1 listed in Tab. 4.3 with the initial porosity of 0.3 and the preheating temperature of  $465 K$ .



(a) At the laser tracks' centers.



(b) At the positions 1-5 between track-3 and track-4



(c) At different depth positions under track-3

Figure B.5: Time evolution of temperature at various positions in the domain mid-width plane (Case 1,  $n_\sigma = 0.7071$ ).

Fig. B.5 shows the temperature time evolution at different positions in the  $n_\sigma = 0.7071$  case: the 5 points from track-1 to track-5, the 5 points 1-5 (see Fig. 4.24 for details) and 5 depth positions under track-3. Compared with the case of  $n_\sigma = 1$  (shown in Fig. 4.25 in chapter 4), the maximum local temperature observed at the track center in the case of  $n_\sigma = 0.7071$  is 17 K higher. Fig. B.6 displays the time evolution of surface temperature averaged over one pixel area of the IR camera for  $n_\sigma = 0.7071$  and  $n_\sigma = 1$  and the corresponding measurement. The maximum temperature reached with  $n_\sigma = 0.7071$  is equal to 542 K while for  $n_\sigma = 1$  it is equal to 542 K. The averaged temperature in one pixel area of the IR camera is about 10 K higher in the case of  $n_\sigma = 0.7071$ .

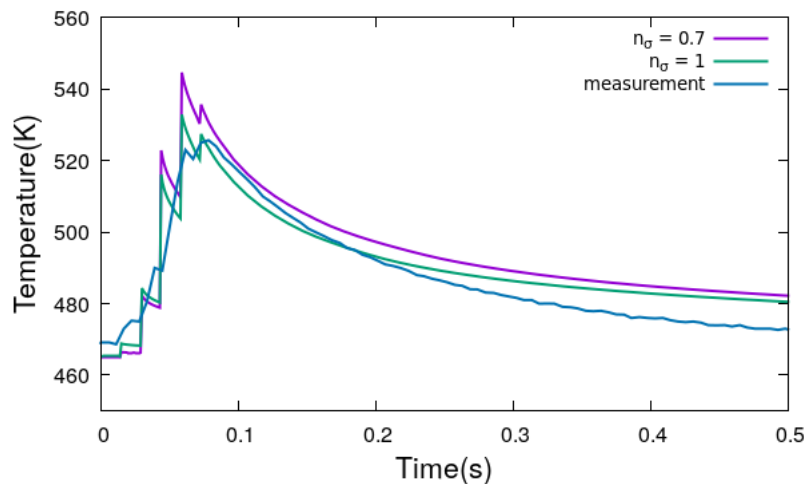


Figure B.6: Time evolution of temperature averaged over one camera pixel area.

### B.3 Multi-layer case

As shown in Chapter 5, the time evolution of surface temperature is independent for each layer. The effects of varying  $n_\sigma$  from 1 to 0.7071 on temperature field remain the same: increase in maximum temperature.

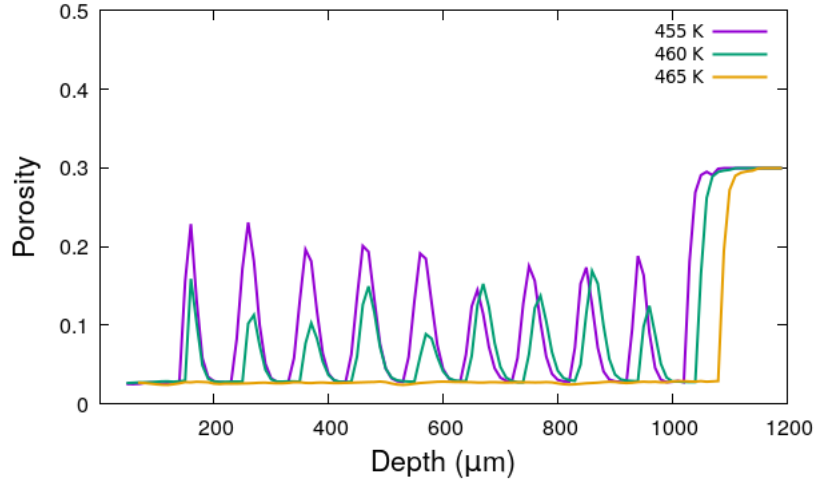


Figure B.7: Vertical profiles of porosity averaged in the  $x - y$  plane obtained with  $n_\sigma = 0.7071$  and the preheating temperature varying from 455  $K$  to 465  $K$ .

In terms of the porosity distribution for  $n_\sigma = 0.7071$ , Fig. B.7 displays the vertical profiles of porosity averaged in the  $x - y$  plane obtained with the preheating temperature varying from 455  $K$  to 465  $K$ , while the initial porosity is kept to be equal to 0.3. Increasing the preheating temperature promotes completing the coalescence process and decreases the samples' porosity. Compared with the porosity distribution obtained with  $n_\sigma = 1$  shown in Fig. 5.27, the vertical distribution of the porosity averaged in the  $x - y$  plane for the preheating temperature of 455  $K$  and 460  $K$  is similar to the results obtained with  $n_\sigma = 1$ . It is only for the preheating temperature of 465  $K$  that the averaged porosity with  $n_\sigma = 0.7071$  decreases to the level of 3% for the whole depth and that there is no longer the oscillatory profile.

In summary, the scattering model obtained with  $n_\sigma = 0.7071$  transmits within the laser beam radius more power than the one obtained with  $n_\sigma = 1$ . The numerical simulations performed using the scattering model with  $n_\sigma = 0.7071$  confirm the conclusions drawn by using the scattering model with  $n_\sigma = 1$ . The maximum temperature is the most sensitive quantity to the models used: the model with  $n_\sigma = 0.7071$  induces higher maximum temperature.



## FOLIO ADMINISTRATIF

### THESE DE L'INSA LYON, MEMBRE DE L'UNIVERSITE DE LYON

NOM : ZHANG  
(avec précision du nom de jeune fille, le cas échéant)

DATE de SOUTENANCE : 14/12/2022

Prénoms : Lan

TITRE : Modeling of additive manufacturing processes: case of polymer laser sintering

NATURE : Doctorat

Numéro d'ordre : 2022ISAL0123

Ecole doctorale : MEGA

Spécialité : Mécanique des fluides

#### RESUME :

Le présent travail s'intéresse à l'un des procédés de Fabrication Additive, SLS (Selective Laser Sintering) des poudres de polymère. Il a pour objectif d'améliorer, qualifier et valider l'outil numérique développé d'une part et d'autre part de comprendre et améliorer les procédés SLS. L'outil numérique développé prend en compte l'interaction laser-poudres de polymère, le processus de fusion, la coalescence, la diffusion d'air, l'évolution de la porosité, et la cristallisation. Afin de qualifier les travaux numériques réalisés, les travaux expérimentaux sont également réalisés pour mesurer la température de surface à l'aide d'une caméra IR, les dimensions des échantillons et la distribution de la porosité dans les échantillons fabriqués à l'aide de la tomographie à rayon X.

L'important travail de modélisation a été réalisé sur l'interaction laser-poudres de polymère: la théorie de Mie et la méthode de Monte-Carlo sont associées pour modéliser la diffusion du laser et proposer des modèles de diffusion. Afin de qualifier les modèles de diffusion proposés, ils sont utilisés dans des simulations numériques et les résultats obtenus sont confrontés avec les mesures expérimentales et les résultats issus du modèle de Beer-Lambert. Le modèle de diffusion distribue la puissance d'un laser sur une zone plus grande et moins profonde par rapport au modèle de Beer-Lambert et son utilisation en simulation permet une meilleure prédiction sur la température de surface et l'épaisseur des échantillons fabriqués.

Les effets des paramètres comme facteur d'anisotropie, porosité du lit et rayon moyen des particules sur les modèles de diffusion ont été étudiés. Les effets des paramètres de procédé comme puissance du laser, vitesse de scan, espacement des scans, longueur scannée, porosité du lit, et température du préchauffe sur les échantillons fabriqués sont aussi explorés.

MOTS-CLÉS : SLS (Selective Laser Sintering), modélisation numérique, modèle de diffusion, distribution et évolution de la température, retrait, porosité.

Laboratoire (s) de recherche : CETHIL

Directeur de thèse: Boutaous Mhamed, Xin Shihe

#### Composition du jury :

RANDRIANALISOA Jaona	Maître des Conférences HDR	Université de Reims Champagne-Ardenne	Rapporteur
SCHMIDT Fabrice	Professeur des Universités	IMT Mines Albi	Rapporteur
BOYER Séverine	Chargé de recherche	CEMEF Mines de Paris	Examinatrice
HAMILA Nahienne	Professeur des Universités	Ecole nationale d'ingénieurs de Brest	Examineur
Boutaous Mhamed	Maître de Conférences HDR	INSA-Lyon	Directeur de thèse
Xin Shihe	Professeur des Universités	INSA-Lyon	Co-directeur de thèse

